Fast pyrolysis oil hydrodeoxygenation kinetics using lignin-derived model compounds

Alexandra Bouriakova

Supervisor: Prof. dr. ir. Joris Thybaut
Counsellor: Daria Otyuskaya

Master's dissertation submitted in order to obtain the academic degree of
Master of Science in Chemical Engineering

Department of Chemical Engineering and Technical Chemistry
Chairman: Prof. dr. ir. Guy Marin
Faculty of Engineering and Architecture
Academic year 2014-2015

UNIVERSITEIT
GENT

Fast pyrolysis oil hydrodeoxygenation kinetics using lignin-derived model compounds

Alexandra Bouriakova

Supervisor: Prof. dr. ir. Joris Thybaut
Counsellor: Daria Otyuskaya

Master's dissertation submitted in order to obtain the academic degree of
Master of Science in Chemical Engineering

Department of Chemical Engineering and Technical Chemistry
Chairman: Prof. dr. ir. Guy Marin
Faculty of Engineering and Architecture
Academic year 2014-2015

UNIVERSITEIT
GENT

UNIVERSITEIT GENT

FACULTY OF **ENGINEERING AND ARCHITECTURE**

Department of Chemical Engineering and Technical Chemistry
Laboratory for Chemical Technology
Director: Prof. Dr. Ir. Guy B. Marin

Laboratory for Chemical Technology

Declaration concerning the accessibility of the master thesis

Undersigned,

Alexandra Bouriakova

Graduated from Ghent University, academic year 2014-2015 and is author of the master thesis with title:

Fast pyrolysis oil hydrodeoxygenation kinetics using lignin-derived model compounds

22/05/2015

Alexandra Bouriakova

Dankwoord

Het lijkt alsof het gisteren was, dat ik mijn eerste voet binnenzette in de Plateau. Enkele jaren later is het einde van mijn thesis en bijgevolg mijn opleiding in zicht. Er zijn enkele mensen die ik graag wil bedanken voor hun directe of indirecte hulp bij het verwezenlijken van deze thesis en/of hun steun tijdens de opleiding.

Allereerst wil ik prof. dr. ir. Guy B. Marin bedanken voor de kans om dit boeiend onderzoek te verrichten op het Laboratorium voor Chemische Technologie.

Daarnaast gaat een woord van dank uit naar mijn promotor, prof. dr. ir. Joris W. Thybaut, voor de begeleiding doorheen dit thesisjaar. Niet alleen wist u raad te bieden op academisch vlak voor mijn thesis maar ook voor MaChT kon ik op uw steun rekenen.

Special thanks go to my coach ir. Daria Otyuskaya. I appreciate your input and enthusiasm on this work very much. Thank you for the support during the year, as well as for improving my Russian vocabulary. Further, I would like to thank some people from the CaRE-group: ir. Tapas Rajkhowa and ir. Jolien De Waele for the technical support and the troubleshooting on the HTK-1, dr. ir. Kenneth Toch and ir. Chetan Raghuveer for the contributions in the field of kinetic modeling and all the other members for making every day an enjoyable day. An extra word of thanks goes to the technical staff of the laboratory for the assistance on the setup.

Daarnaast ook een woordje dank voor mijn vrienden en studiegenoten. Evy en Christof, hoewel ik jullie niet heb kunnen overtuigen dat waterstofbruggen veel interessanter zijn dan metalen bruggen, zouden mijn burgiejaren er een pak saaier uitgezien hebben zonder jullie. Spijtig genoeg heeft de frequentie waarop we elkaar zagen wat geschommeld het voorbije jaar, maar ik zal dat ruimschots goed maken met een lekker etentje (of twee). Ook wil ik Brigitte, Laurenz en Tine bedanken voor de sfeer in ons lokaaltje. Verder bedank ik ook *traiteur* Jenoff en Jessica voor de nodige drank en spijs tijdens de koffie-, middag- en avondpauzes! Ook een dankjewel voor de medebestuursleden van MaChT: Lies, Florence, Timothy, Anton en Jasper. Bedankt voor de afwisseling met het intensive thesiswerk. Ik denk dat we weer mogen spreken van een MaChTig jaar!

Также я хочу от всей души поблагодарить свою маму. Спасибо за каждую даннуювозможность и за то что ты всегда позволяешь мне идти своим путем.

En tot slot, Jean-Luc, bedankt om het afgelopen jaar mijn thesiskuren met de mantel der liefde te bedekken. Ik weet niet of je altijd even goed begreep waarover ik het had, maar je slaagde er telkens in om een glimlach op mijn gezicht te toveren wanneer het eens wat moeilijker ging. Nu mijn studententijd achter de rug ligt, kijk ik er naar uit om met jou aan het echte leven te beginnen.

Fast pyrolysis oil hydrodeoxygenation kinetics using lignin-derived model compounds

by

Alexandra BOURIAKOVA

Master's dissertation submitted in order to obtain the academic degree of
Master of Science in Chemical Engineering

Academic year 2014-2015

Supervisor: prof. dr. ir. Joris W. THYBAUT
Counsellor: ir. Daria OTYUSKAYA

Ghent University
Faculty of Engineering and Architecture
Department of Chemical Engineering and Technical Chemistry
Chairman: prof. dr. ir. Guy B. MARIN

Abstract In this work, catalytic hydrodeoxygenation (HDO) of anisole, a lignin-derived model compound for fast pyrolysis oil, has been investigated in an ideal plug flow reactor at gas phase conditions. Intrinsic kinetic experiments were carried out on a non-sulfided 15wt.%Co-3.8wt.%Mo/γ-Al_2O_3 and a NiCu/ZrO_2 catalyst. Demethylation and methyl transfer are the main reactions on the CoMo/γ-Al_2O_3, while subsequent ring-hydrogenation was also observed on the NiCu/ZrO_2. The intrinsic experimental dataset was used for kinetic modeling of the HDO of anisole. The parameter estimation for CoMo/γ-Al_2O_3 has been performed, resulting in significantly and physically relevant parameters. A kinetic model for NiCu/ZrO_2 has been developed.

Keywords hydrodeoxygenation, anisole, kinetic model, parameter estimation

Fast pyrolysis oil hydrodeoxygenation kinetics using lignin-derived model compounds

Alexandra Bouriakova

Supervisor(s): Daria Otyuskaya, Joris W. Thybaut

Abstract **In this work, catalytic hydrodeoxygenation (HDO) of anisole, a lignin-derived model compound for fast pyrolysis oil, has been investigated in an ideal plug flow reactor at gas phase conditions. Intrinsic kinetic experiments were carried out on a non-sulfided 15wt.%Co-3.8wt.%Mo/γ-Al_2O_3 and a NiCu/ZrO_2 catalyst. Demethylation and methyl transfer are the main reactions on the CoMo/γ-Al_2O_3, while subsequent ring-hydrogenation was also observed on the NiCu/ZrO_2. The intrinsic experimental dataset was used for kinetic modeling of the HDO of anisole. The parameter estimation for CoMo/γ-Al_2O_3 has been performed, resulting in significantly and physically relevant parameters. A kinetic model for NiCu/ZrO_2 has been developed.**

Keywords **fast pyrolysis oil, anisole, hydrodeoxygenation, intrinsic kinetics**

I. Introduction

Due to the depletion of fossil fuels and the accelerated rate of energy consumption[1] the interest in renewable energy sources, such as lignocellulosic biomass, has increased. Lignin, a main component of lignocellulosic biomass[2], can be converted into phenolic monomers via different strategies[3]. One of the most promising valorization techniques is fast pyrolysis[4, 5]. Further catalytic upgrading by means of hydrodeoxygenation (HDO) is necessary due to the high oxygen content, poor chemical stability, and immiscibility with transportation fuels[4].

Typical HDO catalysts are Mo-based catalyst, noble metal catalyst or non-noble transition metal catalysts[6, 7, 8]. The latter are alternatives both for noble catalyst types, due to the relatively low cost, and for sulfided catalyst types, due to the absence of the sulfiding pretreatment[6, 9].

In this work, experiments on anisole HDO are performed to provide insight into the reaction mechanism and used as an input for the construction of a kinetic model.

II. Procedures

A. Experimental

An experimental investigation of anisole HDO over a non-sulfided 15wt.%Co-3.8wt.%Mo/γ-Al_2O_3 and a NiCu/ZrO_2 catalyst have been performed in an ideal plug flow reactor at gas phase conditions. Catalyst particles with diameters between 400 and 600 µm are used in the experiments. The catalyst bed is diluted to avoid heat transfer limitations. The external and internal mass transport limitations remain absent according to the calculated Carberry number and Weisz modulus[10]. The operating conditions used in the experiments are shown in Table 1. The feed consists of anisole and hydrogen as reactants, *n*-hexane as solvent and N_2 as diluent. After a stabilization time of about 1 h, the reactor effluent is sent on-line to the analysis section. The analysis is performed with a FID-equipped GC (Agilent Technologies 6850 series II), with a 60 m DB-1 column (0.25 mm i.d.) with a 0.25 µm dimethylpolysiloxane film.

The weight percentages of the identified components in the reactor effluent are calculated according to

$$x_k = \frac{A_k CF_k}{\sum_{j=1}^{n_C} A_j CF_j} \quad (1)$$

With x_k the weight fraction of the considered component *k*, A_k the surface area on the chromatogram and CF_k the determined calibration factor and n_C the number of components. In the first data set ethane is used as internal standard, in the second, *n*-octane, to confirm that the mass and elemental balance closed within 5 %.

For further data treatment the conversion of a reactant X_A, the selectivity of this reactant A towards product B, $S_{B,A}$, and the yield of a certain product B, $Y_{B,A}$ are calculated.

$$X_A = \frac{F_{A,0} - F_A}{F_{A,0}} \quad (2)$$

$$S_{B,A} = \frac{a_{t,B}(F_B - F_{B,0})}{a_{t,A}(F_{A,0} - F_A)} \quad (3)$$

$$Y_{B,A} = S_{B,A} X_A \quad (4)$$

With $a_{t,j}$ the number of t atoms in component j, $F_{j,0}$ the molar inlet flow rate of component j [mol s^{-1}] and F_j the molar outlet flow rate of component j [mol s^{-1}].

B. Modeling

The outlet flow rates of tubular reactors are modeled using an isobaric and isothermal one-dimensional pseudo-homogenous plug flow reactor model[11]. Radial and axial diffusion are neglected. These assumptions lead to an expression for the axial flow profile for a component j through the reactor, in which F_j is the molar outlet flow rate of component j, W is the catalyst weight and R_j is the net production rate of component j.

$$\frac{dF_j}{dW} = R_j \quad (5)$$

Table 1. Operation conditions for HDO experiments.

	CoMo	*NiCu*
Temperature [K]	548-623	573
Partial pressure anisole [Pa]	150-600	900-1900
H_2/anisole [mol mol^{-1}]	200-400	50-200
Space time [kg_{cat} s mol^{-1}]	500-2500	50-250

E-mail: Alexandra.Bouriakova@UGent.be

The production rates are derived from the kinetic model of which the kinetic parameters are estimated via non-linear regression through the minimization of the weighted sum of square of the residuals (Equation 6). The regression is performed with a commercially available program, Athena Visual Studio, which uses the Levenberg-Marquardt algorithm[12] for the minimization of the sum of squares. This minimization is done by adjusting the model parameter b which is expected to approach the real parameter β when the optimum is reached.

$$SS_{RES} = \sum_{i=1}^{v}\sum_{j=1}^{n} w_i\left(F_{i,j} - \hat{F}_{i,j}\right)^2 \overset{b}{\rightarrow} min \qquad (6)$$

With v the number of responses, n the number of experiments, w_i a weight factor, $F_{i,j}$ the experimental molar outlet flow rate of response i at experiment j [mol s^{-1}] and $\hat{F}_{i,j}$ the corresponding model calculated value [mol s^{-1}].

Statistical *F* tests for the adequacy of the model and the significance of the regression are performed. A high *F* value corresponds to a significant regression, whereas a low *F* value yields an adequate model. The significance of each individual parameter is tested with a *t* test. A high *t* value corresponds to a high significance of the parameter, and hence, a narrow 95 % confidence interval.

III. Results and Discussion

A. Experimental

1) Hydrodeoxygenation of anisole on CoMo/γ-Al_2O_3

An experimental data set containing 18 experiments has been acquired on a CoMo/γ-Al_2O_3 catalyst by systematically varying reaction conditions within intrinsic kinetic regime (Table 1). A product identification by the GC shows that cresol and phenol are the major products of anisole conversion. Small amounts of the deoxygenated products benzene and toluene are observed. The influence of temperature and space time on the anisole conversion and product yields has been explored. The conversion increases from 50 mol% at 548 K to 95 mol% at 623 K (Figure 1). At 548 K and 50 mol% conversion the selectivity towards phenol is 58.4 mol%, towards cresol 40.2 mol%, towards benzene 0.9 mol% and towards toluene 0.4 mol%. The selectivity towards cresol, benzene and toluene increases with increasing temperature, while a decrease is observed for the selectivity of phenol. According to the Arrhenius expression, the HDO rate should increase as the cleavage of the C-O bond requires the most energy[13], resulting in a higher selectivity of the hydrogenated products benzene and toluene. An increasing space time enhances the conversion from 53 mol% for a space time of 722 kg_{cat} s mol^{-1} to 82 mol% for a space time of 2140 kg_{cat} s mol^{-1}. Increasing space time enhances the transalkylation reaction towards cresol.

Thus, the hydrodeoxygenation of anisole over a CoMo/γ-Al_2O_3 catalyst occurs mainly via two pathways: the elimination of the methylgroup or its transfer into the benzene ring. The HDO of cresol and phenol leads to the production of toluene and benzene, respectively. The direct deoxygenation of anisole to benzene does not occur. This is in line with the expectations, since the bond between the aliphatic carbon and oxygen is weaker that that between the aromatic carbon and oxygen[13].

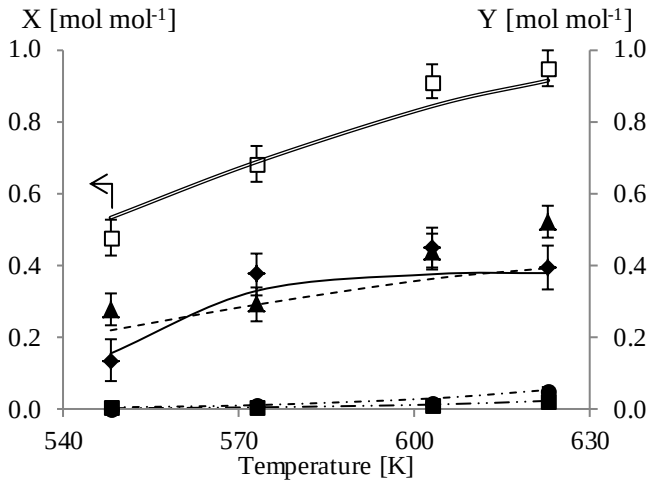

Figure 1. Conversion of anisole (□) and phenol (♦), cresol (▲), toluene (■) and benzene (●) yields as a function of the temperature at 5 MPa and 1170 kg_{cat} s mol^{-1} on CoMo/γ-Al_2O_3. Simulation: anisole (=), phenol (-), cresol (--), benzene (-·), toluene (-··).

2) Hydrodeoxygenation of anisole on NiCu/ZrO_2

A second intrinsic kinetic data set is acquired, containing 35 experiments at 573 K. The HDO of anisole on NiCu/ZrO_2 yield benzene and cyclohexane as main products, small amounts of phenol and traces of cresol, toluene, xylene and methylcyclohexane.

The activity of the catalyst is tested over a longer time on stream. Two deactivation experiments have been performed. A loss in activity of approximately 5% is observed after 12 h on stream. After 50 h on stream the catalyst have lost 50 % of its activity. To maintain the stability during two experiments, a 10 vol% H_2 flow is through the reactor.

An isothermal kinetic dataset is used to investigate the influence of the space time, the inlet partial pressure of anisole and the molar hydrogen to anisole ratio. The conversion increases from 52 mol% for a space time of 66 kg_{cat} s mol^{-1} to 89 mol% for a space time of 140 kg_{cat} s mol^{-1}. The yields of benzene, cyclohexane, toluene and methylcyclohexane increase as a function of the space time. The direct deoxygenation of anisole to benzene is favored by the space time. The hydrogenation of the aromatic ring is enhanced while the methylation of the of the aromatic ring is retained by the increase of space time. The influence of the partial pressure of anisole is investigated in the rage from 1031 Pa to 1584 Pa, which corresponded with a conversion range from 58 mol% to 84 mol%. The higher chemisorbed concentration of anisole results in an increasing demethylation, transalkylation and demethoxylation rate of anisole, and hence, an increased concentration of phenol, cresol and benzene. The yield of cresol decrease as a function of the anisole pressure, together with the increasing yield of toluene and methylcyclohexane, this indicates the HDO of cresol and consecutive hydrogenation to methylcyclohexane. The influence of the molar hydrogen to anisole ratio is investigated 573 K, a space time of 100 kg_{cat} s mol^{-1} and an anisole pressure of 1325 Pa. At this conditions 75 mol% of anisole is converted. With increasing the molar ratio from 90 mol_{H2} $mol_{anisole}^{-1}$ to 186 mol_{H2} $mol_{anisole}^{-1}$ the selectivity towards cyclohexane quadrupled and that of methylcyclohexane doubled. Which is line with the expectations as the higher chemisorbed concentration of hydrogen increases the possibility for reactions with hydrogen.

Based on the obtained data one can suggest that the hydrodeoxygenation of anisole on NiCu/ZrO_2 proceeds via the following steps: the elimination of the methylgroup or its transfer into the aromatic ring, the hydrogenolysis of the $C_{aromatic}$-O bond and the hydrogenation of the aromatic ring. That last is expected as nickel is known for its high hydrogenation capacity[14]. Figure 2 depicts the reaction network on both the catalysts.

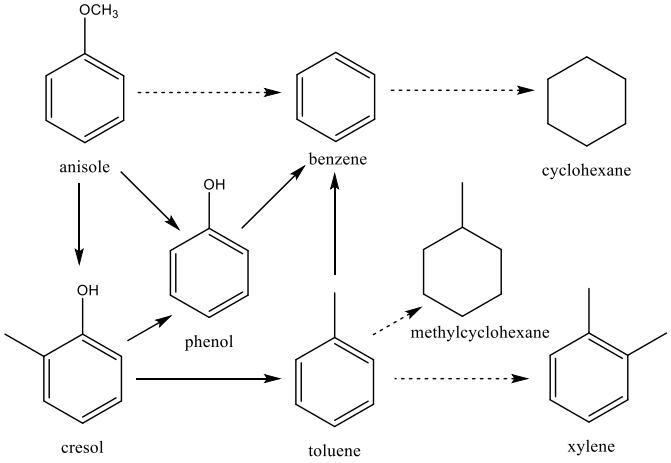

Figure 2. Proposed reaction network for anisole HDO over CoMo/γ-Al_2O_3 (full lines) and NiCu/ZrO_2 (full lines and dashed lines).

B. Modeling

1) Parameter estimation for CoMo/γ-Al_2O_3

Based on the reaction network (Figure 2), three different reaction families are identified, *i.e.* demethylation, transalkylation and HDO (more precisely dehydroxylation). A preliminary power law model is used to determine the activation energies. These are used as initial values for the Langmuir-Hinshelwood (LH) model. It is assumed that the surface reactions are irreversible and the adsorption and the desorption of the reactants and the products is near equilibrium. This resulted in 12 parameters, of which three composed reaction rate coefficient and three activation energies and six adsorption coefficients. The model is found to be significant since the *F* value for model significance is more than three orders of magnitude larger than the tabulated value. No severe correlation between the estimated parameters is found.

The parameter estimates of the LH model are given in Table 2. The high activation energy for HDO is in line with small extent of the hydrodeoxygenated products. The confidence interval of the adsorption coefficient of hydrogen and toluene comprise the zero value. On the other hand, the adsorption coefficient of benzene could not be estimated. Despite this, the performance of the model is acceptable in the experimental range, see Figure 1.

2) Parameter estimation for NiCu/ZrO_2

An empirical power law is proposed to describe the ten reactions from the proposed reaction network (Figure 2). A distinction is made between six reaction families, *i.e.* demethylation, transalkylation, dehydroxylation, methylation, demethoxylation, hydrogenation. Dehydroxylation and demethoxylation are both HDO reactions. This resulted in a model with 25 parameters, of which 6 are reaction rate coefficients and 19 are reaction orders. The regression to the experimental data is found to be significant since the *F* value exceeds the tabulated value. There is no severe correlations between the estimated parameters.

Nine out of 25 parameters are estimated significantly. The rate coefficients are estimated in the following order:

$$k_{demethylation} > k_{hydrogenation} > k_{dehydroxylation} > k_{demethoxylation} > k_{transalkylation} > k_{methylation}$$

Most of the reaction orders are not estimated or comprise the zero value in the confidence interval. There are no clear trends in the reaction orders, since the obtained values are not optimal. Nevertheless, is the performance of the model acceptable for a first attempt. The model is capable of predicting the trends of the main components, which is shown in Figure 3.

In order to improve the model the experimental investigation should be continued to get more insight into the reaction mechanism. The data set on the NiCu/ZrO_2 catalyst should be extended by investigating the influence of the temperature and total pressure.

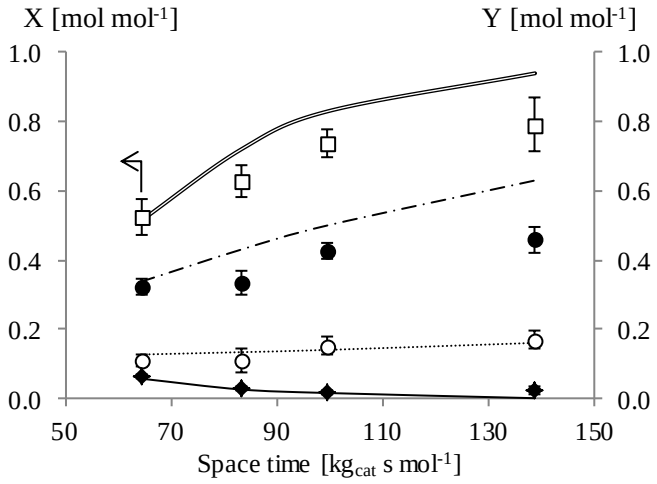

Figure 3. Conversion of anisole (□) and benzene (●), cyclohexane (○) and phenol (♦) yields as a function of the space time at 573 K, an inlet partial pressure of anisole of 1325 Pa and H_2/anisole = 125 mol mol^{-1} on NiCu/ZrO_2. Simulation: anisole (=), benzene(˙·), cyclohexane (··) and phenol (-).

Table 2. Parameter estimates of the LH kinetic model with the corresponding 95% individual confidence interval determined by non-isothermal regression to the experimental dataset on a CoMo/γ-Al_2O_3 catalyst.

Parameter	*Value*	*Parameter*	*Value*
$A'_{demethylation}$	140.41 ± 78.40 µmol g^{-1} s^{-1}	$K_{anisole}$	52.62 ± 12.64 MPa^{-1}
$A'_{transalkylation}$	36.07 ± 30.57 s^{-1}	$K_{benzene}$	0.11 MPa^{-1}
A'_{HDO}	699.59 ± 319.60 µmol g^{-1} s^{-1}	K_{cresol}	0.18 ± 0.09 MPa^{-1}
$E_{a,demethylation}$	41.43 ± 30.05 kJ mol^{-1}	K_{H_2}	26.25 ± 49.82 MPa^{-1}
$E_{a,transalkylation}$	47.78 ± 32.24 kJ mol^{-1}	K_{phenol}	0.43 ± 0.21 MPa^{-1}
$E_{a,HDO}$	79.67 ± 18.57 kJ mol^{-1}	$K_{toluene}$	0.55 ± 14.52 MPa^{-1}

IV. Conclusion and Future work

This work aims on the experimental investigation of the intrinsic reaction kinetics and the construction of a kinetic model for fast pyrolysis oil hydrodeoxygenation using a lignin-derived model compound, *i.e.* anisole. The HDO of anisole is investigated on two different catalysts, a non-sulfided $CoMo/\gamma\text{-}Al_2O_3$ and a $NiCu/ZrO_2$, in an ideal plug flow reactor at gas phase conditions. The $CoMo/\gamma\text{-}Al_2O_3$ catalyst yields mainly phenol and cresol, while a larger HDO extent is observed on the $NiCu/ZrO_2$. This catalyst also shows activity toward hydrogenation.

A preliminary power law model is proposed to describe the overall reaction kinetics, whereas the Langmuir-Hinshelwood model is used to describe the interactions with the catalyst surface. The regression of the kinetic model to the experimental data was rather difficult to perform due to the large number of parameters. Nevertheless, the first simulations with the estimated parameters are capable in predicting the experimentally observed trends.

Acknowledgements

This paper reports work undertaken in the context of the project "FASTCARD, FAST Industrialisation by CAtalysts Research and Development". FASTCARD is a Large Scale Collaborative Project supported by the European Commission in the 7th Framework Programme (GA no 604277).

References

1. International Energy, A., World Energy Outlook 2013. **2013**.

2.Bridgwater, A. V., Review of fast pyrolysis of biomass and product upgrading. *Biomass and Bioenergy* **2012,** 38, (0), 68-94.

3.Naik, S. N.; Goud, V. V.; Rout, P. K.; Dalai, A. K., Production of first and second generation biofuels: A comprehensive review. *Renewable and Sustainable Energy Reviews* **2010,** 14, (2), 578-597.

4.Bridgwater, A. V., Upgrading Biomass Fast Pyrolysis Liquids. *Environ. Prog. Sustain. Energy* **2012,** 31, (2), 261-268.

5.Venderbosch, R. H.; Prins, W., Fast pyrolysis technology development. *Biofuels, Bioproducts and Biorefining* **2010,** 4, (2), 178-208.

6.Furimsky, E., Catalytic hydrodeoxygenation. *Applied Catalysis A: General* **2000,** 199, (2), 147-190.

7.Wildschut, J.; Mahfud, F. H.; Venderbosch, R. H.; Heeres, H. J., Hydrotreatment of Fast Pyrolysis Oil Using Heterogeneous Noble-Metal Catalysts. *Industrial & Engineering Chemistry Research* **2009,** 48, (23), 10324-10334.

8.Bykova, M. V.; Ermakov, D. Y.; Khromova, S. A.; Smirnov, A. A.; Lebedev, M. Y.; Yakovlev, V. A., Stabilized Ni-based catalysts for bio-oil hydrotreatment: Reactivity studies using guaiacol. *Catalysis Today* **2014,** 220–222, (0), 21-31.

9.Mortensen, P. M.; Grunwaldt, J. D.; Jensen, P. A.; Knudsen, K. G.; Jensen, A. D., A review of catalytic upgrading of bio-oil to engine fuels. *Applied Catalysis A: General* **2011,** 407, (1–2), 1-19.

10.Berger, R. J.; Stitt, E. H.; Marin, G.; Kapteijn, F.; Moulijn, J., Eurokin. Chemical Reaction Kinetics in Practice. *CATTECH* **2001,** 5, (1), 36-60.

11.Marin, G. B. *Chemical Reactors: Fundamentals and applications*; Ghent University: 2014.

12.Studio, A. V. *Programming Guide: process modeling, paramter estimation and optimization.*

13.Luo, Y. R., *Comprehensive Handbook of Chemical Bond Energies*. Taylor & Francis: 2007.

14.Yakovlev, V. A.; Khromova, S. A.; Sherstyuk, O. V.; Dundich, V. O.; Ermakov, D. Y.; Novopashina, V. M.; Lebedev, M. Y.; Bulavchenko, O.; Parmon, V. N., Development of new catalytic systems for upgraded bio-fuels production from bio-crude-oil and biodiesel. *Catalysis Today* **2009,** 144, (3–4), 362-366.

Table of content

List of figures

List of tables

List of symbols

Acronyms

AVS	Athena Visual Studio
EOS	equation of state
FID	flam ionization detector
GC	gas chromatography
HDN	hydrodenitrogenation
HDO	hydrodeoxygenation
HDS	hydrodesulphurization
HTK	high throughput kinetic setup
PR	Peng-Robinson equation of state
PSSA	pseudo-steady-state approximation
SRK	Soave-Redlich-Kwong equation of state

Roman symbols

A_j	surface of the peak for component *j*	area
A	composed pre-exponential factor	reaction dependent
$a_{t,j}$	number of *t* atoms in component *j*	-
a_v	specific external surface area of a single catalyst particle	$m_i^2\ m_{cat}^{-3}$
b	vector of least squares estimators	-
b	dilution degree of the catalyst bed	$m_{inert}^3\ m_{inert+cat}^{-3}$
b_i	estimated model parameter	-
Bi_w	Biot number ($= \alpha_w\ d_t\ \lambda_{er}^{-1}$) at the internal wall, ratio of external to internal heat transfer resistance	-
C_j	concentration of component *j*	$mol\ m_{fluid}^{-3}$

CF_j	Calibration factor for component *j*	mol% area^{-1}
c_p	isobaric specific heat capacity	J kg^{-1} K^{-1}
d.f.	degree of freedom	-
d	diameter	m
$D_{A(,eff)}$	(effective) diffusion coefficient of component *A*	m_{fluid}^3 $m_{reactor}^{-1}$ s^{-1}
$D_{a,eff}$	axial effective diffusion coefficient	m_{fluid}^3 $m_{reactor}^{-1}$ s^{-1}
$D_{r,eff}$	radial effective diffusion coefficient	m_{fluid}^3 $m_{reactor}^{-1}$ s^{-1}
d_p	particle diameter	m
d_{pe}	equivalent pellet diameter	m
d_t	reactor diameter	m
$E_{a,i}$	activation energy for reaction *i*	J mol^{-1}
f_m	modified friction factor	-
F_A	molar flow rate of component *A*	mol s^{-1}
F_a	test statistic for lack-of-fit test	-
$F_{A,0}$	molar feed flow rate of component *A*	mol s^{-1}
$F_{i,j}$	molar outlet flow rate of response *i* at experiment *j*	mol s^{-1}
F_s	F value for the significance of a regression	-
$\Delta_r H$	reaction enthalpy	J mol^{-1}
j_D	mass transfer number (= Sh Re^{-1} $Sc^{-1/3}$)	-
j_H	heat transfer number (=Nu Re^{-1} $Pr^{-1/3}$)	-
K	equilibrium coefficient	reaction dependent
$k_{(avg)}$	reaction rate coefficient (at average temperature)	reaction dependent
$k_{f,A}$	mass transfer coefficient of reactant *A*	m_{fluid}^3 m_i^{-2} s^{-1}
k_v	volumetric rate coefficient	reaction dependent
L_{bed}	length of the catalyst bed	m
MM_j	molecular mass of component *j*	kg mol^{-1}

n	reaction order	-
n	number of experiments	-
n	number of reactants	-
N	number of reactions	-
$N_{A,r}$	molar flux of reactant *A* in the radial direction *r*	mol m^{-2} s^{-1}
n_e	number of replicate experiments	-
Nu	Nusselt number (= α_p d_p λ^{-1}), ratio of convective to conductive heat transfer	-
P	pressure	Pa
p_A	partial pressure of component *A*	Pa
P_{tot}	feed pressure	Pa
ΔP	pressure drop	Pa
Pe_a'	Péclet number based on the pellet diameter, (= u d_p $D_{a,eff}^{-1}$)	-
Pe_a	Péclet number for axial effective diffusion based on the length of the catalyst bed (=u L_{bed} $D_{a,eff}^{-1}$)	-
Pe_{mr}'	Péclet number for radial effective diffusion based on the pellet diameter, (=u d_p $D_{r,eff}^{-1}$)	-
Pr	Prandtl number (= c_p μ_g λ^{-1}), the ratio of momentum diffusivity to thermal diffusivity	-
r	radial direction	m
R	universal gas constant, 8.314472	J mol^{-1} K^{-1}
Re	Reynolds number (= ρ_g d_{pe} u_s μ_g^{-1}), ratio of inertial forces to viscous forces	-
r_v	volumetric reaction rate	mol m^{-3} s^{-1}
$R_{v,j}$	volumetric production rate of component *j*	mol m^{-3} s^{-1}
r_w	specific reaction rate	mol kg_{cat}^{-1} s^{-1}
$R_{w,j}$	specific production rate of component *j*	mol kg_{cat}^{-1} s^{-1}

S	surface area through which flow takes place	m^2
$S_{B,A}$	selectivity of reactant *A* towards product *B*	mol%
Sc	Schmidt number ($=\mu_g \rho_g^{-1} D_A^{-1}$), ratio of momentum diffusivity to mass diffusivity	-
Sh	Sherwood number ($= k_{f,A} d_p D_A^{-1}$), ratio of convective to diffusive transport	-
SS	sum of squares	-
T	temperature	K
t	test statistic	-
ΔT_{int}	internal temperature difference between the external surface and the average in the particle	K
ΔT_{film}	temperature difference over the film surrounding the catalyst particle	K
ΔT_{rad}	radial temperature difference	K
u	gas velocity	$m\ s^{-1}$
u_s	superficial velocity	$m_f^3\ m_{reactor}^{-2}\ s^{-1}$
V	volume	m^3
V(b)	covariance matrix	-
W	catalyst mass	kg_{cat}
w_i	diagonal element of the inverse of diagonal variance matrix	-
X_A	fractional conversion of component *A*	mol%
x_A	molar fraction of the component *A*	-
y	vector of measured quantities	-
$Y_{B,A}$	yield of reactant *A* towards product *B*	mol%
$y_{f,A}$	film factor	-

Greek symbols

α	probability level	-
α_p	heat transfer coefficient between the catalyst pellet and the gas	$W\ m_{cat}^{-2}\ K^{-1}$
α_W	heat transfer coefficient between the catalyst bed and the internal reactor wall	$W\ m_{reactor}^{-2}\ K^{-1}$
β	vector of model parameters	-
β_j	model parameter	-
δ_A	dimensionless factor	-
ε_b	bed porosity	$m_{void}^3\ m_{bed}^{-3}$
η	effectiveness factor	-
λ	heat conduction coefficient	$W\ m^{-1}\ K^{-1}$
λ_{er}	effective radial heat conduction coefficient	$W\ m^{-1}\ K^{-1}$
λ_p	thermal conductivity of the catalyst particle	$W\ m^{-1}\ K^{-1}$
μ_g	dynamic gas viscosity	$kg\ m^{-1}\ s^{-1}$
ν	kinematic viscosity	$m^2\ s^{-1}$
ν_j	stoichiometric coefficient of *j*	-
ρ_g	gas density	$kg\ m^{-3}$
$\rho_{i,j}$	binary correlation coefficient	-
ρ_p	density of a catalyst pellet	$kg\ m^{-3}$
τ	space time	$kg_{cat}\ s\ mol_{feed}^{-1}$
φ	Thiele modulus ($= a_v^{-1}\ k_v^{1/2}\ D_A^{1/2}$), ratio of chemical reaction rate to diffusive mass transfer rate	-
Φ_m	mass flux	$kg\ m_{reactor}^{-2}\ s^{-1}$
Φ	Weisz modulus ($= \eta\varphi^2$)	-

Superscripts

0	standard, initial conditions
^	calculated value in objective function
obs	observed
intr	intrinsic

Subscripts

0	initial condition, standard
*	active site
a	axial
A, B, ..	for components A, B, ..
avg	average
b	bulk, bed
dil	dilution
eff	effective
f	fluid
g	gaseous phase
i	interface, internal
intr	intrinsic
IS	internal standard
j	for component *j*
LOF	lack-of-fit
obs	observed
p	particle, pellet
PE	pure error
r	radial

rad	radial
REG	regression
RES	residual
s	(external) surface
t	tube
tot	total
w	wall

Chapter 1

INTRODUCTION

1.1 Justification

The world's population is currently growing at a rate of around 1.14 % per year and already exceeds 7 billion[1]. Together with the increase in welfare levels and the accelerated rate of growth of energy consumption, it causes an exponential growth in the global energy demand. The total primary energy consumption in 2011 was estimated to be around 9 000 Mtoe[2] (megatonnes of oil equivalent), which corresponds to 375 EJ. This value is expected to increase by one-third between 2010 and 2035[3]. Most of the primary energy supply originates from fossil resources such as oil (31.5 %), coal (28.8 %) and natural gas (21.3 %)[3]. Extensive use of these fossil fuels or their derivatives for the production of heat and power increases the greenhouse gases emissions worldwide. The combustion of fossil fuels accounts for two-thirds of global carbon dioxide emissions[4]. The International Energy Agency predicts that the carbon dioxide emissions will increase by 20 % in 2035, which may lead to an average temperature increase of 3.6 K[3].

Due to this climate change effect of carbon dioxide, fossil fuels are now generally recognized as an origin of a serious environmental problem. As a result, the interest in renewable energy sources and the use of biomass has increased rapidly in the last decades. Since the transportation sector is strongly dependent on petroleum, a lot of research is performed in the field of alternative energy sources. Vehicles powered by electricity, solar energy, hydrogen fuel cells and biofuels are being actively researched to reduce the dependence on petroleum[5]. There is a tendency to classify the biofuels into three generations, based on the level of development and commercialization. In contrast to fossil fuels, biofuels provide an environmental advantage: during the plant growth to generate biomass, carbon dioxide is removed from the atmosphere.

The first generation of biofuels are produced from food-based biomass through fermentation of the abstracted oils. The primary sources for bio-ethanol are corn, sugarcane, beet, *etc*., while vegetable oils from rapeseed, sunflower, *etc.* are feeds for the production of biodiesel[6, 7]. These first generation biofuels are characterized by their ability to be blended with petroleum-based fuels. The main drawbacks of first generation biofuels are the competition with the food production and the low energy efficiency. Nevertheless, bio-ethanol and biodiesel are used commercially, with almost 120 billion liters bio-ethanol and 30 billion liters biodiesel produced worldwide in 2014[8]. Currently, the three major producers are the United States of America, Brazil and the European Union[8].

Due to the food-versus-fuel debate, biofuels derived from inedible cellulosic plant matter can offer potential to provide novel biofuels. The lignocellulosic biomass sources are cheap and abundant non-food materials such as woody residues (wood chips) and agricultural residues (*e.g.* straws, bagasse and stover)[6]. Plant biomass can simply be burnt to produce heat and electricity. Further, there is a great potential in the use of plant biomass to produce liquid biofuels. The production of these so-called second generation biofuels is non-commercial at this time, although pilot and demonstration facilities are being developed[7].

Recently, biofuels derived from microalgae have been identified as a third generation of biofuels. Previously, they were lumped in the second generation biofuels[9]. However, due to their higher photosynthetic efficiency, faster growth rate and higher area-specific yield compared with other sources of biomass[6], many suggested that a new category had to be created. One of the other benefits of microalgae cultivation is the lower water demand than land crops. On the other hand, the main disadvantages are the low biomass concentration, the higher capital cost and the rather intensive care[10]. Those factors impedes the commercial implementation of biofuels from microalgae. In 2013, ExxonMobil came to the conclusion that biofuels derived from micro algae will not be viable for at last 25 years[11]. In this respect, second generation biofuels are still extensively investigated as a potential source for energy production.

Several techniques are proposed for lignocellulosic biomass valorization, but the most promising one consists of the following steps: biomass pretreatment, fast pyrolysis followed by adapted upgrading to the desired oil quality. While a lot has already been done in the field of fast pyrolysis process, bio-oil stabilization as well as deeper hydrodeoxygenation still represent significant challenges.

The structural complexity of pyrolysis oil has prompted the use of different model compounds to study hydrodeoxygenation reactions. Among them, phenolics are the most relevant as they exhibit the representative structure of lignin monomers abundantly present in a biomass pyrolysis oil.

1.2 FASTCARD

This thesis is situated within the European FAST industrialization by CAtalyst Research and Development (FASTCARD), an EU FP7-funded project with 14 partners comprising universities, research and development institutes, catalyst and material producers and energy companies from 9 European countries. This project focuses on the faster industrial implementation of catalytic conversion of biomass to biofuels in Europe through innovations in nano-catalysts. FASTCARD focusses on the acceleration of four catalytic steps within two major valorization chains: the gasification route, followed by hydrocarbon reforming and Fischer Tropsch synthesis, and the liquid route, followed by hydrotreating and co-FCC (Figure 1-1). In this way FASTCARD can contribute to the achievements of the 20-20-20 objectives, and the reduction in greenhouse gasses, as targeted in the European Energy Roadmap 2050. The lower energy consumption and optimization of the feedstock utilization will strengthen the economic position of the European Union and secure a sustainable energy supply.

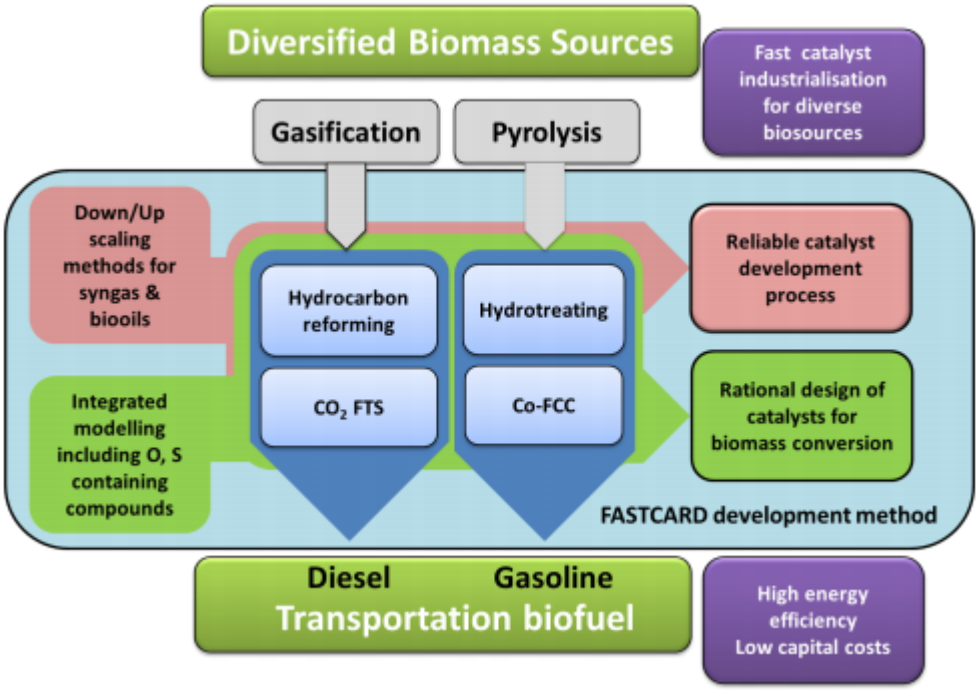

Figure 1-1. The FASTCARD concept.

1.3 Scope of this thesis

This master thesis aims on the experimental investigation of the intrinsic reaction kinetics and the construction of a kinetic model of fast pyrolysis oil hydrodeoxygenation using a lignin-derived model compound, *i.e.* anisole.

The experimental investigation of hydrodeoxygenation will be performed on the high throughput kinetic setup at the Laboratory for Chemical Technology (LCT) at the University of Ghent. Within LCT, hydrodeoxygenation is also investigated in the framework of the iCAD and WAVES projects.

Chapter 2 of this thesis provides an insight into the structure and chemistry of lignocellulosic biomass. Further, it outlines the state of the art of the catalytic lignocellulosic valorization processes, with the stress on the hydrodeoxygenation of fast pyrolysis oil. An overview of the kinetic studies of phenolics in the literature is given.

One of the aspects of this thesis is the performance of an experimental study of anisole hydrodeoxygenation. The setup is described in detail in *Chapter 3*, and hence, the procedures for obtaining experimental data. Several statistical tests that are used to validate the proposed kinetic model and the estimated parameters are explained in this chapter.

The results of the experimental investigation of anisole hydrodeoxygenation over a non-sulphided CoMo/γ-Al_2O_3 are presented in *Chapter 4* and those over a NiCu/ZrO_2 catalyst in *Chapter 5*. For both catalysts, a power law and a Langmuir-Hinselwood type of model are derived. The models and the obtained parameters are subjected to a statistical analysis.

In *Chapter 6* a summary of the findings of this thesis is given, together with some concluding remarks.

1.4 References

1. Current World Population. http://www.worldometers.info/world-population/
2. International Energy, A., Key World Energy STATISTICS. In 2013.
3. International Energy, A., World Energy Outlook 2013. **2013**.
4. Mohan, D.; Pittman, C. U.; Steele, P. H., Pyrolysis of Wood/Biomass for Bio-oil: A Critical Review. *Energy & Fuels* **2006,** 20, (3), 848-889.
5. Alonso, D. M.; Bond, J. Q.; Dumesic, J. A., Catalytic conversion of biomass to biofuels. *Green Chemistry* **2010,** 12, (9), 1493-1513.
6. Furimsky, E., Hydroprocessing challenges in biofuels production. *Catalysis Today* **2013,** 217, (0), 13-56.
7. Naik, S. N.; Goud, V. V.; Rout, P. K.; Dalai, A. K., Production of first and second generation biofuels: A comprehensive review. *Renewable and Sustainable Energy Reviews* **2010,** 14, (2), 578-597.
8. OECD, *Biofuels*. OECD Publishing.
9. Biofuel.org.uk Third Generation Biofuels. http://biofuel.org.uk/third-generation-biofuels.html
10. Demirbas, A., Use of algae as biofuel sources. *Energy Conversion and Management* **2010,** 51, (12), 2738-2749.
11. Herndon, A., Exxon Refocusing Algae Biofuels Program After $100 Million Spend. *Bloomberg* 2013.

Chapter 2

LIGNOCELLULOSIC BIOMASS AS RENEWABLE RESOURCE FOR ENERGY

This chapter provides an overview of the catalytic lignocellulosic valorization literature. First, lignocellulosic biomass and its various compounds are introduced. Next, different strategies for converting lignin are discussed. These strategies include, among others, fast pyrolysis, aimed at making transportation fuels and chemicals. To use the pyrolysis oil as a transportation fuel, a catalytic upgrading is necessary due to the high oxygen content, poor chemical stability, and immiscibility with transportation fuels. The catalytic removal of oxygen is called hydrodeoxygenation. The complexity of lignin, and consequently fast pyrolysis oil, have prompted the use of several, simplified model compounds to study hydrodeoxygenation.

2.1 Composition of lignocellulosic biomass

Lignocellulosic biomass typically consists of 40-50 wt% cellulose, 25-35 wt% hemicellulose, 15-20 wt% lignin and a minor amount of other organics[1, 2]. Certain differences in content of biomass fractions are observed between grasses, softwoods and hardwoods. Hardwoods tend to have more cellulose and hemicellulose, and a lesser percentage of lignin compared to softwoods[3]. Typical lignocellulose content of some plant materials is given in Table 2-1. More profound reviews on the chemical composition of different biomass feed stocks can be found in literature, see Choudhary *et al.*[4], Marsman *et al.*[5, 6].

Table 2-1. The content of cellulose, hemicellulose and lignin in common agricultural residues[7].

Lignocellulosic material	Cellulose [wt%]	Hemicellulose [wt%]	Lignin [wt%]
Hardwoods sterns	40-55	24-40	18-25
Softwood sterns	45-50	25-35	25-35
Nut shells	25-30	25-30	30-40
Corn cobs	45	35	15
Grasses	25-40	35-50	10-30
Paper	85-99	0	0-15
Wheat straw	30	50	15
Sorted refuse	60	20	20
Leaves	15-20	80-85	0
Cotton seed hairs	80-95	5-20	0

2.1.1 Cellulose

Cellulose is a linear polymer of glucose units linked via β-(1-4)-glycosidic bonds with a high degree of polymerization (between 300 and 15000 units)[8]. The basic repeating unit consists of two glucose anhydride units, called a cellobiose unit (Figure 2-1). The cellobiose unit is formed via the removal of water from each glucose unit[9].

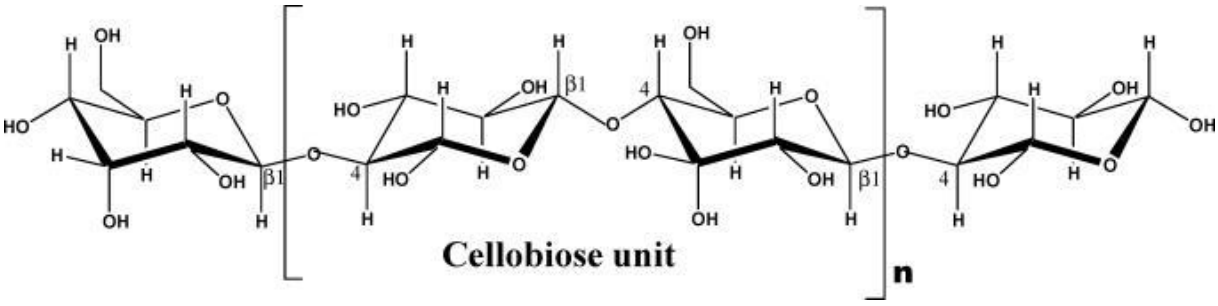

Figure 2-1. Chemical structure of cellulose [9].

Since cellulose is not branched, it possesses a crystalline structure. Hence, the hydrogen bonding is very secure and difficult to fractionate. Therefore cellulose resists thermal decomposition better than hemicellulose. Cellulose degradation occurs at 513-623 K, resulting mainly in anhydrocellulose and levoglucosan[9].

2.1.2 Hemicellulose

Hemicellulose, also called polyose, is a branched and substituted polysaccharide. It is made up of various polymerized monosaccharides, such as glucose, mannose, xilose, arabinose and galacturonic acid residues (Figure 2-2)[9]. Hardwood hemicelluloses are rich in xylan, while the softwood hemicellulose are richer in glucomannan[9].

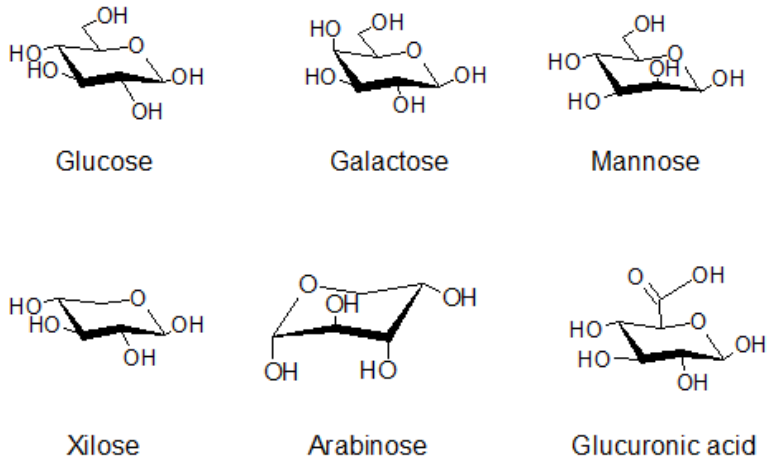

Figure 2-2. Main components of hemicellulose [9].

The degree of polymerization is lower than that of cellulose (70-200 base units[8]) resulting in a lower onset temperature of decomposition. Hemicellulose decomposes at temperatures of 473-533 K and produces more volatiles, less tars and chars than cellulose[9].

2.1.3 Lignin

Lignin is a three-dimensional, highly branched, polyphenolic substance that consists of variously bonded hydroxyl substituted and methoxy substituted phenylpropane units. These so-called phenylpropanes, consisting of a three-carbon chain attached to rings of six carbons, are believed to be the building blocks of lignin[10]. The three general phenylpropane units are *p*-coumaryl alcohol, confineryl alchol and sinapyl alcohol. Typically the ratio between these building blocks is 100:70:7 for hardwood lignin[9]. Softwood lignin contains fewer sinapyl alcohol units[9].

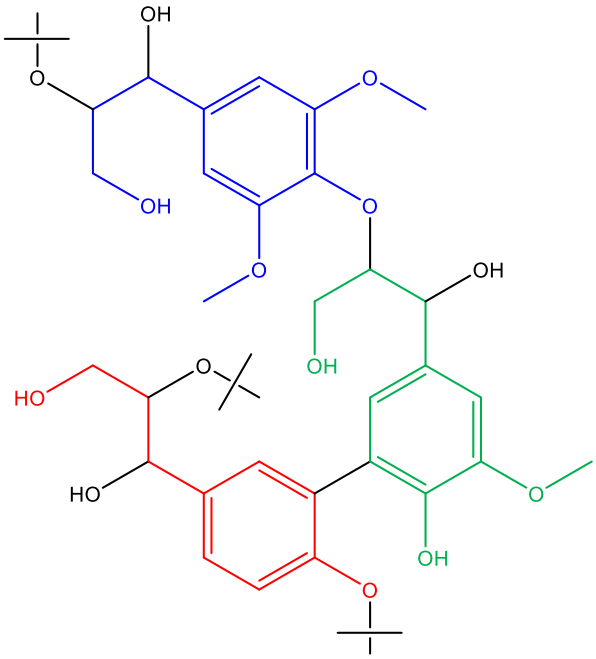

Figure 2-3. Representation of lignin. The sinapyl, conferyl and *p*-coumaryl alcohol building blocks are depicted in blue, green and red, respectively.

Lignin decomposes over a broader temperature range than cellulose and hemicellulose, due to the different thermal stabilities of the oxygen functional groups[9]. Lignin starts to decompose at 553 K which continues up to 1073-1173 K with a maximum rate being observed at 623-723 K[11]. At temperatures around 773 K the conversion of lignin is limited to 40 %[12].

2.1.4 Other

Besides cellulose, hemicellulose and lignin, biomass also contains a small fraction of inorganic minerals and organic extractives. Potassium, sodium, phosphorus, calcium and magnesium typically end up in the pyrolysis ash[13]. Organic extractives can be extracted from the biomass with polar (such as water or alcohols) or non-polar solvents (such as toluene or hexane). Examples of extractives are fats, waxes, proteins, phenolics, simple sugars, pectins, resins, *etc.*[9].

2.2 Methods for converting lignocellulosic biomass

There are four strategies for converting biomass, *i.e.* physical, chemical, biological and thermochemical processes, as shown in Figure 2-4. A comprehensive review on the different aspects of those processes is given by Naik *et al.*[14]. The two main routes for producing liquid biofuels are thermochemical processes and biochemical processes. Thermochemical processes

convert all the organic components of the biomass, whereas biochemical processes focus mainly on the polysaccharides[15]. This section focuses on the thermochemical processes for lignocellulosic biomass and more precisely on the pyrolysis of biomass.

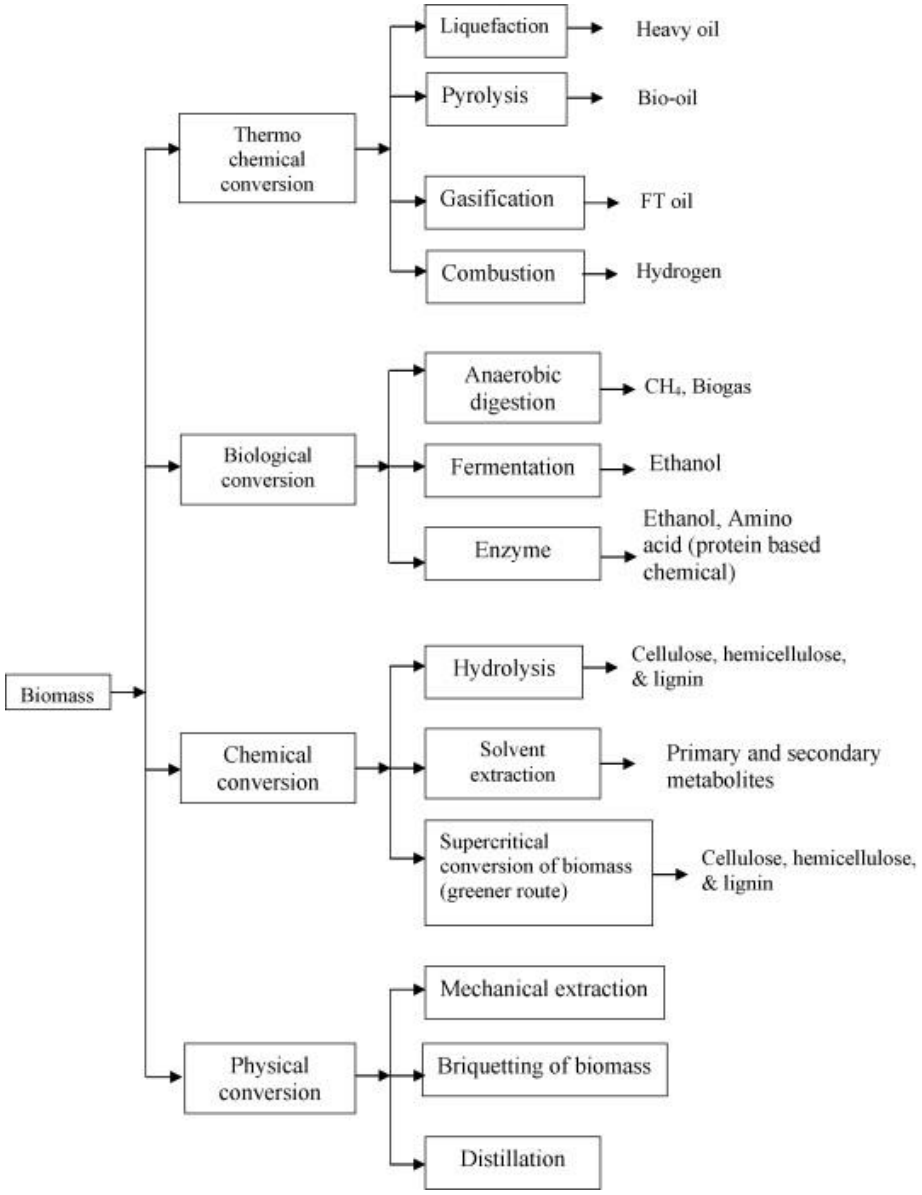

Figure 2-4. Overview of conversion processes for lignocellulosic biomass[14].

In direct combustion, the lignin is used as a low-energy source. Air is used to convert chemical energy of biomass into heat, electricity, mechanical power, *etc*. Theoretically, any type of lignin can be burnt. Although in practice, direct combustion is only feasible for biomass with moisture content lower than 50 %[10].

In recent years, more attention has been paid to the production of liquid fuels and chemicals by thermal treatment of lignin. A first way is the gasification of biomass to produce syngas. Gasification is typically carried out at temperatures over 973 K[1] in insufficient supply of air.

Any plant-based biomass is appropriate for partial combustion to produce syngas. Further upgrading by for example Fisher-Tropsch synthesis, results in liquid fuels such as diesel and gasoline. A drawback of this method is the large amount of water and impurities in the biomass which can be problematic in the following Fisher-Tropsch process[1].

The chemical structure of lignin suggests that it has a great potential to be used as a feedstock for value-added chemicals, such as acids, alcohols, phenols, aldehydes and aromatics (benzene, toluene, xylene)[16, 17]. Two approaches to produce liquid products for fuels and chemicals are liquefaction and pyrolysis.

During pyrolysis, biomass is decomposed at temperatures from 573 K to 773 K in the absence of oxygen. The process conditions have a large influence on the formation of products, *i.e.* gases, liquid oil and solid products, and the proportion between them. There are several types of pyrolysis, which mainly differ in their residence time and heating rate. Slow pyrolysis is performed at heating rates of 0.1-1 K s^{-1} and a residence time from 5 minutes to 30 minutes[9, 18, 19]. A promising new technology is fast pyrolysis. The temperature is achieved at high heating rates of 10-10^4 K s^{-1} and a short residence time is used (< 2 s)[20]. The aim of slow pyrolysis process is to produces charcoal, whereas the fast pyrolysis process converts biomass into a liquid product. The fast pyrolysis process is described more detailed in section 2.3.

Liquefaction is carried out at elevated temperatures (523-723 K) and pressure (0.5-2 MPa) in the presence of a catalyst, typically sodium carbonate, with a residence time of 4-30 minutes[1]. The combination of these factors results in a more expensive process in comparison to the pyrolysis. But the lower oxygen content of the liquefaction product (5.1 wt%[21]) compared to the bio-oil produced by pyrolysis (12-30 wt%[21]), results in a less extensive post processing.

2.3 Fast pyrolysis

A simplified block diagram of the overall fast pyrolysis process is given in Figure 2-5. First, the biomass feedstock is dried and ground into smaller particles before it is fed to the reactor operating at approximately 773 K. An extensive review of reactors and their products is given by Bridgwater[7], and Venderbosch and Prins[12]. Heating rates from the heat source, *i.e.* sand, to the surface of the particle of 10^3 K s^{-1} or even 10^4 K s^{-1} have been claimed[22]. This heat will initiate primary pyrolysis reactions, such as dehydration, depolymerization, re-polymerization, fragmentation and rearrangement[23], which convert biomass into a complex mixture of more than 300 products[24]. The produced ash will act as a cracking catalyst at the

operating temperatures for the organic molecules in the volatile pyrolysis products[18]. Therefore, an effective ash separation is important. One or more cyclones will separate the sand and char from the gases and pyrolysis oil vapor. The hot vapor is rapidly quenched by cooled pyrolysis oil to reduce secondary pyrolysis reactions which produce small non-condensable gases and more char. The pyrolysis oil is collected while the remaining gases are recycled back to the reactor.

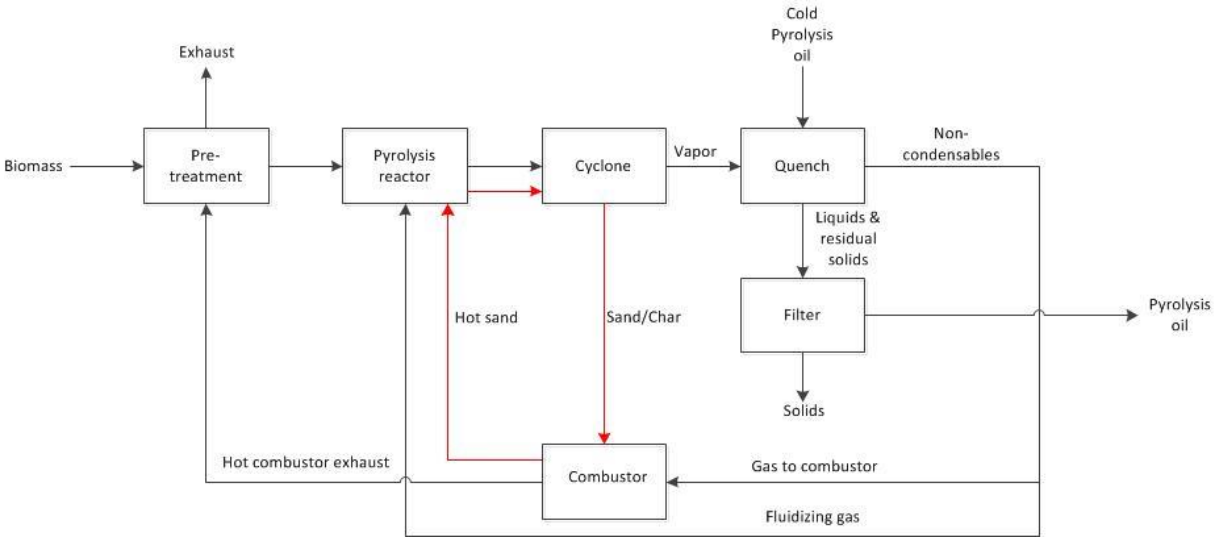

Figure 2-5. Block diagram of fast pyrolysis[25].

Pyrolysis oil is composed of different-sized molecules derived from the decomposition of the three key biomass building blocks (cellulose, hemicellulose and lignin). Five major groups of compounds can be distinguished in pyrolysis oil: (1) hydroxyaldehydes, (2) hydroxyketones, (3) sugars and dehydrosugars, (4) carboxylic acids and (5) phenolic compounds[26]. Maggi and Delmon[27, 28] performed an extensive characterization of pyrolysis oil compounds. Typical oxygen containing compounds that were identified in these studies are shown in Figure 2-6.

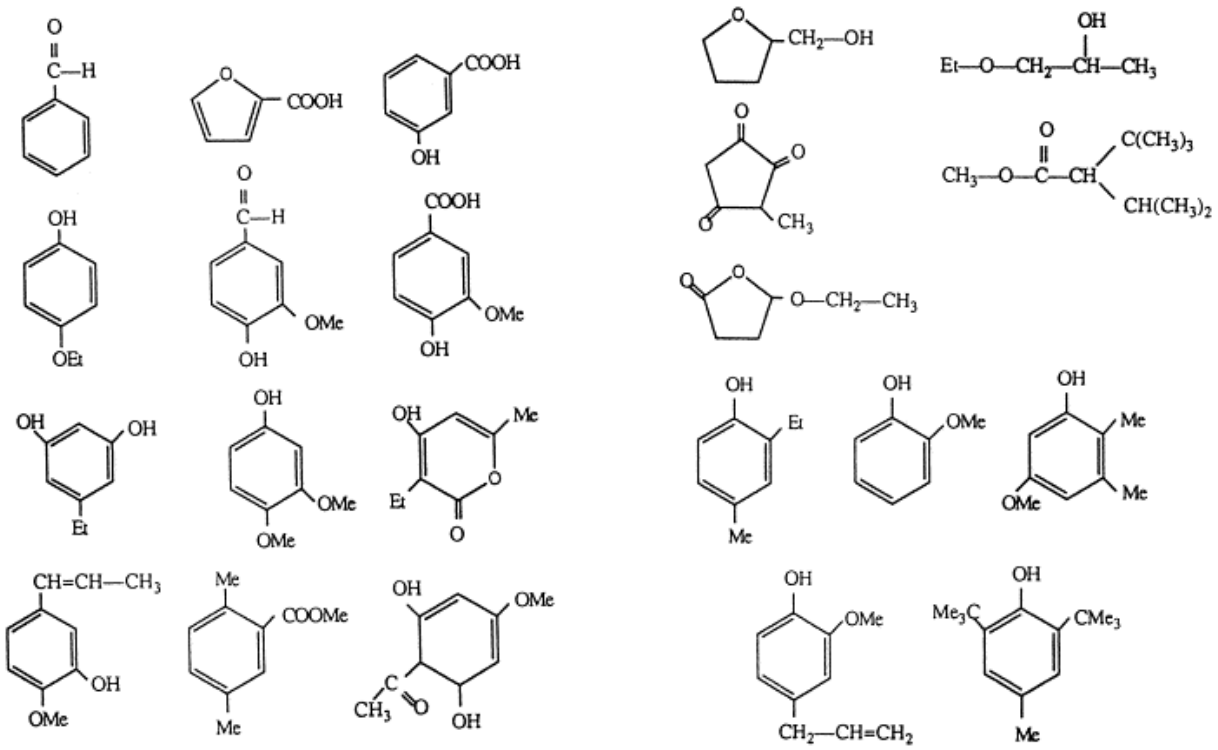

Figure 2-6. Oxygen compounds identified in wood pyrolysis oil[28].

The chemical composition and the physical properties of the pyrolysis oil are well-described in the literature[4-6, 24, 29], and depend strongly on the pyrolysis conditions as well on the feedstock composition. The characteristics of pyrolysis oil are excellently summarized by Bridgwater[30] and Zhang *et al.*[31]. Typical properties for pyrolysis oil are compared to those of heavy fuel oil in Table 2-2. The primary reason for the difference in properties between pyrolysis oil and heavy oil is the larger content of moisture and oxygen. Therefore, the pyrolysis oil has a limited storage stability and tendency towards excessive coke formation at elevated temperatures. The aldehydes, ketones and other compounds can react via an aldol condensation reaction causing an increase in viscosity and water content. Those reactions are temperature driven and therefore pyrolysis oil has to be stored below room temperature. The high water content causes the lower heating value of pyrolysis oil to be only 40-45 wt% of that exhibited by hydrocarbons. Furthermore, due to high polarity and hydrophilic nature of the pyrolysis oil it is immiscible with hydrocarbons, but it is with polar solvents such as methanol or ethanol. To increase the miscibility with fossil fuels, emulsified systems have been developed. Their performance in diesel engines are promising, however, the high energy requirement for the production is the main drawback[29]. Another important characteristic of pyrolysis oil is the high acidity, which causes corrosion of vessels and pipe-work. Therefore extra attention has to be paid to the material choice.

Table 2-2. Typical properties of wood pyrolysis oil and heavy fuel oil [24, 29, 31].

Property	Pyrolysis oil	Heavy oil
Moisture content, [wt%]	15-30	0.1
Elemental composition, [wt%]		
C	54-58	85
H	5.5-7.0	11
O	35-40	1.0
N	0-0.2	0.3
Ash	0-0.2	0.1
Solids, [wt%]	0.2-1.0	1
Distillation residue, [wt%]	Up to 50	1
pH, [-]	2.5	
Specific gravity, [-]	1.2	0.94
HHV, [MJ kg^{-1}]	16-19	40
Viscosity at 773 K, [cP]	40-100	180

The direct use of pyrolysis oil as a transport fuel is unlikely due to the properties described above. Bio-oil can be upgraded chemically, physically and catalytically. This has been reviewed in literature[18, 32]. The most common methods are gasification to syngas followed by synthesis to hydrocarbons or alcohols, zeolite cracking and by hydrotreating. A summary of these main methods is shown in Figure 2-7[30].

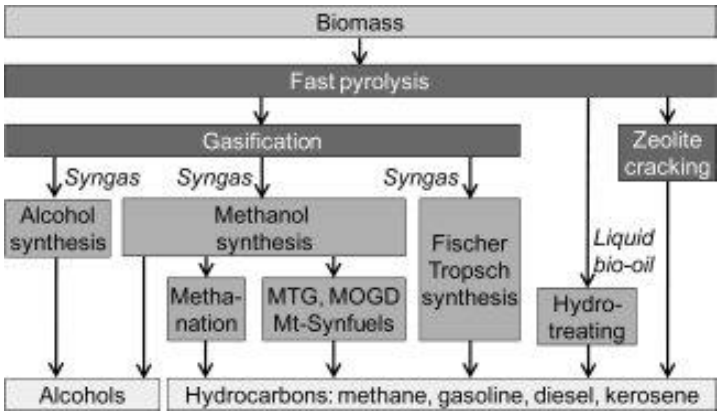

Figure 2-7. Upgrading fast pyrolysis oil to alcohols and hydrocarbons[30].

2.4 Catalytic upgrading of fast pyrolysis oil by hydrotreatment

Catalytic upgrading enhance the properties of the bio-oil by removing oxygen compounds via H_2O, reducing molecular weight and altering chemical structure to resemble those of fossil fuels[23]. Typical reactions that are enhanced by the catalyst are cracking, decarbonylation, decarboxylation, hydrocracking, hydrodeoxygenation, and hydrogenation as summarized in Figure 2-8.

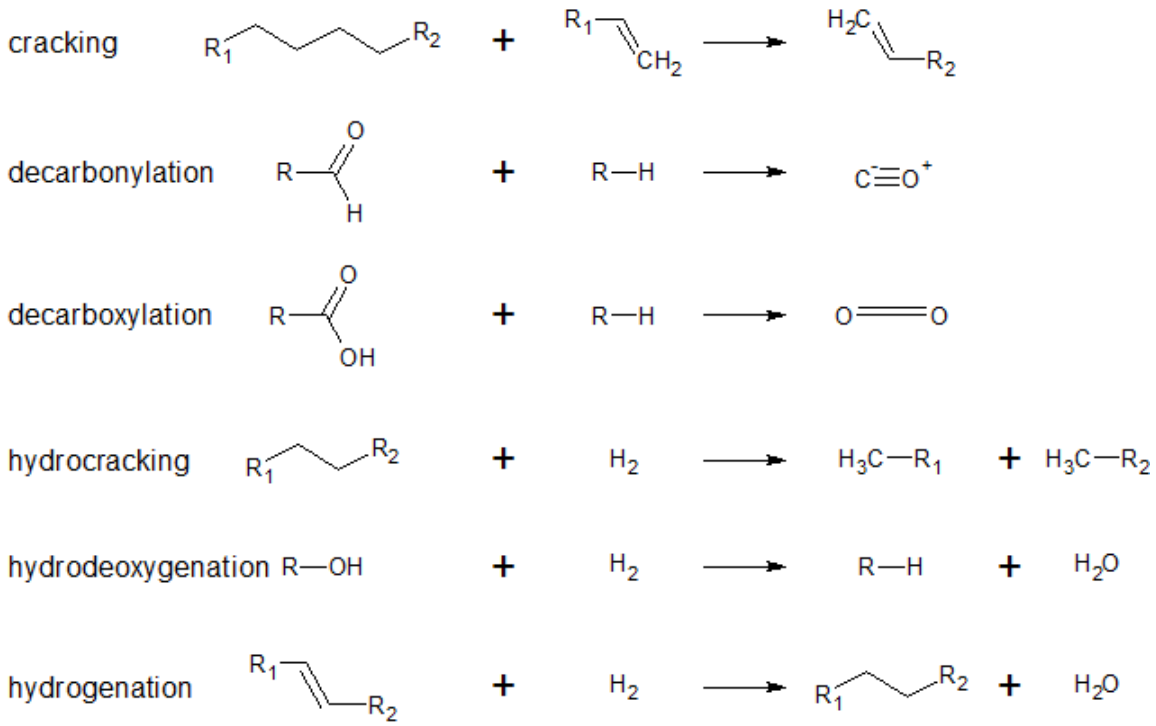

Figure 2-8. Representative catalytic upgrading reactions[24].

The removal of oxygen from pyrolysis oil by catalytic reaction with hydrogen is called hydrodeoxygenation (HDO). This is a typical hydrolysis reaction, where the carbon-oxygen bond are cleaved with hydrogen in the presence of a catalyst. Simplified, the overall reaction stoichiometry of HDO can be represented by equation 2-1, where CH_2 refers to unspecified hydrocarbons[33].

$$CH_{1.4}O_{0.4} + 0.7\,H_2 \rightarrow CH_2 + 0.4\,H_2O \qquad 2\text{-}1$$

Due to the similarity with hydrodesulfurization (HDS) and hydrodenitrogenation (HDN), well-studied processes in the petroleum industry, much of the knowledge have been extrapolated from HDS and HDN experience with common cobalt-molybdenum, nickel-molybdenum and their oxides on silica and alumina supports[23, 31, 34]. According to Furimsky[35],

the relative heteroatom removing takes place in the order of HDS > HDO > HDN. Ramatahan *et al.* [36] reported a special case, over a vanadium nitride catalyst, where the HDO was 10 times greater than HDS. A more profound review on the catalyst used for hydrodeoxygenation is done in section 2.5.

Regarding operation conditions, HDO is carried out at elevated temperatures (523-723 K[4, 24, 37]) and high pressure (7.5-30 MPa[12, 24]) and a typical range of liquid hourly space velocity of 0.1-1.5 h^{-1} [24]. The high pressure ensures higher solubility of the hydrogen in the pyrolysis oil[24]. Thereby more hydrogen will be available in the vicinity of the catalyst which will enhance the complete hydrogenation of unsaturated hydrocarbon products[37].

Typically, HDO is carried out in two stages as a result of the different reactivity of the molecules and groups present in pyrolysis oil[31, 35, 37, 38]. The first stage is the so-called stabilization stage and is performed below 573 K. This mild hydrotreating step convert reactive oxygen containing groups (for example acids) into less reactive ones (for example alcohols). Therefore, mild hydrotreating will not always result in a decrease in oxygen content, but rather increase the stability of the oil. Due to more complex bound or sterically hindered oxygen, phenols and furans have lower HDO reactivity. Therefore, the second stage is performed around 623 K to reduce the oxygen content even more. Furimsky[35] has summarized the HDO reactivity of the oxygen groups in the tentative order as shown in 2-2.

$$\begin{aligned} &alcohols > ketons > alkylethers > carboxylic acids \approx m-phenol \\ &\approx p-phenols \approx napthol > phenol > diarylethers \approx o-phenols \\ &\approx alkylfurans > benzofurans > dibenzofurans \end{aligned} \qquad 2\text{-}2$$

The first stage produces a partially deoxygenated, stabilized bio-oil which can be used for heat and electricity generation or stored before further upgrading. The second stage is applied to generate fully or deeply deoxygenated fuels that can be used for transportation fuel[39].

Another important aspect is the hydrogen consumption during HDO reaction. Hydrogen has two effects in the upgrading of pyrolysis oil: removing oxygen (decreased O/C ratio) and saturating double bounds (increased H/C ratio). Venderbosch *et al.*[40] investigated the hydrogen consumption as a function of the deoxygenation rate over a Ru/C catalyst in a fixed bed reactor at 448-673 K and 20-25 MPa. From the experiments it was clear that the hydrogen consumption increases steep as a function of the deoxygenation rate. This is the consequence of the different reactivity of the compounds in pyrolysis oil. Highly reactive compounds, such as ketones, are easily converted with low hydrogen consumption. The more stable

compounds, such as furans, are first saturated resulting in a higher hydrogen consumption at complete deoxygenation. The effect of the degree of deoxygenation (and consequently the hydrogen consumption) on the oil yield was investigated by Samolada *et al.*[41] on a Co-MoS_2/Al_2O_3 catalyst. The oil yield decreases as a function of the deoxygenation[24, 41]. Therefore it is important to evaluate to which extent the oxygenates should be removed.

2.5 Hydrodeoxygenation of fast pyrolysis oil

2.5.1 Model compounds

The complexity of lignin, and consequently fast pyrolysis oil, have prompted the use of several simplified model compounds to study hydrodeoxygenation. These model compounds contain linkages and functional groups that resemble those found in lignin. Often only one type of functional group is contained in a representative compound, reducing the analysis of the reaction paths and product analysis. For the elimination of oxygen, several chemical bonds have to be broken. Phenolics are the most commonly studied model compounds, due to their relatively high amount in pyrolysis oil (25 wt%) and their low HDO reactivity[35]. Table 2-3 shows the bond dissociation energies. Due to the higher bond strength of an oxygen attached to the aromatic ring compared to that of an oxygen attached to an aliphatic carbon, the elimination of oxygen from phenolics will be more difficult.

Table 2-3. Bond dissociation energies[42].

	Bond strength [kJ mol^{-1}]
CH_3O-R	360
HO-R	392
CH_3O-C_6H_5	418
HO-C_6H_5	464

Typical examples of lignin-derived model compounds that are often used in literature are depicted in Figure 2-9.

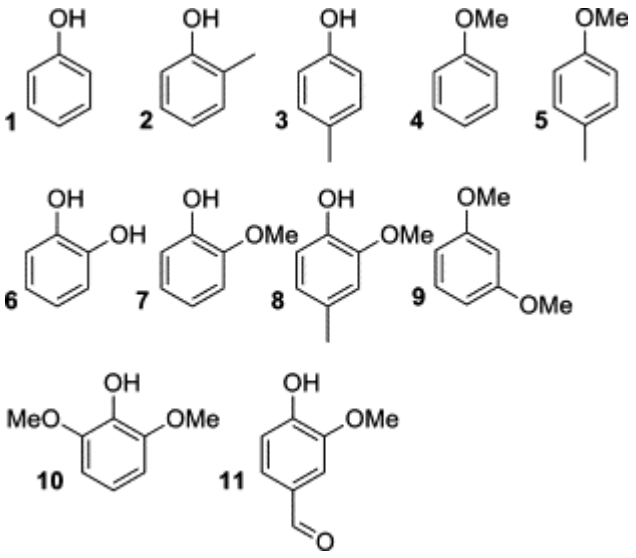

Figure 2-9. Monomeric model compounds: (1) phenol, (2) *o*-cresol, (3), *p*-cresol, (4) anisole, (5) 4-methylanisole, (6) catechol, (7) guaiacol, (8) 4-methylguaiacol, (9) 1,3-dimethoxybenzene, (10) syringol and (11) vanillin.

This thesis focusses on the hydrodeoxygenation of anisole, which incorporate the methoxyl group present in lignin.

2.5.2 Catalyst studies on hydrodeoxygenation of lignin-derived model compounds

A variety of different kinds of catalysts have been used in the study of HDO processes. In the following sections, those will be discussed as either conventional hydrotreating catalyst or novel catalyst.

2.5.2.1. Conventional hydrotreating catalysts

Conventional catalysts that are used in the industry for hydrotreating consist of molybdenum which is the active component and cobalt or nickel as promotors typically on γ-Al_2O_3. To increase the activity of the catalyst, a small quantity of co-promoter such as tungsten can be impregnated[43].

Early studies on the HDO of pyrolysis oil were performed with sulfided HDS catalysts. It is usually assumed that the vacancies on the edge of MoS_2 slabs are the active sites of the catalyst. Due to the Lewis acid character of this sites, molecules with electron rich functional groups can adsorb[24, 43]. Romero *et al.*[44] proposed a mechanism for the HDO of 2-ethylphenol on a $CoMoS_2$ catalyst, which is depicted in Figure 2-10. The presence of hydrogen in the feed will generate S-H and Mo-H species along the edge of the catalyst. Using DFT calculations, it is assumed that the 2-ethylphenol adsorbs through the oxygen atom on the vacancy on the catalyst surface. The S-H species enables proton donation to the attached molecule, forming a

carbocation. This adsorbed intermediate undergoes a C-O cleavage and the aromaticity is restored with the formation of ethylbenzene. The oxygen is removed by formation of water, restoring the vacancy on the catalyst.

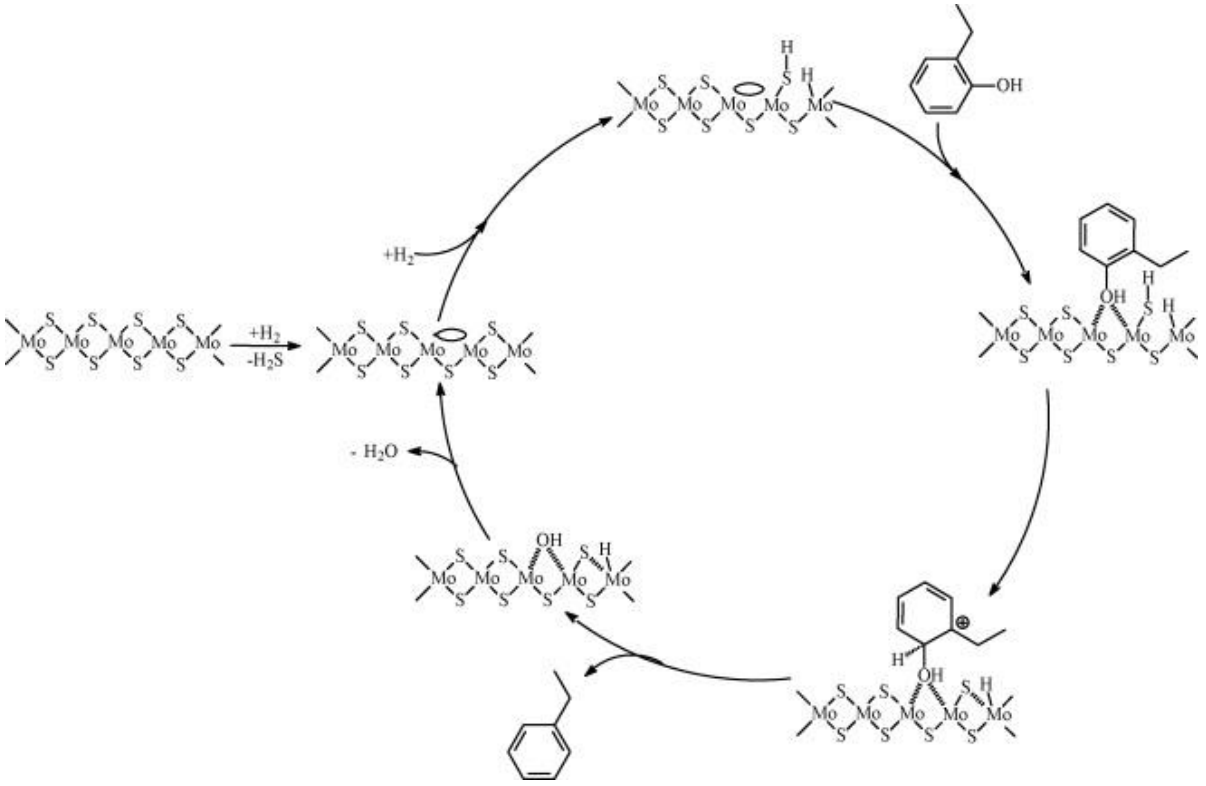

Figure 2-10. Proposed mechanism for hydrodeoxygenation of 2-ethylphenol over a $CoMoS_2$ catalyst[44]. The circles indicate the active vacancy site.

Although deoxygenation degree up to 99.9 % are reported[45], the conventional sulfided catalysts have a drawback. To remain the catalyst's activity, a continuous supply of sulfur-containing compounds such as H_2S is needed. This is undesirable from an environmental point of view, since it results in a contamination of the product and off gas[46]. Wildschut *et al.*[47] showed that the activity of non-sulfided form of the HDS catalysts is lower, which indicates that the addition of a sulfur-containing source is beneficial.

2.5.2.2. Novel catalysts

To avoid the need for catalyst presulfiding, non-conventional catalysts have been evaluated. Noble catalysts such as ruthenium, palladium and platinum are being investigated in several research groups. Wildschut *et al.*[47] tested several noble metal catalyst (Ru/C, Ru/TiO_2, Ru/Al_2O_3, Pt/C and Pd/C) in a batch reactor at 523K and 10 MPa (mild HDO), and 623 K and 20 MPa (deep HDO) and compared the results with those obtained with typical HDS catalysts such as NiMo and CoMo supported by Al_2O_3. The oil yields range between 21 and 70 wt% and the oxygen content vary between 5 and 27 wt% for the noble catalyst. The conventional

HDS catalysts have a lower oil yield (25-30 wt%) and a higher oxygen content (8-27 wt%) under these operation conditions. Gutierrez *et al.*[48] investigated the activity and selectivity of mono- and bimetallic noble metal catalysts in the hydrodeoxygenation of guaiacol in a batch reactor at 373 K and 8 MPa. They found that bimetallic noble catalysts (RhPt and RhPd) give noticeably better results than the monometallic Pt and Pd catalysts while the performance of the bimetallic PtPd catalyst is worse. It can be concluded that noble metal catalysts show relatively good performance compared to HDS catalysts, but the high price of those metals make them unattractive.

As alternative to the noble catalysts, base metal catalysts are being investigated as they have potentially a relatively low cost. Yakovlev *et al.*[49] used nickel and nickel-copper based catalysts on different supports for the HDO of anisole in a fixed bed reactor. From the results of these experiments, it is seen that the bimetallic NiCu catalyst is more active than the monometallic catalysts for the hydrodeoxygenation. This indicates that the HDO reaction requires at least two active sites: one for the activation of the hydrogen and one for the activation of the oxy-compounds. Khromova *et al.*[50] studied the effect of the Ni/Cu ratio in bimetallic $NiCu/SiO_2$ on the selectivity of anisole hydrodeoxygenation. The conversion of anisole increases with the increase of the nickel content. However, the catalytic activity drops at 40-60 % of Ni in the active component NiCu. This drop in activity can be explained by electron-band theory. Nickel has free d-orbitals delocalized in the conductivity band, while copper has free d-electron. When alloying nickel with copper, the catalytic activity will change due to the filling of the d-band. In the range of 40-60 % of nickel, the d-band is completely filled resulting in the drop of activity[50]. Other transition metals like cobalt, molybdenum, iron, and tungsten have also been tested[24, 48, 51, 52]. Zhao *et al.*[51] focused on the potential of phosphide catalysts (Ni_2P, Co_2P, Fe_2P, WP and MoP) supported on SiO_2 for the HDO of guaiacol. The activity of those catalysts is found to be less than the Pd/Al_2O_3, but higher than the conventional sulfide $CoMo/Al_2O_3$. Various metal nitride catalysts have been tested for the HDO activity by Monnier *et al.*[52]. Mo_2N/Al_2O_3 showed a high HDO activity while WN/Al_2O_3 and VN favored decarboxylation and decarbonylation.

A general mechanism for HDO on transition metal catalysts is shown in Figure 2-11, taking into account the findings of Popov *et al.*[53] and Olcese *et al.*[54] The valence electrons of the oxygen atom in a phenolic are more basic than the π-electrons of the unsaturated C=C. It is expected that the acidic Si-OH sites interact with the oxygen atoms from the oxy-compounds.

The hydrogen is activated by the transition metal and spills over to the adsorbed oxygen atom which causes a C-O cleavage.

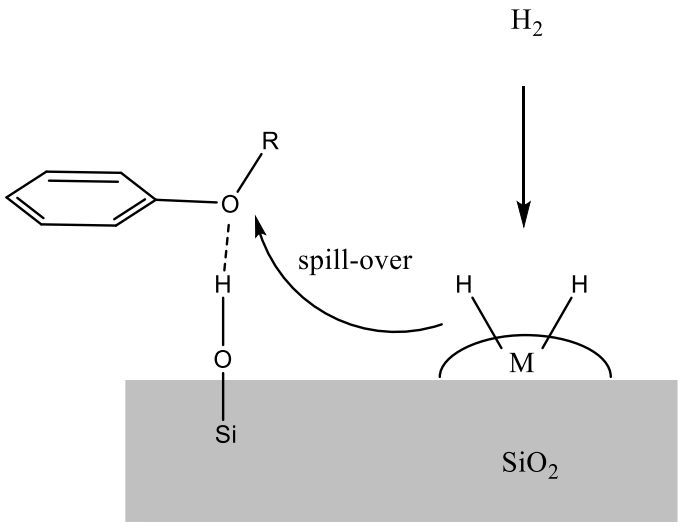

Figure 2-11. Proposed mechanism for hydrodeoxygenation of guaiacol over a transition metal catalysts[53, 54].

It appears that transition metals are alternatives both for sulfided catalyst types and noble catalyst types, but further research is needed in order to evaluate their potential.

2.5.2.3. Effect of support

The support can have an important role in the activity of the catalyst. It is found that due to the presence of water in pyrolysis oil convert γ-Al_2O_3 into its crystalline phase, boehmite (AlO(OH))[40, 55]. Moreover, the acidity of Al_2O_3 promotes hydrocracking, which enhance carbon deposition on the catalyst. As an alternative to Al_2O_3, neutral support like carbon seems to be promising. The lower tendency for carbon formation is advantageous compared to Al_2O_3[24]. Nevertheless, their application is limited as carbon catalyst cannot be regenerated by oxidation. Other attractive supports like ZrO_2, TiO_2 and CeO_2. ZrO_2 and CeO_2 have tendency to activate oxy-compounds on their surface[49]. TiO_2 and ZrO_2 have some acidic character, but less than Al_2O_3[24]. When selecting a support, two aspects should be taken into account: (i) the affinity for carbon formation should be low (low acidity of the catalyst), (ii) the ability to activate oxy-compound should be sufficient.

2.5.2.4. Catalyst deactivation

Catalysts lose their activity after some time on stream. Most common causes for deactivation are coking, sintering, poisoning and inhibition[35, 56, 57].

The main reason for catalyst deactivation during bio-oil hydrotreating is coke formation[24, 35]. The extent of coking depends on the structure and support of the catalyst, the feed (type of

oxygen compounds) and process conditions. Generally it is assumed that sulfided HDS catalysts form more coke than noble catalysts, bimetallic catalysts have better coke resistance than mono metallic catalysts and transition metal oxides form less coke than Al_2O_3[39]. Unsaturated hydrocarbons, which are present in bio-oils, have a high reactivity and are prone to coke formation. Polymerization and condensation reactions lead to coke that blocks the catalyst pores. Further, it is observed that phenolics adsorb on the support and hinder the accessibility of the active sites[58]. The coke formation is also affected by pressure and temperature. Elevated temperatures enhance polymerization and condensation reactions, whereas high hydrogen pressure benefits the coking removal by saturating the carbon.

Sintering is a thermally activated process resulting in the loss of active surface via structural modification of the catalyst[57]. Since hydrodeoxygenation reactions are exothermic and carried out at elevated temperatures[24], sintering may occur at these conditions. The high amount of moisture (Table 2-2) in the bio-oils is beneficial to reduce the sintering rate, since the heat generated by the reactions may be used to evaporate the water and avoid excessive temperatures.

Deactivation of the catalyst may also occur due to chemisorption of impurities present in the feed. One can distinguish poisons and inhibitors. A substance that interacts strongly and irreversible with the active sites, is called a poison. Whereas inhibitors generally adsorb weakly and reversibly on the catalyst surface. Water has an inhibiting effect on the conventional Al_2O_3 support, since alumina is turned into boehmite[40, 55]. Sulfide structures in catalyst can convert to oxide due to the presence of water or other oxy-compounds[34].

2.5.3 Mechanism of hydrodeoxygenation

To investigate the mechanism of hydrodeoxygenation, studies have been performed involving different model compounds. A lot of attention has been paid to phenols[56, 59-61], anisole[50, 62-64] and guaiacols[48, 65-67]. In this section, the reaction networks proposed for the hydrodeoxygenation of phenols and anisole by different authors will be compared.

2.5.3.1. Phenols

Phenol is the simplest monomeric model compound which incorporates the aromatic ring and hydroxyl group that are typical for lignin. The aromatic carbon-oxygen bond is about 70 kJ mol^{-1} stronger than the aliphatic carbon-oxygen bond[35] (Table 2-3). Since phenol and its derivatives are formed as intermediates in the reactions of more complicated lignin-derived model compounds, it is important to understand their reaction network.

The gas phase conversion of phenol occurs via two pathways which are shown in Figure 2-12[56, 60, 68]. Reaction path (1) is the direct hydrogenolysis to give benzene and water. Partial hydrogenation of benzene gives cyclohexene, which is further hydrogenated to cyclohexane. In the alternative path (2), the aromatic ring is partially hydrogenated to 1-hydroxy-cyclohexene, which is a tautomer of cyclohaxone. Further hydrogenation of 1-hydroxy-cyclohexene results in cyclohexanol. The hydroxyl-group on cyclohexanol can be removed through dehydration, and further hydrogenation is needed to produce cyclohexane. Cyclohexanol can be converted to cyclohexane in one step through hydrogenolysis. Shin *et al.*[60] calculated the Gibbs energy at 498 K in each step for phenol HDO. The values are listed below the arrow in Figure 2-12. All steps, with the exception of the partial hydrogenation of benzene, are negative and are considered to be irreversible.

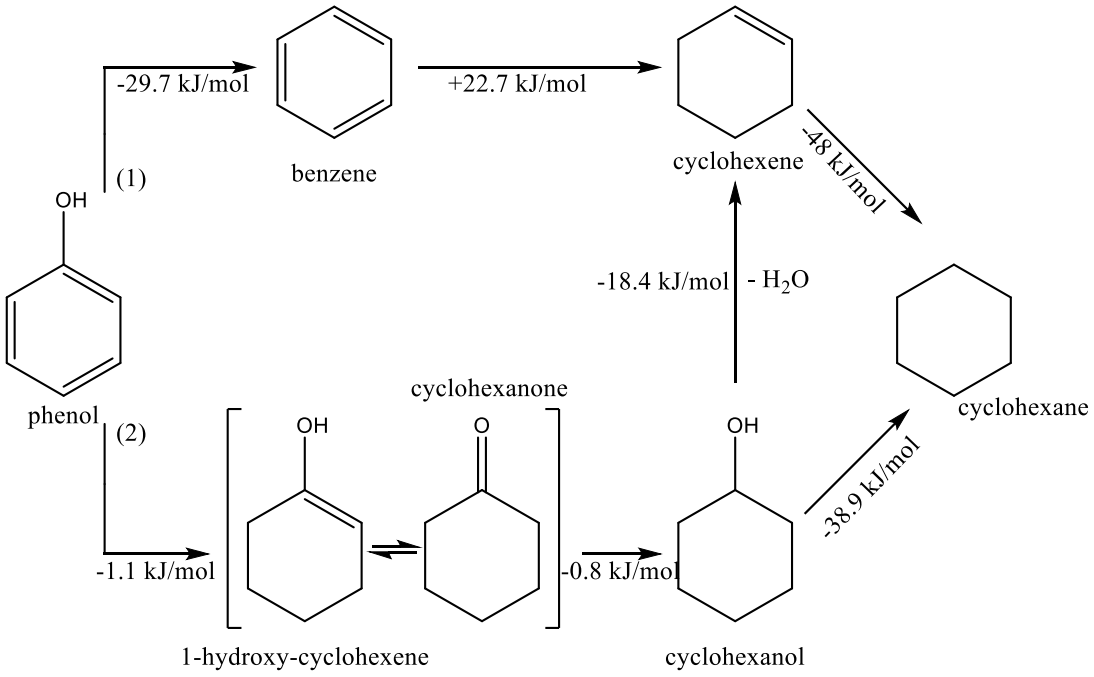

Figure 2-12. Reaction network proposed for phenol HDO. The Gibbs free energy is listed for each step[60].

The effect of substitution on the hydrodeoxygenation rate is investigated by different authors[56, 61, 69].

Massoth *et al.*[56] studied the hydrodeoxygenation mechanism of methyl-substituted phenols in a flow microreactor at 573 K and 2.85 MPa hydrogen pressure, catalyzed by sulfided CoMo/γ-Al_2O_3. They proposed that the conversion of substituted phenols occurs via two reaction paths, as shown in Figure 2-13. The first reaction path is the direct hydrogenolysis of phenol leading to benzene. In the second reaction step, the C-O cleavage occurs in succession of full hydrogenation. It appears that the substitution on the *ortho*-position slightly lowers the conversion, especially when methyl groups appear in both *ortho*-positions. From the experiments it is found that the direct hydrogenolysis pathway is favored independent of the methyl-group position.

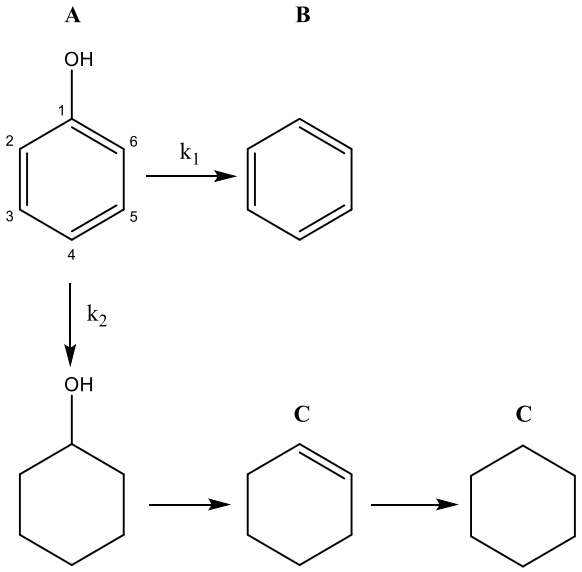

Figure 2-13. Reaction network for phenol[56]. The numbers represent the convention for substituents, whereas B and C are the convention for the products of the dehydrodeoxygenation and hydrogenation reaction paths.

Odebunmi and Ollis[61] investigated the hydrodeoxygenation of cresols (*i.e.* methylphenols) on fresh and aged sulfided CoMo/γ-Al_2O_3 in an continuous microreactor operating at a hydrogen pressure between 3.4 and 12 MPa. The experiments are performed at two different temperature ranges using different catalyst charges. At low temperatures (498-548 K) on a fresh catalyst, the HDO mechanism of cresol proceeds by direct hydrogenolysis to give toluene, consequently hydrogenated to methylcyclohexane. On aged catalysts (623-673 K), the subsequent hydrogenation of toluene disappears, and methylcyclohexane is directly formed from the cresol. The HDO reactivity of the cresols is found to be $meta > para > ortho$, which is consequent with the founding of other authors[70, 71]. An overall mechanism for the HDO of *ortho*-substituted phenols is given in Figure 2-14[69]. Two main pathways for the conversion of cresol are direct hydrodeoxygenation (1a) and hydrodeoxygenation in

succession of hydrogenation (2a). Alkylcyclohexenes, and methylcyclopentanes are minor products and are only detected at high reactant conversions[35].

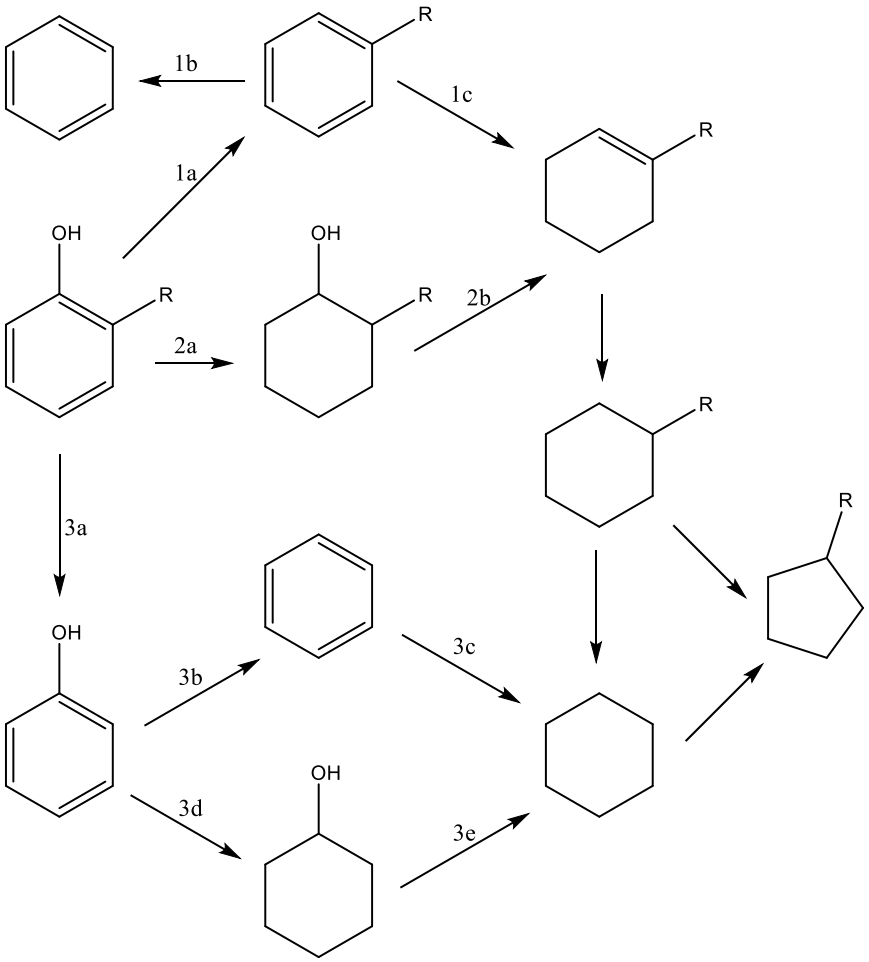

Figure 2-14. Overall HDO mechanism of *ortho*-substituted phenols[69].

2.5.3.2. Anisole

Anisole has a methoxyl group attached to the aromatic ring, instead of the hydroxyl group in phenol. This methoxyl group incorporate a C-O-C moiety, which is prevalent in lignin. The oxygen-aromatic carbon bond is about 45 kJ mol^{-1} weaker compared to phenol. The second oxygen-carbon bond, between the oxygen and the alicyclic carbon, is weaker than the bond between the aromatic carbon and oxygen[35] (Table 2-3). Due to this methyl group, there are more reaction products which complicates the reaction network.

Viljava *et al.*[62] studied the HDO of anisole first in a batch reactor on a sulfided CoMo catalyst. Later, research was performed in a plug flow reactor using sulfided and non-sulfided CoMo/γ-Al_2O_3. The simplified reaction network based on the experimental identified reaction products is shown in Figure 2-15. To cleave the oxygen from the aromatic ring the sulfided form of the catalyst is required. The demethylation route is observed on the oxide catalyst

(non-sulfide form) and on the alumina support. The methylated products, *e.g.* cresol, *o*-methylanisole and 2,6-xylenol, are observed on all types of catalyst. Jongerius *et al.*[72] investigated the conversion of different monomeric and dimeric model compounds over sulfided $CoMo/Al_2O_3$ catalysts at 573 K and 5.0 MPa hydrogen in a batch reactor. The conversion of anisole is found to be 96 % after four hours of reaction. The selectivities towards phenol, benzene and methylated products are 64 %, 10 % and 10 % respectively.

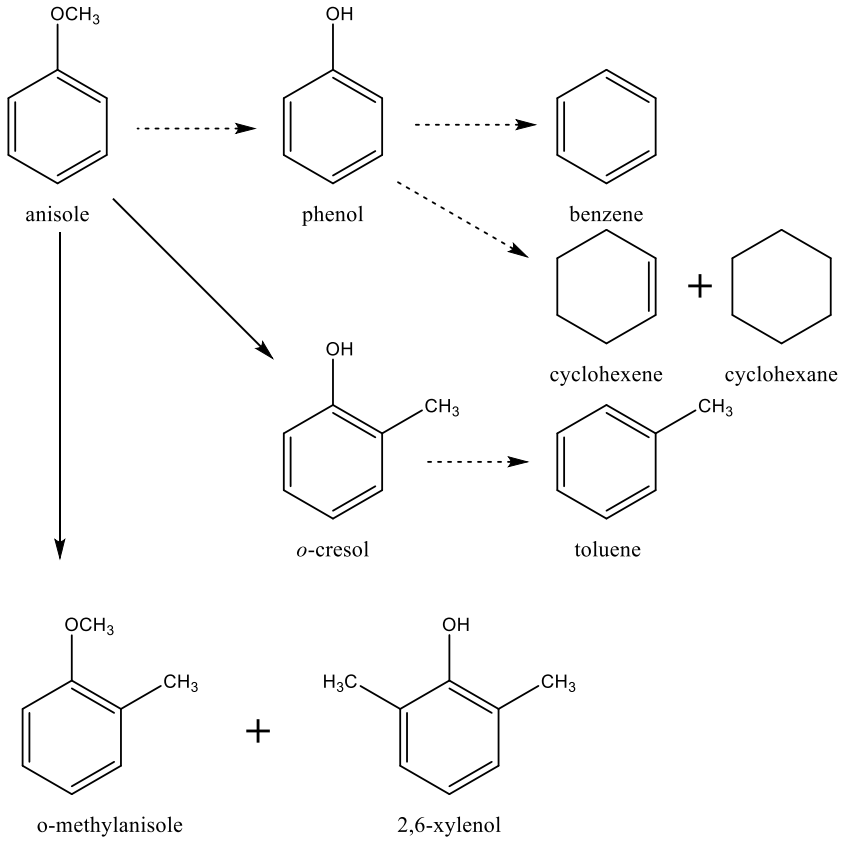

Figure 2-15. Simplified reaction network for the HDO of anisole on CoMo catalysts[62]. The dashed arrows represent hydrodeoxygenation, hydrogenolysis or hydrogenation reactions, while the solid arrows represent the methyl group transfer reactions.

Figure 2-16 represent the reaction network for the conversion of anisole on a Pt/Al_2O_3 catalyst at 573 K corresponding to the results of Runnebaum *et al.*[64]. The first pathway is the full hydrogenation of anisole to methoxycyclohexane. The second pathway, is the direct hydrodeoxygenation leading to benzene and methanol. An alternative way to form benzene is the cleavage of the $C_6H_5O\text{-}CH_3$ bond and form phenol and methane (demethylation). The phenol can further undergo reactions that were discussed before or react with anisole to form more substituted aromatics (condenses). Another anisole conversion path is methyl group transfer reactions with cresol formation. Subsequent conversion of cresol results in toluene (HDO) or condenses.

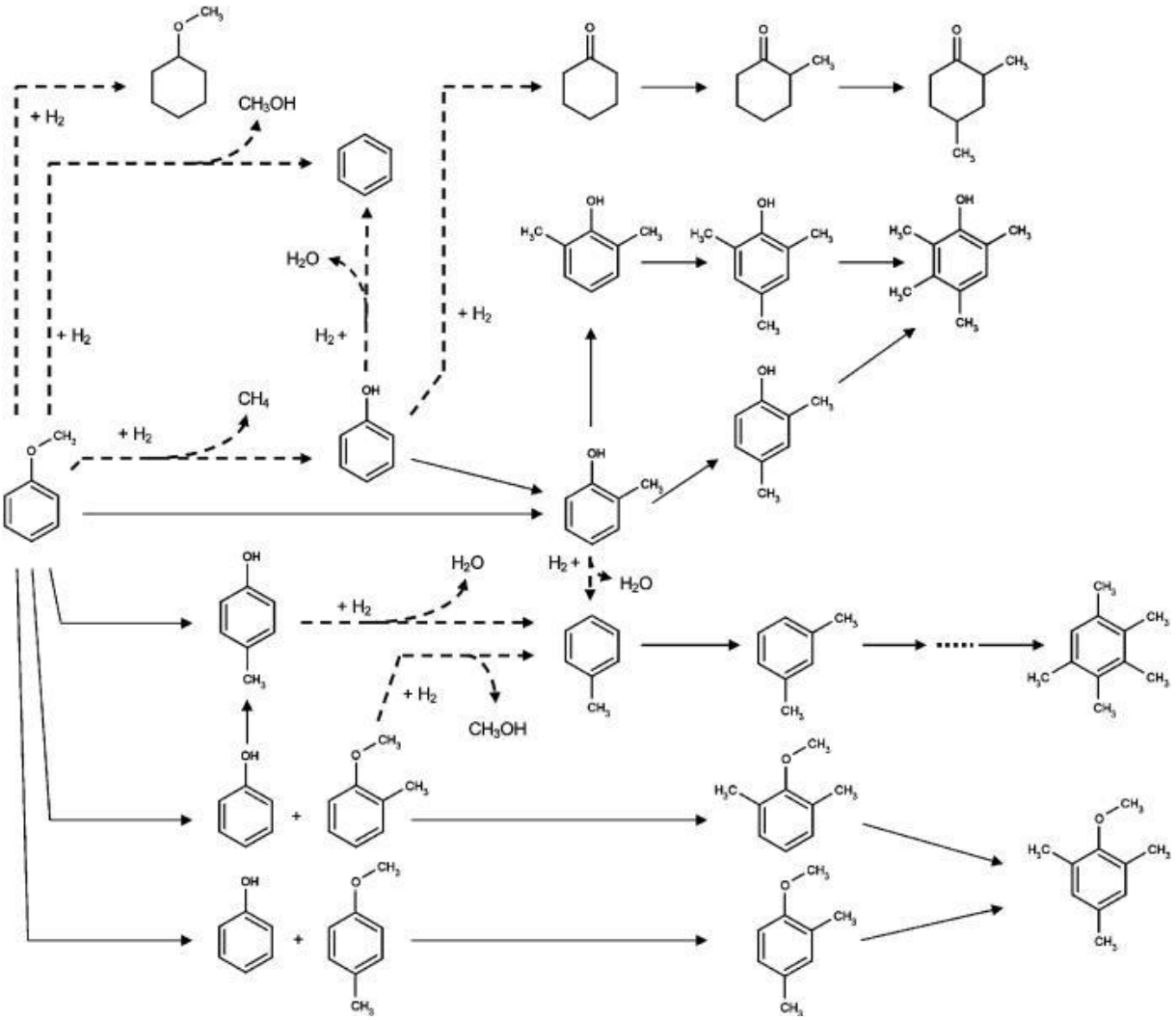

Figure 2-16. Reaction network for anisole HDO catalyzed by Pt/Al_2O_3[64]. The dashed arrows represent hydrodeoxygenation, hydrogenolysis or hydrogenation reactions, while the solid arrows represent the methyl group transfer reactions.

Bykova *et al.*[67, 73] investigated $NiCu/SiO_2$-ZrO_2 bimetallic catalysts for the hydrotreatment of guaiacol (compound (7) in Figure 2-9). Guaiacol (2-methoxyphenol) is an aromatic ring with both a methoxy-group and a hydroxy-group. Hydrodeoxygenation of guaiacol results in phenol or anisole. Therefore, a reaction network for anisole HDO can be extracted from the conversion pathways of guaiacol and is pictured in Figure 2-17. Compared to the reaction network on the Pt/Al_2O_3 (Figure 2-16), no complete hydrogenation of anisole to methoxycyclohexane is observed. Another difference is the higher selectivity towards aliphatic products. Condenses can be formed as well, but the corresponding reaction routes were not included in Figure 2-17. Yakolov *et al.*[49, 74] studied the conversion of anisole using non-sulfided bimetallic Ni-Cu catalysts on different supports at 573 K. The total conversion of anisole varied from 63.5 to 100 mol%, however the dependency on the Ni/Cu ratio is not clear[74]. The degree of oxidation varied from 60 to 100 mol%. Typical HDO products as

benzene, toluene and the consecutive hydrogenation products were observed. Furthermore oxygenates, such as phenol and cyclohexanol, are still present.

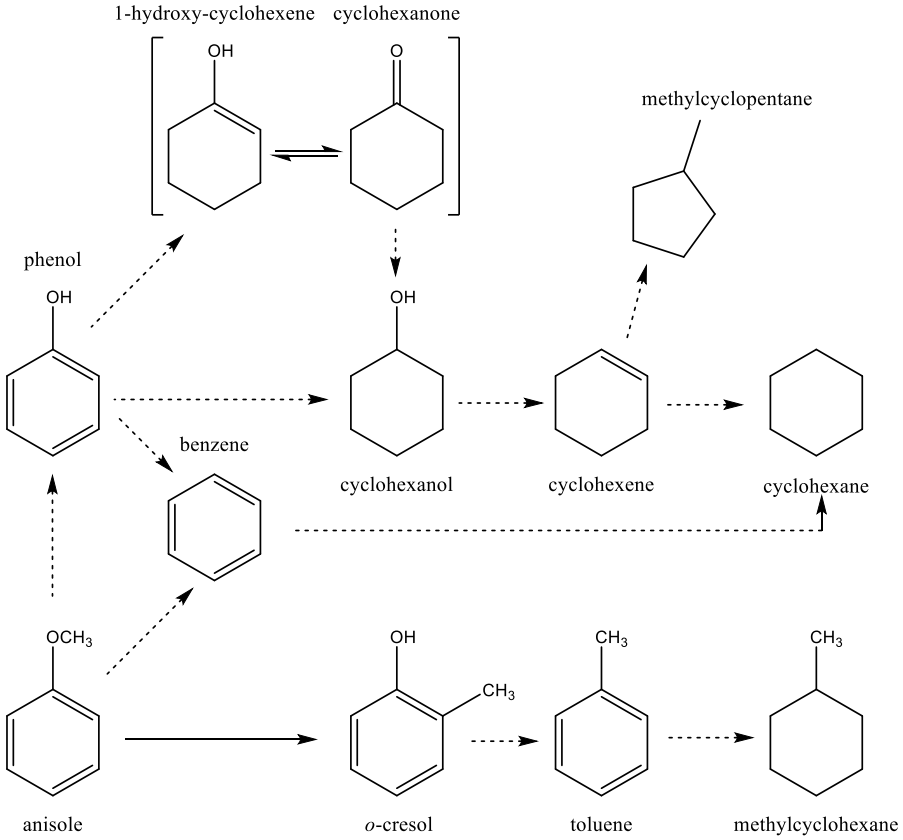

Figure 2-17. Reaction network for anisole HDO on nickel-based catalyst. Adapted from Bykova *et al.*[73] The dashed arrows represent hydrodeoxygenation, hydrogenolysis or hydrogenation reactions, while the solid arrows represent the methyl group transfer reactions.

2.5.4 Kinetics of hydrodeoxygenation

A profound review of the HDO kinetics has been made by Furmisky[35]. Different model compounds have been studied to understand the HDO mechanism of bio-oil. When comparing the different kinetic parameters found in literature attention has to be paid to the type of reactor, the type of catalyst, the reactant concentration, the type of solvent, *etc*.

2.5.4.1Phenols

Massoth *et al.*[56] used Langmuir-Hinshelwood kinetics to extract the values of the adsorption constant for the phenolic feed, the rate constants characterizing the two reaction pathways and the adsorption constants of their products. It is found that the denominator in the Langmuir-Hinshelwood equations equals two. A squared denominator term can be interpreted as an reaction between an adsorbed species and an active site[75]. The dependence of the position of the methyl substitution on the adsorption coefficient is depicted in Figure 2-18 a. Phenol and

phenols with an *ortho*-substituted methyl group have rather small adsorption coefficients compared to the other positions.

The reaction rate coefficients k_1 (direct hydrodeoxygenation) and k_2 (hydrogenation of the aromatic ring) are shown in Figure 2-18 b and c. Phenol shows the lowest rate coefficient for the C-O bond cleavage (k_1), whereas 3,5-dimethylphenol has the largest rate coefficient. It can be seen that the presence of an *ortho*-substituted methyl group, in the presence of a 3-, 4- or 5-methyl group has a little effect on this rate coefficient. Thus, an *ortho*-substituted methyl group does not affect the C-O bond cleavage reactivity. For the hydrogenation reaction, the rate coefficient k_2 can be divided into two groups: one group with lower k_2 having an *ortho*-methyl substitution, and one with higher k_2, but no *ortho*-methyl substitution.

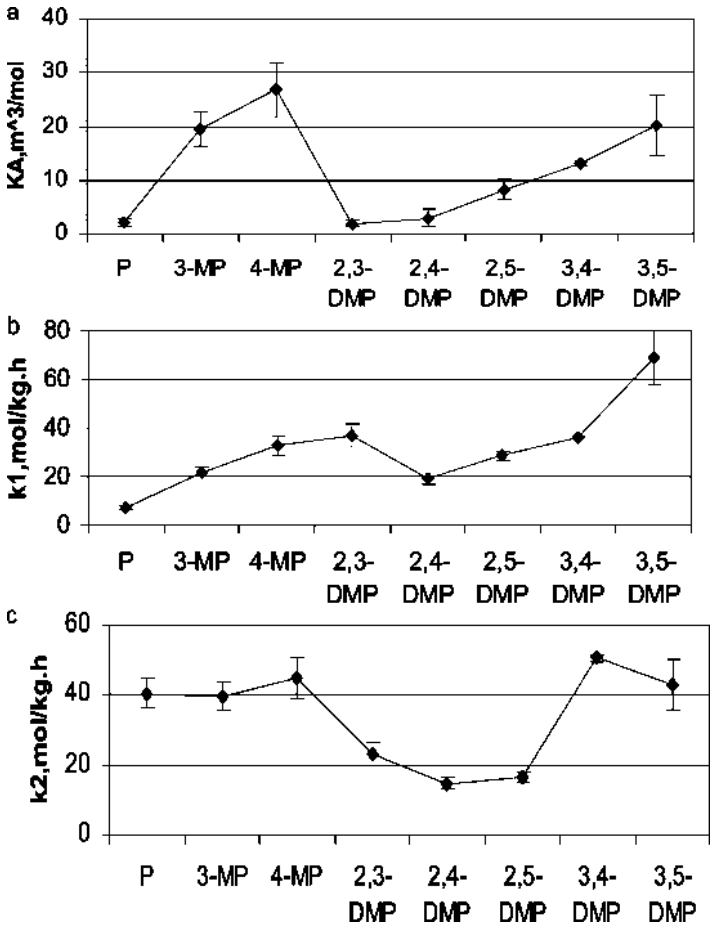

Figure 2-18. Effect of the methyl position in methylphenols on (a) adsorption coefficient of the reactant, (b) the rate coefficient of the direct deoxygenation and (c) the rate coefficient of the hydrogenation over a sulfided CoMo/γ-Al_2O_3[56].

The dependencies of the adsorption coefficients K_A (phenolic feed), K_B (direct hydrogenation product) and K_C (product of the hydrogenation reaction pathway) on the methyl position are summarized in Table 2-4.

Table 2-4. Effect of the methyl position in methylphenols on adsorption coefficients of the phenolic (K_A) feed and the products (K_B and K_C) over a sulfided CoMo/γ-Al_2O_3[56].

	K_B [m³ mol^{-1}]	K_C [m³ mol^{-1}]	K_A [m³ mol^{-1}]
P	2.1 ± 0.6	2.1 ± 4.1	2.0 ± 0.7
3-MP	19.2 ± 3.2	15.4 ± 7.1	21.3 ± 6.1
4-MP	26.4 ± 5.0	26.4 ± 11.3	26.4 ± 8.5
2,3-MP	1.9 ± 0.6	1.7 ± 0.9	2.4 ± 1.6
2,4-MP	3.0 ± 1.5	3.1 ± 2.73	3.1 ± 3.5
2,5-MP	8.2 ± 1.9	8.2 ± 3.3	8.1 ± 5.6
3,4-MP	12.9 ± 0.4	12.8 ± 1.1	3.0 ± 0.8
3,5-MP	19.7 ± 5.2	19.5 ± 9.4	20.0 ± 15.1

The kinetics of the hydrodeoxygenation of substituted phenols was also studied by Gevert *et al.*[59], focusing on 2-, 4- and 2,6-substituted phenols. The experiments were carried out at 5 MPa and 573 K in a batch reactor using a commercial CoMo catalyst. Two main reaction path are observed. Direct hydrodeoxygenation of the substituted phenol results in toluene (k_1), while partial hydrogenation of the phenolics, followed by fast hydrodeoxygenation, forms methylcyclohexenes and methylcyclohexanes (k_2). The pseudo-first-order rate coefficients for the HDO of the substituted phenols are summarized in Table 2-5. A methyl substitution adjacent to the hydroxyl group has an retarding effect for both reactions. Additional methyl substituents lower the rate coefficients even more, as a result of steric hindrance during adsorption.

Table 2-5. Pseudo-first-order rate coefficients for the HDO of substituted phenols at 5 MPa and 573 K over a sulfided CoMo/γ-Al_2O_3[59].

	k_1 [l g_{cat}^{-1} h^{-1}]	k_2 [l g_{cat}^{-1} h^{-1}]
2-MP	0.0756 ± 0.0048	0.0102 ± 0.0006
4-MP	0.144 ± 0.006	0.0312 ± 0.009
2,4-MP	0.09	0.108
2,6-MP	0.0162 ± 0.0006	0.0066 ± 0.0006
2,4,6-MP	0.027 ± 0.009	0.003 ± 0.0012

2.5.4.2Anisole

Runnebaum *et al.*[64] determined the pseudo-first-order rate coefficients for some of the reactions of anisole HDO at 573 K on a Pt/Al_2O_3 catalyst based on analysis of the conversion-selectivity plots of the individual products. The observed rate coefficients for the formation of the primary products, which are phenol, *o*-cresol, benzene, *o*-methylanisole and *p*-cresol, are 12, 2.8, 0.86, 0.14 and 0.0039 l g_{cat}^{-1} h^{-1} respectively. It should be kept in mind, that some products, *e.g.* benzene and phenol, are formed in more than one reaction path way. The pseudo-first-order rate coefficient for the conversion of anisole was found to be 19 l g_{cat}^{-1} h^{-1}. The selectivity towards phenol is the largest. The selectivity towards *o*-cresol is four times smaller. This is in turn almost two magnitudes larger than the selectivity of anisole towards *p*-cresol, indicating a kinetic preference for substitution at the *ortho*-position. Figure 2-19 summarizes the pseudo-first-order rate coefficients.

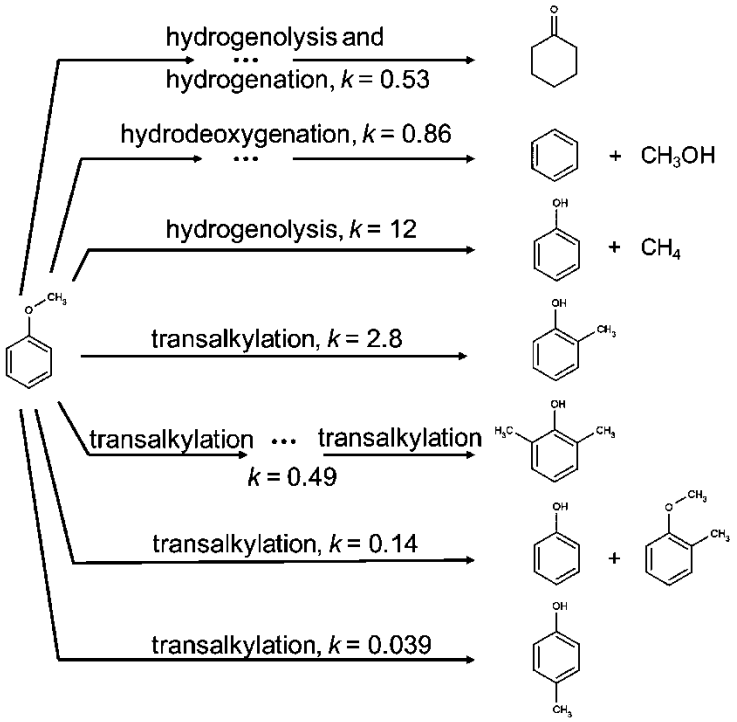

Figure 2-19. Pseudo-first-order rate coefficients (in l g_{cat}^{-1} h^{-1}) for the primary products of anisole HDO at 573 K on Pt/Al_2O_3[64].

Viljava *et al.*[76] determined pseudo-first-order rate coefficients for anisole hydrodeoxygenation at 498 K and a total pressure between 6.2 and 8.6 MPa on sulfided $CoMo/\gamma\text{-}Al_2O_3$. In anisole, two types of C-O cleavages can take place: the cleavage between the aromatic carbon and the oxygen atom, giving benzene, or between the aliphatic carbon and the oxygen atom, giving phenol. The stronger bond between the aromatic carbon and the oxygen atom results in a lower pseudo-first-order rate coefficient compared to the pseudo-first-order rate for the

cleavage between the aliphatic carbon and the oxygen atom, respectively 0.5 g_{cat}^{-1} h^{-1} and 4.4 g_{cat}^{-1} h^{-1}. The pseudo-first-order rate coefficient for the transalkylation to cresol is estimated at 0.7 g_{cat}^{-1} h^{-1}.

2.6 Conclusion

The accelerated rate of energy consumption and demand for fuels has increased the interest in renewable energy sources, such as lignocellulosic biomass. However, the biomass derived fuels have some drawbacks: they have a high oxygen content, they are thermally unstable, they are immiscible with fossil fuel and they give a low heating value. Therefore, upgrading of the bio-oil is required.

Catalytic hydrodeoxygenation seems a promising option to remove the oxy-compounds from the bio-oils. HDO removes oxygen by hydrogen treatment at pressures up to 30 MPa and temperatures in the range of 523 to 723 K. The complexity of the bio-oils has prompted the use of model compounds to study the HDO process. These compounds have functional groups that resemble those found in lignin. The use of the lignin-derived model compounds simplifies the analysis of the reaction paths and product analysis.

A challenge for the hydrodeoxygenation process is to find a catalyst with a high HDO activity and a sufficient lifetime. For example, due to the low sulfur content in bio-oils, a sulfur compound should be added to maintain the stability of a commercial sulfided hydrotreating catalyst. This is undesirable from an environmental point of view, since it result in a contamination of the product and off gas. Noble catalysts show good HDO reactivity, the high price of those metals make them unattractive. The last decades, non-noble transition metal catalysts are being investigated for hydrodeoxygenation, as alternative to both sulfided and noble metal catalysts.

Considerable effort has been devoted to developing a wide variety of reaction networks for lignin-derived model compounds. However, there is a lack of detailed kinetic information regarding the HDO of those model compounds.

2.7 References

1. Alonso, D. M.; Bond, J. Q.; Dumesic, J. A., Catalytic conversion of biomass to biofuels. *Green Chemistry* **2010,** 12, (9), 1493-1513.
2. Roger C, P., The Chemical Composition of Wood. In *The Chemistry of Solid Wood*, American Chemical Society: 1984; Vol. 207, pp 57-126.
3. *Handbook of Plant Science*. John Wiley & Sons.
4. Choudhary, T. V.; Phillips, C. B., Renewable fuels via catalytic hydrodeoxygenation. *Appl. Catal. A-Gen.* **2011,** 397, (1-2), 1-12.
5. Marsman, J. H.; Wildschut, J.; Evers, P.; de Koning, S.; Heeres, H. J., Identification and classification of components in flash pyrolysis oil and hydrodeoxygenated oils by two-dimensional gas chromatography and time-of-flight mass spectrometry. *Journal of Chromatography A* **2008,** 1188, (1), 17-25.
6. Marsman, J. H.; Wildschut, J.; Mahfud, F.; Heeres, H. J., Identification of components in fast pyrolysis oil and upgraded products by comprehensive two-dimensional gas chromatography and flame ionisation detection. *Journal of Chromatography A* **2007,** 1150, (1–2), 21-27.
7. Bridgwater, A. V., Review of fast pyrolysis of biomass and product upgrading. *Biomass and Bioenergy* **2012,** 38, (0), 68-94.
8. Ragauskas, A. J.; Williams, C. K.; Davison, B. H.; Britovsek, G.; Cairney, J.; Eckert, C. A.; Frederick, W. J.; Hallett, J. P.; Leak, D. J.; Liotta, C. L.; Mielenz, J. R.; Murphy, R.; Templer, R.; Tschaplinski, T., The Path Forward for Biofuels and Biomaterials. *Science* **2006,** 311, (5760), 484-489.
9. Mohan, D.; Pittman, C. U.; Steele, P. H., Pyrolysis of Wood/Biomass for Bio-oil: A Critical Review. *Energy & Fuels* **2006,** 20, (3), 848-889.
10. Goyal, H.; Seal, D.; Saxena, R., Bio-fuels from thermochemical conversion of renewable resources: a review. *Renewable and sustainable energy reviews* **2008,** 12, (2), 504-517.
11. Berkowitz, N., On the differential Thermal Analysis of Coal. *Fuel Processing Technology* **1957,** 36, (3), 355-373.
12. Venderbosch, R. H.; Prins, W., Fast pyrolysis technology development. *Biofuels, Bioproducts and Biorefining* **2010,** 4, (2), 178-208.
13. Jenkins, B. M.; Baxter, L. L.; Miles Jr, T. R.; Miles, T. R., Combustion properties of biomass. *Fuel Processing Technology* **1998,** 54, (1–3), 17-46.
14. Naik, S. N.; Goud, V. V.; Rout, P. K.; Dalai, A. K., Production of first and second generation biofuels: A comprehensive review. *Renewable and Sustainable Energy Reviews* **2010,** 14, (2), 578-597.
15. Gomez, L. D.; Steele-King, C. G.; McQueen-Mason, S. J., Sustainable liquid biofuels from biomass: the writing's on the walls. *New Phytologist* **2008,** 178, (3), 473-485.
16. Pandey, M. P.; Kim, C. S., Lignin Depolymerization and Conversion: A Review of Thermochemical Methods. *Chemical Engineering & Technology* **2011,** 34, (1), 29-41.
17. Jongerius, A. L. Catalytic Conversion of Lignin for the Production of Aromatics. Utrecht University, 2013.
18. Bridgwater, A. V., Catalysis in thermal biomass conversion. *Applied Catalysis A: General* **1994,** 116, (1–2), 5-47.
19. Bridgwater, A. V., A survey of thermochemical biomass processing activities. *Biomass* **1990,** 22, (1–4), 279-292.
20. Bridgwater, A. V.; Peacocke, G. V. C., Fast pyrolysis processes for biomass. *Renewable and Sustainable Energy Reviews* **2000,** 4, (1), 1-73.
21. Huber, G. W.; Iborra, S.; Corma, A., Synthesis of transportation fuels from biomass: chemistry, catalysts, and engineering. *Chemical reviews* **2006,** 106, (9), 4044-4098.

22. Bridgwater, A. V., Renewable fuels and chemicals by thermal processing of biomass. *Chemical Engineering Journal* **2003,** 91, (2–3), 87-102.
23. Dickerson, T.; Soria, J., Catalytic Fast Pyrolysis: A Review. *Energies* **2013,** 6, (1), 514-538.
24. Mortensen, P. M.; Grunwaldt, J. D.; Jensen, P. A.; Knudsen, K. G.; Jensen, A. D., A review of catalytic upgrading of bio-oil to engine fuels. *Applied Catalysis A: General* **2011,** 407, (1–2), 1-19.
25. Jones, S. B.; Valkenburg, C.; Walton, C. W.; Elliott, D. C.; Holladay, J. E.; Stevens, D. J.; Kinchin, C.; Czernik, S. *Production of Gasoline and Diesel from Biomass via Fast Pyrolysis, Hydrotreating and Hydrocracking: A Design Case*; 2009.
26. Piskorz, J.; Scott, D. S.; Radlein, D., Composition of Oils Obtained by Fast Pyrolysis of Different Woods. In *Pyrolysis Oils from Biomass*, American Chemical Society: 1988; Vol. 376, pp 167-178.
27. Maggi, R.; Delmon, B., Characterization and upgrading of bio-oils produced by rapid thermal processing. *Biomass and Bioenergy* **1994,** 7, (1–6), 245-249.
28. Maggi, R.; Delmon, B., *Advances in thermochemical biomass conversion*. Blackie Academic & Professional: 1992; Vol. 2.
29. Oasmaa, A.; Czernik, S., Fuel Oil Quality of Biomass Pyrolysis OilsState of the Art for the End Users. *Energy & Fuels* **1999,** 13, (4), 914-921.
30. Bridgwater, A. V., Upgrading Biomass Fast Pyrolysis Liquids. *Environ. Prog. Sustain. Energy* **2012,** 31, (2), 261-268.
31. Zhang, Q.; Chang, J.; Wang, T.; Xu, Y., Review of biomass pyrolysis oil properties and upgrading research. *Energy Conversion and Management* **2007,** 48, (1), 87-92.
32. Bridgwater, A. V., Upgrading Fast Pyrolysis Liquids. In *Thermochemical Processing of Biomass*, John Wiley & Sons, Ltd: 2011; pp 157-199.
33. de Miguel Mercader, F.; Groeneveld, M. J.; Kersten, S. R. A.; Way, N. W. J.; Schaverien, C. J.; Hogendoorn, J. A., Production of advanced biofuels: Co-processing of upgraded pyrolysis oil in standard refinery units. *Applied Catalysis B: Environmental* **2010,** 96, (1–2), 57-66.
34. Saidi, M.; Samimi, F.; Karimipourfard, D.; Nimmanwudipong, T.; Gates, B. C.; Rahimpour, M. R., Upgrading of lignin-derived bio-oils by catalytic hydrodeoxygenation. *Energy & Environmental Science* **2014,** 7, (1), 103-129.
35. Furimsky, E., Catalytic hydrodeoxygenation. *Applied Catalysis A: General* **2000,** 199, (2), 147-190.
36. Ramanathan, S.; Oyama, S. T., New Catalysts for Hydroprocessing: Transition Metal Carbides and Nitrides. *The Journal of Physical Chemistry* **1995,** 99, (44), 16365-16372.
37. Bu, Q.; Lei, H.; Zacher, A. H.; Wang, L.; Ren, S.; Liang, J.; Wei, Y.; Liu, Y.; Tang, J.; Zhang, Q.; Ruan, R., A review of catalytic hydrodeoxygenation of lignin-derived phenols from biomass pyrolysis. *Bioresource Technology* **2012,** 124, (0), 470-477.
38. Jacobson, K.; Maheria, K. C.; Kumar Dalai, A., Bio-oil valorization: A review. *Renewable and Sustainable Energy Reviews* **2013,** 23, (0), 91-106.
39. He, Z.; Wang, X., Hydrodeoxygenation of model compounds and catalytic systems for pyrolysis bio-oils upgrading. *Catalysis for sustainable energy* **2012,** 1, 28-52.
40. Venderbosch, R. H.; Ardiyanti, A. R.; Wildschut, J.; Oasmaa, A.; Heeres, H. J., Stabilization of biomass-derived pyrolysis oils. *Journal of Chemical Technology & Biotechnology* **2010,** 85, (5), 674-686.
41. Samolada, M. C.; Baldauf, W.; Vasalos, I. A., Production of a bio-gasoline by upgrading biomass flash pyrolysis liquids via hydrogen processing and catalytic cracking. *Fuel* **1998,** 77, (14), 1667-1675.

42. Luo, Y. R., *Comprehensive Handbook of Chemical Bond Energies*. Taylor & Francis: 2007.
43. Furimsky, E., Hydroprocessing challenges in biofuels production. *Catalysis Today* **2013,** 217, (0), 13-56.
44. Romero, Y.; Richard, F.; Brunet, S., Hydrodeoxygenation of 2-ethylphenol as a model compound of bio-crude over sulfided Mo-based catalysts: Promoting effect and reaction mechanism. *Applied Catalysis B: Environmental* **2010,** 98, (3–4), 213-223.
45. Baldauf, W.; Balfanz, U.; Rupp, M., Upgrading of flash pyrolysis oil and utilization in refineries. *Biomass and Bioenergy* **1994,** 7, (1–6), 237-244.
46. Ardiyanti, A. R.; Gutierrez, A.; Honkela, M. L.; Krause, A. O. I.; Heeres, H. J., Hydrotreatment of wood-based pyrolysis oil using zirconia-supported mono- and bimetallic (Pt, Pd, Rh) catalysts. *Applied Catalysis A: General* **2011,** 407, (1–2), 56-66.
47. Wildschut, J.; Mahfud, F. H.; Venderbosch, R. H.; Heeres, H. J., Hydrotreatment of Fast Pyrolysis Oil Using Heterogeneous Noble-Metal Catalysts. *Industrial & Engineering Chemistry Research* **2009,** 48, (23), 10324-10334.
48. Gutierrez, A.; Kaila, R. K.; Honkela, M. L.; Slioor, R.; Krause, A. O. I., Hydrodeoxygenation of guaiacol on noble metal catalysts. *Catalysis Today* **2009,** 147, (3–4), 239-246.
49. Yakovlev, V. A.; Khromova, S. A.; Sherstyuk, O. V.; Dundich, V. O.; Ermakov, D. Y.; Novopashina, V. M.; Lebedev, M. Y.; Bulavchenko, O.; Parmon, V. N., Development of new catalytic systems for upgraded bio-fuels production from bio-crude-oil and biodiesel. *Catalysis Today* **2009,** 144, (3–4), 362-366.
50. Khromova, S. A.; Smirnov, A. A.; Bulavchenko, O. A.; Saraev, A. A.; Kaichev, V. V.; Reshetnikov, S. I.; Yakovlev, V. A., Anisole hydrodeoxygenation over Ni–Cu bimetallic catalysts: The effect of Ni/Cu ratio on selectivity. *Applied Catalysis A: General* **2014,** 470, (0), 261-270.
51. Zhao, H. Y.; Li, D.; Bui, P.; Oyama, S. T., Hydrodeoxygenation of guaiacol as model compound for pyrolysis oil on transition metal phosphide hydroprocessing catalysts. *Applied Catalysis A: General* **2011,** 391, (1–2), 305-310.
52. Monnier, J.; Sulimma, H.; Dalai, A.; Caravaggio, G., Hydrodeoxygenation of oleic acid and canola oil over alumina-supported metal nitrides. *Applied Catalysis A: General* **2010,** 382, (2), 176-180.
53. Popov, A.; Kondratieva, E.; Goupil, J. M.; Mariey, L.; Bazin, P.; Gilson, J.-P.; Travert, A.; Maugé, F., Bio-oils Hydrodeoxygenation: Adsorption of Phenolic Molecules on Oxidic Catalyst Supports. *The Journal of Physical Chemistry C* **2010,** 114, (37), 15661-15670.
54. Olcese, R. N.; Bettahar, M.; Petitjean, D.; Malaman, B.; Giovanella, F.; Dufour, A., Gas-phase hydrodeoxygenation of guaiacol over Fe/SiO2 catalyst. *Applied Catalysis B: Environmental* **2012,** 115–116, (0), 63-73.
55. Elliott, D. C., Historical Developments in Hydroprocessing Bio-oils. *Energy & Fuels* **2007,** 21, (3), 1792-1815.
56. Massoth, F. E.; Politzer, P.; Concha, M. C.; Murray, J. S.; Jakowski, J.; Simons, J., Catalytic hydrodeoxygenation of methyl-substituted phenols: correlations of kinetic parameters with molecular properties. *The journal of physical chemistry. B* **2006,** 110, (29), 14283-91.
57. Forzatti, P.; Lietti, L., Catalyst deactivation. *Catalysis today* **1999,** 52, (2), 165-181.
58. Honkela, M. L.; Viljava, T.-R.; Gutierrez, A.; Krause, A. O. I., Chapter 11 Hydrotreating for Bio-Oil Upgrading. In *Thermochemical Conversion of Biomass to Liquid Fuels and Chemicals*, The Royal Society of Chemistry: 2010; pp 288-306.

59. Gevert, B. S.; Otterstedt, J. E.; Massoth, F. E., Kinetics of the HDO of methyl-substituted phenols. *Applied Catalysis* **1987,** 31, (1), 119-131.
60. Shin, E.-J.; Keane, M. A., Gas-Phase Hydrogenation/Hydrogenolysis of Phenol over Supported Nickel Catalysts. *Industrial & Engineering Chemistry Research* **2000,** 39, (4), 883-892.
61. Odebunmi, E. O.; Ollis, D. F., Catalytic hydrodeoxygenation: I. Conversions of o-, p-, and m-cresols. *Journal of Catalysis* **1983,** 80, (1), 56-64.
62. Viljava, T. R.; Komulainen, R. S.; Krause, A. O. I., Effect of H2S on the stability of CoMo/Al2O3 catalysts during hydrodeoxygenation. *Catalysis Today* **2000,** 60, (1–2), 83-92.
63. Jin, S. H.; Xiao, Z. H.; Li, C.; Chen, X.; Wang, L.; Xing, J. C.; Li, W. Z.; Liang, C. H., Catalytic hydrodeoxygenation of anisole as lignin model compound over supported nickel catalysts. *Catalysis Today* **2014,** 234, 125-132.
64. Runnebaum, R. C.; Lobo-Lapidus, R. J.; Nimmanwudipong, T.; Block, D. E.; Gates, B. C., Conversion of Anisole Catalyzed by Platinum Supported on Alumina: The Reaction Network. *Energy & Fuels* **2011,** 25, (10), 4776-4785.
65. Runnebaum, R. C.; Nimmanwudipong, T.; Block, D. E.; Gates, B. C., Catalytic conversion of compounds representative of lignin-derived bio-oils: a reaction network for guaiacol, anisole, 4-methylanisole, and cyclohexanone conversion catalysed by Pt/[gamma]-Al2O3. *Catalysis Science & Technology* **2012,** 2, (1), 113-118.
66. Olcese, R. N.; Francois, J.; Bettahar, M. M.; Petitjean, D.; Dufour, A., Hydrodeoxygenation of Guaiacol, A Surrogate of Lignin Pyrolysis Vapors, Over Iron Based Catalysts: Kinetics and Modeling of the Lignin to Aromatics Integrated Process. *Energy & Fuels* **2013,** 27, (2), 975-984.
67. Bykova, M. V.; Ermakov, D. Y.; Kaichev, V. V.; Bulavchenko, O. A.; Saraev, A. A.; Lebedev, M. Y.; Yakovlev, V. A., Ni-based sol–gel catalysts as promising systems for crude bio-oil upgrading: Guaiacol hydrodeoxygenation study. *Applied Catalysis B: Environmental* **2012,** 113–114, (0), 296-307.
68. Zhao, C.; He, J.; Lemonidou, A. A.; Li, X.; Lercher, J. A., Aqueous-phase hydrodeoxygenation of bio-derived phenols to cycloalkanes. *Journal of Catalysis* **2011,** 280, (1), 8-16.
69. Furimsky, E.; Mikhlin, J.; Jones, D.; Adley, T.; Baikowitz, H., On the mechanism of hydrodeoxygenation of ortho substituted phenols. *The Canadian Journal of Chemical Engineering* **1986,** 64, (6), 982-985.
70. Shin, E.-J.; Keane, M. A., Detoxifying chlorine rich gas streams using solid supported nickel catalysts. *Journal of Hazardous Materials* **1999,** 66, (3), 265-278.
71. Bataille, F.; Lemberton, J.-L.; Michaud, P.; Pérot, G.; Vrinat, M.; Lemaire, M.; Schulz, E.; Breysse, M.; Kasztelan, S., Alkyldibenzothiophenes Hydrodesulfurization-Promoter Effect, Reactivity, and Reaction Mechanism. *Journal of Catalysis* **2000,** 191, (2), 409-422.
72. Jongerius, A. L.; Jastrzebski, R.; Bruijnincx, P. C. A.; Weckhuysen, B. M., CoMo sulfide-catalyzed hydrodeoxygenation of lignin model compounds: An extended reaction network for the conversion of monomeric and dimeric substrates. *Journal of Catalysis* **2012,** 285, (1), 315-323.
73. Bykova, M. V.; Ermakov, D. Y.; Khromova, S. A.; Smirnov, A. A.; Lebedev, M. Y.; Yakovlev, V. A., Stabilized Ni-based catalysts for bio-oil hydrotreatment: Reactivity studies using guaiacol. *Catalysis Today* **2014,** 220–222, (0), 21-31.
74. Ardiyanti, A. R.; Khromova, S. A.; Venderbosch, R. H.; Yakovlev, V. A.; Heeres, H. J., Catalytic hydrotreatment of fast-pyrolysis oil using non-sulfided bimetallic Ni-Cu

catalysts on a δ-Al2O3 support. *Applied Catalysis B: Environmental* **2012,** 117–118, (0), 105-117.
75. Froment, G. F.; Bischoff, K. B.; De Wilde, J., *Chemical Reactor Analysis and Design, 3rd Edition*. John Wiley & Sons: 2010.
76. Viljava, T. R.; Saari, E. R. M.; Krause, A. O. I., Simultaneous hydrodesulfurization and hydrodeoxygenation: interactions between mercapto and methoxy groups present in the same or in separate molecules. *Applied Catalysis A: General* **2001,** 209, (1–2), 33-43.

Chapter 3

PROCEDURES

The main aspects of this thesis are performing an experimental study and proposing a kinetic model for hydrodeoxygenation of lignin-derived model compounds. In this chapter, the procedures for obtaining experimental data and the parameter estimation will be discussed. The experiments are performed on the High-Throughput Kinetic setup (HTK-1) at the Laboratory for Chemical Technology. The analysis of the obtained experimental data leads to a kinetic model. The parameters of the model are estimated using the regression software Athena Visual Studio. The validation of the estimated parameters is done by several statistical tests, which will be explained in this chapter.

3.1 Experimental setup

The experimental work on the HDO of anisole is performed on the High-Throughput Kinetic setup (HTK-1), constructed by Zeton B.V., available within the Laboratory for Chemical Technology. The setup consists of eight plug flow reactors, grouped per two in one furnace (Figure 3-1). Reactors 5 and 6 are used for the HDO experiments.

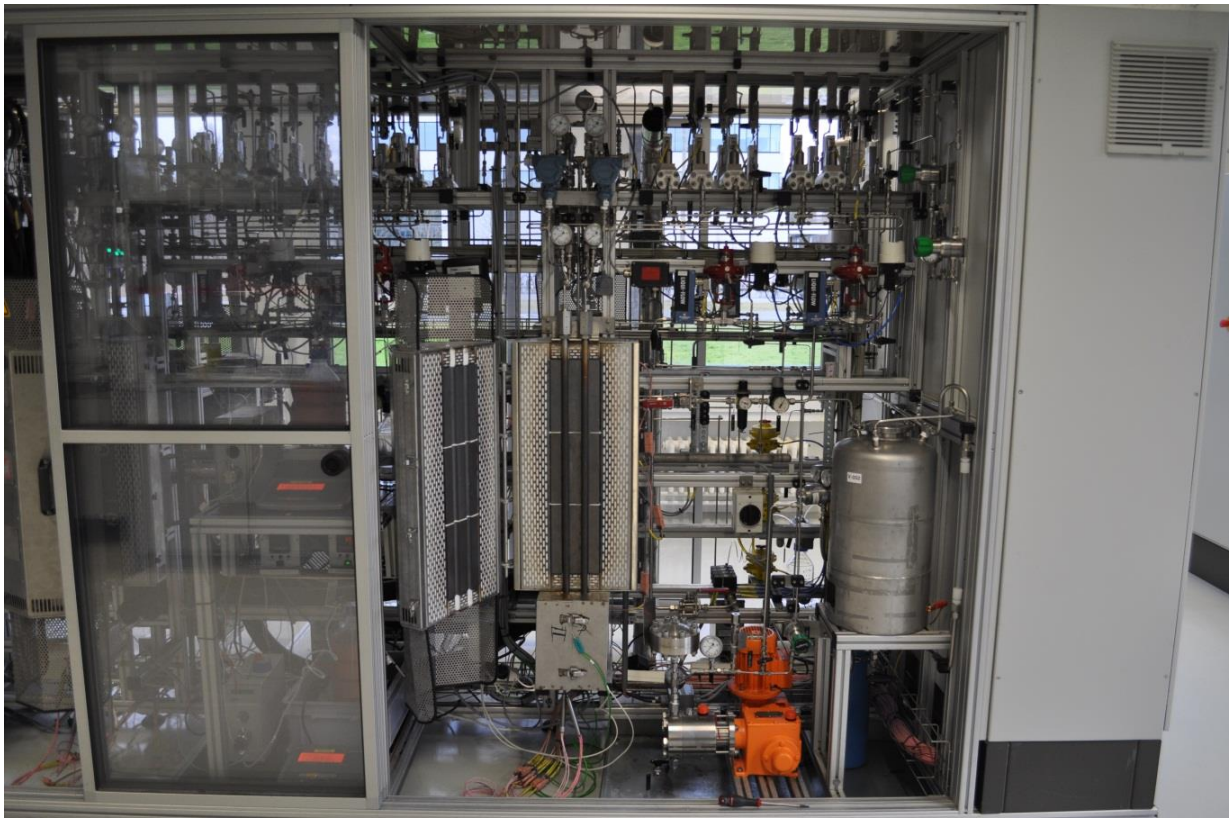

Figure 3-1. Reactor block 3, *i.e.* reactor 5 and 6, of the HTK-1.

A general flow scheme of one reactor can be found in Figure 3-2. One can distinguish six different sections: the gas feed section, the liquid feed section, the reactor section, the reactor overpressure safety system, the reactor back pressure section and an analysis section. There are both manual and pneumatic valves present in the setup. The pneumatic valves are controlled with LabVIEW control program. With this software it is possible to control the feed, the reactor and the product section.

In the next paragraphs, the three most essential sections for experiments will be discussed in detail: the feed section, the reaction section and the analysis section.

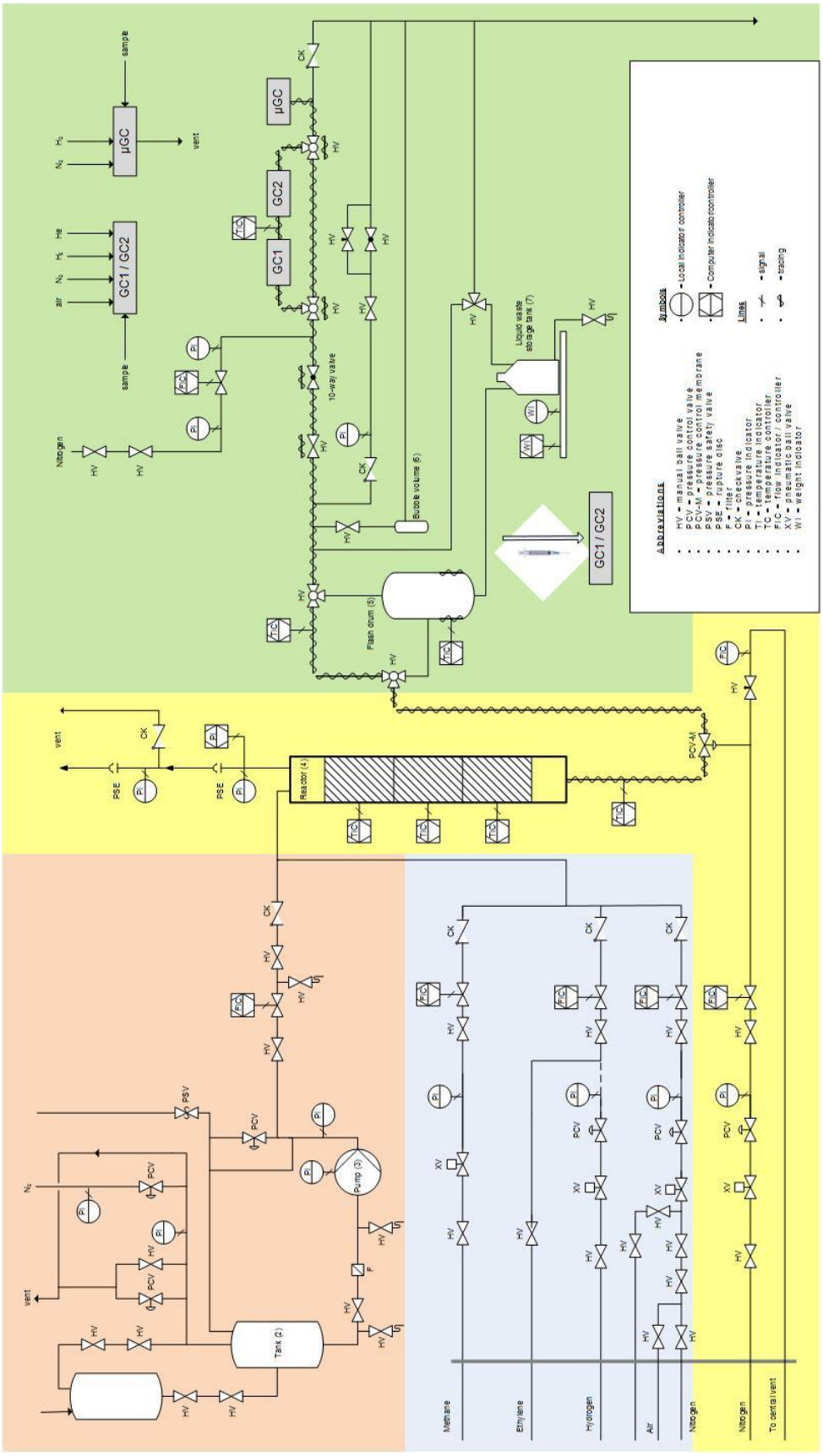

Figure 3-2. Flow diagram of one reactor in the HTK-1.

3.1.1 Feed section

The feed section contains a liquid feed and several gas feeds, which can be sent with different flow rates to the reactor. In the HDO experiments, the liquid feed consisting of the reactant, solvent and internal standard, while the gas feed consists of hydrogen, nitrogen as diluent and ethane as internal standard.

The liquid feed is supplied from a stainless steel storage vessel via a plunjer-diaphragm dosing pump. A liquid mass flow controller (Bronkhorst®) with an operational range between 10 and 50 g h^{-1} regulates the liquid flow to the reactor[1].

The gaseous feed is supplied from gas cylinders. The hydrogen cylinder is installed in a safety cabinet and equipped with its own safety device. For each of the gases, a pneumatic valve is present which closes in cases of shutdown of emergency. After this valve, the gas flow is sent to thermal mass flow controller (Bronkhorst®) which are expressed in norm liters per hour. The controllers are available in three different ranges[1]: 0.1-10 Nl h^{-1} (type 1), 0.1-100 Nl h^{-1} (type 2), and 0.1-1000 Nl h^{-1} (type 3).

All of the controllers are calibrated for a reference component. The gas flow controllers are calibrated with different reference gasses, which are methane, hydrogen and nitrogen for respectively the type 1, type 2 and type 3 controllers. The liquid flow controller is calibrated for *n*-octane. When using a different gas or liquid than the reference one, a correction factor has to be taken into account due to the difference in heat capacity, in order to define the setup value for the LabVIEW interface. The flow rate that has to be set, is hence:

$$F_0^k = \alpha F_0^{ref} \qquad 3\text{-}1$$

With α: the correction factor

F_0^{ref}: the flow rate set in the LabVIEW interface

F_0^k: the feed flow rate of the actual component fed

The correction factor can be calculated with the web application Fluidat® or be determined experimentally.

Before entering the reactor, the liquid feed is mixed with the gas feed after passing a check valve which prevents backflow from the reactor.

3.1.2 Reaction section

Each reactor in the HTK-1 is a tube made of AISI 316 cold worked steel with an inner diameter of 1.9 mm and a height of 89 cm, which allows pressures up to 20.5 MPa and temperatures up to 922 K[1]. The reactor tube is paired with a second reactor and placed in a single reactor block. For each block, the temperature and pressure can be regulated. The gas and liquid flow rates of each tube in a block can be regulated individually.

Per block, the temperature is regulated at three places along the reactor with two N-type thermocouples (o.d. 3 mm). One thermocouple is place at the outer wall of the tube, while the other is placed in the catalyst bed. The choice of regulation (inside the catalyst bed or at the wall) can be specified in the LabVIEW interface. For measuring intrinsic kinetics, it is more interesting to use the one inside the catalyst bed. However, a better temperature control is obtained by the one at the reactor wall due to the reduction in response time in the control system.

The pressure in the reactor is controlled by a back pressure regulator. The reactor effluent passes through one side of the pressure control valve, while nitrogen is sent to the other side of the membrane. When the pressure at the reactor side is slightly higher than the back pressure, the reactor effluent will flow towards the analysis section.

To maintain completely in the gas phase, an infrared oven is available to heat the reactor outlet and tracings (up to 573 K) are placed on the transfer lines to the analysis section.

3.1.3 Analysis section

The reactor effluent is separated in a flash drum at temperatures of maximum 313 K and atmospheric pressure. The liquids are subsequently sent to the liquid storage tanks. As no liquids are present, the flash drum is bypassed and the gaseous stream is directly sent via a ten-way valve to one of two available gas chromatographs (GC). To prevent any condensation of the heavy compounds near the GC sampling valves, an additional nitrogen dilution line was installed.

The analysis is performed with a FID-equipped GC (Agilent Technologies 6850 series II network GC system), loaded with a non-polar capillary column (DB-1, 60 m x 0.25 mm i.d. x 0.25 µm dimethylpolysiloxane). The Flame Ionization Detector (FID) detects the ions that are formed by combustion of these compounds in a hydrogen flame. The quantity of these ions is proportional to the concentration of the different compounds in the mixture. Since the FID has

different sensitivity dependent on the compound, a correction factor has to be used to obtain quantitative results.

3.2 Reactor loading

The catalyst is a fine powder and, hence it should be pelletized into particles of a larger diameter to prevent it being blown out of the reactor by the gas flow. The diameter of the pellets is determined by correlations to avoid transport limitations (Appendix D), and is in the range of 400 to 600 µm.

The catalyst bed should be placed in the isothermal area of the reactor to ensure preheating and mixing of the gasses. Inert material is used to place the catalyst at the desired position. The used inert material is α-alumina which is available in the different ranges: 0.5-1.5 mm, 1.5-2.5 mm and 2.5-3.5 mm. The largest particles are placed at the bottom of the reactor to prevent entrainment of the smaller inert particles. The middle-size and small-size particles are used to place the catalyst in the middle of the reactor. Then, the catalyst bed itself is added. The catalyst bed consists of catalyst pellets diluted with inert material of the smallest size. The amount of dilution is determined to minimize the temperature gradient (Appendix D). On top of the catalyst, inert material is placed to ensure a good mixing of the gases and a plug flow over the catalyst bed.

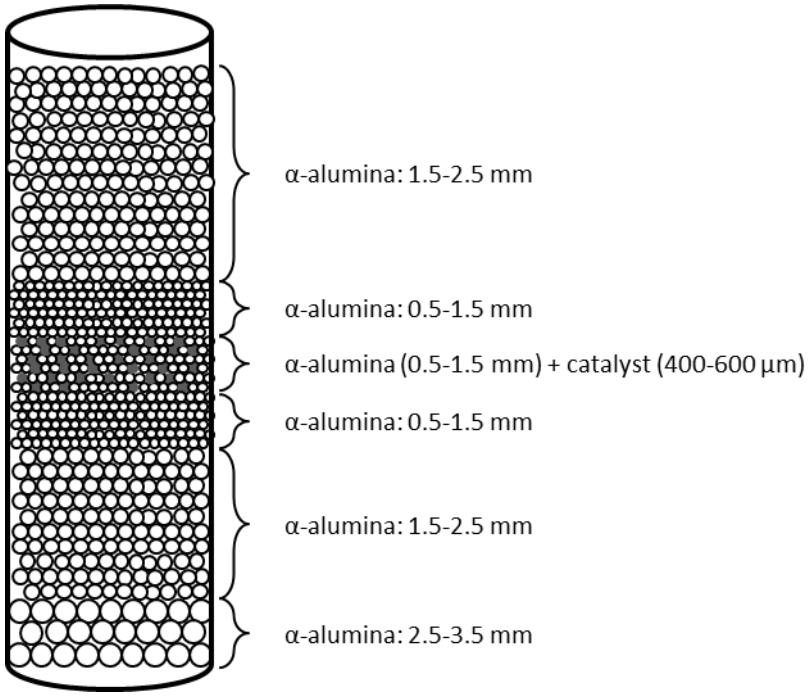

Figure 3-3. Schematic overview of the reactor filling.

3.3 Calculations and analysis

3.3.1 Space time and weight hourly space velocity

Besides temperature and pressure, the space time defines the reaction conditions. Space time τ is the ratio between the catalyst mass W [kg_{cat}] and the molar inlet flow rate of the feed F_0 [mol_{feed} s^{-1}], hence the units of space time are kg_{cat} s mol_{feed}^{-1}. It quantifies the time that an average molecule has for reaction[2].

$$\tau = \frac{W}{F_0} \qquad 3\text{-}2$$

In the industry, the weight hourly space velocity ($WHSV$) is more frequently used. The $WHSV$ is defined as the mass inlet flow rate of the feed F_0^{wt} [kg_{feed} s^{-1}] divided by the catalyst mass W [kg_{cat}] in the reactor.

$$WHSV = \frac{F_0^{wt}}{W} \qquad 3\text{-}3$$

3.3.2 Calculation of the outlet composition

The composition of the reactor effluent is analyzed by the gas chromatograph (see 3.1.3). For the anisole HDO experiments an optimized GC method was developed which leads to a qualitative separation of the different components without being too time-consuming. More details about the temperature profile and other specifications of the GC-column for the analysis are given in Appendix B. To translate the chromatograms into mixture compositions, the calibration factors for different components must be known. During this thesis, the calibration factors were determined experimentally (Appendix C). Using these calibration factors, CF_k, the relative molar composition of the reactor effluent can be calculated via 3-4, in which A_k is the peak surface area obtained from raw GC data[3].

$$x_k = \frac{A_k CF_k}{\sum_{j=1}^{n} A_j CF_j} \qquad 3\text{-}4$$

The outlet flow rates are defined using an internal standard (IS). The molar flow rate of every component F_k [mol s^{-1}] can be calculated when the molar fraction of the component x_k and the total molar flow rate F_{tot} [mol s^{-1}] are known. Since the outlet flow rate of the internal standard is assumed to be equal to inlet flow rate, the total flow rate can be calculated.

$$F_k = x_k F_{tot} = x_k \frac{F_{IS,0}}{x_{IS}} \quad 3\text{-}5$$

Water and hydrogen cannot be detected with a FID, therefore elemental balances ϕ_{e_t} must be used to calculate the complete composition of the outlet stream. Combination of the oxygen balance with the hydrogen balance allows to determine the amount of water and hydrogen in the product mixture. By introducing the molar outlet flow rate of every component, the element balances, can be written as in 3-6[3].

$$\phi_{e_t} = \frac{\sum_{j=1}^{n} a_{t,j} F_j}{\sum_{j=1}^{n} a_{t,j} F_{j,0}} \quad 3\text{-}6$$

With $a_{t,j}$: the number of *t* atoms in component *j* [-]

$F_{j,0}$: the molar inlet flow rate of component *j* [mol s^{-1}]

F_j: the molar outlet flow rate of component *j* [mol s^{-1}]

The total mass inlet flow rate must be equal to the total mass outlet flow rate, or ϕ_m must be equal to 1. However, small deviations may occur due to leaks in the setup, bad separation on the column, *etc.* and thus it is considered that the mass balance ϕ_m is closed if $0.95 < \phi_m < 1.05$.

$$\phi_m = \frac{\sum_{j=1}^{n} MM_j F_j}{\sum_{j=1}^{n} MM_j F_{j,0}} \quad 3\text{-}7$$

With MM_j: the molecular mass of component *j* [kg mol^{-1}]

Another method to calculate the composition of the mass outlet flow is the normalization method, which assumes a 100 % mass balance. When only a gas phase is present, the closed mass balance can be written as in equations 3-8 and 3-9.

$$\sum_{j=1}^{n} MM_j F_{j,0} = \sum_{j=1}^{n} MM_j F_j \quad 3\text{-}8$$

$$F_0 \sum_{j=1}^{n} MM_j y_{j,0} = F_{tot} \sum_{j=1}^{n} MM_j y_j \quad 3\text{-}9$$

Solving equation 3-9 to F_{tot} and substituting in equation 3-5 yields equation 3-10.

$$F_k = x_k F_0 \frac{\sum_{j=1}^{n} MM_j y_{j,0}}{\sum_{j=1}^{n} MM_j y_j} \quad 3\text{-}10$$

3.3.3 Conversion, selectivity and yield

To describe the reactor output and compare experimental results, the conversion of reactant *A*, the selectivity of this reactant *A* towards product *B* and the yield of a certain product *B* are calculated.

The conversion of reactant *A*, X_A, is calculated via the molar inlet flow rate $F_{A,0}$ [mol s^{-1}] and molar outlet flow rate F_A [mol s^{-1}].

$$X_A = \frac{F_{A,0} - F_A}{F_{A,0}} \qquad 3\text{-}11$$

The selectivity of reactant *A* towards product *B*, $S_{B,A}$, is calculated on elemental basis (carbon, oxygen, hydrogen or nitrogen[3]) from the molar flow rates of the reactant and product.

$$S_{B,A} = \frac{a_{t,B}(F_B - F_{B,0})}{a_{t,A}(F_{A,0} - F_A)} \qquad 3\text{-}12$$

The yield of a product *B*, $Y_{B,A}$, is expressed as the conversion multiplied by the selectivity of that product.

$$Y_{B,A} = S_{B,A}X_A = \frac{a_{t,B}(F_B - F_{B,0})}{a_{t,A}F_{A,0}} \qquad 3\text{-}13$$

3.4 Modeling

3.4.1 Reactor model

The outlet flow rates of tubular reactors can be modeled using a one-dimensional pseudo-homogenous plug flow reactor model. An ideal plug flow regime can be assumed as the criteria for the absence for axial and radial dispersion are satisfied. In addition, an isothermal and isobaric operation is always assumed. The external and internal mass transport limitations remain absent according to the calculated Carberry number and Weisz modulus. A detailed description of the different criteria can be found in Appendix D.

As a result, the axial flow profile for a component *j* through the reactor can be expressed via 3-14[2], in which F_j is the molar outlet flow rate of component *j*, W is the catalyst weight and R_j is the netto production rate of component *j*. The production rate follows from the kinetic model and is dependent of the temperature, partial pressure of the components and the performance of the catalyst.

$$\frac{dF_j}{dW} = R_j \qquad 3\text{-}14$$

A set of differential equations is obtained, since every component *j* has a different equation 3-14. Together with the boundary conditions ($F_i = F_{i,0}\ at\ W = 0$) for every component, the set of equations can be solved.

3.4.2 Parameter estimation

3.4.2.1 Determination of optimal parameters

The kinetic parameters from the model are estimated by minimizing the (weighted) sum of square of the residuals between the experimental molar outlet flow rates and the model calculated ones. The minimization is done by adjusting the model parameter b which is expected to approach the real parameter β when the optimum is reached[4].

$$SS_{RES} = \sum_{i=1}^{v}\sum_{j=1}^{n} w_i\left(F_{i,j} - \widehat{F}_{i,j}\right)^2 \overset{b}{\rightarrow} min \qquad 3\text{-}15$$

With v: the number of responses [-]

n: the number of experiments [-]

w_i: the weight factor [-]

$F_{i,j}$: the experimental molar outlet flow rate of response *i* at experiment *j* [mol s^{-1}]

$\widehat{F}_{i,j}$: the corresponding model calculated value [mol s^{-1}]

The weight factor w_i gives an indication about the importance of the response variable. It is calculated as the inverse of the diagonal elements of the covariance matrix, see 3-16 in which p is the number of parameters, v is the number of responses, n is the number of experiments.

$$w_i = \frac{1}{\sigma_{ii}^2} = \frac{nv - p}{\sum_{j=1}^{n}\left(F_{i,j} - \widehat{F}_{i,j}\right)^2} \qquad 3\text{-}16$$

Because of the non-linear character of the sum of squares, the system of normal equations is not linear and contains possibly more than one solution. One of these solutions corresponds to the wanted global minimum. To find this minimum of the residual sum of squares several methods are available, *e.g.* Rosenbrock method, method of the steepest descendent or Levenberg-Marquardt method. In Athena Visual Studio (AVS), which is the Fortran-based program that is used to perform the regression, the Levenberg-Marquardt method is used[5]. This method works iteratively and therefore needs initial values for the parameters to start from. These initial values need to be as close as possible to the real values, otherwise it is

likely that the regression method will end up in a local minimum instead of the global minimum.

3.4.2.2 Statistical analysis

To evaluate the parameter estimation, several test are available. The most important ones, will be discussed in the next paragraphs.

Significance of the parameters

The individual significance of each parameter is tested with comparison of the calculated *t* value and the tabulated *t* value. The *t* test verifies whether the estimate b_i deviates significantly from a predetermined value β_i. Usually, the estimates b_i are tested with respect to the value zero. To calculate the *t* value equation 3-17[4] is used, in which b_i is the value of the estimated value, β_i is the exact parameter value (zero) and $V(b)_{i,i}$ is the element on position *(i,i)* of the covariance matrix $V(b)$.

$$t_{cal} = \frac{b_i - \beta_i}{\sqrt{V(b)_{i,i}}} \qquad 3\text{-}17$$

The null hypothesis can be rejected with a probability α when the calculated t-value exceeds the tabulated one. The test is commonly performed with a probability of 95 %.

The binary correlation coefficient $\rho_{i,j}$ between two parameters *i* and *j* expresses the relationship between these parameters, via the (co)variances of these parameters. A small binary correlation coefficient indicates low dependency between the parameters. In practice, the binary correlation coefficient should be smaller than 0.95.

$$\rho_{i,j} = \frac{V(b)_{i,j}}{\sqrt{V(b)_{i,i}V(b)_{j,j}}} \qquad 3\text{-}18$$

Besides the statistical significance of the parameters, the physical significance of the parameters should be verified. For example, the sign of the parameter (no negative values for rate constants or equilibrium constants) or the order of magnitude of the parameter should have a physical meaning.

Significance of the regression

Instead of checking every parameter individually, which is done in the *t* value, the *F* test is used to test the significance of the complete model. To check whether the whole regression is significant, the calculated *F* value is compared to the tabulated *F* value. If the actual value of F_s, which is calculated by 3-19, is larger than the corresponding tabulated *F* value for the selected probability level 1-α, the null hypothesis is rejected and the regression is considered to be meaningful. The confidence interval used in this *F* test is 95 %.

$$F_s = \frac{\frac{SS_{REG}}{d.f._{REG}}}{\frac{SS_{RES}}{d.f._{RES}}} \qquad 3\text{-}19$$

Where SS_{REG} is the regression sum of square, SS_{RES} is the residual sum of square and *d.f.* the corresponding degrees of freedom. The definitions of SS_{REG}, SS_{RES}, $d.f._{REG}$ and $d.f._{RES}$ to calculate the *F* value are given below, in 3-20 till 3-23[4, 6].

$$SS_{REG} = \sum_{i=1}^{v}\sum_{j=1}^{n} w_i \hat{y}_{i,j}^{\,2} \qquad 3\text{-}20$$

$$d.f._{REG} = p \qquad 3\text{-}21$$

$$SS_{RES} = \sum_{i=1}^{v}\sum_{j=1}^{n} w_i (y_{i,j} - \hat{y}_{i,j})^2 \qquad 3\text{-}22$$

$$d.f._{RES} = nv - p \qquad 3\text{-}23$$

With $y_{i,j}$: the *i*-th response to the *j*-th experimental observation

$\hat{y}_{i,j}$: the model prediction of the *i*-th response to the *j*-th experimental observation

p: the number of parameters

v: the number of responses

n: the number of experiments

Adequacy of the model

To investigate the adequacy of a model, a lack-of-fit test is performed. The hypothesis of the test is that the model is adequate, meaning that the deviations between the experimental observations and the model predictions can be attributed solely to the experimental error and not a lack-of-fit of the model. If the calculated *F* value is larger than the corresponding tabulated one, for a selected probability level 1-α, the hypothesis is rejected and the model is considered to be not adequate. This test is usually calculated for a probability value of 95 %. The *F* value for the adequacy test is calculated by 3-24.

$$F_a = \frac{\frac{SS_{LOF}}{d.f._{LOF}}}{\frac{SS_{PE}}{d.f._{PE}}} = \frac{\frac{SS_{RES} - SS_{PE}}{d.f._{LOF}}}{\frac{SS_{PE}}{d.f._{PE}}} \qquad 3\text{-}24$$

With SS_{LOF}: the lack-of-fit sum of squares

SS_{PE}: the pure-error sum of squares

SS_{RES}: the residual sum of squares (3-22)

d.f.: the corresponding degrees of freedom

The definitions of SS_{PE}, $d.f._{LOF}$ and $d.f._{PE}$ to calculate the *F* value are given below, in 3-25 till 3-27[4, 6].

$$SS_{PE} = \sum_{i=1}^{k} \sum_{j=1}^{\nu} \sum_{l=1}^{n_e(i)} w_j \left(y_{j,l}^{(i)} - \bar{y}_l^{(i)} \right)^2 \qquad 3\text{-}25$$

$$d.f._{LOF} = \nu \left(n - \sum_{i=1}^{k} n_e(i) - 1 \right) - p \qquad 3\text{-}26$$

$$d.f._{PE} = \nu \left(\sum_{i=1}^{k} n_e(i) - 1 \right) \qquad 3\text{-}27$$

With $n_e(i)$: the number of repeat experiments at the *i*-th set of repeat experiments

$y_{j,l}^{(i)}$: the *i*-th experimental observation corresponding to the *i*-th set of repeat experiments and the *j*-th response

$\bar{y}_l^{(i)}$: the average value of the *i*-th set of repeat experiments and the *j*-th response.

3.5 References

1. Toch, K.; Bogaert, M. *High-Througput Kinetic Setup: Manual and safety guidelines*; Ghent Univeristy: 2012.
2. Marin, G. B. *Chemical Reactors: Fundamentals and applications*; Ghent University: 2014.
3. Toch, K.; Marin, G. B. *Calculation of outlet composition, flow rates, conversion and selectivities in continuous flow (multiphase) reactors)*; Ghent University: 2011.
4. Thybaut, J. W. *Kinetic Modeling and Simulation*; Ghent University: 2013.
5. Studio, A. V. *Programming Guide: process modeling, paramter estimation and optimization*.
6. Toch, K.; Thybaut, J. W.; Marin, G. B., A systematic methodology for kinetic modeling of chemical reactions applied to n-hexane hydroisomerization. *AIChE Journal* **2014**, n/a-n/a.

Chapter 4

KINETIC MODELING OF GAS PHASE ANISOLE HYDRODEOXYGENATION OVER A COMO/γ-AL_2O_3 CATALYST

This chapter gives an overview of the hydrodeoxygenation of anisole performed in an ideal plug flow reactor over a CoMo/γ-Al_2O_3 catalyst in the temperature range of 548 K to 623 K, and different space times at 0.5 MPa. The demethylation of anisole to form phenol, and the transalkylation of anisole to cresol were found to be the primary reaction pathways. The CoMo/γ-Al_2O_3 shows only a small extent towards the deoxygenated products benzene and toluene. Two kinetic models, i.e. a power law model and a Langmuir-Hinshelwood kinetic model, were developed to describe the observed kinetics. From the regression to the intrinsic kinetic data set, the parameters of these models were determined. Based on statistical tests on the parameters and regression, as on the comparison of the simulated behavior with the experimental observations, the parameter values and the performance of the model are verified.

4.1 Reaction conditions for gas phase reaction

Before performing any experiments, the reaction conditions for gas phase reaction has to be determined. To prevent condensation, the transfer lines from the reactor to the analysis section are heated. Another precaution, is the dilution of the feed flow with nitrogen. Aspen Plus © is used to simulate the HTK-1, as depicted in Figure 4-1, and to determine the amount of nitrogen that is needed to maintain in the gas phase.

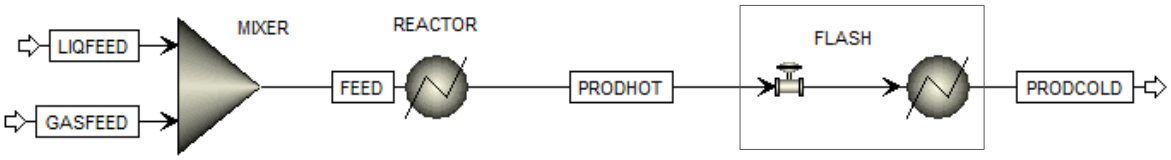

Figure 4-1. Representation of the HTK-1 in Aspen Plus ©.

The hydrodeoxygenation of anisole is simulated at 573 K and 5 MPa, using an appropriate property method. A property method is a collection of estimation methods to calculate the thermodynamic and transport properties of pure components. Several property methods were tested based on the Aspen Plus Best Practice guidelines. Since there are no important polar components present in the system, an equation of state (EOS) model is selected. Typically, the Peng-Robinson EOS (and its variations) and the Soave-Redlich-Kwong EOS (and its variations) are used for non-polar systems with real components. In these thesis, the SRK property method was selected in all simulations since the SRK property method has some benefits over the PR property method. First of all, SRK can be used for hydrocarbon systems that include the common light gases, such as N_2. Secondly, it uses volume corrections to improve the liquid molar volume calculated from the cubic equation of state[1]. Typical experimental conditions are simulated, *e.g.* anisole flow rate of 1 to 5 g h^{-1}, in combination with the worst-case scenario, *i.e.* no anisole conversion observed.

The nitrogen dilution flow is varied from 0 to 200 Nl h^{-1}, in combination of a varying temperature of the flash vessel, which is the coldest point in the system, in the range of 298-343 K. The pressure after the expansion is 1 MPa. The simulation results indicate that no condensation will occur in any of the tested conditions.

4.2 Reaction conditions for intrinsic kinetics

The hydrodeoxygenation of anisole is a complex process with different interacting phenomena such as catalytic reaction of the adsorbed species, heat and mass transfer between

the catalyst surface and the gas phase, as well as heat and mass transport within the catalyst pellet.

The experiments are performed with the aim of constructing a kinetic model, in which the effect of the reaction conditions on the reaction rate is negligible for transport and transfer resistances, *i.e.* the so-called intrinsic kinetic regime. There exist several theoretical criteria to detect non-ideal reactor behavior, which are discussed in detail in Appendix D. The operating condition for the hydrodeoxygenation experiments over the CoMo/γ-Al_2O_3 catalyst are summarized in Table 4-1.

Table 4-1. Summary of the operation conditions for intrinsic kinetics over the CoMo/γ-Al_2O_3 catalyst.

Operating condition	Experimental range
Catalyst pellet diameter	400-600 µm
Temperature	548-623 K
Anisole inlet partial pressure	150-600 Pa
Space time	500-2500 kg_{cat} s $mol_{anisole}^{-1}$
H_2/anisole	200-400 mol_{H2} $mol_{anisole}^{-1}$

4.3 Influence of the reaction conditions on anisole HDO over a CoMo/γ-Al_2O_3 catalyst

An experimental data set containing 18 experiments (Appendix A) has been acquired on the HTK-1 (described in Chapter 2) with a CoMo/γ-Al_2O_3 catalyst by systematically varying reaction conditions within intrinsic kinetic regime (section 4.2). The feed consist of anisole and hydrogen as reactants, *n*-hexane as solvent, ethane as internal standard and N_2 as diluent. In the following subsections the influence of temperature and space time on the anisole conversion and product yields will be discussed.

4.3.1 Influence of the temperature

The influence of the temperature on the products yields is presented in Figure 4-2. The increasing trend is in line with the expectations, since the reaction rates of the reactions increase with increasing temperature. The conversion increases from 50 mol% at 548 K to 95 mol% at 623 K.

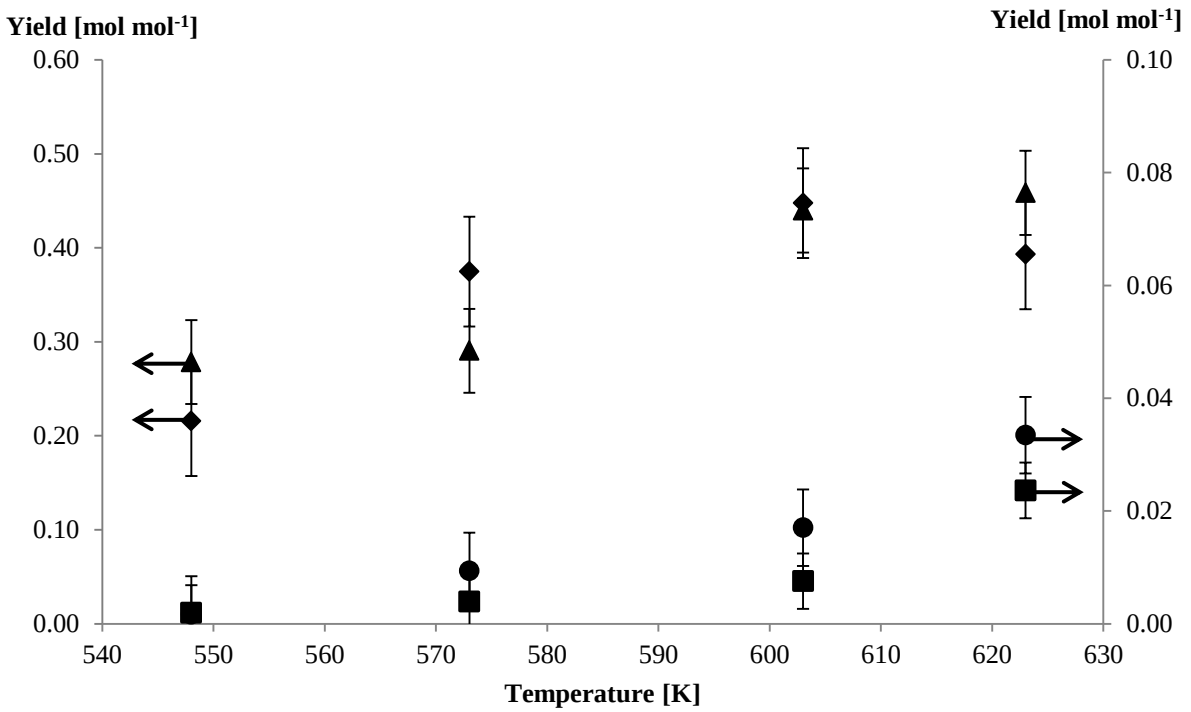

Figure 4-2. Influence of temperature on the product yields of anisole HDO on a CoMo/γ-Al_2O_3 catalyst. Conversion: 50 mol% at 548 K, 68 mol% at 573 K, 91 mol% at 603 K and 95 mol% at 623 K. Reaction conditions: space time = 1170 kg_{cat} $mol_{anisole}^{-1}$ s^{-1}, total pressure = 0.5 MPa, H_2/anisole = 400 mol_{H2} $mol_{anisole}^{-1}$. Experimental: ♦ = phenol, ▲ = cresol, ● = benzene, ■ = toluene.

The yield of phenol shows a maximum at 603 K, while the yield of cresol, benzene and toluene continuously increase with temperature. This phenomenon can indicate that with increasing temperature, the reactions leading to the hydrodeoxygenation products are more sensitive to temperature change.

This is confirmed by Figure 4-3, where the influence of the temperature on the product selectivity is presented. The experiments that have been depicted in this figure have a conversion of 50 mol%. It is clear that the selectivity of phenol decrease, while that of the other products increases. This is an indication that temperature sensitivity of the rate coefficients for the reactions to cresol and benzene are more pronounced compared to the other rate coefficients.

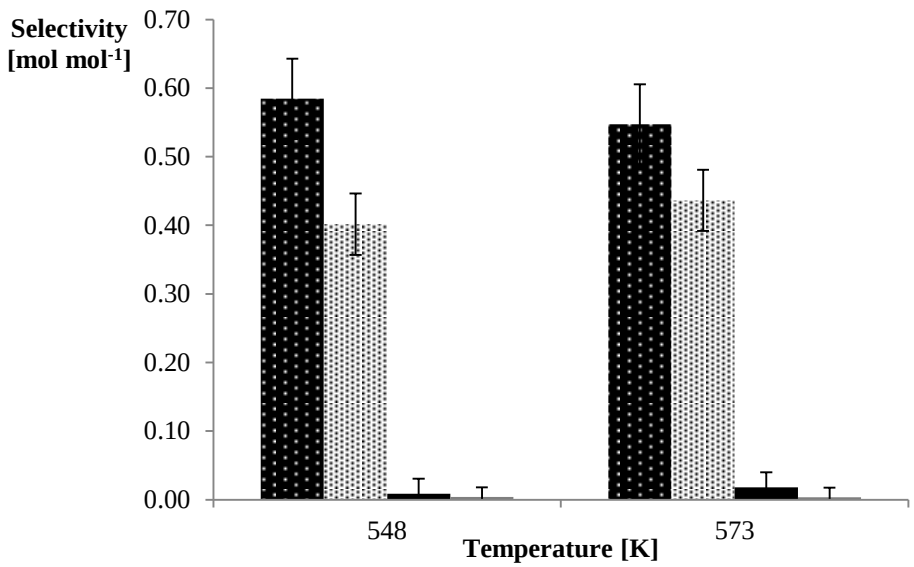

Figure 4-3. Product distribution at approximately 50 mol% conversion on a CoMo/γ-Al_2O_3 catalyst. Reaction conditions: total pressure = 0.5 MPa, space time = 722 kg_{cat} s $mol_{anisole}^{-1}$, H_2/anisole = 400 mol_{H2} $mol_{anisole}^{-1}$. Experimental: ▩ = phenol, ▩ = cresol, ■ = benzene, ■ = toluene.

4.3.2 Influence of the space time

Figure 4-4 depicts the influence of the space time on the products yields. An increasing space time enhances the conversion from 53 mol% for a space time of 722 kg_{cat} s $mol_{anisole}^{-1}$ to 82 mol% for a space time of 2140 kg_{cat} s $mol_{anisole}^{-1}$. This tendency can be understood by considering a constant catalyst mass with a decreasing anisole molar inlet flow rate, resulting in an increasing number of active catalyst sites for the reactant and thus enhancing the conversion and the yields.

The yield of phenol shows a maximum and that of benzene a minimum at 1282 kg_{cat} s $mol_{anisole}^{-1}$, while the yields of cresol and toluene increase with space time. Such a maximum for phenol was also observed as a function of the temperature. This phenomenon can indicate that with increasing space time, the transalkylation of anisole as favored and benzene is formed via the demethylation of toluene and not by the HDO of phenol.

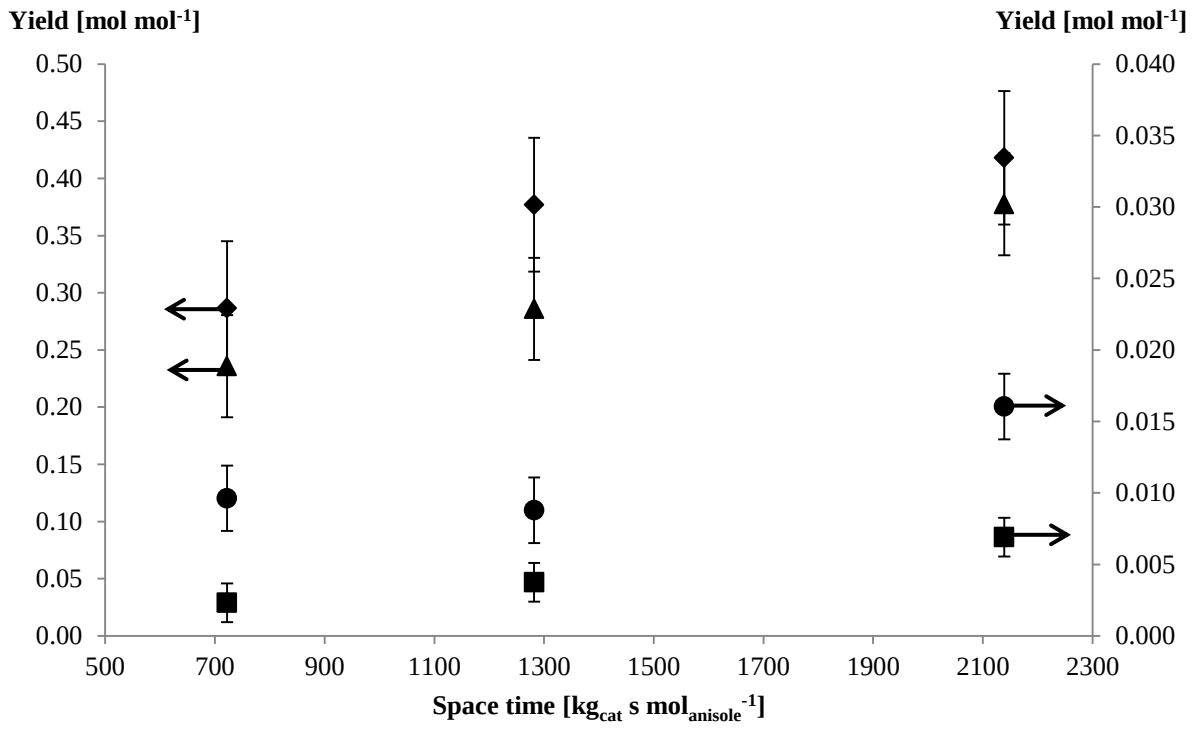

Figure 4-4. Influence of the space time on product yields of anisole HDO over a CoMo/γ-Al_2O_3 catalyst. Conversion: 53 mol% for 722 kg_{cat} s $mol_{anisole}^{-1}$, 68 mol% for 1282 kg_{cat} s $mol_{anisole}^{-1}$ and 82 mol% for 2140 kg_{cat} s $mol_{anisole}^{-1}$. Reaction conditions: temperature = 573 K, total pressure = 0.5 MPa, H_2/anisole = 400 mol_{H2} $mol_{anisole}^{-1}$. Experimental: ♦ =phenol, ▲ = cresol, ● = benzene, ■ = toluene.

4.4 Kinetic modeling

Based on the experimental observations presented earlier and the literature review, see Chapter 2, the following reaction mechanism for anisole HDO (Figure 4-5) has been proposed. The main reactions occurring on the CoMo/γ-Al_2O_3 catalyst are demethylation of anisole towards phenol (reaction 1) and transalkylation towards cresol (reaction 2). The direct deoxygenation of anisole towards benzene is omitted from the reaction scheme, since no methanol was observed in the experimental investigation. This is correspond with the literature since the bond between the aliphatic carbon and the oxygen is weaker than the bond between the aromatic carbon and the oxygen[2]. The hydrodeoxygenation of phenol (reaction 3) and cresol (reaction 4) results in benzene and toluene, respectively. Both cresol (reaction 5) as toluene (reaction 6) can have a hydrogenolysis of the $C_{aromatic}$-$C_{aliphatic}$ bond, resulting in phenol and benzene respectively.

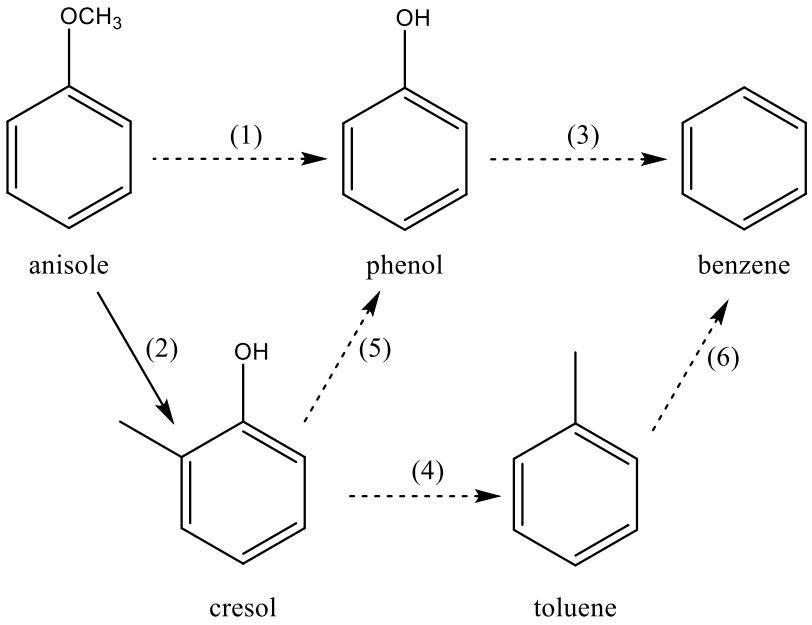

Figure 4-5. Proposed reaction mechanism for anisole HDO over a CoMo/γ-Al_2O_3 catalyst. The dashed arrows represent hydrodeoxygenation or hydrogenolysis reactions, while the solid arrows represent the methyl group transfer reactions.

Two most commonly used models in kinetic studies are the power law model and the Langmuir-Hinshelwood model. The power law models are used to describe the overall reaction order, whereas the Langmuir-Hinshelwood model takes into account the interaction with the catalyst surface. In the following subsections those two models are discussed.

4.4.1 Power law model of anisole HDO over a CoMo/γ-Al_2O_3 catalyst

Generally, an equilibrium reaction can be described assuming empirical power-law kinetics for the forward and reverse reaction rates, equation 4-1 and 4-2 respectively.

$$r^+ = k^+ p_A^\alpha p_B^\beta \qquad 4\text{-}1$$

$$\mathrm{r}^- = \mathrm{k}^- \mathrm{p}_\mathrm{C}^\gamma \qquad 4\text{-}2$$

By assuming that $k^+ > k^-$, the rate equations can be described by equation 4-3 till 4-8, with A = anisole, P = phenol, C = cresol, B = benzene, T = toluene.

$$r_1 = k_1 p_{H_2}^{\alpha_1} p_A^{\beta_1} \qquad 4\text{-}3$$

$$r_2 = k_2 p_A^{\beta_2} \qquad 4\text{-}4$$

$$r_3 = k_3 p_{H_2}^{\alpha_3} p_P^{\beta_3} \qquad 4\text{-}5$$

$$r_4 = k_4 p_{H_2}^{\alpha_4} p_C^{\beta_4} \qquad 4\text{-}6$$

$$r_5 = k_5 p_{H_2}^{\alpha_5} p_C^{\beta_5} \quad 4\text{-}7$$

$$r_6 = k_6 p_{H_2}^{\alpha_6} p_T^{\beta_6} \quad 4\text{-}8$$

In the above equations, k follows an Arrhenius dependence, and α and β are the kinetic orders.

Because the concentration of hydrogen is significantly high compared to the other reactants, it can be assumed that the change in concentration, and hence the partial pressure, of hydrogen during the reaction is negligible. Due to this assumption, composed reaction rate coefficients k' can be introduced in the new rate equations given by equations 4-9 till 4-14.

$$r_1 = k_1' p_A^{\beta_1} \quad 4\text{-}9$$

$$r_2 = k_2 p_A^{\beta_2} \quad 4\text{-}10$$

$$r_3 = k_3' p_P^{\beta_3} \quad 4\text{-}11$$

$$r_4 = k_4' p_C^{\beta_4} \quad 4\text{-}12$$

$$r_5 = k_5' p_C^{\beta_5} \quad 4\text{-}13$$

$$r_6 = k_6' p_T^{\beta_6} \quad 4\text{-}14$$

The composed reaction rate coefficients can be used to determine the activation energies for the different reaction families, *i.e.* demethylation, transalkylation and hydrodeoxygenation (C-O cleavage) reactions. A reparametrization is carried out to reduce the correlation between the pre-exponential factor and the activation energy.

$$k_1' = k_{1,avg} e^{-\frac{E_{a,demehtylation}}{R}\left(\frac{1}{T}-\frac{1}{T_{avg}}\right)} p_{H_2}^{\alpha_1} = A_1' e^{-\frac{E_{a,demehtylation}}{R}\left(\frac{1}{T}-\frac{1}{T_{avg}}\right)} \quad 4\text{-}15$$

$$k_2 = k_{2,avg} e^{-\frac{E_{a,transalkylation}}{R}\left(\frac{1}{T}-\frac{1}{T_{avg}}\right)} \quad 4\text{-}16$$

$$k_3' = k_{3,avg} e^{-\frac{E_{a,HDO}}{R}\left(\frac{1}{T}-\frac{1}{T_{avg}}\right)} p_{H_2}^{\alpha_3} = A_3' e^{-\frac{E_{a,HDO}}{R}\left(\frac{1}{T}-\frac{1}{T_{avg}}\right)} \quad 4\text{-}17$$

$$k_4' = k_{4,avg} e^{-\frac{E_{a,HDO}}{R}\left(\frac{1}{T}-\frac{1}{T_{avg}}\right)} p_{H_2}^{\alpha_4} = A_4' e^{-\frac{E_{a,HDO}}{R}\left(\frac{1}{T}-\frac{1}{T_{avg}}\right)} \quad 4\text{-}18$$

$$k_5' = k_{5,avg} e^{-\frac{E_{a,demehtylation}}{R}\left(\frac{1}{T}-\frac{1}{T_{avg}}\right)} p_{H_2}^{\alpha_5} = A_5' e^{-\frac{E_{a,demehtylation}}{R}\left(\frac{1}{T}-\frac{1}{T_{avg}}\right)} \quad 4\text{-}19$$

$$k_6' = k_{6,avg} e^{-\frac{E_{a,demehtylation}}{R}(\frac{1}{T}-\frac{1}{T_{avg}})} p_{H_2}^{\alpha_6} = A_6' e^{-\frac{E_{a,demehtylation}}{R}(\frac{1}{T}-\frac{1}{T_{avg}})} \quad 4\text{-}20$$

To reduce the amount of parameters, the pre-exponential factors of the same reaction families are assumed to be equal. In this way, the amount of parameters is reduced from 18 to 12 and results in equations 4-21 till 4-26.

$$k_1' = k_{1,avg} e^{-\frac{E_{a,demehtylation}}{R}(\frac{1}{T}-\frac{1}{T_{avg}})} \quad 4\text{-}21$$

$$k_2 = k_{2,avg} e^{-\frac{E_{a,transalkylation}}{R}(\frac{1}{T}-\frac{1}{T_{avg}})} \quad 4\text{-}22$$

$$k_3' = k_{1,avg} e^{-\frac{E_{a,HDO}}{R}(\frac{1}{T}-\frac{1}{T_{avg}})} \quad 4\text{-}23$$

$$k_4' = k_3' \quad 4\text{-}24$$

$$k_5' = k_1' \quad 4\text{-}25$$

$$k_6' = k_1' \quad 4\text{-}26$$

The 12 parameters that needs to be determined are the composed pre-exponential factors, the activation energies, and the kinetic orders of the reactants.

The net rate of formation of a component in the reaction network, see Figure 4-5, is obtained from the individual reactions by accounting for the stoichiometry.

$$R_A = -r_1 - r_2 \quad 4\text{-}27$$

$$R_B = r_3 + r_6 \quad 4\text{-}28$$

$$R_C = r_2 - r_4 - r_5 \quad 4\text{-}29$$

$$R_{CH_4} = r_1 + r_5 + r_6 \quad 4\text{-}30$$

$$R_{H_2} = -r_1 - r_3 - r_4 - r_5 - r_6 \quad 4\text{-}31$$

$$R_{H_2O} = r_3 + r_4 \quad 4\text{-}32$$

$$R_P = r_1 - r_3 + r_5 \quad 4\text{-}33$$

$$R_T = r_4 - r_6 \quad 4\text{-}34$$

4.4.1.1Regression analysis

The intrinsic kinetic data obtained via the hydrodeoxygenation of anisole over a CoMO/γ-Al_2O_3 catalyst in a plug flow reactor (Appendix A) is used to estimate the kinetic parameters by performing non-isothermal regression using the Levenberg-Mardquardt algorithm.

The *F* value for the model significance corresponds to 5198 which exceeds the tabulated value of 3.97 at 95 % confidence with respectively 9 and 1 degrees of freedom, indicating that the model is regression is significant. The parameter estimates with the 95% confidence interval are given in Table 4-2.

Table 4-2. Parameter estimates with the corresponding 95% individual confidence interval determined by non-isothermal regression of the experimental data set on a CoMo/γ-Al_2O_3 catalyst, of the power law kinetic model determined by solving equation 3-11, in which the net rates of formation are given by equations 4-27 till 4-34.

Parameter	Value
A_1'	59.92 ± 93.64 µmol g^{-1} s^{-1} $MPa^{-\beta 1}$
A_2	25.21 ± 42.47 µmol g^{-1} s^{-1} $MPa^{-\beta 2}$
A_3'	19.48 ± 106.40 µmol g^{-1} s^{-1} $MPa^{-\beta 3}$
A_4'	19.48 ± 106.40 µmol g^{-1} s^{-1} $MPa^{-\beta 4}$
A_5'	59.92 ± 93.64 µmol g^{-1} s^{-1} $MPa^{-\beta 5}$
A_6'	59.92 ± 93.64 µmol g^{-1} s^{-1} $MPa^{-\beta 6}$
$E_{a,demethylation}$	34.70 ± 10.13 kJ mol^{-1}
$E_{a,transalkylation}$	49.68 ± 12.05 kJ mol^{-1}
$E_{a,HDO}$	57.64 ± 31.75 kJ mol^{-1}
β_1	0.66 ±0.19
β_2	0.61 ± 0.20
β_3	0.88 ± 0.52
β_4	0.94 ± 0.50
β_5	0.94 ± 0.40
β_6	2.86

The limited hydrodeoxygenation extent is in line with the high activation energy, compared to the one for the other reactions. A higher activation energy for the transalkylation compared to the demethylation is in agreement with the experimental findings. A reaction with a higher

activation energy is more sensitive to a change in temperature compared to a reaction with lower activation energy, as can be seen in Figure 4-2 and Figure 4-3. Further, the higher activation energy for transalkylation can be explained by the complexity of the reactions. The transalkylation reactions consists of four steps: the cleavage of the aliphatic C-O bond, the cleavage of an aromatic C-H bond, the formation of an aromatic C-O bond and the formation of an O-H bond. The demethylation reactions also consist of four steps, although, no aromatic C-H bond is broken.

The reaction order of anisole is around 0.6, that of phenol is slightly below unity (0.8) and those of cresol are around unity. Fractional reaction orders usually indicate complex reaction mechanisms.

Due to the relatively small experimental data set, not all of the parameters are estimated significantly. The confidence interval of the composed pre-exponential factors comprise the zero value meaning that the corresponding *t* value is smaller than the tabulated *t* value. On the other hand, the reaction orders β_6 could not be estimated.

Further, the reaction orders are correlated to the composed pre-exponential factors (Table 4-3). This is probably due to the fact that the same pre-exponential factors and activation energies were used for the same reaction families. Nevertheless, the multiple correlation coefficient, R^2, equals 0.998 indicating a qualitative regression.

Despite this, one can see that the model predicts the outlet flow rates quite good for all the responses when comparing the predicted outlet rates to the observed outlet flow rates in Figure 4-6. The secondary products are more difficult to estimated due to their low responses compared to those of the reactant and primary products, hence, benzene is overestimated at low outlet flows and the reverse is observed for toluene.

Table 4-3. Binary correlation coefficient matrix, determined by non-isothermal regression of the experimental data set on a CoMo/γ-Al_2O_3 catalyst, of the power law kinetic model determined by solving equation 3-11, in which the net rates of formation are given by equations 4-27 till 4-34. Subscript D stands for demethylation, T for transalkylation and H for HDO.

	A_1'	A_2	A_3'	$E_{a,D}$	$E_{a,T}$	$E_{a,H}$	β_1	β_2	β_3	β_4	β_5	β_6
A_1'	1.00	0.00	-0.34	-0.28	0.49	0.21	-0.01	-0.35	-0.35	-0.34	0.86	0.00
A_2	0.00	1.00	0.09	0.19	0.18	-0.09	0.99	0.09	0.09	0.10	-0.87	0.00
A_3'	-0.34	0.09	1.00	0.74	-0.58	-0.82	0.13	0.13	0.99	0.99	-0.04	0.00
$E_{a,D}$	-0.28	0.19	0.74	1.00	-0.31	-0.61	0.21	0.21	0.74	0.74	0.94	0.00
$E_{a,T}$	0.49	0.18	-0.58	-0.31	1.00	0.39	0.23	0.23	-0.59	-0.58	0.23	0.00
$E_{a,H}$	0.21	-0.09	-0.82	-0.61	0.39	1.00	-0.12	-0.12	-0.74	-0.74	0.31	0.00
β_1	1.00	0.01	-0.35	-0.23	0.50	0.21	1.00	0.00	-0.36	-0.35	-0.86	0.00
β_2	-0.01	0.99	0.13	0.21	0.23	-0.12	0.00	1.00	0.12	0.14	0.89	0.00
β_3	-0.35	0.09	0.99	0.74	-0.59	-0.74	-0.36	0.12	1.00	1.00	0.14	0.00
β_4	-0.34	0.10	0.99	0.74	-0.58	-0.74	-0.35	0.14	1.00	1.00	-0.17	0.00
β_5	0.86	-0.87	-0.04	0.94	0.23	0.31	-0.86	0.89	0.14	-0.17	1.00	0.00
β_6	0.00	0.00	0.00	0.00	0.00	0.00	0.00	0.00	0.00	0.00	0.00	0.00

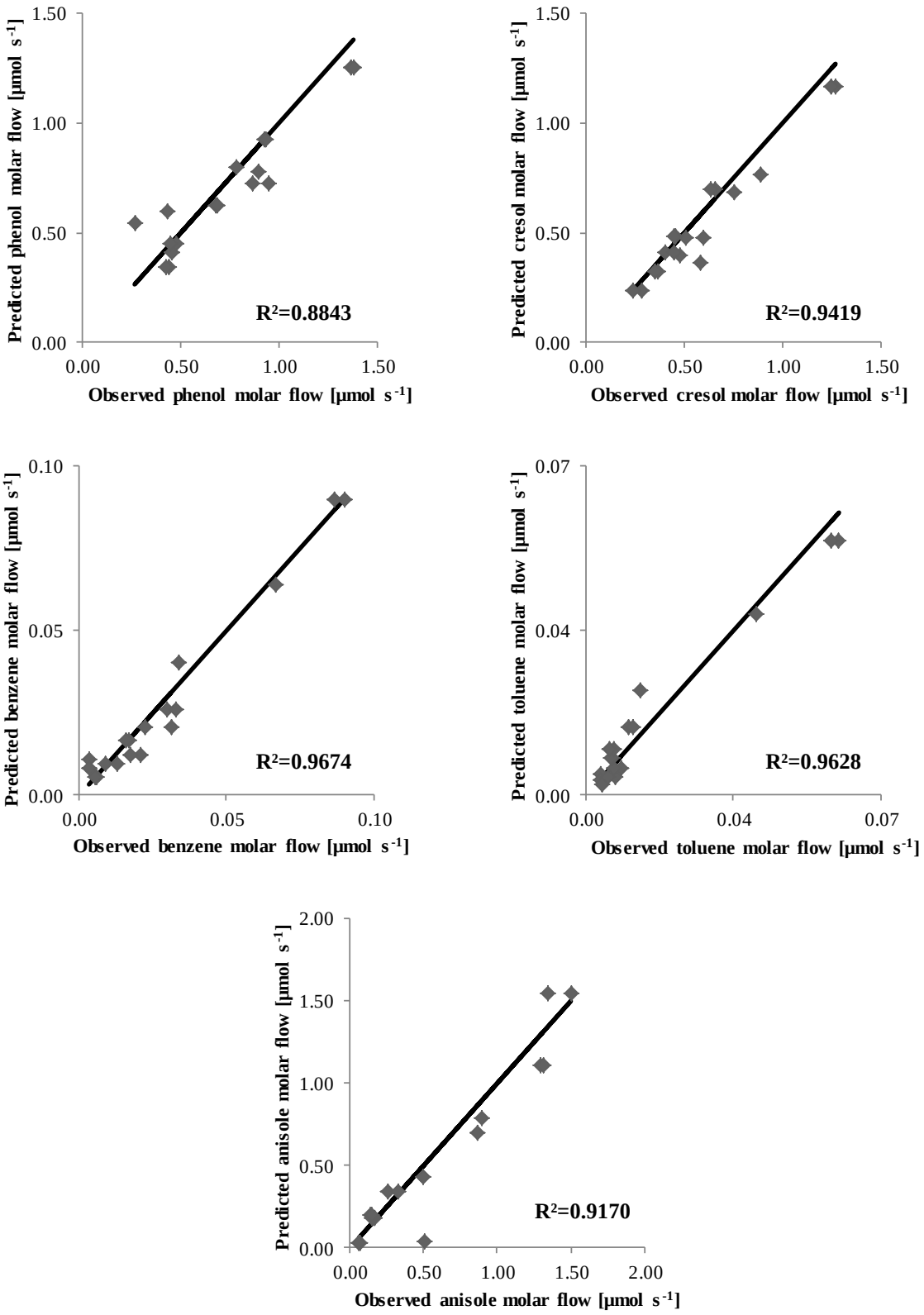

Figure 4-6. Parity diagrams for the molar outlet flow of phenol (top left), cresol (top right), benzene (middle left), toluene (middle right) and anisole (bottom), determined by solving equation 3-11 in which the net rates of formation are given by equations 4-27 till 4-34 using the parameters from Table 4-2.

From the lack-of-fit test follows that the model is, statistically, not adequate, since the calculated *F* value equals 16.8 which is larger than the tabulated value at 95 % confidence with respectively 40 and 38 degrees of freedom, that equals, 1.7. From practice, it is found that the model lack-of-fit test is very difficult to pass[3]. Failing the test means that the some deviations between the model predicted and the observed values, cannot be solely attributed to experimental errors. Although, when residual figures of the outlet flow as a function of the temperature and space time (Figure 4-7 and Figure 4-8) do not show a significant trend. When one look closely, the residuals for cresol as a function of the temperature show a little parabolic trend. Such a trend suggests the introduction of extra terms, such as quadratic or cross-product terms, in the model[4].

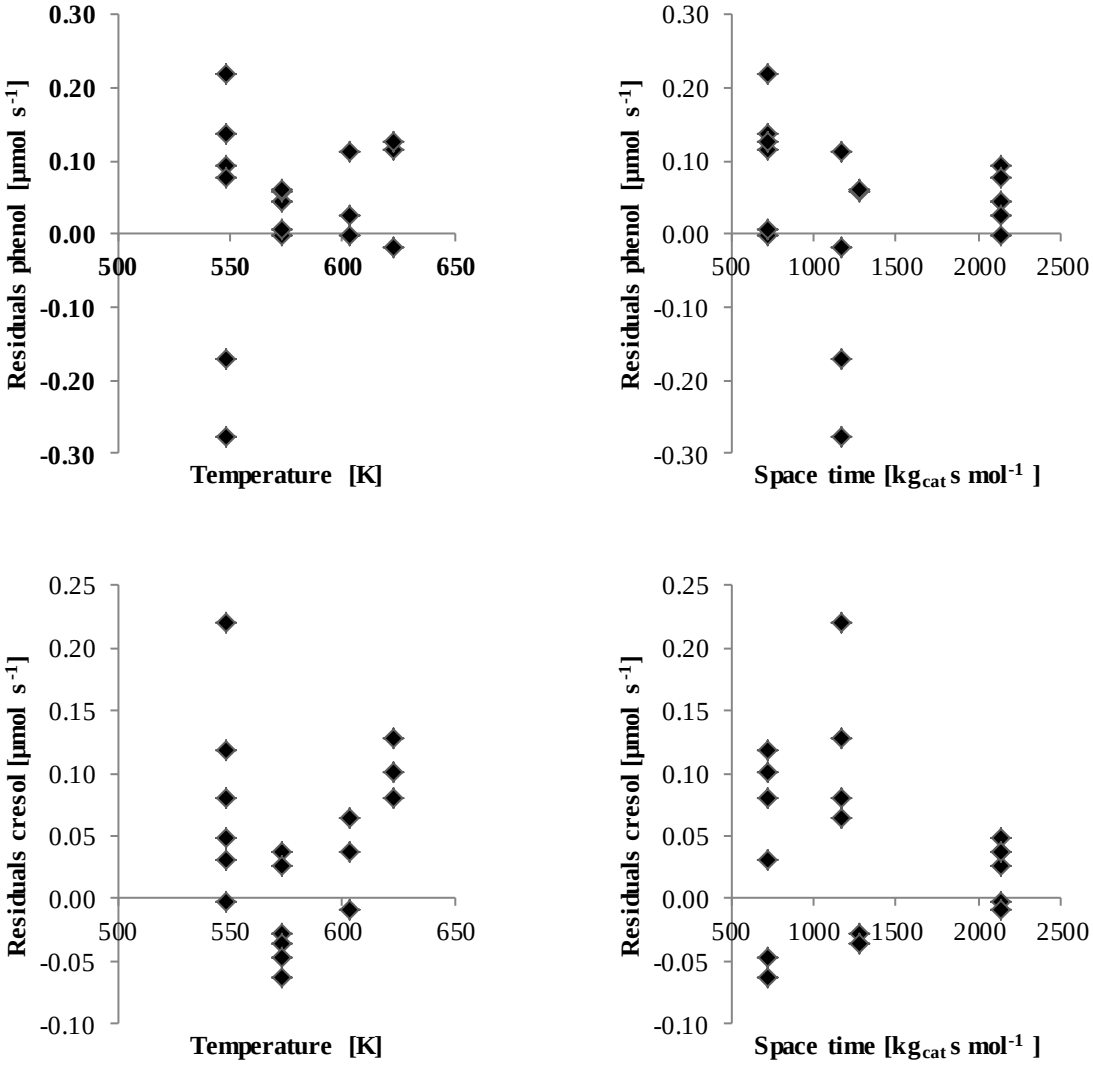

Figure 4-7. Residual figures of the outlet molar flow of phenol (top) and cresol (bottom) as a function of the temperature (left) and the space time (right) determined by solving equation 3-11 in which the net rates of formation are given by equations 4-27 till 4-34 using the parameters from Table 4-2.

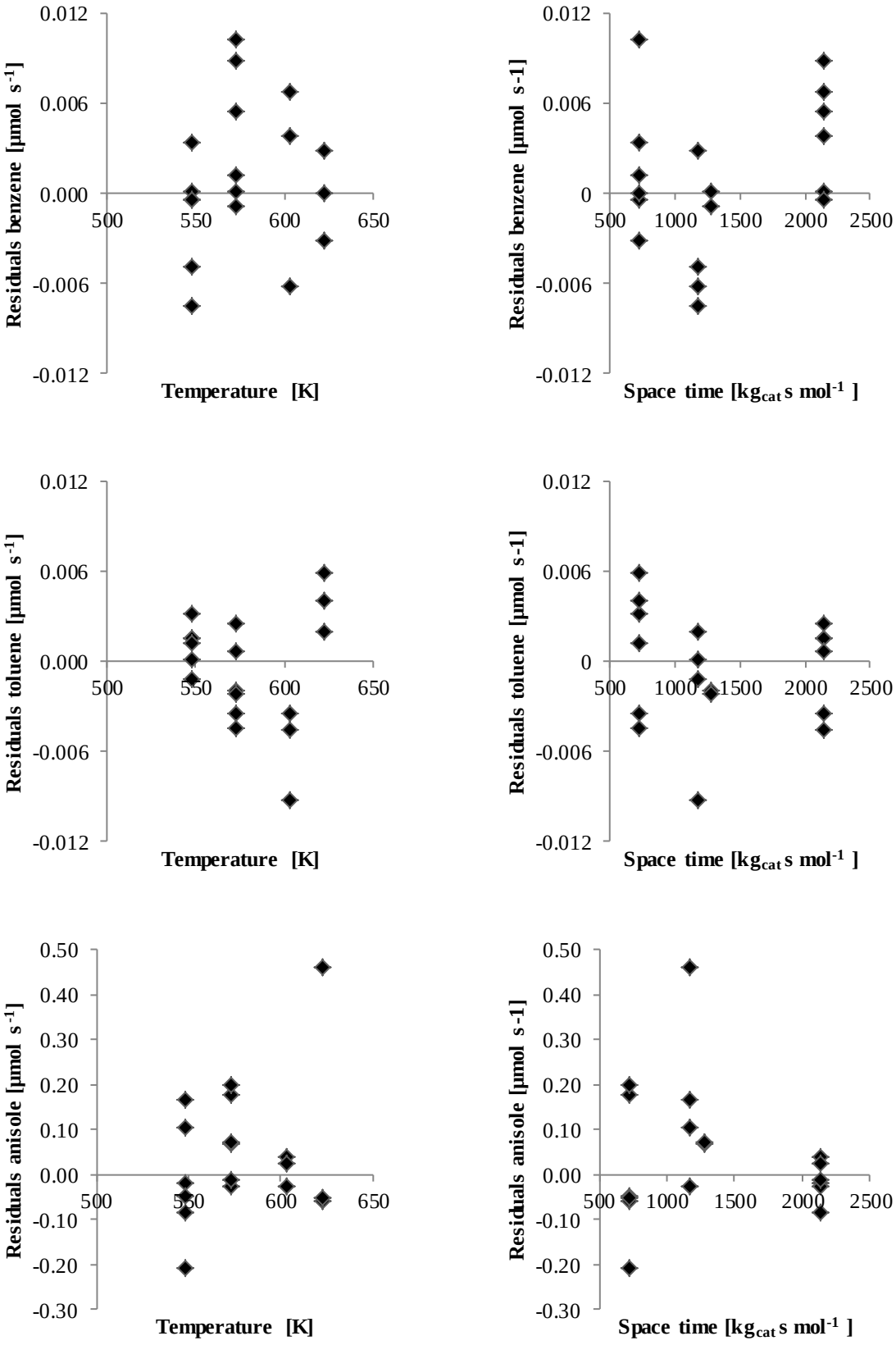

Figure 4-8. Residual figures of the outlet molar flow of benzene (top), toluene (middle) and anisole (bottom) as a function of the temperature (left) and the space time (right) determined by solving equation 3-11 in which the net rates of formation are given by equations 4-27 till 4-34 using the parameters from Table 4-2.

4.4.1.2Model performance

To validate the power law model, the influence of temperature (Figure 4-9 and Figure 4-10) and space time (Figure 4-11 and Figure 4-12) on the yields and the conversion is evaluated. From the simulations, one can see that the model is capable to predict the trend. The influence of temperature on the product yields is simulated within the experimental error. This is not the case for the influence of the space time, especially for the hydrodeoxygenation products benzene and toluene.

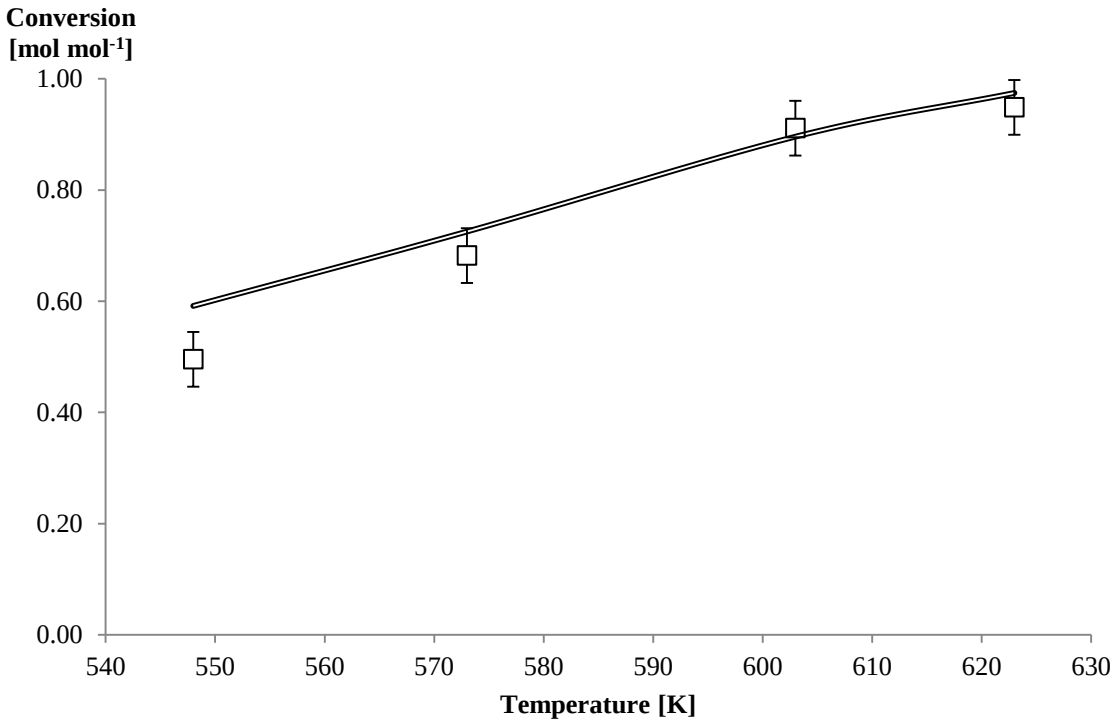

Figure 4-9. Influence of the temperature on anisole conversion on CoMo/γ-Al_2O_3 catalyst. Reaction conditions: space time = 1170 kg_{cat} s $mol_{anisole}^{-1}$, total pressure = 0.5 MPa, H_2/anisole = 400 mol_{H2} $mol_{anisole}^{-1}$. □ = Experimental conversion, double line = simulated conversion.

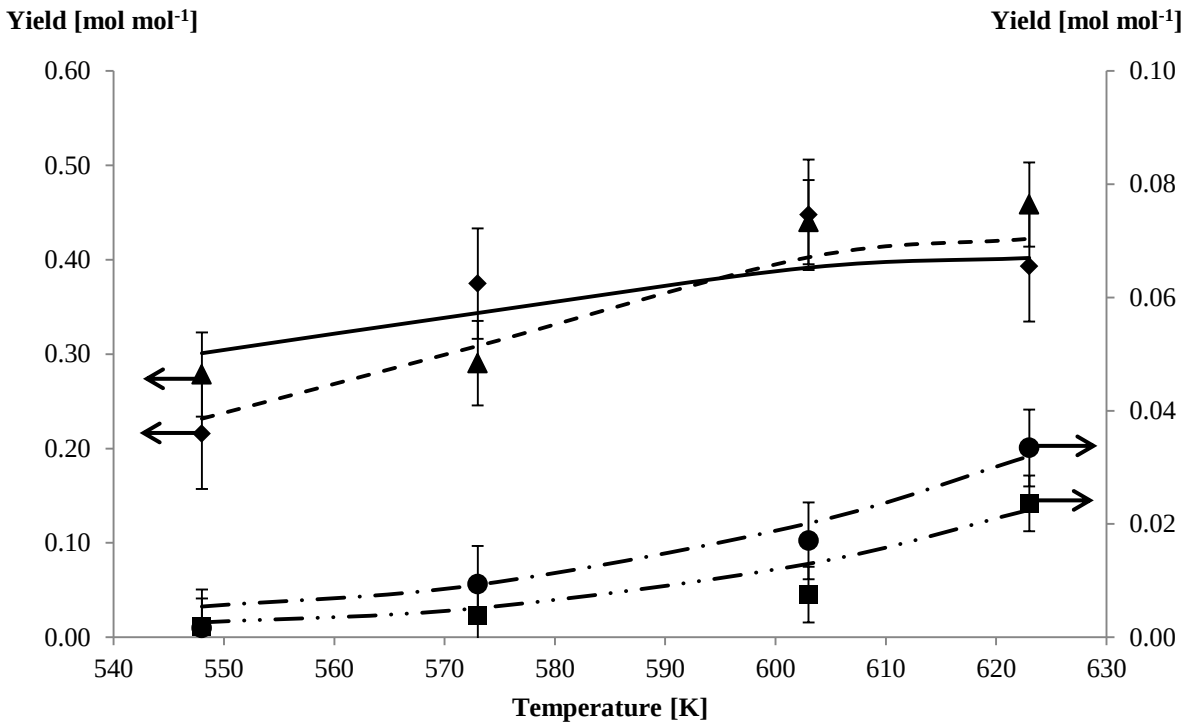

Figure 4-10. Influence of the temperature on product yields on CoMo/γ-Al_2O_3 catalyst. Reaction conditions: space time = 1170 kg_{cat} s $mol_{anisole}^{-1}$, total pressure = 0.5 MPa, H_2/anisole = 400 mol_{H2} $mol_{anisole}^{-1}$. Experimental: ♦ = phenol, ▲ = cresol, ● = benzene, ■ = toluene. Simulation: full line = phenol, dashed line = cresol, dash-dotted line = benzene, dash-dot-dotted line = toluene.

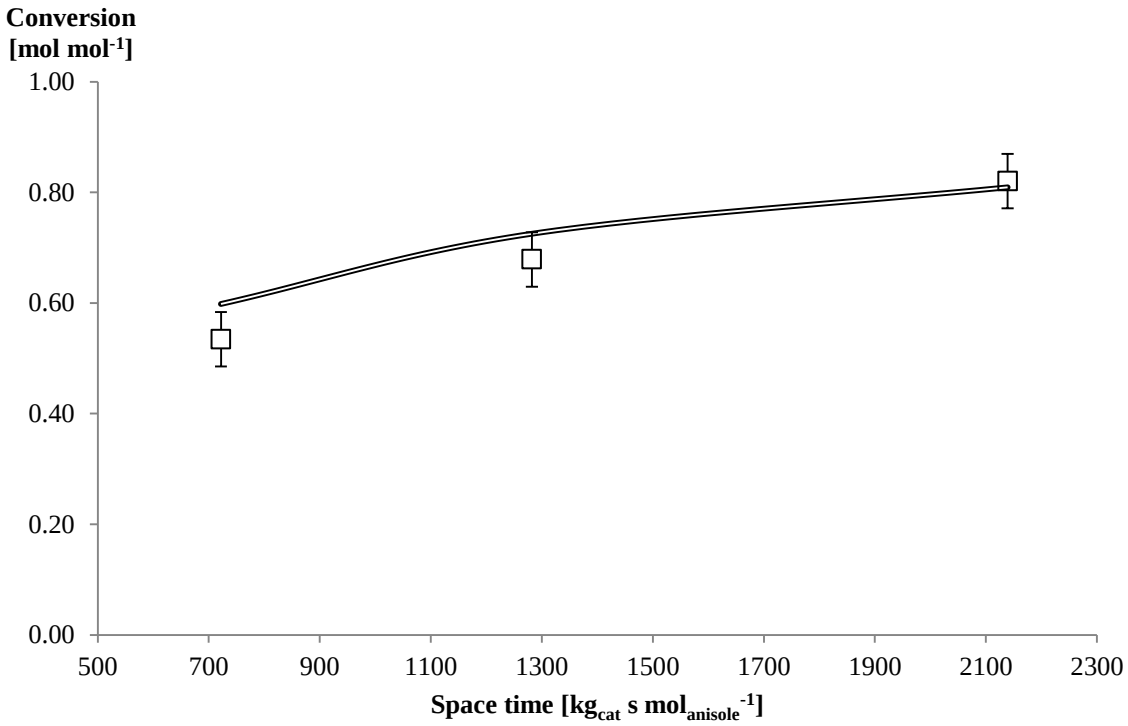

Figure 4-11. Influence of the space time on anisole conversion on CoMo/γ-Al_2O_3 catalyst. Reaction conditions: temperature = 573 K, total pressure = 0.5 MPa, H_2/anisole = 400 mol_{H2} $mol_{anisole}^{-1}$. □ = Experimental conversion, double line = simulated conversion.

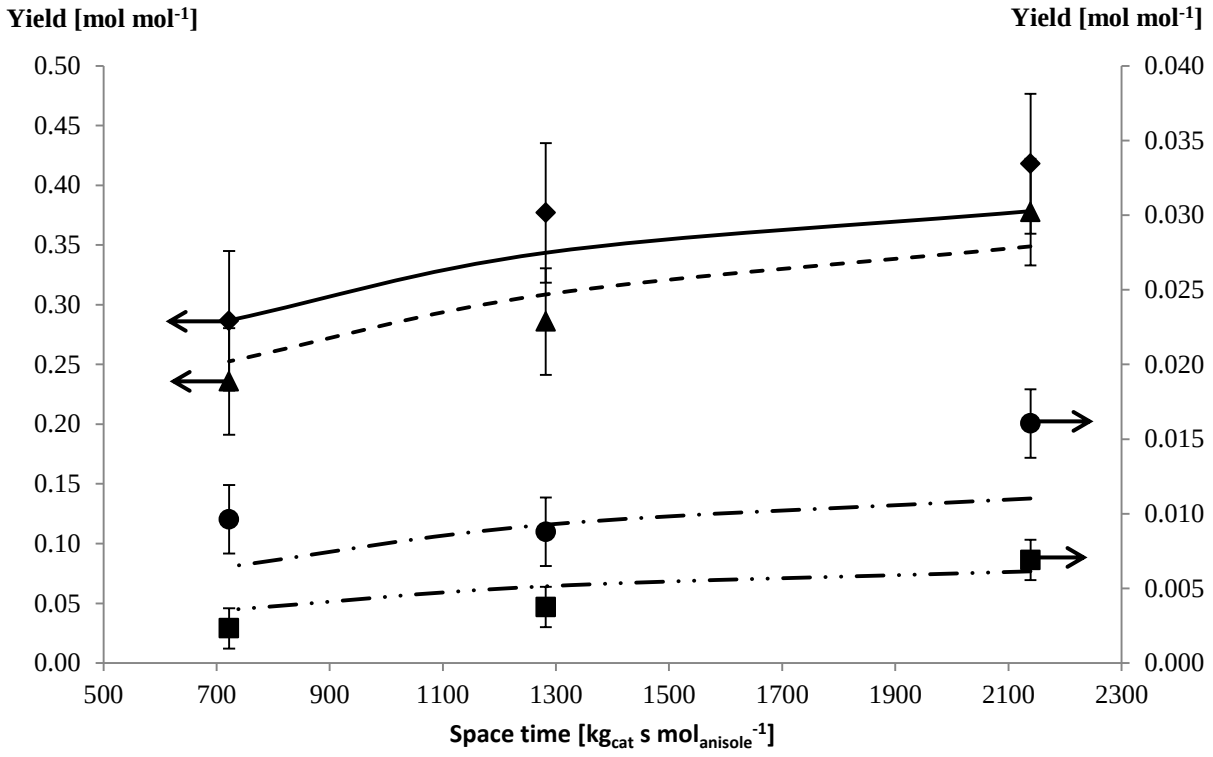

Figure 4-12. Influence of the space time on product yields on CoMo/γ-Al_2O_3 catalyst. Reaction conditions: temperature = 573 K, total pressure = 0.5 MPa, H_2/anisole = 400 mol_{H2} $mol_{anisole}^{-1}$. Experimental: ♦ = phenol, ▲ = cresol, ● = benzene, ■ = toluene. Simulation: full line = phenol, dashed line = cresol, dash-dotted line = benzene, dash-dot-dotted line = toluene.

Generally, power law models fit easier the experimental data, but they neglects the mechanistic aspects of adsorption/desorption and the surface reaction on the catalyst. Hence, a Langmuir-Hinshelwood model is derived.

4.4.2 Langmuir-Hinshelwood model of anisole HDO over a CoMo/γ-Al_2O_3 catalyst

Langmuir-Hinshelwood models are regarded as "standards" to describe the kinetics of heterogeneously catalyzed reaction. There are seven elementary steps for a heterogeneously catalyzed reaction[5], as shown in Figure 4-13, *i.e.*

1. The reactant diffuses from the bulk to the external catalyst surface.
2. The reactant diffuses from the external catalyst surface to the active sites inside the catalyst pellet.
3. The reactant adsorbs on the active site.
4. The surface reaction takes place.
5. The product desorbs from the active site.
6. The product diffuses from the active site inside the catalyst pellet to the external catalyst surface.

7. The product diffuses from the external catalyst surface to the bulk.

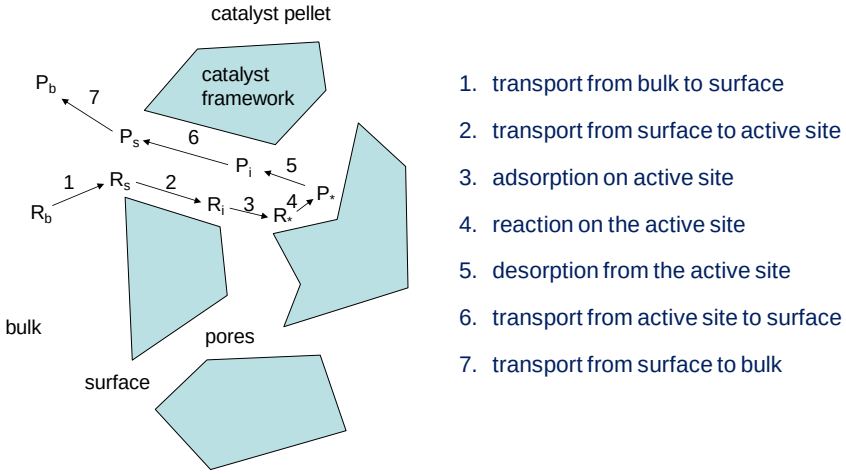

Figure 4-13. Schematic representation of the elementary steps in a heterogeneous catalyzed reaction[5]. R represent a reactant, P a product. Subscripts b, s and p stand for bulk, surface and pores respectively.

Steps 2 and 6 occur in parallel with steps 3, 4 and 5 occur consecutively at a given active catalyst site. Steps 1 and 7 occur consecutively to the other steps. Since the measured kinetics are in the intrinsic kinetic regime (see section 4.2), *i.e.* the regime where the observed kinetics are only dependent on the chemical adsorption and reaction phenomena, one is most interested in steps 3, 4 and 5[5]. The reaction on the surface is usually considered to be the rate determining step, while the other steps are assumed to be near equilibrium[5, 6].

The Langmuir-Hinshelwood theory is based on the following three hypotheses[5, 7]:

1. There are fixed adsorption sites on the catalyst surface. These adsorption sites are energetically uniform.
2. Each active site on the catalyst surface can hold one adsorbed species (monolayer coverage).
3. There is no interaction between the adsorbed species on different sites.

The hydrodeoxygenation of anisole, based on the reaction mechanism shown in Figure 4-5, can be described according to the following sequence of reactions.

$$A \overset{K_A}{\rightleftharpoons} A^* \qquad 4\text{-}35$$

$$H_2 + 2^* \overset{K_{H2}}{\rightleftharpoons} 2\,H^* \qquad 4\text{-}36$$

$$A^* + 2\,H^* \xrightarrow{k_1} P^* + CH_4 + 2^* \qquad 4\text{-}37$$

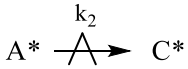

4-38

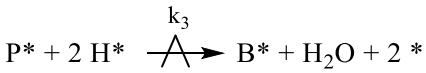

4-39

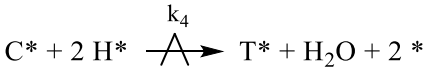

4-40

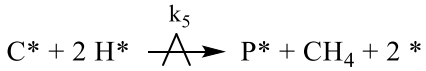

4-41

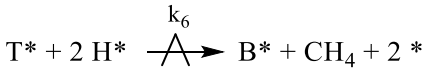

4-42

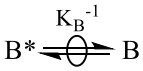

4-43

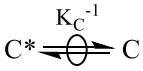

4-44

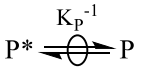

4-45

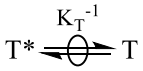

4-46

The term $*$ indicates a vacant active site, and A^*, B^*, C^*, H^*, P^* and T^* are the adsorbed species, anisole, benzene, cresol, hydrogen, phenol and toluene respectively. The adsorption and desorption reactions are equilibrated, where the equilibrium coefficient can be expressed in terms of the concentration of the adsorbed species. The equilibrium coefficients are not expressed according to the Van't Hoff equation, since this would introduce a total of 12 parameters.

$$K_A = \frac{[A^*]}{p_A[*]} \quad 4\text{-}47$$

$$K_B = \frac{[B^*]}{p_B[*]} \quad 4\text{-}48$$

$$K_C = \frac{[C^*]}{p_C[*]} \quad 4\text{-}49$$

$$K_{H_2} = \frac{[H^*]^2}{p_{H_2}[*]^2} \quad 4\text{-}50$$

$$K_P = \frac{[P^*]}{p_P[*]} \quad 4\text{-}51$$

$$K_T = \frac{[T^*]}{p_T[*]} \quad 4\text{-}52$$

All the adsorbed species compete for the same active sites, resulting in the following balance of adsorption sites:

$$[*]_{tot} = [*] + [A^*] + [B^*] + [C^*] + [P^*] + [T^*] + [H^*] \quad 4\text{-}53$$

Assuming that all the surface reactions are irreversible, the reaction rates can be expressed as follow:

$$r_1 = k_1[A^*][H^*]^2 \quad 4\text{-}54$$

$$r_2 = k_2[A^*] \quad 4\text{-}55$$

$$r_3 = k_3[P^*][H^*]^2 \quad 4\text{-}56$$

$$r_4 = k_4[C^*][H^*]^2 \quad 4\text{-}57$$

$$r_5 = k_5[C^*][H^*]^2 \quad 4\text{-}58$$

Substituting all the above expressions into the reaction rates, the following Langmuir-Hinshelwood rate equations are obtained.

$$r_1 = \frac{k_1 K_A K_{H_2} [*]_{tot}{}^3 p_A p_{H_2}}{\left(1 + K_A p_A + K_B p_B + K_C p_C + K_P p_P + K_T p_T + \sqrt{K_{H_2} p_{H_2}}\right)^3} \quad 4\text{-}59$$

$$r_2 = \frac{k_2 K_A [*]_{tot} p_A}{1 + K_A p_A + K_B p_B + K_C p_C + K_P p_P + K_T p_T + \sqrt{K_{H_2} p_{H_2}}} \quad 4\text{-}60$$

$$r_3 = \frac{k_3 K_P K_{H_2} [*]_{tot}{}^3 p_P p_{H_2}}{\left(1 + K_A p_A + K_B p_B + K_C p_C + K_P p_P + K_T p_T + \sqrt{K_{H_2} p_{H_2}}\right)^3} \quad 4\text{-}61$$

$$r_4 = \frac{k_4 K_C K_{H_2} [*]_{tot}{}^3 p_C p_{H_2}}{\left(1 + K_A p_A + K_B p_B + K_C p_C + K_P p_P + K_T p_T + \sqrt{K_{H_2} p_{H_2}}\right)^3} \quad 4\text{-}62$$

$$r_5 = \frac{k_5 K_C K_{H_2} *_{tot}{}^3 p_C p_{H_2}}{\left(1 + K_A p_A + K_B p_B + K_C p_C + K_P p_P + K_T p_T + \sqrt{K_{H_2} p_{H_2}}\right)^3} \quad 4\text{-}63$$

$$r_6 = \frac{k_6 K_T K_{H_2} [*]_{tot}{}^3 p_T p_{H_2}}{\left(1 + K_A p_A + K_B p_B + K_C p_C + K_P p_P + K_T p_T + \sqrt{K_{H_2} p_{H_2}}\right)^3} \quad 4\text{-}64$$

In the above rate equations, k follows an Arrhenius dependence.

It is assumed that the activation energies and the pre-exponential factors for the different reaction families, *i.e.* demethylation, transalkylation and hydrodeoxygenation (C-O hydrogenolysis), are the same. A reparametrization is carried out to reduce the correlation between the pre-exponential factor and the activation energy.

$$k_1 = A_1 e^{-\frac{E_{a,demethylation}}{R}(\frac{1}{T}-\frac{1}{T_{avg}})} \quad 4\text{-}65$$

$$k_2 = A_2 e^{-\frac{E_{a,transalkylation}}{R}(\frac{1}{T}-\frac{1}{T_{avg}})} \quad 4\text{-}66$$

$$k_3 = A_3 e^{-\frac{E_{a,HDO}}{R}(\frac{1}{T}-\frac{1}{T_{avg}})} \quad 4\text{-}67$$

$$k_4 = k_3 \quad 4\text{-}68$$

$$k_5 = k_1 \quad 4\text{-}69$$

$$k_6 = k_1 \quad 4\text{-}70$$

To reduce further the number of parameters, the total concentration of the active sites, $[*]_{tot}$, is lumped into the pre-exponential factor. In this way, the amount of parameters is reduced from 19 to 12. These parameters are the three composed pre-exponential factors, the three activation energies, and the six adsorption coefficients.

The net rates of formation of each of the components are given by equations 4-27 till 4-34.

4.4.2.1Regression analysis

The same experimental data set is used for the non-linear multivariable regression using the Levenberg-Mardquardt algorithm.

The model is significant since the calculated *F* value, that is 3 10^4, exceeds the tabulated *F* value of 3.97 at 95 % confidence with respectively 9 and 1 degrees of freedom, indicating that the model is regression is significant. The parameter estimates with the 95% confidence interval are given in Table 4-4.

Table 4-4. Parameter estimates with the corresponding 95% individual confidence interval determined by non-isothermal regression of the experimental data set on a CoMo/γ-Al_2O_3 catalyst, of the Langmuir-Hinshelwood kinetic model determined by solving equation 3-11, in which the net rates of formation are given by equations 4-27 till 4-34. (a) indicates that the parameters are estimated with the other parameters fixed.

Parameter	Value
$A_1' = A_1[*]_{tot}^3$	140.41 ± 78.40 µmol g^{-1} s^{-1}
$A_2' = A_2[*]_{tot}$	36.07 ± 30.57 s^{-1}
$A_3' = A_3[*]_{tot}^3$	699.59 ± 319.60 µmol g^{-1} s^{-1}
$E_{a,demethylation}$	41.43 ± 30.05 kJ mol^{-1}
$E_{a,transalkylation}$	47.78 ± 32.24 kJ mol^{-1}
$E_{a,HDO}$	79.67 ± 18.57 kJ mol^{-1}
K_A (a)	52.62 ± 12.64 MPa^{-1}
K_B (b)	0.11 MPa^{-1}
K_C	0.18 ± 0.09 MPa^{-1}
K_{H_2}	26.25 ± 49.82 MPa^{-1}
K_P	0.43 ± 0.21 MPa^{-1}
K_T (a)	0.55 ± 14.52 MPa^{-1}

The activation energies calculated with the Langmuir-Hinshelwood model are quit close to those of the power law model. The same order in activation energy is obtained: $E_{a,HDO} > E_{a,transalkylation} > E_{a,demethylation}$, which is in line with the experimental findings. The activation energy for the hydrodeoxygenation correspond to the value found in literature for guaiacol HDO on a CoMo catalyst, which is 71.2 kJ mol^{-1} [8].

The experimental data set was not sufficient to estimate all the parameters significantly. The confidence interval of the adsorption coefficient of hydrogen and toluene comprise the zero value. On the other hand, the adsorption coefficient of benzene could not be estimated. Nevertheless, those parameters have an expected order of magnitude.

The multiple correlation coefficient, R^2, equals 0.999 which indicates a qualitative regression. The binary correlation coefficient matrix is given in Table 4-5. No severe correlation between the parameters is observed.

Table 4-5. Binary correlation coefficient matrix, determined by non-isothermal regression of the experimental data set on a CoMo/γ-Al_2O_3 catalyst, of the Langmuir-Hinshelwood kinetic model, determined by solving equation 3-11 in which the net rates of formation are given by equations 4-27 till 4-34. Subscript D stands for demethylation, T for transalkylation and H for HDO.

	A_1'	A_2'	A_3'	$E_{a,D}$	$E_{a,T}$	$E_{a,H}$	K_A	K_B	K_C	K_{H_2}	K_P	K_T
A_1'	1.00	0.21	-0.76	-0.82	-0.50	0.79	0.00	0.00	0.09	-0.09	-0.09	0.00
A_2'	0.21	1.00	-0.17	-0.40	-0.57	0.14	0.00	0.00	-0.12	0.65	0.11	0.00
A_3'	-0.76	-0.17	1.00	0.50	0.20	-0.77	0.00	0.00	-0.13	-0.09	-0.69	0.00
$E_{a,D}$	-0.82	-0.40	0.50	1.00	0.71	-0.81	0.00	0.00	0.14	-0.07	-0.14	0.00
$E_{a,T}$	-0.50	-0.57	0.20	0.71	1.00	-0.48	0.00	0.00	-0.18	0.06	0.18	0.00
$E_{a,H}$	0.79	0.14	-0.77	-0.81	-0.48	1.00	0.00	0.00	-0.25	-0.19	0.25	0.00
K_A	0.00	0.00	0.00	0.00	0.00	0.00	0.00	0.00	0.00	0.00	0.00	0.00
K_B	0.00	0.00	0.00	0.00	0.00	0.00	0.00	0.00	0.00	0.00	0.00	0.00
K_C	0.09	-0.12	-0.13	0.14	-0.18	-0.25	0.00	0.00	1.00	-0.01	0.00	0.00
K_{H_2}	-0.09	0.65	-0.09	-0.07	0.06	-0.19	0.00	0.00	-0.01	1.00	0.01	0.00
K_P	-0.09	0.11	-0.69	-0.14	0.18	0.25	0.00	0.00	0.00	0.01	1.00	0.00
K_T	0.00	0.00	0.00	0.00	0.00	0.00	0.00	0.00	0.00	0.00	0.00	0.00

In Figure 4-14 the parity diagrams for phenol, cresol, benzene, toluene and anisole are depicted for the Langmuir-Hinshelwood model. As can be seen, the predicted outlet flow rates are acceptable for all the responses. The hydrodeoxygenation products benzene and toluene are better predicted compared to the power law model.

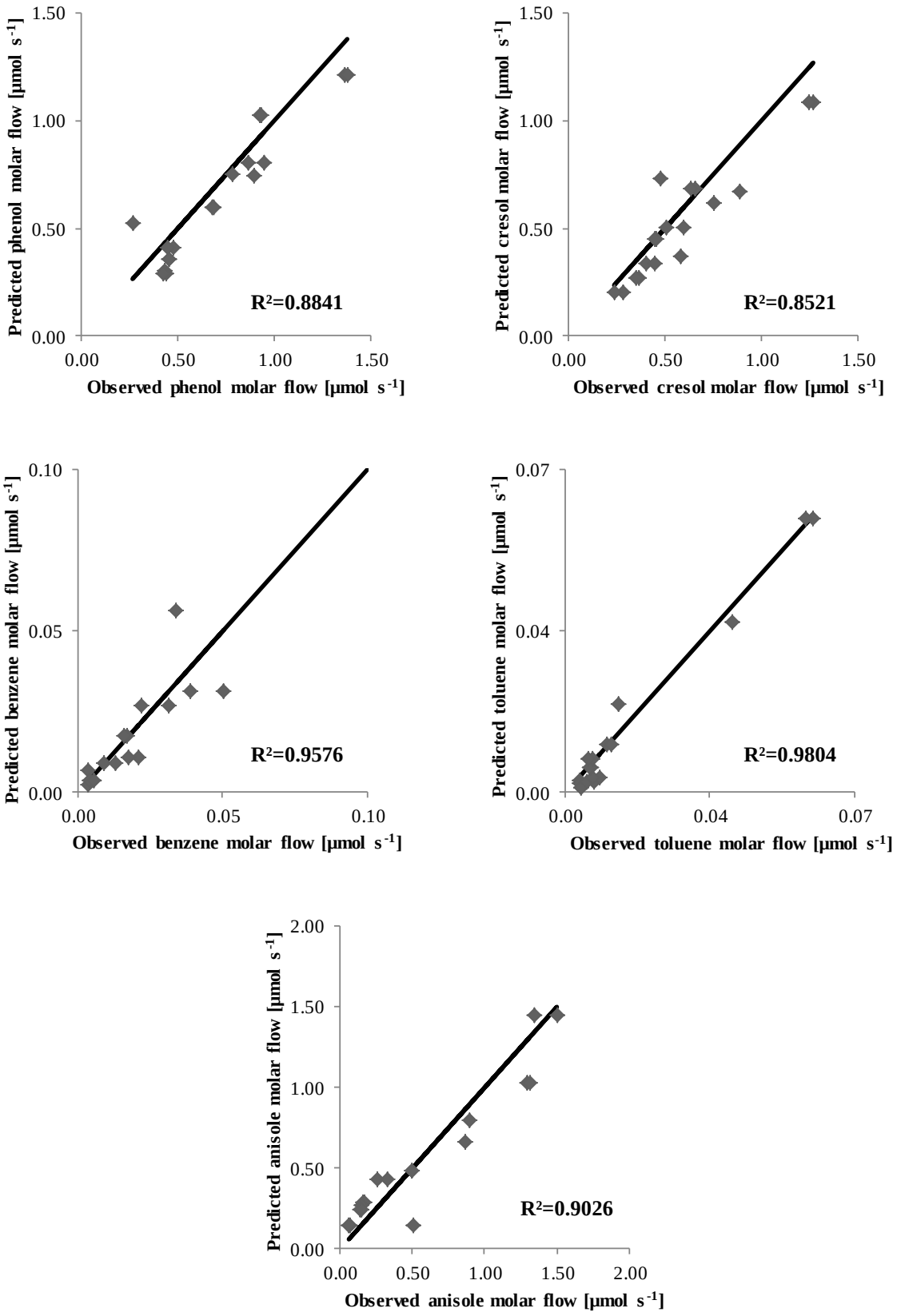

Figure 4-14. Parity diagrams for the molar outlet flow of phenol (top left), cresol (top right), benzene (middle left), toluene (middle right) and anisole (bottom), determined by solving equation 3-11 in which the net rates of formation are given by equations 4-27 till 4-34 using the parameters from Table 4-4.

The *F* value for the model adequacy, which equals to 13.68, is lower than that of the power law model, however, it still exceeds the tabulated value at 95 % confidence with respectively 40 and 38 degrees of freedom, that equals, 1.7. Despite this, no significant trends are observed in the residual figures in Figure 4-15 and Figure 4-16 of the outlet flow as a function of the temperature and the space time.

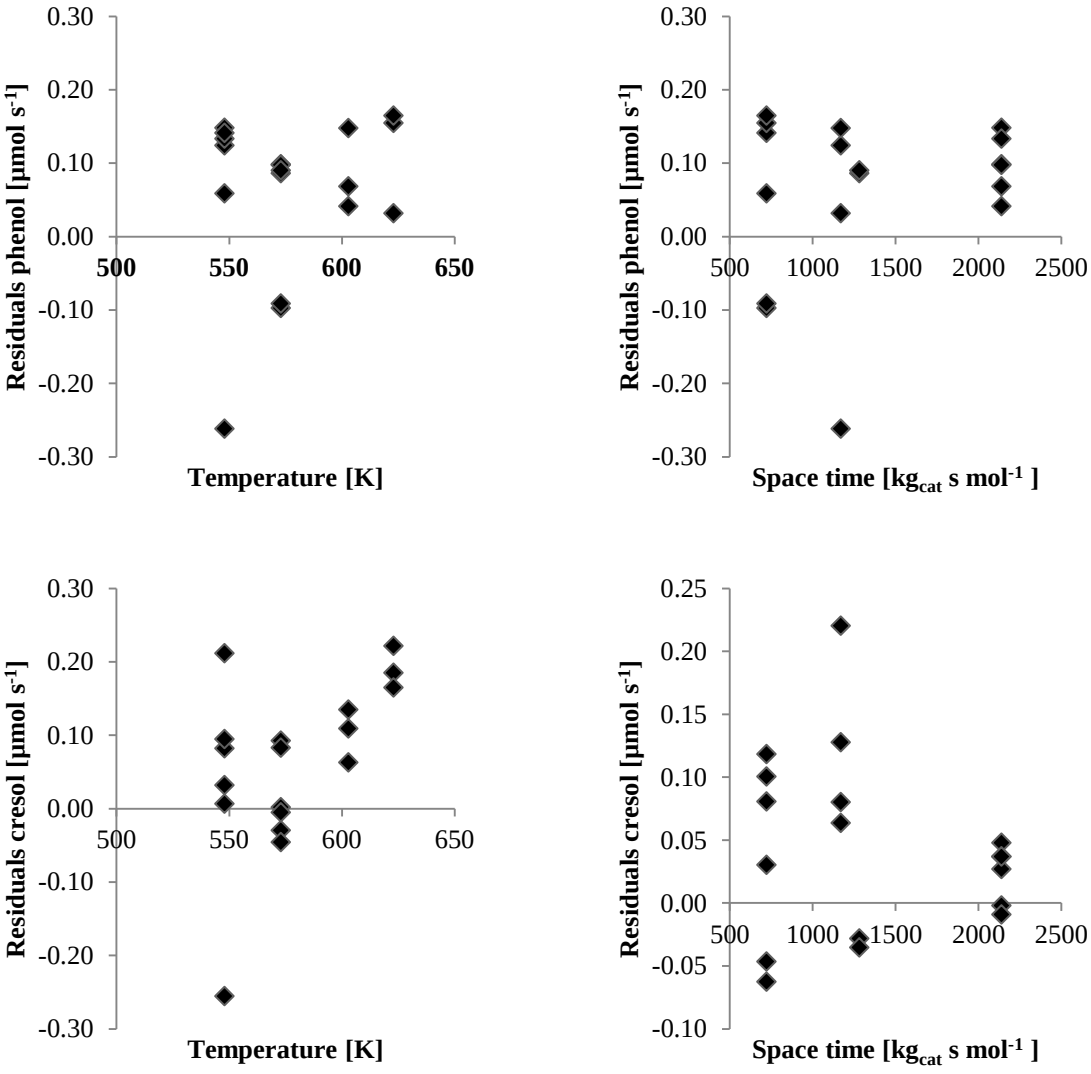

Figure 4-15. Residual figures of the outlet molar flow of phenol (top) and cresol (bottom) as a function of the temperature (left) and the space time (right) determined by solving equation 3-11 in which the net rates of formation are given by equations 4-27 till 4-34 using the parameters from Table 4-4.

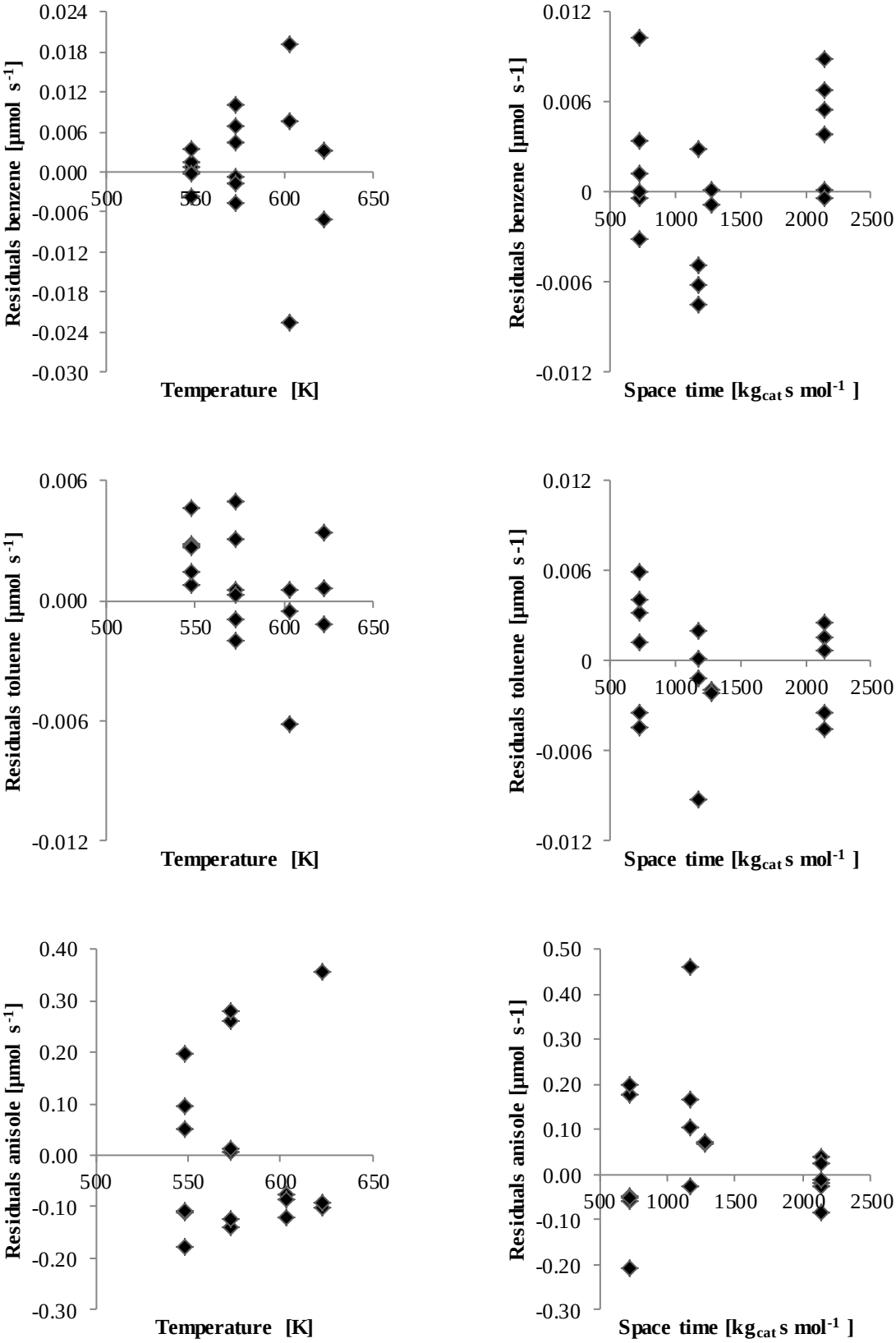

Figure 4-16. Residual figures of the outlet molar flow of benzene (top), toluene (middle) and anisole (bottom) as a function of the temperature (left) and the space time (right) determined by solving equation 3-11 in which the net rates of formation are given by equations 4-27 till 4-34 using the parameters from Table 4-4.

4.4.2.2Model performance

This model is also validated by performing a simulation with the parameters from Table 4-4. The influence of temperature on the conversion and the product yields is depicted in Figure 4-17 and Figure 4-18, while the influence of space time is shown in Figure 4-19 and Figure 4-20 respectively. As one can see, the Langmuir-Hinshelwood model predicts the trends as a function of the temperature. On the other hand, there is still room for improvement for the influence of the space time.

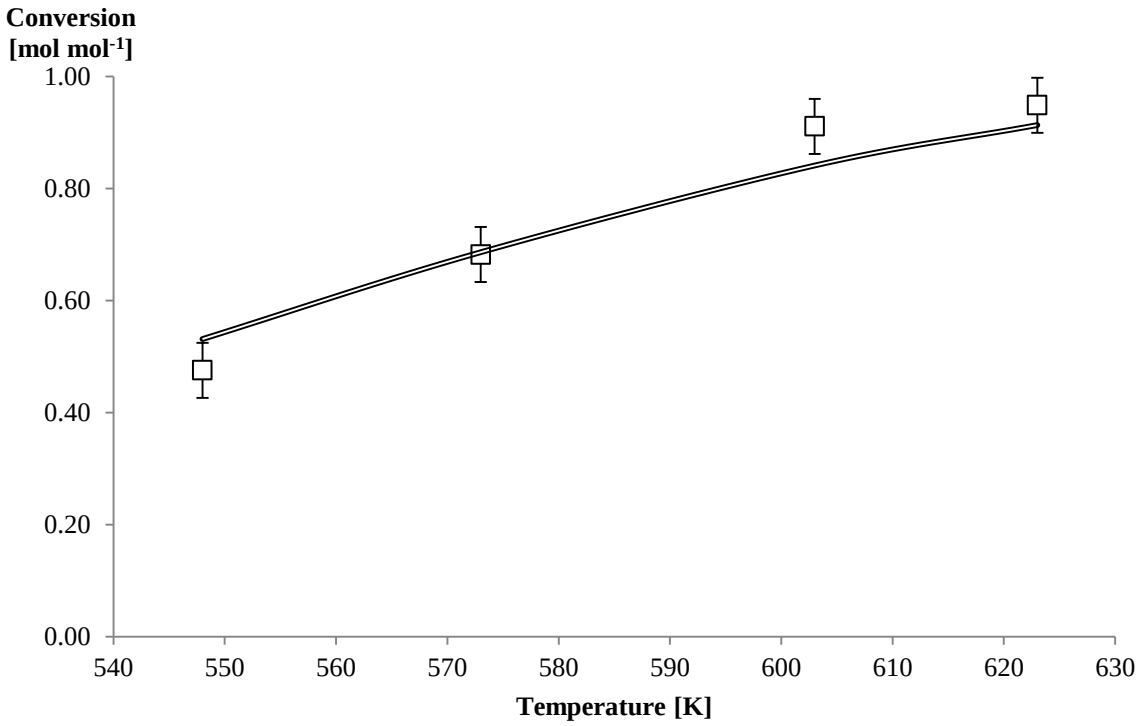

Figure 4-17. Influence of the temperature on anisole conversion on CoMo/γ-Al_2O_3 catalyst. Reaction conditions: space time = 1170 kg_{cat} s $mol_{anisole}^{-1}$, total pressure = 0.5 MPa, H_2/anisole = 400 mol_{H2} $mol_{anisole}^{-1}$. □ = Experimental conversion, double line = simulated conversion

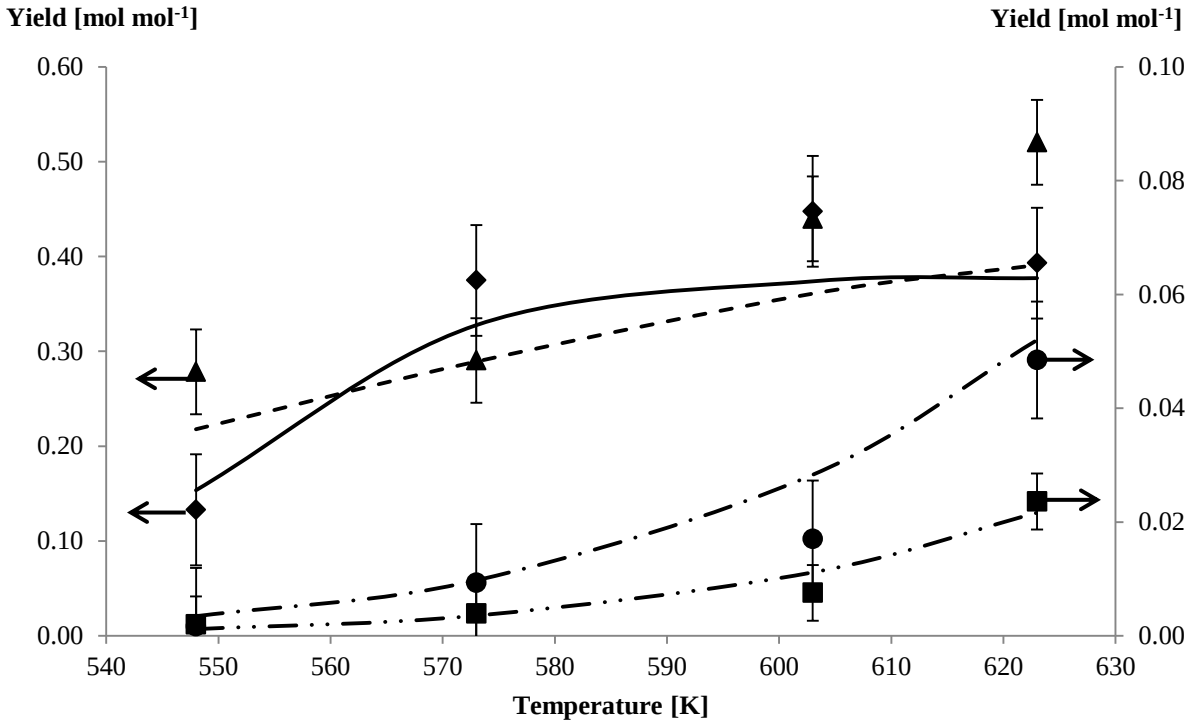

Figure 4-18. Influence of the temperature on product yields on CoMo/γ-Al_2O_3 catalyst. Reaction conditions: space time = 1170 kg_{cat} s $mol_{anisole}^{-1}$, total pressure = 0.5 MPa, H_2/anisole = 400 mol_{H2} $mol_{anisole}^{-1}$. Experimental: ♦ = phenol, ▲ = cresol, ● = benzene, ■ = toluene. Simulation: full line = phenol, dashed line = cresol, dash-dotted line = benzene, dash-dot-dotted line = toluene.

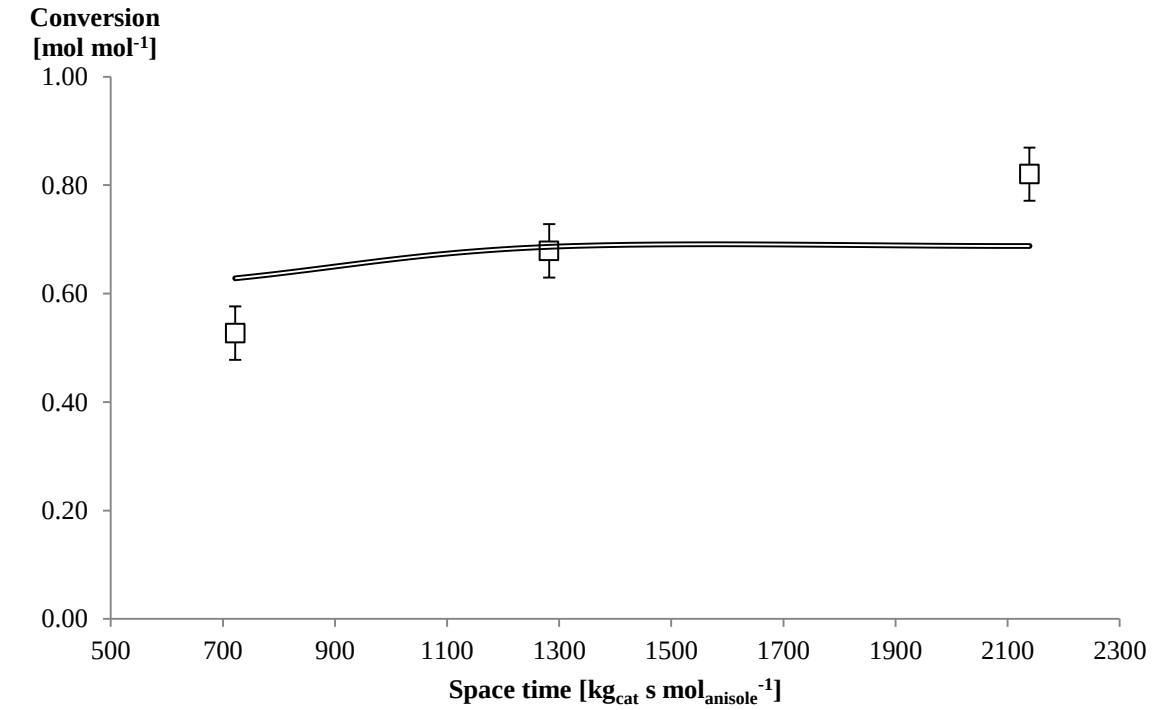

Figure 4-19. Influence of the space time on anisole conversion on CoMo/γ-Al_2O_3 catalyst. Reaction conditions: temperature = 573 K, total pressure = 0.5 MPa, H_2/anisole = 400 mol_{H2} $mol_{anisole}^{-1}$. □ = Experimental conversion, double line = simulated conversion

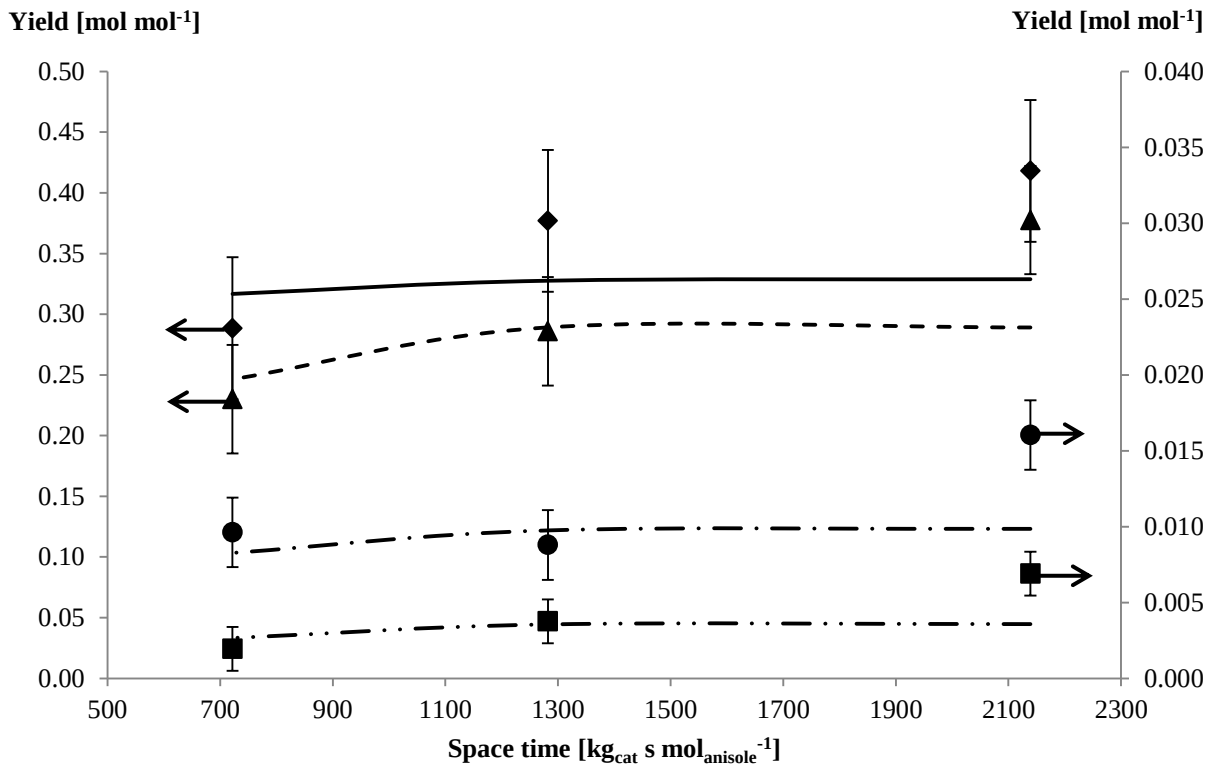

Figure 4-20. Influence of the space time on product yields on CoMo/γ-Al_2O_3 catalyst. Reaction conditions: temperature = 573 K, total pressure = 0.5 MPa, H_2/anisole = 400 mol_{H2} $mol_{anisole}^{-1}$. Experimental: ♦ = phenol, ▲ = cresol, ● = benzene, ■ = toluene. Simulation: full line = phenol, dashed line = cresol, dash-dotted line = benzene, dash-dot-dotted line = toluene.

The poor fitting of this model can be the result of the bad parameter estimation, as only eight of the twelve parameters are estimated at ones. Further, the adsorption coefficients of the components are considered to be constants and do not vary according to the Van't Hoff equation.

4.5 Conclusion

Intrinsic kinetic experiments are performed in an ideal plug flow reactor on a lignin derived model compound, *i.e.* anisole, over a CoMo/γ-Al_2O_3 catalyst in the temperature range of 548 K to 623 K, and different space times at 0.5 MPa. A product analysis shows that the anisole conversion takes place via demethylation and transalkylation, resulting in high selectivities for phenol and cresols. These compounds seem to be stable under the reactions conditions, and only a small extent of the deoxygenated products benzene and toluene are observed.

The effect of temperature and space time on the product distribution and the hydrodeoxygenation extent is investigated. With increasing the temperature from 548 K to 623 K, the conversion increases from 50 mol% to 95 mol%. The yield of phenol shows a maximum at 603 K, while the yield of cresol, benzene and toluene continuously increase with

temperature. An increasing space time enhance the conversion from 53 mol% to 82 mol% when increasing the space time from 722 kg_{cat} s $mol_{anisole}^{-1}$ to 2140 kg_{cat} s $mol_{anisole}^{-1}$. The yield of phenol shows a maximum and that of benzene a minimum at 1282 kg_{cat} s $mol_{anisole}^{-1}$, while the yields of cresol and toluene increase with space time. Those phenomena indicate a stronger Arrhenius dependency of the hydrodeoxygenation reactions, compared to the demethylation and transalkylation reactions.

A reaction network containing six reactions is proposed to described the observed kinetics. The conversion of anisole occurs mainly via two pathways: the elimination of the methylgroup or its transfer into the benzene ring. The HDO of cresol and phenol led to the production of toluene and benzene, respectively. The direct deoxygenation of anisole to benzene did not occur, due to the strong both between the aromatic carbon and the oxygen. Two models are developed to describe this reaction network. The power law model is used to describe the overall reaction order. Since it neglects the mechanistic aspects of adsorption/desorption and the surface reaction on the catalyst, a Langmuir-Hinshelwood kinetic model was developed, assuming that the surface reactions are irreversible and the adsorption and the desorption of the reactants and the products are near equilibrium.

The kinetic parameter estimation is performed by minimization of the residual sum of squares using a Levenberg-Marquardt algorithm. Both models are found to be significant since the F value for model significance is more than three orders of magnitude larger than the tabulated value. Not all of the estimated parameters are statistically significant, but all of the parameters have a clear physical meaning. In the power law model, 11 out of the 12 parameters were estimated significantly, in the Langmuir-Hinshelwood model 9 out of the 12 parameters. In the Langmuir-Hinshelwood model, the adsorption coefficients were the most difficult to estimate.

For both models, the highest activation energy was found for the hydrodeoxygenation reactions, which is in line with the small extent of the hydrodeoxygenation products. A higher activation energy for the transalkylation compared to the demethylation is also in agreement with the experimental findings.

The temperature dependency of the Langmuir-Hinshelwood model could be improved by introducing the Van't Hoff equation for the adsorption coefficients. The influence of space time could be improved by deriving a model with only elementary reaction steps, which would increase the accuracy of the reaction network. Those implementations would introduce

additional parameters to be estimated, therefore some parameters, like the pre-exponential factors, should be a priori estimated and kept constant during the regression.

4.6 References

1. Technology, A. P. *Aspen Physical Property System*; 2001.
2. Luo, Y. R., *Comprehensive Handbook of Chemical Bond Energies*. Taylor & Francis: 2007.
3. Toch, K.; Thybaut, J. W.; Marin, G. B., A systematic methodology for kinetic modeling of chemical reactions applied to n-hexane hydroisomerization. *AIChE Journal* **2014**, n/a-n/a.
4. Thybaut, J. W. *Kinetic Modeling and Simulation*; Ghent University: 2013.
5. Thybaut, J. W.; Marin, G. B., Kinetics of Catalyzed Reactions—Heterogeneous. In *Encyclopedia of Catalysis*, John Wiley & Sons, Inc.: 2002.
6. Zamostny, P.; Belohlav, Z., Identification of kinetic models of heterogeneously catalyzed reactions. *Applied Catalysis A: General* **2002,** 225, (1–2), 291-299.
7. Froment, G. F.; Bischoff, K. B., *Chemical reactor analysis and design*. Wiley: 1990.
8. Bykova, M. V.; Zavarukhin, S. G.; Trusov, L. I.; Yakovlev, V. A., Guaiacol hydrodeoxygenation kinetics with catalyst deactivation taken into consideration. *Kinet Catal* **2013,** 54, (1), 40-48.

Chapter 5

KINETIC MODELING OF GAS PHASE ANISOLE HYDRODEOXYGENATION OVER A NICU/ZRO_2 CATALYST

The hydrogenation of anisole catalyzed by a NiCu/ZrO_2 catalyst is studied in an ideal plug flow reactor at 573 K, anisole pressure in the range of 900 to 1900 Pa and different space times. Based on the experimental investigation a reaction network is proposed where the hydrodeoxygenation of anisole proceeds via the elimination of the methylgroup or its transfer into the aromatic ring, the hydrogenolysis of the bond between the aromatic carbon and the oxygen and the hydrogenation of the aromatic ring. A power law model is developed and from the regression to the data set, the parameters of this model are determined. The performance of the model has been verified based on statistical tests and the comparison of the simulated behavior with the experimental observations. A Langmuir-Hinshelwood model based on elementary steps has been derived.

5.1 Reaction conditions for gas phase reaction

During the experimental investigation, one want to avoid condensation in both the reactor as in the transfer lines from the reactor to the analysis section. Therefore, the transfer lines are traced and is the feed flow diluted with nitrogen. A simulation of the HTK-1 is performed in Aspen Plus © to determine the amount of nitrogen needed to maintain in the gas phase. Typical experimental conditions (Table 5-1) are simulated with the SRK property method. This method is selected based on the Aspen Plus Best Practice guidelines, as previously discussed in section 4.1. The simulation results indicate that no condensation will occur in the tested conditions.

Table 5-1. Simulated range of experimental conditions to prevent condensation.

	Simulation range
Anisole flow rate	1-5 g h^{-1}
Nitrogen flow rate	0-200 Nl h^{-1}
Reactor temperature	573 K
Reactor pressure	5 MPa
Flash vessel temperature	298-343 K
Pressure after expansion	1 MPa

5.2 Reaction conditions for intrinsic kinetics

Performing experiments with the aim for kinetic modeling, it is important to gather an intrinsic kinetic data set. In the intrinsic kinetic regime the effect of the reaction conditions on the reaction rate is negligible for transport and transfer limitations. The criteria which have to be satisfied to maintain in intrinsic regime are discussed in detail in Appendix D. The operating condition for the hydrodeoxygenation experiments of anisole over the $NiCu/ZrO_2$ catalyst are summarized in Table 5-2.

Table 5-2. Summary of the operation conditions for intrinsic kinetics over the $NiCu/ZrO_2$ catalyst.

Operating condition	Experimental range
Catalyst pellet diameter	400-600 µm
Temperature	523-623 K
Anisole inlet partial pressure	900-1900 Pa
Space time	50-250 kg_{cat} s mol^{-1}
H_2/anisole	50-200 mol_{H2} $mol_{anisole}^{-1}$

5.3 Influence of the reaction conditions on anisole HDO over a $NiCu/ZrO_2$ catalyst

The experimental data set on a $NiCu/ZrO_2$ catalyst, containing 35 experiments (Appendix A), has been acquired on the HTK-1 (a description of the set-up can be found in Chapter 2) by systematically varying the reaction conditions within the intrinsic kinetic regime (section 5.2). The feed consist of anisole and hydrogen as reactants, *n*-hexane as solvent, *n*-octane as internal standard and N_2 as diluent. In the following subsections the activity of the catalyst is discussed. Further, the influence of the space time, the inlet partial pressure of anisole and the molar hydrogen to anisole ratio on the conversion and product yields is investigated.

5.3.1 Deactivation experiments

To investigate the stability of the catalyst, it was tested for a longer time on stream. Two deactivation experiments has been performed on the $NiCu/ZrO_2$ catalyst, both at 573 K with a space time of 100 kg_{cat} s mol^{-1} and a molar hydrogen to anisole ratio of 125, but at different inlet partial pressures of anisole.

As can be seen in Figure 5-1, a small loss in activity is observed after 12 h. The overall deactivation of the $NiCu/ZrO_2$ catalyst is shown in Figure 5-2. After 50 h on stream there is severe deactivation observed. This decrease in activity is probably due to the carbon decomposition on the catalyst, which was evidenced by the discoloration of the inert material in the reactor.

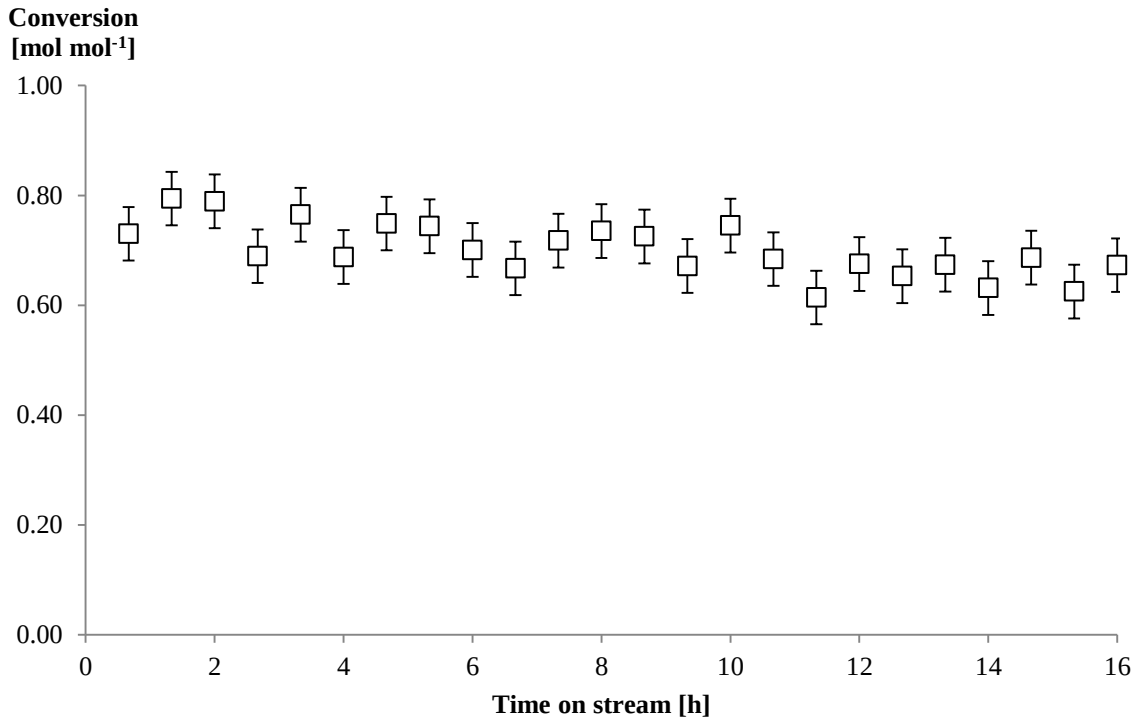

Figure 5-1. The conversion of anisole as a function of time on stream over a $NiCu/ZrO_2$ catalyst. Reaction conditions: space time = 100 kg_{cat} $mol_{anisole}^{-1}$ s^{-1}, temperature = 573 K, H_2/anisole = 125 mol_{H2} $mol_{anisole}^{-1}$, inlet partial pressure of anisole = 1140 Pa.

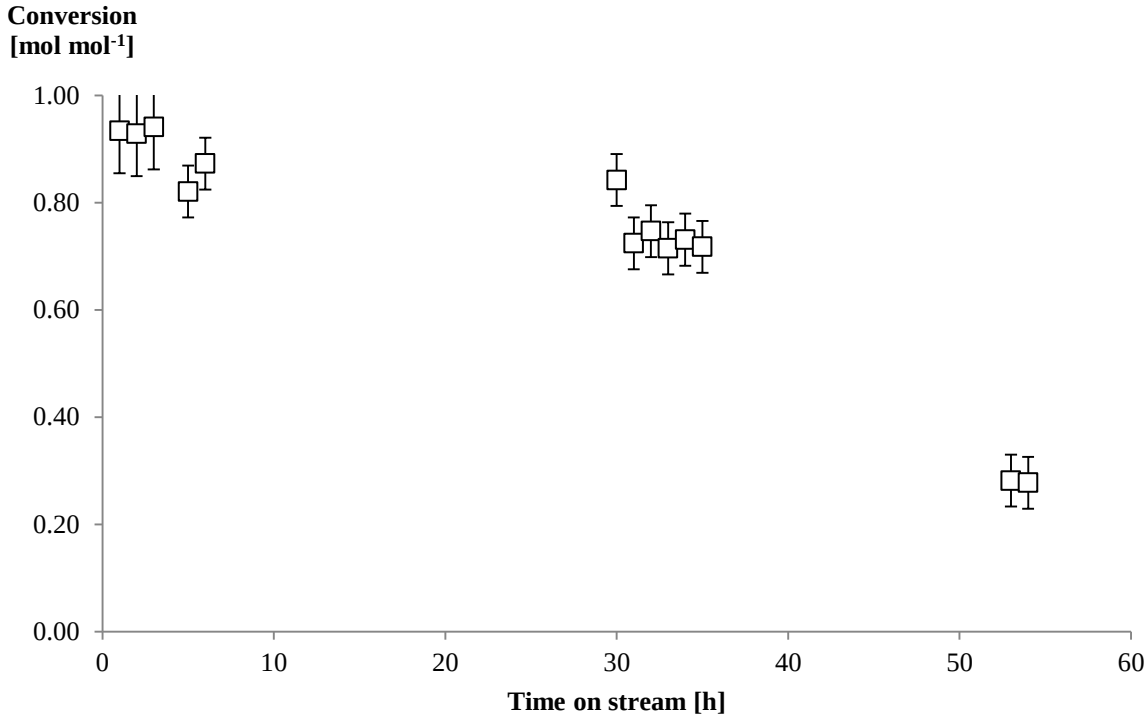

Figure 5-2. The conversion of anisole as a function of time on stream over a $NiCu/ZrO_2$ catalyst. Reaction conditions: space time = 100 kg_{cat} s $mol_{anisole}^{-1}$, temperature = 573 K, H_2/anisole = 125 mol_{H2} $mol_{anisole}^{-1}$, inlet partial pressure of anisole = 1325 Pa.

Due to the slight decrease in catalytic activity during the prolonged experimental run, a 10 vol% H_2 flow was sent through the reactor to minimize the catalyst deactivation between two experiments.

5.3.2 Influence of the space time

Figure 5-3 presents the influence of space time on the product yields at 573 K. The conversion increases from 52 mol% for a space time of 66 kg_{cat} s $mol_{anisole}^{-1}$ to 89 mol% for a space time of 140 kg_{cat} s $mol_{anisole}^{-1}$. This phenomenon is expected since space time enhances the conversion. As a result, the yields of the products should increase with increasing space time. This trend is observed for the yields of benzene, cyclohexane, toluene and methylcyclohexane. However, a decrease is found in the yields of phenol and cresol. This effect can be contributed to the reactions in which those compounds are involved. The HDO of phenol and cresol results respectively in benzene and toluene, for both an increasing yield is observed. The yield of xylene, decreases with the space time. The methylation of the aromatic ring seems to be retained by the increase of space time.

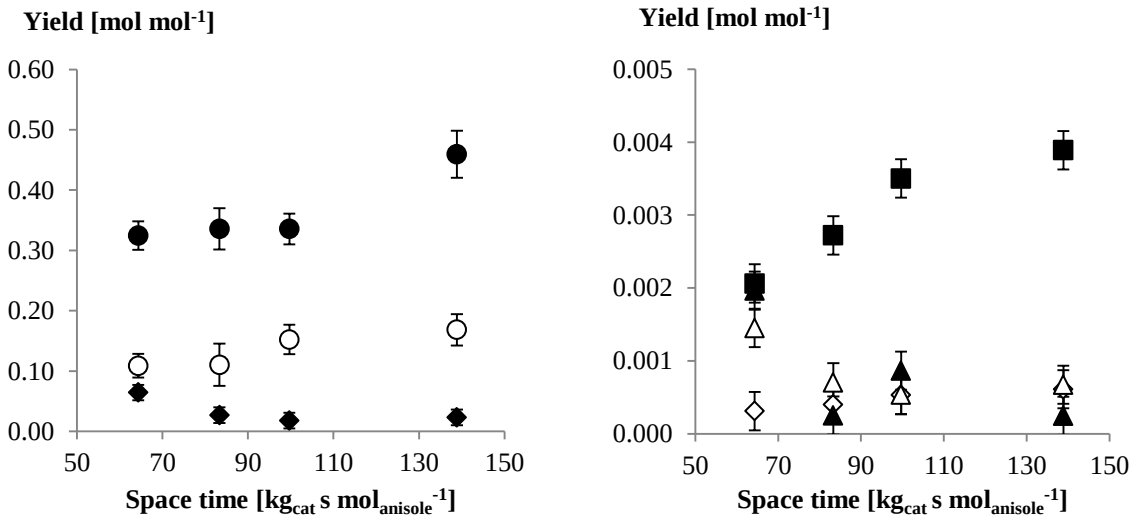

Figure 5-3. Influence of the space time on product yields of anisole HDO over a $NiCu/ZrO_2$ catalyst. Conversion: 52 mol% for 66 kg_{cat} s $mol_{anisole}^{-1}$, 63 mol% for 83 kg_{cat} s $mol_{anisole}^{-1}$, 73 mol% for 100 kg_{cat} s $mol_{anisole}^{-1}$ and 89 mol% for 140 kg_{cat} s $mol_{anisole}^{-1}$. Reaction conditions: temperature = 573 K, H_2/anisole = 125 mol_{H2} $mol_{anisole}^{-1}$, inlet partial pressure of anisole = 1325 Pa. Experimental: ● = benzene, ○ = cyclohexane, ♦ = phenol, ■ = toluene, Δ = xylene, ▲ = cresol, ◊ = methylcyclohexane.

The Delplot technique[1] is used to identify the primary, secondary and tertiary products. A first order Delplot is shown in Figure 5-4. Such a plot is used to rank primary from secondary products. A second order Delplot is used to differentiate secondary products from tertiary products. The first order Delplot plot suggests that phenol and cresol are primary products, cyclohexane, toluene and methylcyclohexane secondary or tertiary. The rank of benzene is not clear, it could be a primary or a secondary product. Based on the second order Delplot

cyclohexane and toluene are identified as a secondary product and methylcyclohexane as a tertiary product. The rank of xylene could not be identified based on the Delplot technique.

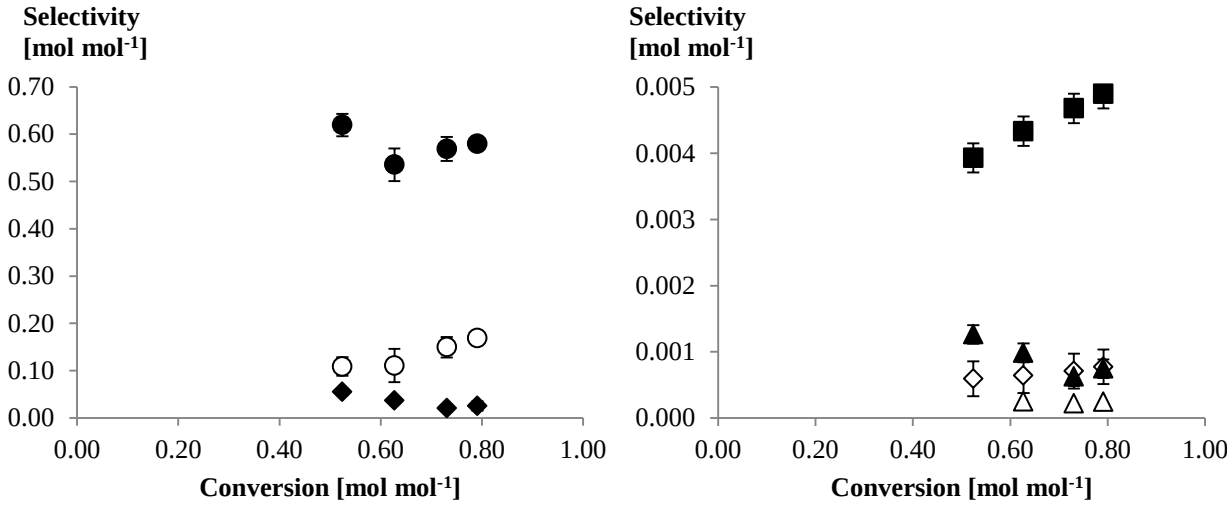

Figure 5-4. First order Delplot for the products of anisole HDO on a $NiCu/ZrO_2$ catalyst. Reaction conditions: temperature = 573 K, H_2/anisole = 125 mol_{H2} $mol_{anisole}^{-1}$, inlet partial pressure of anisole = 1325 Pa. Experimental: ● = benzene, ○ = cyclohexane, ♦ = phenol, ■ = toluene, Δ = xylene, ▲ = cresol, ◊ = methylcyclohexane.

5.3.3 Influence of the inlet partial pressure of anisole

During the experimental investigation of anisole HDO on the $NiCu/ZrO_2$ catalyst at 573 K, the inlet partial pressure of anisole was varied from 1031 Pa to 1584 Pa. Increasing anisole pressure enhanced the conversion from 58 mol% to 84 mol%. This phenomenon is the result of higher catalyst surface occupancy by anisole. With increasing partial pressure of anisole, the chemisorbed concentration of anisole will increase as long as the surface is not saturated.

As can be seen in Figure 5-5, a higher occupancy of the catalyst surface by anisole enhance the yields of benzene, cyclohexane, toluene and methylcyclohexane, while the yields of phenol, cresol and xylene decrease. The higher chemisorbed concentration of anisole results in an increasing demethylation, transalkylation and demethoxylation rate of anisole, and hence, an increased concentration of phenol, cresol and benzene.

The fact that the yields of benzene and cyclohexane increase with increasing anisole pressure and that of phenol decreases, indicates that there is a hydrogenolysis reaction of phenol with the formation of benzene which is further hydrogenated into cyclohexane. The decreasing trend in the yield of cresol and the increasing trend in the yield of toluene, also indicate a hydrodeoxygenation reaction of cresol. The yield of toluene shows a maximum at 1325 Pa. The yields of the possible products of toluene, *i.e.* benzene, xylene and methylcyclohexane, indicate that toluene will most probably undergo a demethylation with the formation of benzene or a hydrogenation with methylcyclohexane as product.

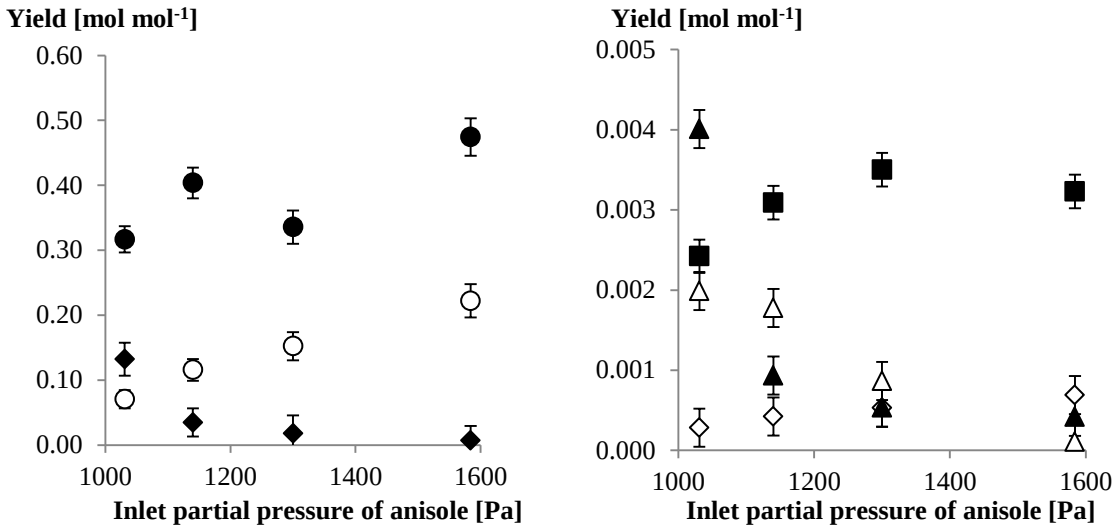

Figure 5-5. Influence of the inlet partial pressure of anisole on product yields over a $NiCu/ZrO_2$ catalyst. Conversion: 58 mol% for 1031 Pa, 66 mol% for 1183 Pa, 73 mol% for 1325 Pa and 84 mol% for 1584 Pa. Reaction conditions: space time = 100 kg_{cat} s $mol_{anisole}^{-1}$, temperature = 573 K, H_2/anisole = 125 mol_{H2} $mol_{anisole}^{-1}$. Experimental: ● = benzene, ○ = cyclohexane, ♦ = phenol, ■ = toluene, Δ = xylene, ▲ = cresol, ◊ = methylcyclohexane.

5.3.4 Influence of the molar hydrogen to anisole ratio

The increase of the molar hydrogen to anisole ratio from 90 mol_{H2} $mol_{anisole}^{-1}$ to 186 mol_{H2} $mol_{anisole}^{-1}$ is investigated at 573 K, a space time of 100 kg_{cat} s mol^{-1} and an anisole pressure of 1325 Pa. At this conditions 75 mol% of anisole is converted. Figure 5-6 depicts the influence of the molar ratio on the products.

There is slight decrease in the selectivity towards phenol and cresol, indicating secondary reactions with those products. There is no significant trend observed within the experimental error in the selectivities towards benzene, while the selectivity towards methanol decreases. This could be an indication that with increasing hydrogen pressure, the direct deoxygenation of anisole rate decreases. There is a clear increase of the hydrogenated products, cyclohexane and methylcyclohexane, which is in line with the expectations. A higher molar hydrogen to anisole ratio at constant anisole partial pressure is equivalent with an increasing hydrogen partial pressure. As a result, the occupancy of the catalyst surface with hydrogen will increase, and hence, enhancing the possibility of the reactions with hydrogen. Based on the decreasing trend in the selectivity of methane one should expect an increasing trend in the methylated product, xylene. However, this trend is not fully visible by the experiments.

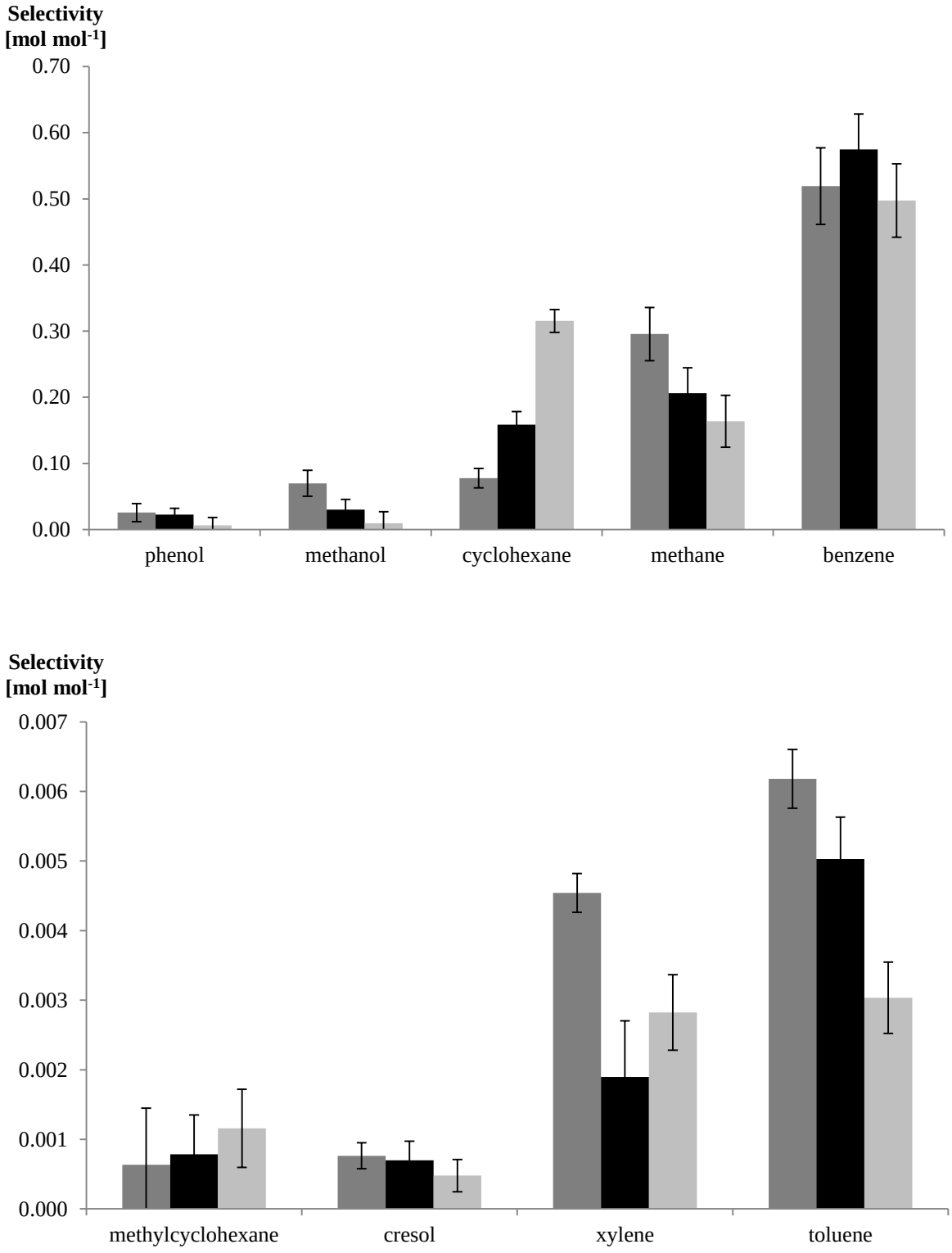

Figure 5-6. The influence of the molar hydrogen to anisole ratio on the selectivities towards the major products (top) and minor product (bottom). Hydrogen to anisole ratio: dark grey = 90 mol_{H2} $mol_{anisole}^{-1}$, black = 125 mol_{H2} $mol_{anisole}^{-1}$, light grey = 186 mol_{H2} $mol_{anisole}^{-1}$. Reaction conditions: space time = 100 kg_{cat} s $mol_{anisole}^{-1}$, temperature = 573 K, conversion = 75 mol%, inlet partial pressure of anisole = 1325 Pa.

5.4 Kinetic modeling

Based on the obtained data one can suggest that the hydrodeoxygenation of anisole proceeds via the following steps: the elimination of the methylgroup or its transfer into the benzene ring, the hydrogenolysis of the $C_{aromatic}$-O bond and the hydrogenation of the aromatic ring. That last is expected as nickel is known for its high hydrogenation capacity[2].

The reaction network for the hydrodeoxygenation of anisole on a $NiCu/ZrO_2$ is proposed in Figure 5-7.

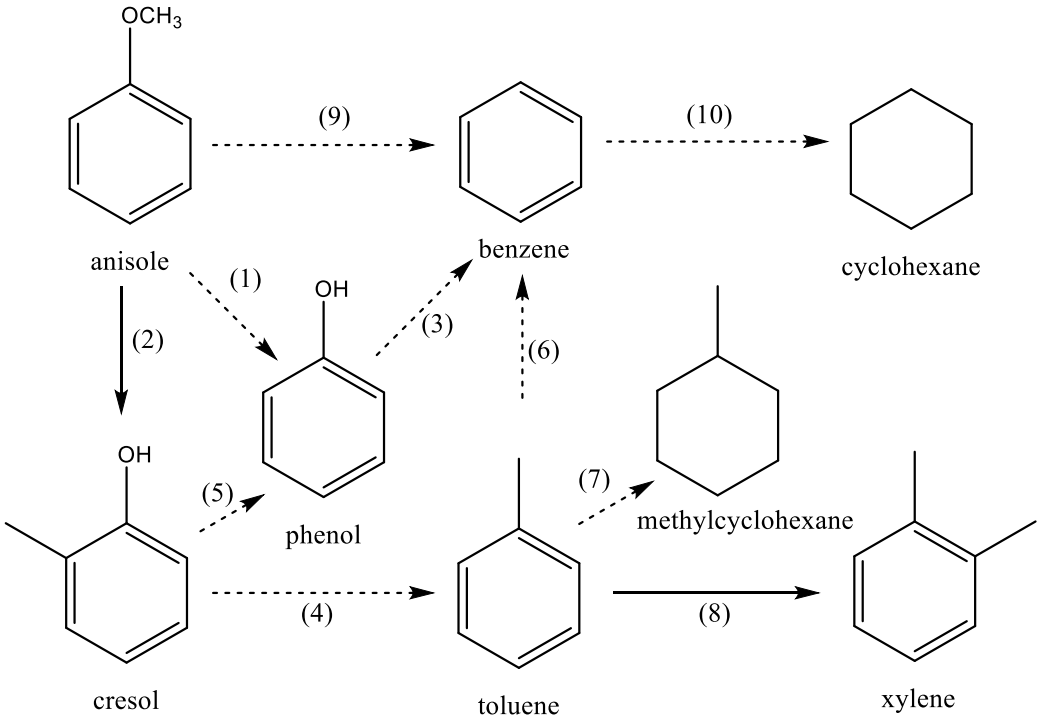

Figure 5-7. Proposed reaction mechanism for anisole HDO over a $NiCu/ZrO_2$ catalyst. The dashed arrows represent hydrodeoxygenation, hydrogenolysis or hydrogenation reactions, while the solid arrows represent the methyl group transfer reactions.

The conversion of anisole can occur via one of three reactions pathways, *i.e.* the transalkylation towards cresol (reaction 2), the demethylation towards phenol (reaction 1) or the direct deoxygenation towards benzene (reaction 9). There are two possible cleavages in cresol: the $C_{aromatic}$-$C_{aliphatic}$ cleavage with the formation of toluene (reaction 4) or the $C_{aromatic}$-O cleavage resulting in phenol (reaction 5). Methylcyclohexane is the product of full hydrogenation of toluene (reaction 7), while xylene can be formed via methylation of toluene (reaction 8). The hydrodeoxygenation of phenol results in benzene (reaction 3) which can be consecutively hydrogenated to cyclohexane (reaction 10).

In the following subsections, a power law model and a Langmuir-Hinshelwood model are described for the proposed reaction mechanism.

5.4.1 Power law model for the HDO of anisole over a $NiCu/ZrO_2$ catalyst

The empirical power law rate equations are used for the description of the overall reaction orders of the proposed reaction network in Figure 5-7.

$$r_1 = k_1 p_{H_2}^{\alpha_1} p_A^{\beta_1} \quad 5\text{-}1$$

$$r_2 = k_2 p_A^{\beta_2} \quad 5\text{-}2$$

$$r_3 = k_3 p_{H_2}^{\alpha_3} p_P^{\beta_3} \quad 5\text{-}3$$

$$r_4 = k_4 p_{H_2}^{\alpha_4} p_C^{\beta_4} \quad 5\text{-}4$$

$$r_5 = k_5 p_{H_2}^{\alpha_5} p_C^{\beta_5} \quad 5\text{-}5$$

$$r_6 = k_6 p_{H_2}^{\alpha_6} p_T^{\beta_6} \quad 5\text{-}6$$

$$r_7 = k_7 p_{H_2}^{\alpha_7} p_T^{\beta_7} \quad 5\text{-}7$$

$$r_8 = k_8 p_T^{\beta_8} p_{CH_4}^{\gamma} \quad 5\text{-}8$$

$$r_9 = k_9 p_{H_2}^{\alpha_9} p_A^{\beta_9} \quad 5\text{-}9$$

$$r_{10} = k_{10} p_{H_2}^{\alpha_{10}} p_B^{\beta_{10}} \quad 5\text{-}10$$

In the above equations, k is the isothermal rate coefficient of a reaction, α, β and γ are the kinetic orders and A = anisole, P = phenol, C = cresol, B = benzene, T = toluene.

There are six different reaction families, *i.e.* demethylation (reactions 1, 5 and 6), transalkylation (reaction 2), dehydroxylation (reaction 3 and 4), hydrogenation of the aromatic ring (reaction 7 and 10), methylation (reaction 8) and demethoxylation (reaction 9). The dehydroxylation and the demethylation reaction are both hydrodeoxygenation reactions. It is assumed that the rate coefficient are the same for a reaction family, and thus $k_1 = k_5 = k_6$, $k_3 = k_4$, and $k_7 = k_{10}$.

In this empirical model 25 parameters has to be determined, of which 6 are rate coefficients and 19 are reaction orders.

The net rate of formation of all components in the reaction network, shown in Figure 5-7, is obtained from the individual reactions by accounting for the stoichiometry. Subscripts A, B, C, CHA, $MCHA$, P, T and X indicate respectively anisole, benzene, cresol, cyclohexane, methylcyclohexane, phenol, toluene and xylene.

$$R_A = -r_1 - r_2 - r_9 \quad 5\text{-}11$$

$$R_B = r_3 + r_6 + r_9 - r_{10} \quad 5\text{-}12$$

$$R_C = r_2 - r_4 - r_5 \quad 5\text{-}13$$

$$R_{CHA} = r_{10} \quad 5\text{-}14$$

$$R_{CH_3OH} = r_9 \quad 5\text{-}15$$

$$R_{CH_4} = r_1 + r_5 + r_6 - r_8 \quad 5\text{-}16$$

$$R_{H_2} = -r_1 - r_3 - r_4 - r_5 - r_6 - 3r_7 + r_8 - 3r_{10} \quad 5\text{-}17$$

$$R_{H_2O} = r_3 + r_4 \quad 5\text{-}18$$

$$R_{MCHA} = r_7 \quad 5\text{-}19$$

$$R_P = r_1 - r_3 + r_5 \quad 5\text{-}20$$

$$R_T = r_4 - r_6 - r_7 - r_8 \quad 5\text{-}21$$

$$R_X = r_8 \quad 5\text{-}22$$

5.4.1.1Regression analysis

The experimental data set of 35 experiments containes several deactivation experiments, therefore a set of 28 experiments is used for the isothermal regressing.

The model regression is significant as the F value is 10 orders of magnitude larger than the tabulated value of 3.84 at 95 % confidence with respectively 8 and 1 degrees of freedom. The parameter estimates with the corresponding 95 % confidence interval are given in Table 5-3.

Table 5-3. Parameter estimates with the corresponding 95% individual confidence interval determined by isothermal regression of the experimental data set on a $NiCu/ZrO_2$ catalyst, of the power law kinetic model determined by solving equation 3-11, in which the net rates of formation are given by equations 5-11 till 5-22. (a) indicates that the parameters are estimated with the other parameters fixed.

Parameter	Value
k_1 [(a)]	54.90 ± 12.2 μmol g^{-1} s^{-1} $MPa^{-(\alpha1+\beta1)}$
k_2	1.58 μmol g^{-1} s^{-1} $MPa^{-\beta2}$
k_3	14.43 ± 3.91 μmol g^{-1} s^{-1} $MPa^{-(\alpha3+\beta3)}$
k_4 [(a)]	14.43 ± 3.91 μmol g^{-1} s^{-1} $MPa^{-(\alpha4+\beta4)}$
k_5	54.90 ± 12.2 μmol g^{-1} s^{-1} $MPa^{-(\alpha5+\beta5)}$
k_6	54.90 ± 12.2 μmol g^{-1} s^{-1} $MPa^{-(\alpha6+\beta6)}$
k_7	19.55 ± 16.1 μmol g^{-1} s^{-1} $MPa^{-(\alpha7+\beta7)}$
k_8	1.32 μmol g^{-1} s^{-1} $MPa^{-(\gamma+\beta8)}$
k_9	14.30 μmol g^{-1} s^{-1} $MPa^{-(\alpha9+\beta9)}$
k_{10}	19.55 ± 16.1 μmol g^{-1} s^{-1} $MPa^{-(\alpha10+\beta10)}$
α_1	0.01
α_3	0.11
α_4	0.99 ± 2.99
α_5	0.48 ± 0.13
α_7	0.87
α_8	1.28 ± 2.99
α_9	0.82
α_{10}	0.48 ± 0.74
β_1 [(a)]	0.14 ± 0.03
β_2	0.07
β_3	0.06
β_4 [(a)]	0.28 ± 0.97
β_5	0.14 ± 0.01
β_6	0.51 ± 2.69
β_7	0.37 ± 0.36
β_8	0.49
β_9	0.40 ± 0.12
β_{10}	0.17 ± 0.08
γ	0.49

The isothermal rate coefficients are in line with the experiments. One could say that a large rate coefficient corresponds with a small activation energy, while a smaller rate coefficient is equivalent with a large activation energy, if the pre-exponential factors are the same. The smallest rate coefficients are found to be for the transalkylation of anisole to cresol reaction and the methylation reaction of toluene to xylene, which is in line with the small extent of the products cresol and xylene. The rate coefficients of the three HDO reactions are in the same order of magnitude. The rate coefficient for demethylation reactions are found to be the highest.

Most of the reaction orders are not estimated or comprise the zero value in the confidence interval. The trends in the reaction orders are not clear because the values are not optimal. Intuitively one would expect one negative partial reaction order for in each reaction as there is competition in the chemisorption of the different components.

There is no severe correlation found between the estimated parameters, all the binary correlation coefficients are smaller than 0.95. The multiple correlation coefficient equals 0.999, indicating a qualitative regression.

The parity diagrams of are shown in Figure 5-8 and Figure 5-9. Despite the fact that the regression is not very significant, the model is able to predict some outlet flows quite good. The parity diagrams of xylene is retained from the figure since the model is not able to predict this flow.

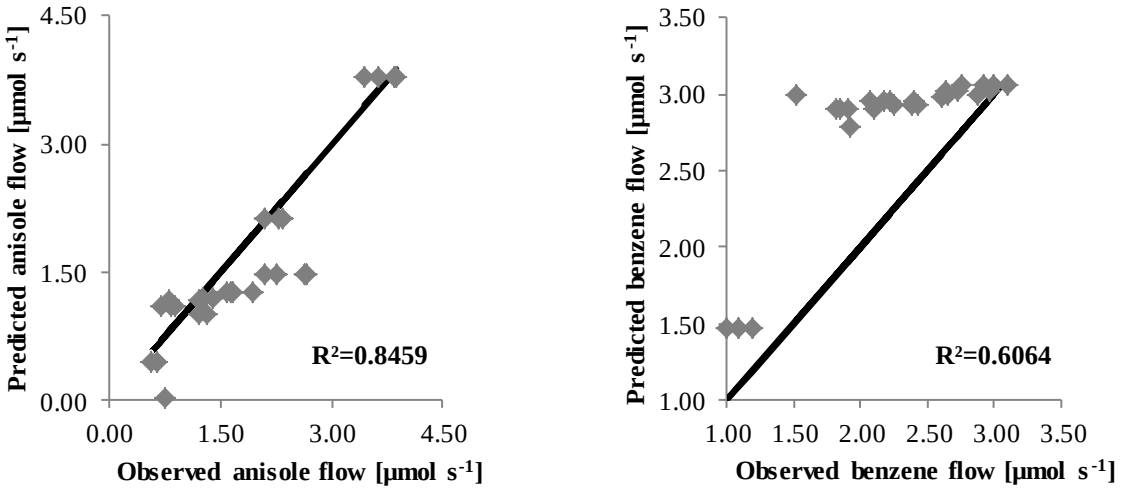

Figure 5-8. Parity diagrams for the molar outlet flow of anisole (left), benzene (right), determined by solving equation 3-11 in which the net rates of formation are given by equations 5-11 till 5-22 using the parameters from Table 5-3.

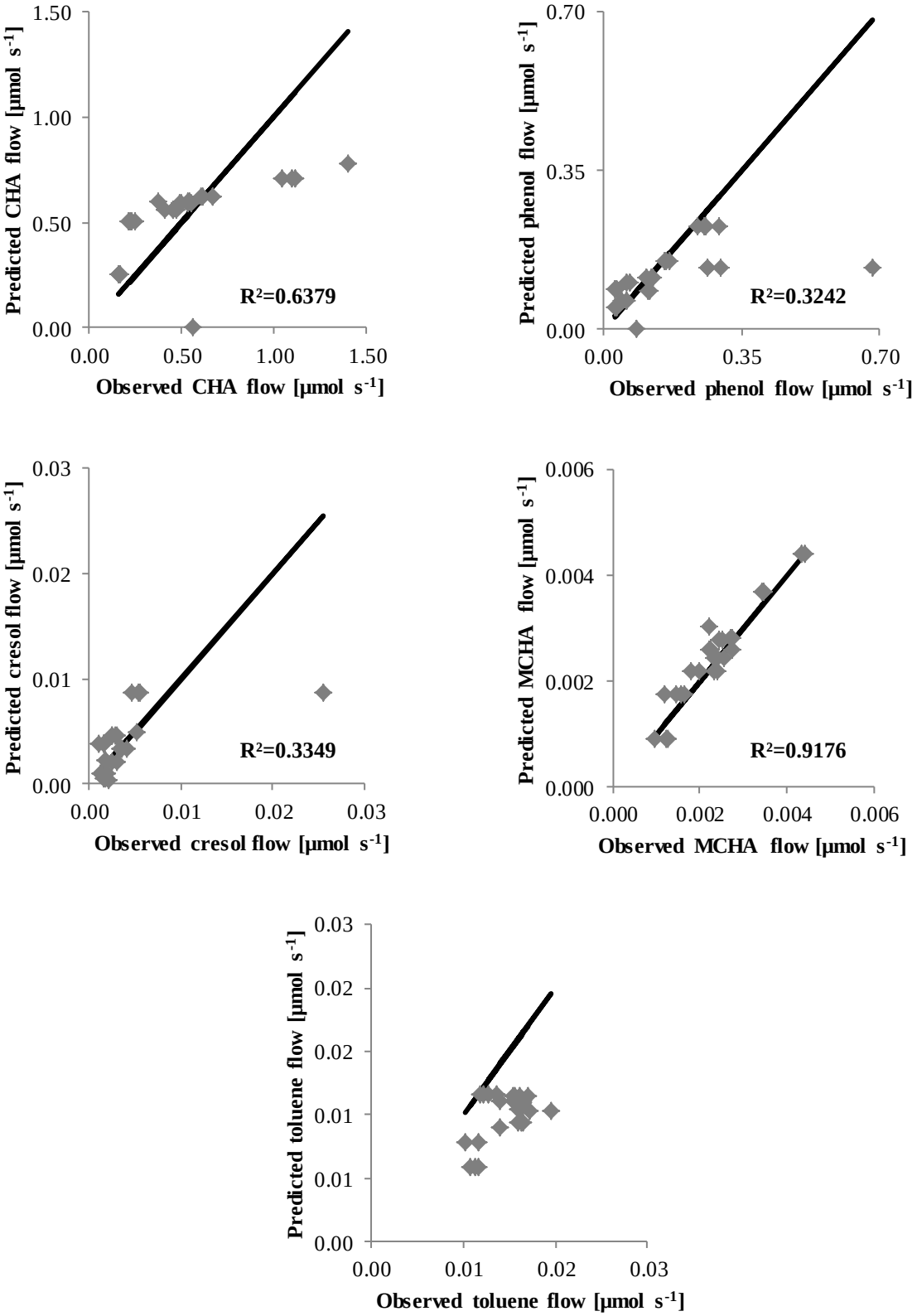

Figure 5-9. Parity diagrams for the molar outlet flow of cyclohexane (top left), phenol (top right), cresol (middle left) and methylcyclohexane (middle right) and toluene determined by solving equation 3-11 in which the net rates of formation are given by equations 5-11 till 5-22 using the parameters from Table 5-3.

The *F* value for model adequacy is four magnitudes larger that the tabulated value at 95 % confidence interval with respectively 228 and 83 degrees of freedom, that equals 1.4, indicating an inadequate model. When one takes a look at the residual figures of the components in Figure 5-10 till Figure 5-12, one can see some trends in the outlet flow as a function of the inlet partial pressure of anisole. These trends could be the consequence of the bad estimation of the reactions orders of the partial pressures.

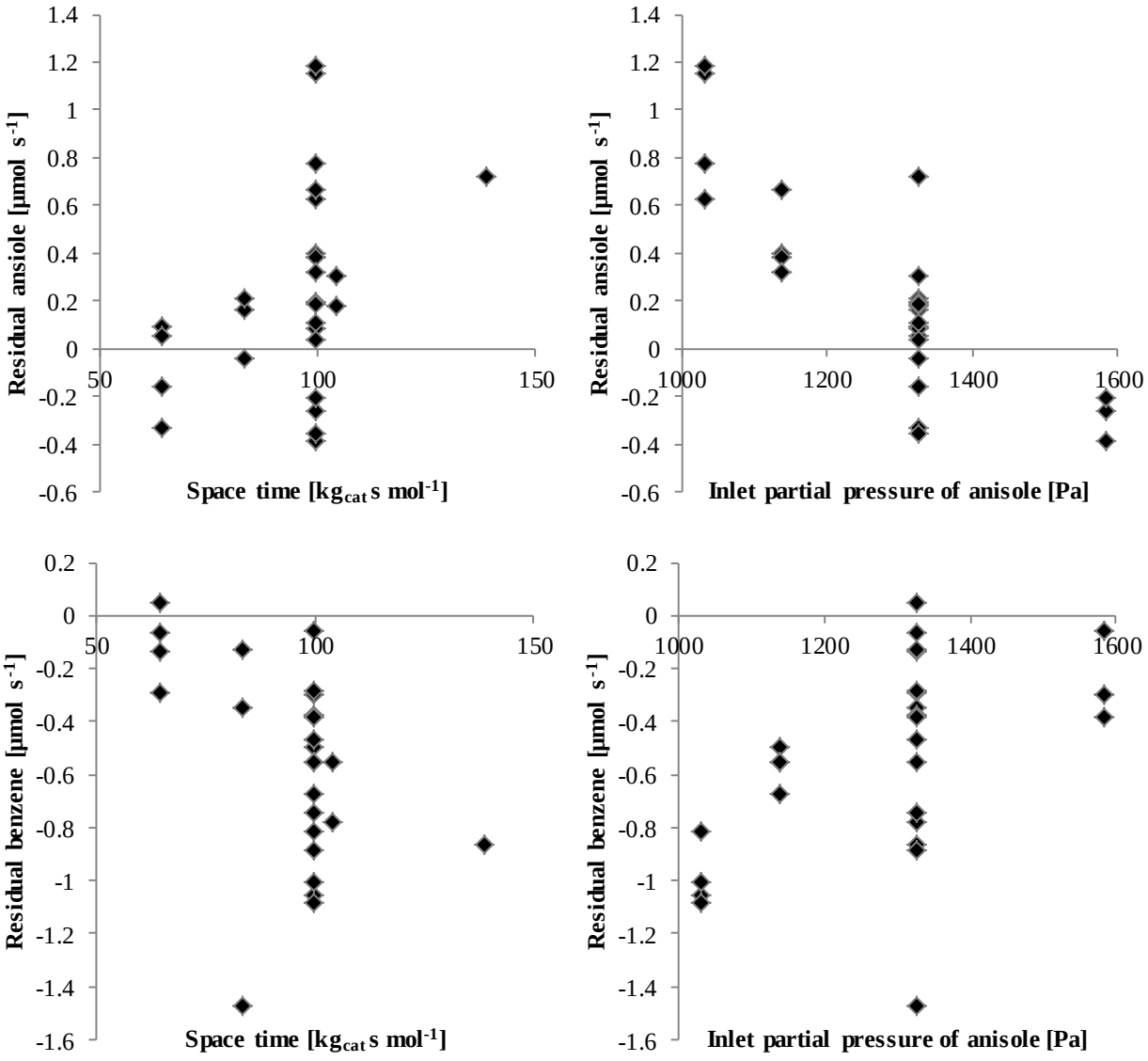

Figure 5-10. Residual figures of the outlet molar flow of anisole (top) and benzene (bottom) as a function of the space time (left) and inlet partial pressure of anisole (right) determined by solving equation 3-11 in which the net rates of formation are given by equations 5-11 till 5-22 using the parameters from Table 5-3.

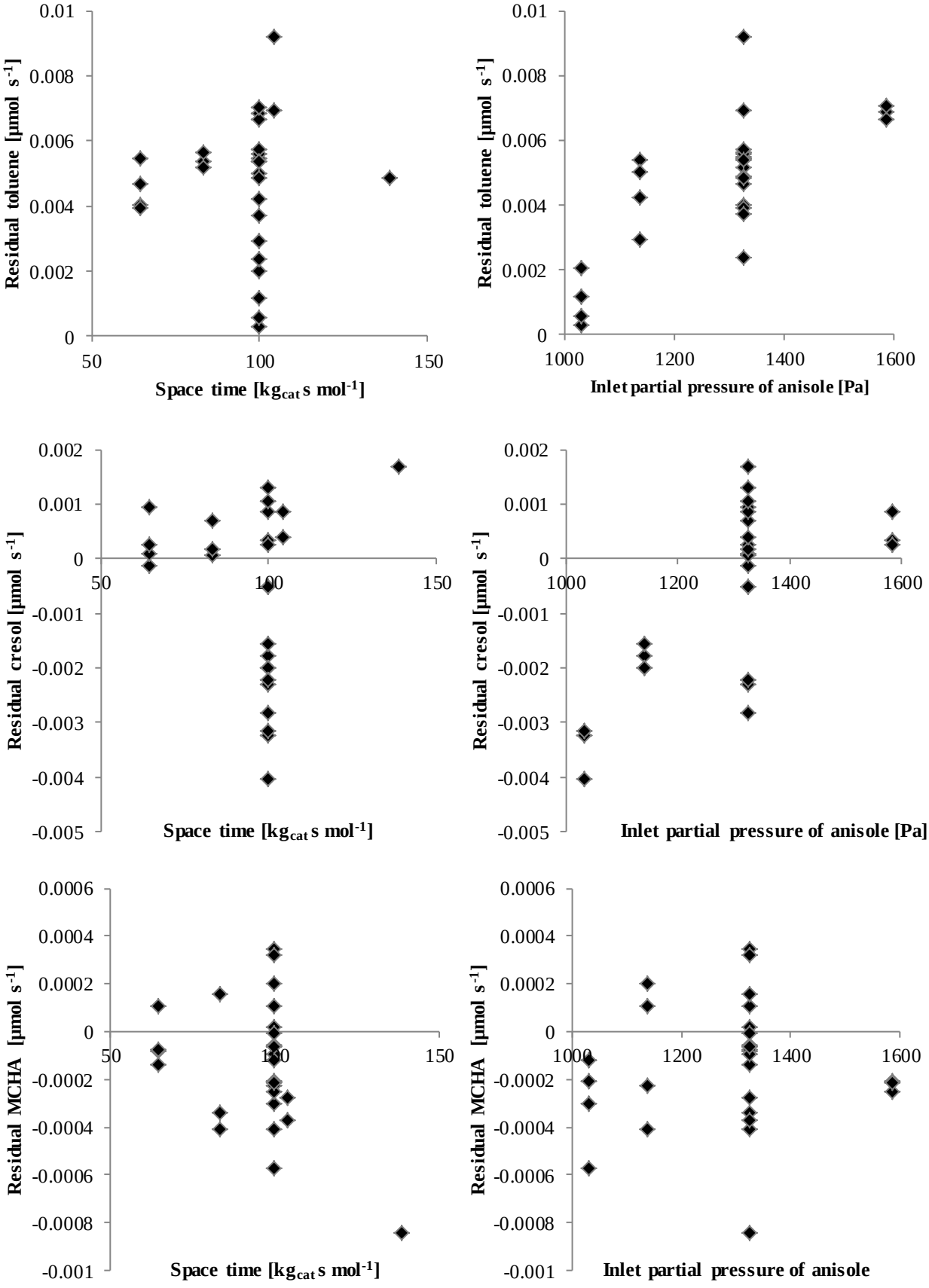

Figure 5-11. Residual figures of the outlet molar flow of toluene (top), cresol (middle) and methylcyclohexane (bottom) as a function of the space time (left) and inlet partial pressure of anisole (right) determined by solving equation 3-11 in which the net rates of formation are given by equations 5-11 till 5-22 using the parameters from Table 5-3.

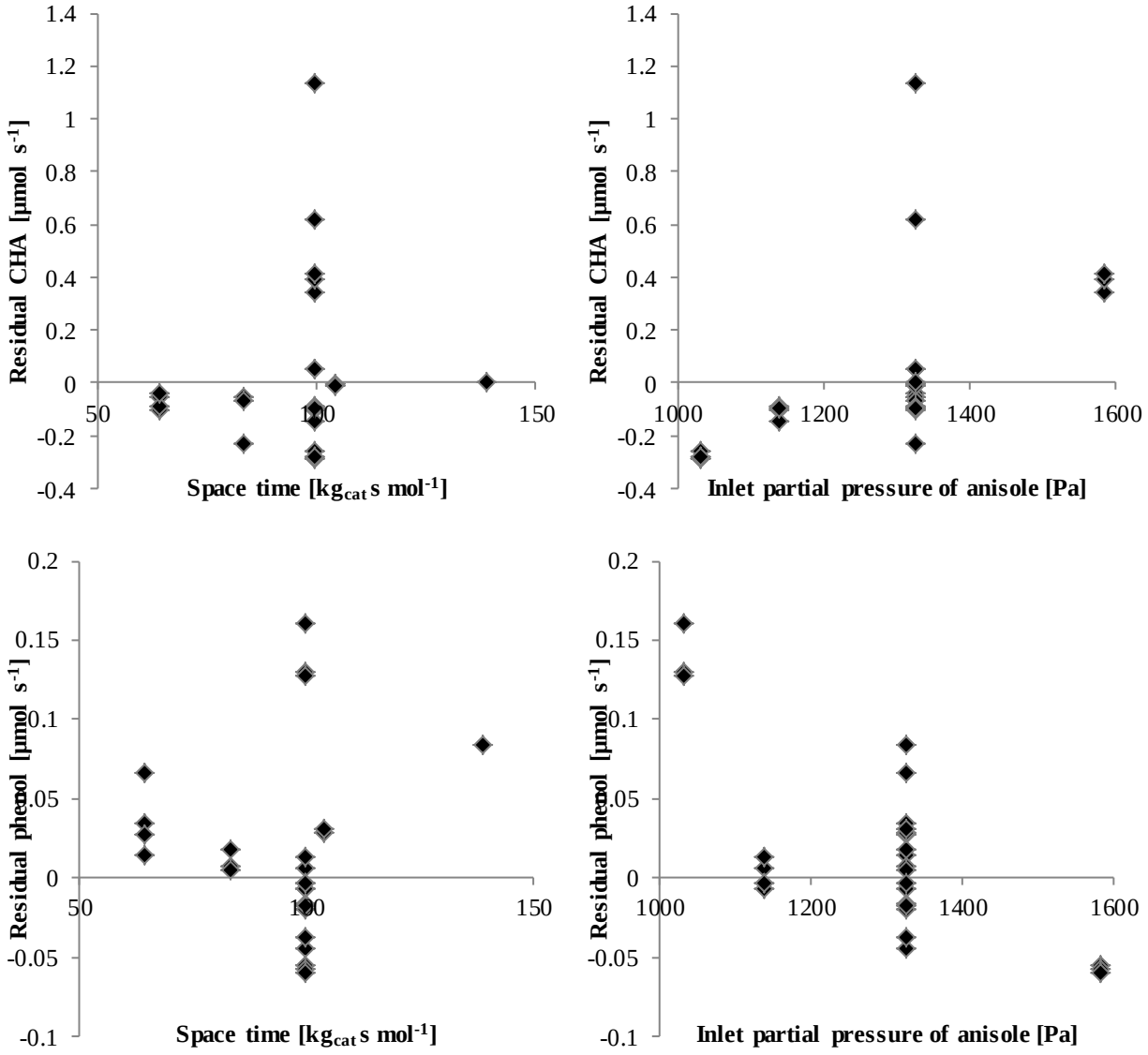

Figure 5-12. Residual figures of the outlet molar flow of cyclohexane (top) and phenol (bottom) as a function of the space time (left) and inlet partial pressure of anisole (right) determined by solving equation 3-11 in which the net rates of formation are given by equations 5-11 till 5-22 using the parameters from Table 5-3.

5.4.1.2Model performance

A simulations is performed with the obtained parameters from Table 5-3. Figure 5-13 till Figure 5-16 depict the performance of the model in the experimental range. As one can see, the model is able to predict the trend of each component, with the exception of xylene which is excluded from the figures. This indicates that the proposed model is correct, however, further optimization of the parameters is required.

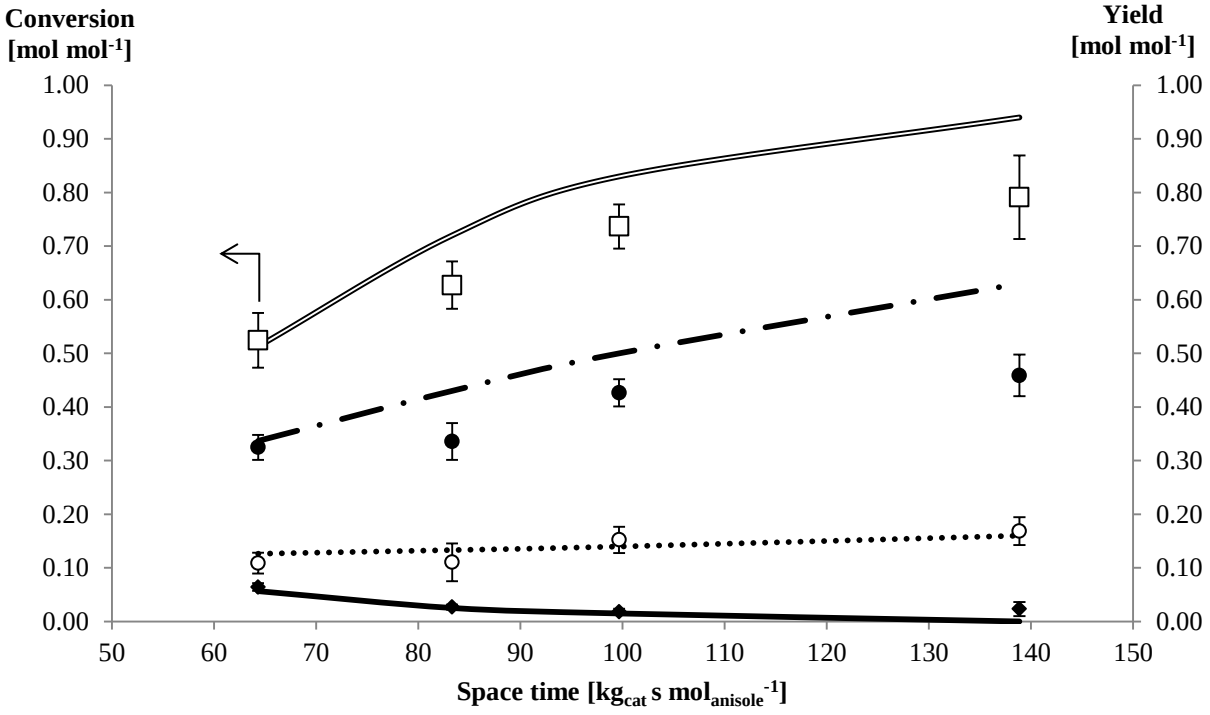

Figure 5-13. Influence of the space time on anisole conversion and product yields over a $NiCu/ZrO_2$ catalyst. Reaction conditions: temperature = 573 K, H_2/anisole = 125 mol_{H2} $mol_{anisole}^{-1}$, inlet partial pressure of anisole = 1325 Pa. Experimental: □ = anisole,● = benzene, ○ = cyclohexane, ♦ = phenol. Simulation: double line = anisole, dash-dotted line = benzene, dotted line = cyclohexane, full line = phenol.

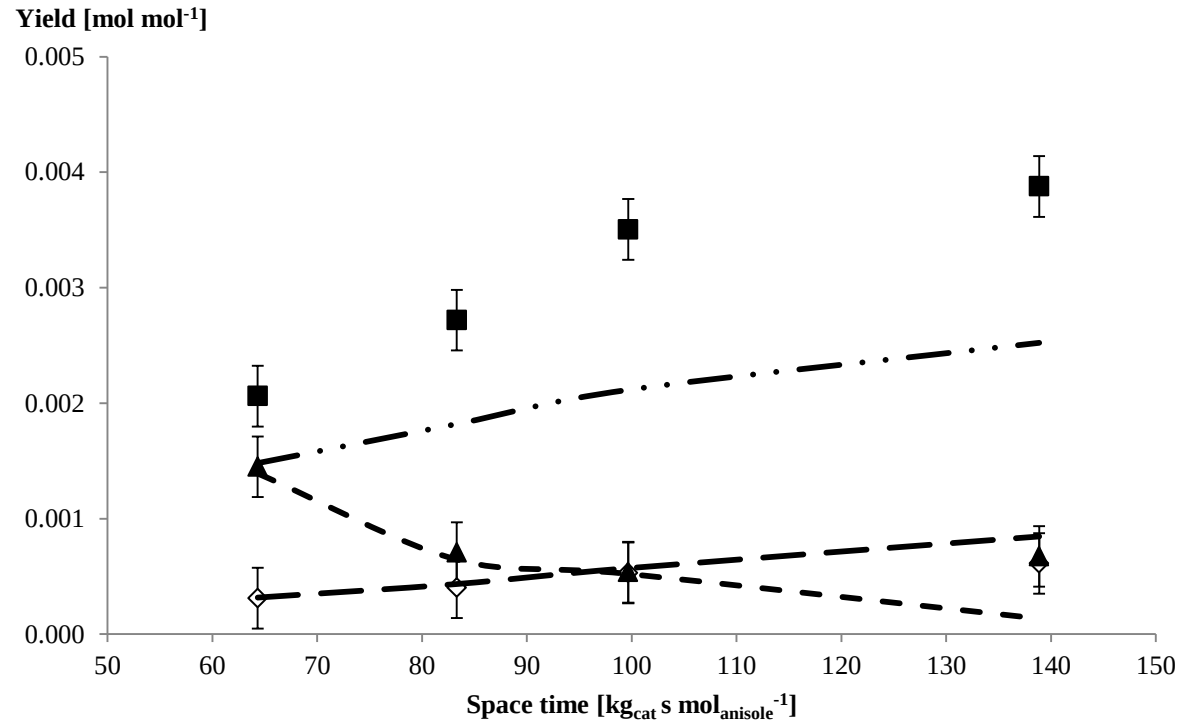

Figure 5-14. Influence of the space time on product yields over a $NiCu/ZrO_2$ catalyst. Reaction conditions: temperature = 573 K, H_2/anisole = 125 mol_{H2} $mol_{anisole}^{-1}$, inlet partial pressure of anisole = 1325 Pa. Experimental: ■ = toluene, ▲ = cresol, ◊ = methylcyclohexane. Simulation: dash-dot-dotted line = toluene, dashed line = cresol, long dashed line = methylcyclohexane.

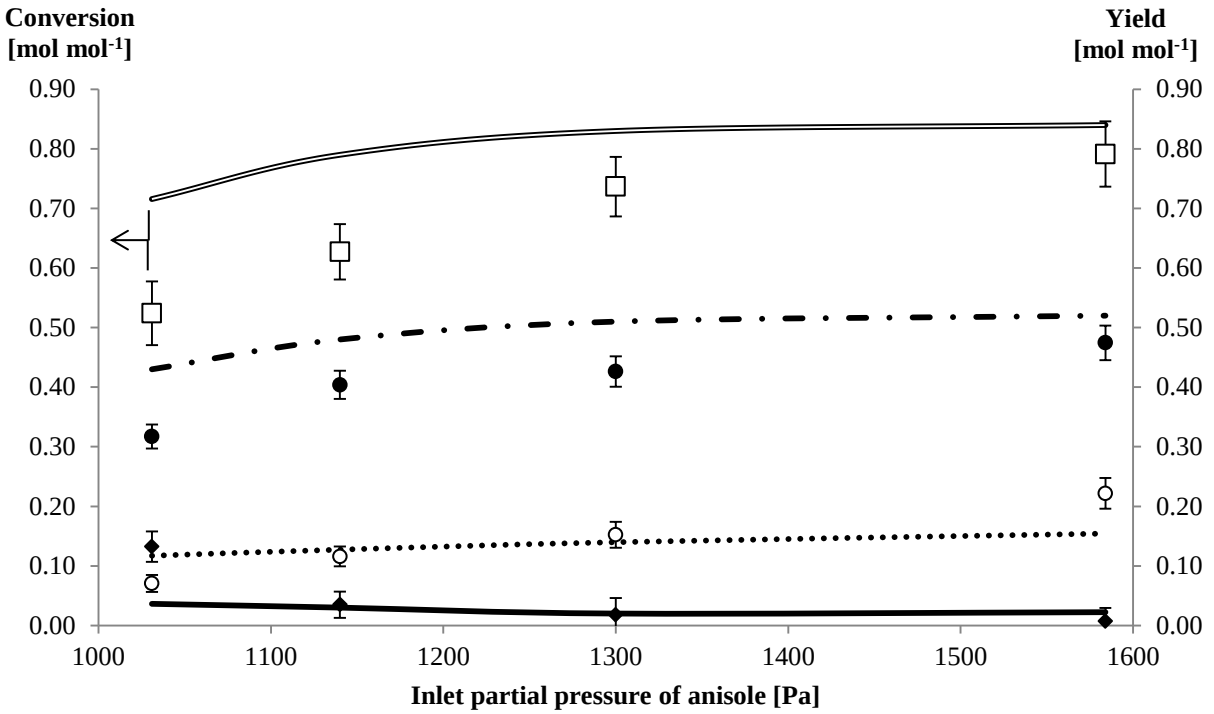

Figure 5-15. Influence of the inlet partial pressure of anisle on anisole conversion and product yields over a $NiCu/ZrO_2$ catalyst. Reaction conditions: temperature = 573 K, H_2/anisole = 125 mol_{H2} $mol_{anisole}^{-1}$, space time = 100 kg_{cat} s mol^{-1}. Experimental: □ = anisole,● = benzene, ○ = cyclohexane, ♦ = phenol. Simulation: double line = anisole, dash-dotted line = benzene, dotted line = cyclohexane, full line = phenol.

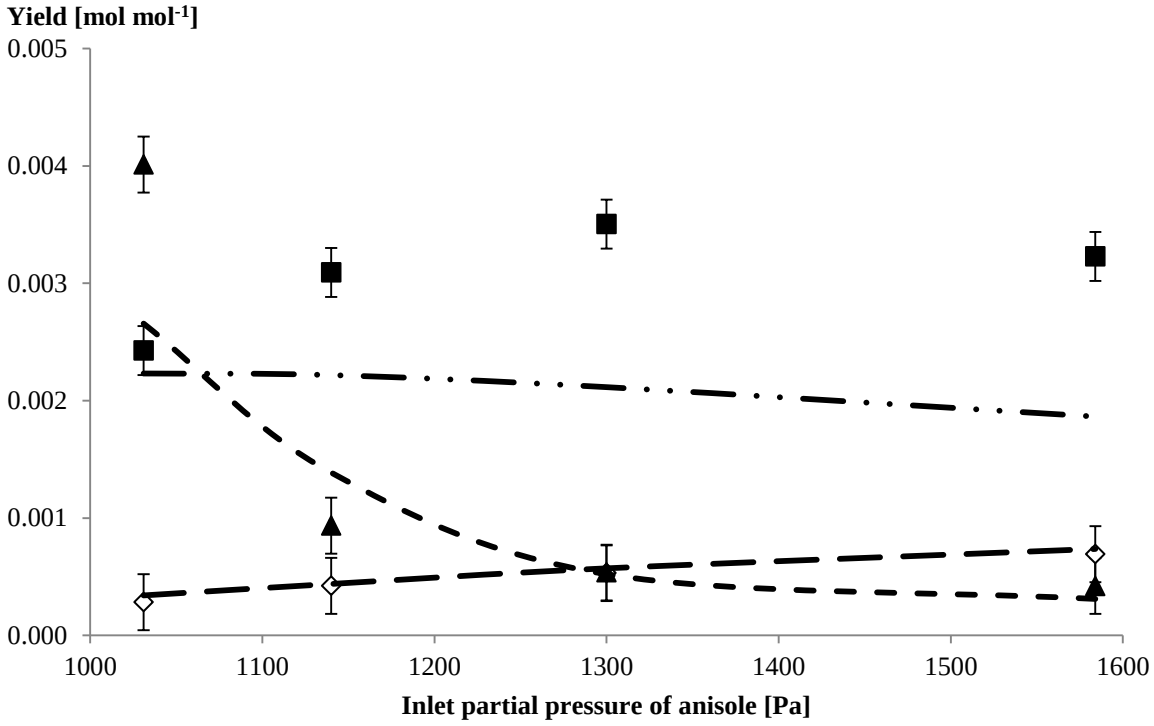

Figure 5-16. Influence of the inlet partial pressure of anisole on product yields over a $NiCu/ZrO_2$ catalyst. Reaction conditions: temperature = 573 K, H_2/anisole = 125 mol_{H2} $mol_{anisole}^{-1}$, space time = 100 kg_{cat} s mol^{-1}. Experimental: ■ = toluene, ▲ = cresol, ◊ = methylcyclohexane. Simulation: dash-dot-dotted line = toluene, dashed line = cresol, long dashed line = methylcyclohexane.

A better initial value of the rate coefficient and the reaction orders will be beneficial for the parameter estimation. Initial values for the rate coefficients and the reaction orders can be found by performing experiments in the so-called, differential regime. This is a regime where the conversion is directly proportional to the space time. Such a regime is obtained at low space time, this by lowering the amount of catalyst in the reactor or by increasing the flow rate of anisole. While increasing the flow rate of anisole, one should keep in mind that the anisole is not 100% soluble in *n*-hexane. Experimentally it is found that saturation is reached around 30 wt%. When the conversion and selectivities are plotted as a function of the space time or inlet partial pressures of anisole or hydrogen, the slope is an estimation of the reaction coefficient or the reaction orders. Further, the kinetic data set should be expended towards non-isothermal conditions, since the temperature has an large influence one the product distribution. An estimation of the pre-exponential factor and the activation energy is then obtained by means of an Arrhenius-plot.

5.4.2 Langmuir-Hinshelwood model for the HDO of anisole over a $NiCu/ZrO_2$ catalyst

The aim of this thesis is to derive an kinetic model for anisole HDO based on elementary reaction steps. As mentioned in section 4.4.2, Langmuir-Hinshelwood models are frequently used for the kinetic modeling of heterogeneous catalyzed processes. The overall reaction in heterogeneous catalysis consists of a sequence of consecutive steps (Figure 4-13), *i.e.* diffusion of the reactants through the bulk and the pores, the adsorption of the reactants on the active sites, the surface reaction, the desorption of the products from the active sites and the diffusion of the products through the pores and the bulk. In the intrinsic kinetic regime, the observed kinetics only depend on the chemical adsorption-desorption phenomena and the reaction.

The elementary reactions of a Langmuir-Hinshelwood model of the HDO of anisole, based on the proposed reaction mechanism in Figure 5-7, are given in Figure 5-17, Figure 5-18 and Figure 5-19. It is assumed that almost all cleavages are irreversible, with exception of reaction step 7 and reaction step 10. These steps are in equilibrium because the intermediates of both sides are necessary for the reaction network. Reaction step 13 is assumed to be the rate determining step, since the $C_{aromatic}$-OH bond has the highest bond dissociation energy (Table 2-3). Various experimental kinetic studies are found in literature for the hydrogenation of aromatics[3-6]. Based on physicochemical arguments, Thybaut *et al.*[5] suggested a model for toluene hydrogenation on Pt/ZSM-22 with equal rate coefficients for the first four hydrogen

addition steps and irreversible addition of the fifth and sixth hydrogen. In the Langmuir-Hinshelwood model, the same assumptions are made for the hydrogenation of benzene and toluene.

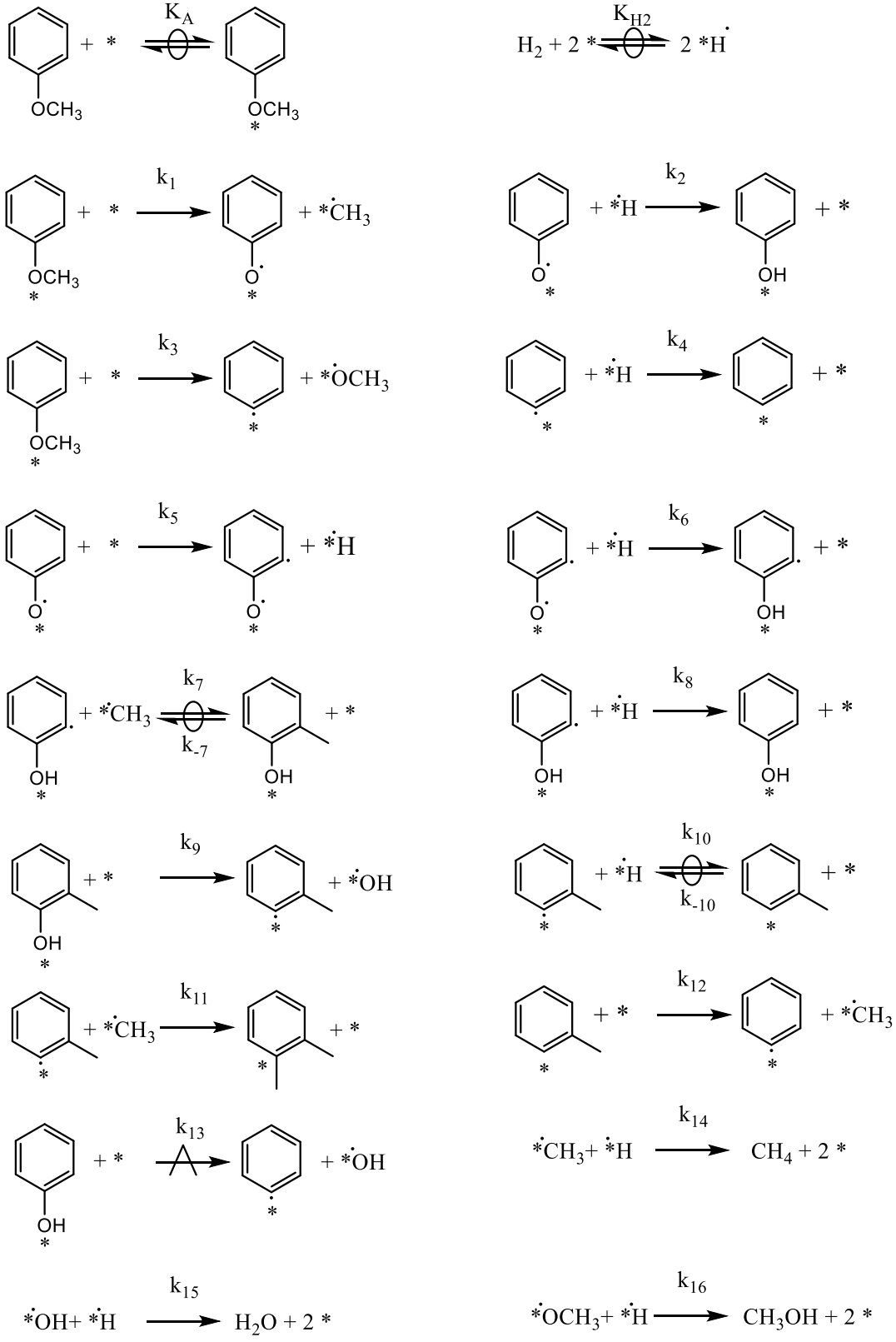

Figure 5-17. Proposed elementary reaction steps for anisole HDO over a $NiCu/ZrO_2$ catalyst.

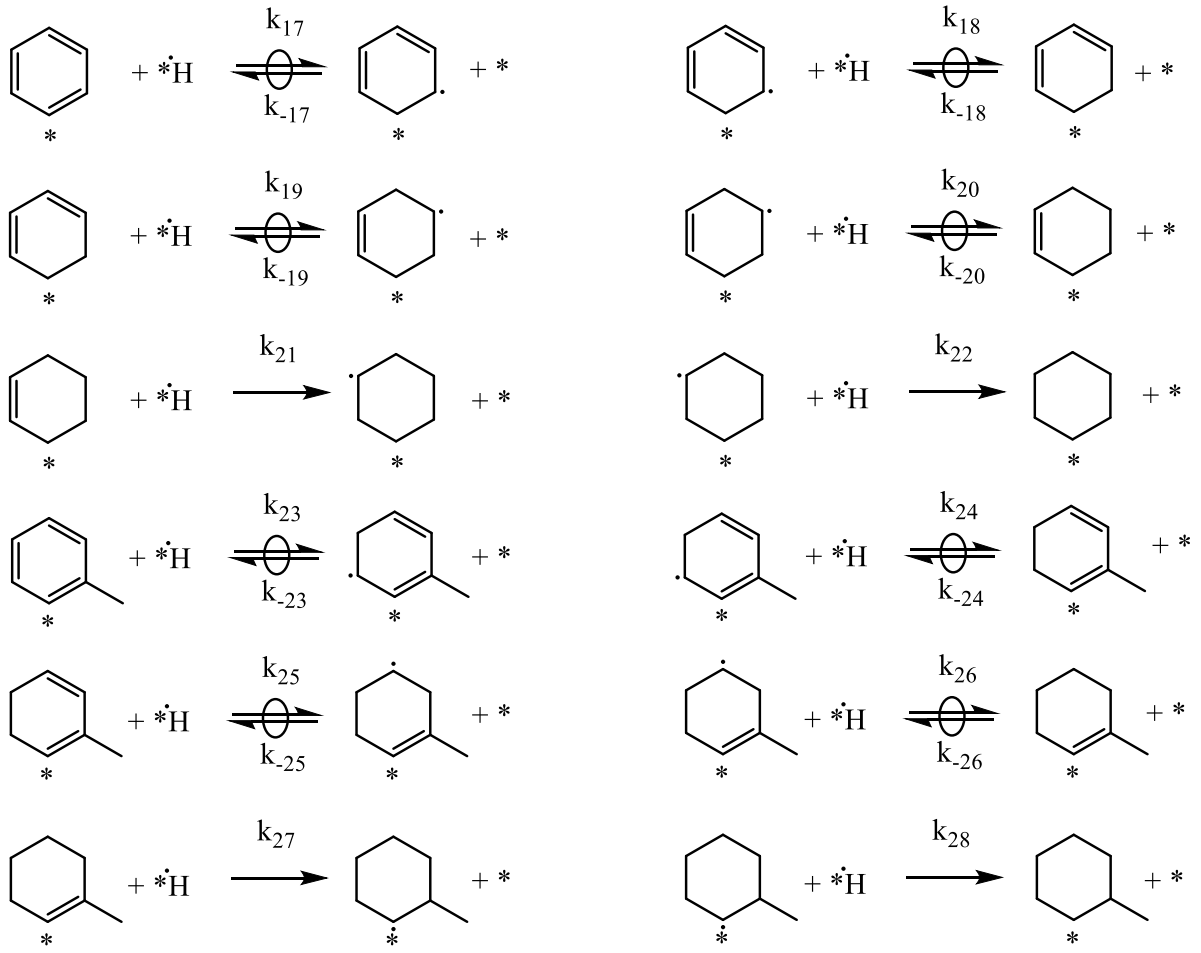

Figure 5-18. Proposed elementary reaction steps for hydrogenation of benzene and toluene over a NiCu/ZrO2 catalyst, based on the work of Saeys et al.[3, 7].

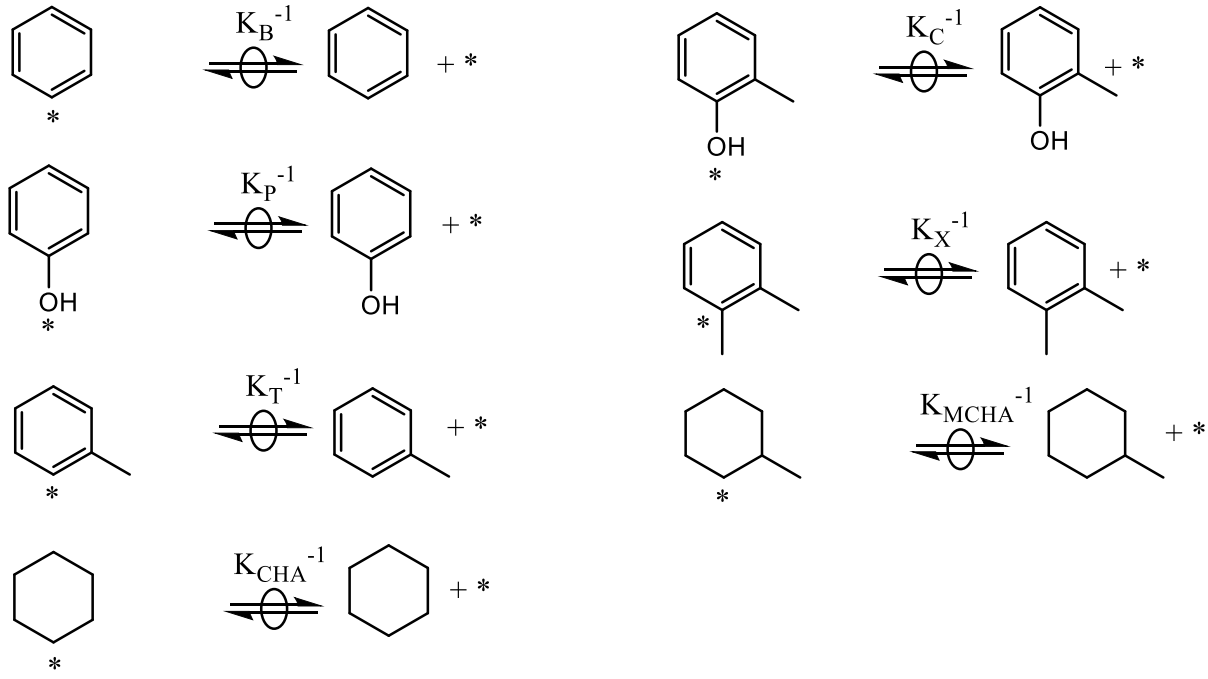

Figure 5-19. Proposed product desorption steps.

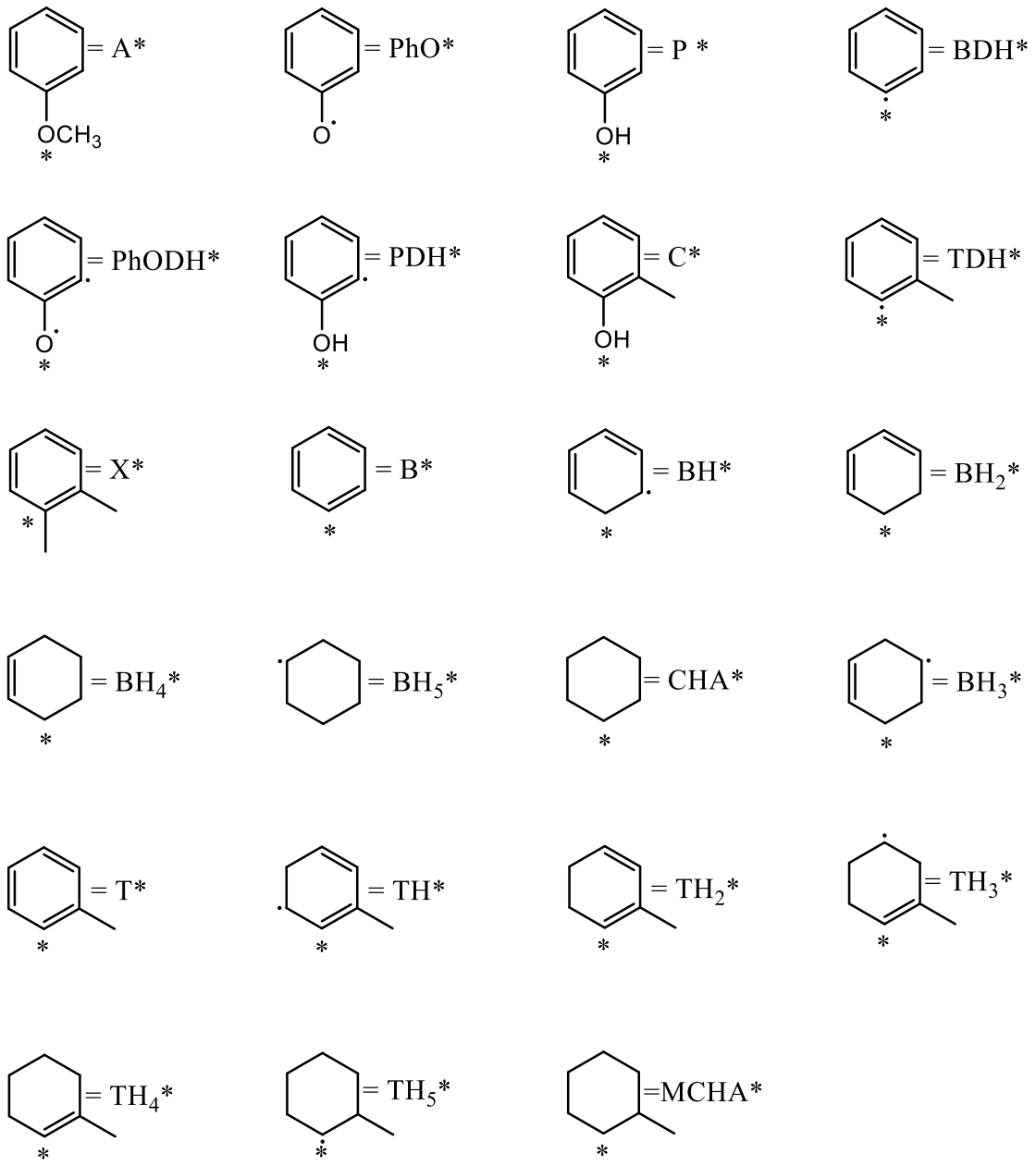

Figure 5-20. Overview of the different adsorbed species, based on the proposed elementary steps in anisole HDO over a $NiCu/ZrO_2$ catalyst.

In the approximation that the adsorption of the reactants and the desorption of the products are equilibrated, the equilibrium coefficients can be expressed in terms of the concentration of the adsorbed species and the gas phase partial pressure. For anisole, benzene, cresol, cyclohexane, methylcyclohexane, phenol, toluene and xylene equation 5-23 is valid, for hydrogen equation 5-24.

$$K_i = \frac{[i^*]}{p_i[*]} \qquad 5\text{-}23$$

$$K_{H_2} = \frac{[H^*]^2}{p_{H_2}[*]^2} \quad 5\text{-}24$$

In the proposed reaction mechanism, several surface reaction steps are in quasi-equilibrium. The equilibria coefficients are related to the concentration of the adsorbed species.

$$K_7 = \frac{[PhODH^*][CH_3^*]}{[C^*][*]} \quad 5\text{-}25$$

$$K_{10} = \frac{[PhODH^*][CH_3^*]}{[C^*][*]} \quad 5\text{-}26$$

$$K_{17} = \frac{[BH^*][*]}{[B^*][H^*]} \quad 5\text{-}27$$

$$K_{18} = \frac{[BH_2^*][*]}{[BH^*][H^*]} \quad 5\text{-}28$$

$$K_{19} = \frac{[BH_3^*][*]}{[BH_2^*][H^*]} \quad 5\text{-}29$$

$$K_{20} = \frac{[BH_4^*][*]}{[BH_3^*][H^*]} \quad 5\text{-}30$$

$$K_{23} = \frac{[TH^*][*]}{[T^*][H^*]} \quad 5\text{-}31$$

$$K_{24} = \frac{[TH_2^*][*]}{[TH^*][H^*]} \quad 5\text{-}32$$

$$K_{25} = \frac{[TH_3^*][*]}{[TH_2^*][H^*]} \quad 5\text{-}33$$

$$K_{26} = \frac{[TH_4^*][*]}{[TH_3^*][H^*]} \quad 5\text{-}34$$

The pseudo-steady-state approximation (PSSA) is applied for the intermediates in the reaction mechanism. The PSSA assumes that there is no change in concentrations in time for all intermediates. Applying the PSSA for the intermediate species OCH_3^*, PhO^*, $PhODH^*$, CH_3^*, OH^*, BDH^*, PDH^*, BH_5^*, TH_5^* and TDH^*, in combination with the chemisorption equilibria and the quasi-equilibria, it is possible to express the concentrations of the intermediates.

$$[OCH_3^*] = \frac{k_3 K_A p_A}{k_{16} K_{H_2}^{1/2} p_{H_2}^{1/2}}[*] \quad 5\text{-}35$$

$$[PhO^*] = \frac{k_1 K_A p_A}{k_2 K_{H_2}^{1/2} p_{H_2}^{1/2} + k_5} [*] \quad 5\text{-}36$$

$$[PhODH^*] = \frac{k_1 k_5 K_A p_A}{k_2 k_6 K_{H_2} p_{H_2} + k_5 k_6 K_{H_2}^{1/2} p_{H_2}^{1/2}} [*] \quad 5\text{-}37$$

$$[CH_3^*] = \frac{k_5 k_8 K_C K_{H_2}^{1/2} p_{H_2}^{1/2} p_C + k_2 k_8 K_{H_2} K_C p_C p_{H_2}}{k_1 k_5 K_7 K_A p_A} [*] \quad 5\text{-}38$$

$$[OH^*] = \frac{k_9 K_C p_C + k_{13} K_p p_P}{k_{15} K_{H_2}^{1/2} p_{H_2}^{1/2}} [*] \quad 5\text{-}39$$

$$[BDH^*] = \frac{k_3 K_A p_A + k_{12} K_T p_T + k_{13} K_p p_P}{k_4 K_{H_2}^{1/2} p_{H_2}^{1/2}} [*] \quad 5\text{-}40$$

$$[PDH^*] = \frac{k_1 k_5 K_A p_A}{k_2 k_8 K_{H_2} p_{H_2} + k_5 k_8 K_{H_2}^{1/2} p_{H_2}^{1/2}} [*] \quad 5\text{-}41$$

$$[BH_5^*] = \frac{k_{21} K_{17} K_{18} K_{19} K_{20} K_B K_{H_2}^2 p_B p_{H_2}^2}{k_{22}} [*] \quad 5\text{-}42$$

$$[TH_5^*] = \frac{k_{27} K_{23} K_{24} K_{25} K_{26} K_T K_{H_2}^2 p_T p_{H_2}^2}{k_{28}} [*] \quad 5\text{-}43$$

$$[TDH^*] = \frac{(k_1 k_5 k_9 K_7 K_A K_C p_A p_C + k_1 k_5 k_{-10} K_7 K_A K_T p_A p_T)[*]}{(k_1 k_5 k_{10} K_7 K_A K_{H_2}^{1/2} p_A p_{H_2}^{1/2} + k_2 k_8 k_{11} K_C K_{H_2} p_C p_{H_2} + k_5 k_8 k_{11} K_C K_{H_2}^{1/2} p_C p_{H_2}^{1/2})} \quad 5\text{-}44$$

A site balance is used to eliminate $[*]$ from the expressions.

$$\begin{aligned}[*]_{tot} = {} & [*] + [A^*] + [H^*] + [B^*] + [C^*] + [CHA^*] + [MCHA^*] + [P^*] \\ & + [T^*] + [X^*] + [OCH_3^*] + [OH^*] + [CH_3^*] + [PhO^*] \\ & + [PhODH^*] + [BDH^*] + [PDH^*] + [TDH^*] + [BH^*] \\ & + [BH_2^*] + [BH_3^*] + [BH_4^*] + [BH_5^*] + [TH^*] + [TH_2^*] \\ & + [TH_3^*] + [TH_4^*] + [TH_5^*]\end{aligned} \quad 5\text{-}45$$

The net rate of formation of all reactants and products in the reaction network, is obtained from the individual reactions by accounting for the stoichiometry.

$$R_A = -r_1 - r_3 \quad 5\text{-}46$$

$$R_B = r_4 + r_{17} - r_{-17} \quad 5\text{-}47$$

$$R_C = r_7 - r_{-7} - r_9 \quad 5\text{-}48$$

$$R_{CHA} = r_{22} \quad 5\text{-}49$$

$$R_{CH_4} = r_{14} \quad 5\text{-}50$$

$$R_{CH_3OH} = r_{16} \quad 5\text{-}51$$

$$R_{H_2} = \frac{1}{2}\left(r_5 + \sum_{i}^{10,17-28} r_{-i} - \sum_{i}^{2,4,6,8,10,14-28} r_i \right) \quad 5\text{-}52$$

$$R_{H_2O} = r_{15} \quad 5\text{-}53$$

$$R_{MCHA} = r_{28} \quad 5\text{-}54$$

$$R_P = r_2 + r_8 - r_{13} \quad 5\text{-}55$$

$$R_T = r_{10} - r_{-10} - r_{12} - r_{23} + r_{-23} \quad 5\text{-}56$$

$$R_X = r_{11} \quad 5\text{-}57$$

In this proposed model, 37 different parameters are involved. These are nine adsorption coefficients, ten surface reaction equilibrium coefficients and 18 forward rate coefficients. The extension towards non-isothermal coefficients would increase the number of parameters with a factor two. It is clear that for estimation of this number of parameters is not straight-forward. Good initial values should be found in literature or via isothermal regression. The estimation of the parameters was not possible with the acquired kinetic data set. Therefore, a more extensive experimental investigation should be performed in order to access all the kinetics of the system.

5.5 Conclusion

A second kinetic data set for HDO of anisole in an ideal plug flow reactor is obtained on a $NiCu/ZrO_2$ catalyst. The data set contains 35 isothermal experiments at 573 K with a space time between 66 kg_{cat} s $mol_{anisole}^{-1}$ and 140 kg_{cat} s $mol_{anisole}^{-1}$, an inlet partial pressure of anisole in the range of 1031 Pa and 1584 Pa and a molar hydrogen to anisole ratios of 90 mol_{H2} $mol_{anisole}^{-1}$ and 125 mol_{H2} $mol_{anisole}^{-1}$.

The conversion increases from 52 mol% for a space time of 66 kg_{cat} s $mol_{anisole}^{-1}$ to 89 mol% for a space time of 140 kg_{cat} s $mol_{anisole}^{-1}$. An analysis of the reactor effluent yielded that benzene and cyclohexane are the main products, with phenol as minor product. Traces of toluene, cresol, methylcyclohexane and xylene are found. An Delplot is used to identify the primary and secondary reaction products. Phenol and cresol are ranked as primary products,

toluene and cyclohexane as secondary, while methylcyclohexane as tertiary. The rank of benzene is not clear, and hence, it is proposed that benzene could be formed either a primary or a secondary product. Increasing anisole pressure enhanced the conversion from 58 mol% to 84 mol%. The increase concentration of the chemisorbed anisole has the same influence on the product yields as the increase in space time. By increasing the molar hydrogen to anisole ratio, a higher yield for the hydrogenation products cyclohexane and methylcyclohexane is observed.

A reaction network out of 10 reactions is proposed. Anisole can be converted via three pathways: the direct deoxygenation towards benzene, the demethylation with the production of phenol or a methyl transfer to the aromatic ring yielding cresol. The dehydroxylation of cresol and phenol yield respectively toluene and benzene. The former can react via three pathways, the demethylation towards benzene, the methylation with the formation of xylene or a full hydrogenation yielding methylcyclohexane. A second hydrogenation product, cyclohexane, is obtained by hydrogenate the aromatic ring of benzene.

An empirical power law is proposed to describe the reactions. The kinetic parameter estimation is performed by minimization of the residual sum of squares using a Levenberg-Marquardt algorithm. The regression is found to be significant since the *F* value exceeds the tabulated value. Nine out of 25 parameters are estimated significantly. The rate coefficients are estimated in the following order, $k_{demethylation} > k_{hydrogenation} > k_{dehydroxylation} > k_{demethoxylation} > k_{transalkylation} > k_{methylation}$. This is in line with the experimental findings. The performance of the model is tested by performing an simulation. The model is able to predict the trends of the components, however, there is still room for improvement. This could be achieved by first investigating the influence of the temperature and total pressure. One the other hand, the space time could be reduced, with kinetics in the differential regime as a consequence. In this regime, an initial value for the rate coefficients can be obtained from the slope of the influence of the space time and the partial pressure.

At last, a Langmuir-Hinshelwood model based on elementary steps is derived for the proposed reaction network. This model consists of nine near equilibrium adsorption and desorption steps, ten equilibrated surface reactions and 18 forward reactions, resulting in 37 different parameters under isothermal conditions. The extension towards non-isothermal conditions would increase the number of parameters with factor two. With the obtained data set, it was not possible to perform the regression for this model.

5.6 References

1. Bhore, N. A.; Klein, M. T.; Bischoff, K. B., The delplot technique: a new method for reaction pathway analysis. *Industrial & Engineering Chemistry Research* **1990,** 29, (2), 313-316.
2. Yakovlev, V. A.; Khromova, S. A.; Sherstyuk, O. V.; Dundich, V. O.; Ermakov, D. Y.; Novopashina, V. M.; Lebedev, M. Y.; Bulavchenko, O.; Parmon, V. N., Development of new catalytic systems for upgraded bio-fuels production from bio-crude-oil and biodiesel. *Catalysis Today* **2009,** 144, (3–4), 362-366.
3. Saeys, M.; Reyniers, M.-F.; Thybaut, J. W.; Neurock, M.; Marin, G. B., First-principles based kinetic model for the hydrogenation of toluene. *Journal of Catalysis* **2005,** 236, (1), 129-138.
4. Thybaut, J. W. *Kinetic Modeling and Simulation*; Ghent University: 2013.
5. Thybaut, J. W.; Saeys, M.; Marin, G. B., Hydrogenation kinetics of toluene on Pt/ZSM-22. *Chemical Engineering Journal* **2002,** 90, (1–2), 117-129.
6. Castaño, P.; Arandes, J. M.; Pawelec, B.; Fierro, J. L. G.; Gutiérrez, A.; Bilbao, J., Kinetic Model Discrimination for Toluene Hydrogenation over Noble-Metal-Supported Catalysts. *Industrial & Engineering Chemistry Research* **2007,** 46, (23), 7417-7425.
7. Saeys, M.; Reyniers, M.-F.; Neurock, M.; Marin, G., Ab initio reaction path analysis of benzene hydrogenation to cyclohexane on Pt (111). *The Journal of Physical Chemistry B* **2005,** 109, (6), 2064-2073.

Chapter 6

Conclusions and Future Work

6.1 Conclusions

In recent years, due to the depletion of fossil fuels and environmental concerns, exploring green and renewable routes with commercial viability for the increased demand of energy and chemicals has become one of the most urgent challenges. In this light, valorization of biomass looks as an attractive alternative route for fuels production. Several techniques were proposed for lignocellulosic biomass valorization, among others, fast pyrolysis, aimed at making transportation fuels and chemicals. To use the pyrolysis oil as a transportation fuel, a catalytic upgrading is necessary due to the high oxygen content, poor chemical stability, and immiscibility with transportation fuels. This process is called hydrodeoxygenation.

The work of this master thesis is performed within the framework of FASTCARD, *i.e.* an European project focusing on the faster industrial implementation of catalytic conversion of biomass to biofuels. This master thesis aims on the experimental investigation of the intrinsic reaction kinetics and the construction of a kinetic model for fast pyrolysis oil hydrodeoxygenation using a lignin-derived model compound, *i.e.* anisole.

The experimental investigation is performed on the high throughput kinetic setup at the Laboratory for Chemical Technology at the University of Ghent. The hydrodeoxygenation of anisole is investigated in an ideal plug flow reactor at gas phase conditions. The experiments are performed in the intrinsic kinetic regime, *i.e.* a regime without external and internal heat transfer and mass transport limitations. The feed consist of anisole and hydrogen as reactants, *n*-hexane as solvent and N_2 as diluent. A kinetic data set of 18 experiments has been acquired on a non-sulfided 15wt.%Co-3.8wt.%Mo/γ-Al_2O_3 catalyst, one of 35 experiments has obtained on a NiCu/ZrO_2 catalyst. In the first data set ethane is used as internal standard, in the second, *n*-octane, to confirm that the mass and elemental balance closed within 5 %. The catalysts show different behavior at the same operating conditions. The major products on the CoMo/γ-Al_2O_3 were phenol and cresol. The catalyst has a small extent for hydrodeoxygenation, resulting in minor production of benzene and toluene. A higher hydrodeoxygenation activity is observed on the NiCu/ZrO_2 catalyst, with benzene as main product. Additionally, a subsequent hydrogenation of the aromatic ring is observed, with the formation of cyclohexane. Other products as phenol, cresol, toluene, methylcyclohexane and xylene are observed in a small amount.

Based on the Delplot technique, an identification of the primary, secondary and tertiary products is achieved. The identification suggests that phenol and cresol are primary products,

toluene a secondary product. Benzene could be either a primary or a secondary product. The additional observed products on the $NiCu/ZrO_2$ catalyst, cyclohexane and methylcyclohexane are identified as tertiary products. The combination of this ranking with the literature resulted in the following reaction network. The conversion of anisole occurs via one of three pathways: the transalkylation towards cresol, the demethylation yielding phenol or the direct deoxygenation with the formation of benzene. Cresol can be subjected to two reactions, the cleavage between the aromatic and the aliphatic carbon yielding phenol or the cleavage between the aromatic carbon and the oxygen with the formation of toluene. Benzene can also be formed via the hydrodeoxygenation of phenol or the demethylation of toluene. Three additional reaction steps are suggested for the $NiCu/ZrO_2$ catalyst, the full hydrogenation of the aromatic ring in toluene and benzene yielding respectively methylcyclohexane and cyclohexane. And a methylation of the aromatic ring yield in xylene.

A preliminary power law model is proposed to describe the overall reaction kinetics, whereas the Langmuir-Hinshelwood model is used to describe the interaction with the catalyst surface. From a non-isothermal regression to the experimental data obtained on the $CoMo/\gamma\text{-}Al_2O_3$ catalyst it was possible to estimate the model parameters, *i.e.* activation energies, composed pre-exponential rate coefficients and adsorption coefficients in case of the Langmuir-Hinshelwood model. The activation energies were estimated significantly and physically relevant for both the power law and the Langmuir-Hinshelwood model on the $CoMo/\gamma\text{-}Al_2O_3$ catalyst. The order of the activation energies is found to be $E_{a,hydrodeoxygenation} > E_{a,transalkylation} > E_{a,demethylation}$, which is in line with the experimental findings. The parameters of an empirical power law for the description of the kinetics on the $NiCu/ZrO_2$ catalyst are estimated via an isothermal regression. The reaction coefficients can be ranked in the following order: $k_{demethylation} > k_{hydrogenation} > k_{dehydroxylation} > k_{demethoxylation} > k_{transalkylation} > k_{methylation}$. The regression was rather difficult to perform due to the large number of parameters in combination with a limited number of experiments.

The simulations with the estimated parameters indicate an acceptable performance of the proposed models. The models are able to predict the experimental trends. Nevertheless, there is still room for improvement. How this could be done is discussed in the following section.

6.2 Future work

The following suggestions can be made for the continuation and improvement of this work. First, the experimental investigation should be continued to get more insight into the reaction mechanism. The data set on the $NiCu/ZrO_2$ catalyst should be extended by investigating the influence of the temperature. Further, the influence of the space time at different temperatures as well as the influence of the pressure should be explored. It is worth mentioning that from the investigation in the so-called differential regime, *i.e.* a regime where the conversion is directly proportional to the space time, an initial value of the rate coefficients and the reactions orders can be obtained.

Improvements concerning the modeling part are the extension of the elementary step-based kinetic model which includes catalyst descriptors, such as adsorption entropies, adsorption enthalpies and active sites concentration.

Appendix A
Experimental dataset

A.1. Reaction conditions for anisole HDO catalyzed by CoMo/γ-Al_2O_3

Table A-1. Experimental conditions for anisole HDO on CoMo/γ-Al_2O_3.

	T [K]	P [Pa]	W [g]	$F_{anisole}$ [mol s^{-1}]	F_{hexane} [mol s^{-1}]	F_{ethane} [mol s^{-1}]	F_{N2} [mol s^{-1}]	F_{H2} [mol s^{-1}]
1	548	506625	2.00	$9.35\ 10^{-7}$	$9.49\ 10^{-6}$	$3.10\ 10^{-6}$	$2.48\ 10^{-3}$	$6.21\ 10^{-4}$
2	548	506625	2.00	$9.35\ 10^{-7}$	$9.49\ 10^{-6}$	$3.10\ 10^{-6}$	$2.48\ 10^{-3}$	$6.21\ 10^{-4}$
3	548	506625	2.00	$1.71\ 10^{-6}$	$1.74\ 10^{-5}$	$3.10\ 10^{-6}$	$2.48\ 10^{-3}$	$6.21\ 10^{-4}$
4	548	506625	2.00	$1.71\ 10^{-6}$	$1.74\ 10^{-5}$	$3.10\ 10^{-6}$	$2.48\ 10^{-3}$	$6.21\ 10^{-4}$
5	548	506625	2.00	$2.77\ 10^{-6}$	$2.82\ 10^{-5}$	$3.10\ 10^{-6}$	$2.48\ 10^{-3}$	$9.93\ 10^{-4}$
6	548	506625	2.00	$2.77\ 10^{-6}$	$2.82\ 10^{-5}$	$3.10\ 10^{-6}$	$2.48\ 10^{-3}$	$9.93\ 10^{-4}$
7	573	506625	2.00	$9.35\ 10^{-7}$	$9.49\ 10^{-6}$	$3.10\ 10^{-6}$	$2.48\ 10^{-3}$	$6.21\ 10^{-4}$
8	573	506625	2.00	$9.35\ 10^{-7}$	$9.49\ 10^{-6}$	$3.10\ 10^{-6}$	$2.48\ 10^{-3}$	$6.21\ 10^{-4}$
9	573	506625	2.00	$1.56\ 10^{-6}$	$1.58\ 10^{-5}$	$3.10\ 10^{-6}$	$2.48\ 10^{-3}$	$6.20\ 10^{-4}$
10	573	506625	2.00	$1.56\ 10^{-6}$	$1.58\ 10^{-5}$	$3.10\ 10^{-6}$	$2.48\ 10^{-3}$	$6.20\ 10^{-4}$
11	573	506625	2.00	$2.77\ 10^{-6}$	$2.82\ 10^{-5}$	$3.10\ 10^{-6}$	$2.48\ 10^{-3}$	$9.93\ 10^{-4}$
12	573	506625	2.00	$2.77\ 10^{-6}$	$2.82\ 10^{-5}$	$3.10\ 10^{-6}$	$2.48\ 10^{-3}$	$9.93\ 10^{-4}$
13	603	506625	2.00	$9.35\ 10^{-7}$	$9.49\ 10^{-6}$	$3.10\ 10^{-6}$	$2.48\ 10^{-3}$	$6.21\ 10^{-4}$
14	603	506625	2.00	$9.35\ 10^{-7}$	$9.49\ 10^{-6}$	$3.10\ 10^{-6}$	$2.48\ 10^{-3}$	$6.21\ 10^{-4}$
15	603	506625	2.00	$1.71\ 10^{-6}$	$1.74\ 10^{-5}$	$3.10\ 10^{-6}$	$2.48\ 10^{-3}$	$6.21\ 10^{-4}$
16	623	506625	2.00	$1.71\ 10^{-6}$	$1.74\ 10^{-5}$	$3.10\ 10^{-6}$	$2.48\ 10^{-3}$	$6.21\ 10^{-4}$
17	623	506625	2.00	$2.77\ 10^{-6}$	$2.82\ 10^{-5}$	$3.10\ 10^{-6}$	$2.48\ 10^{-3}$	$6.21\ 10^{-4}$
18	623	506625	2.00	$2.77\ 10^{-6}$	$2.82\ 10^{-5}$	$3.10\ 10^{-6}$	$2.48\ 10^{-3}$	$6.21\ 10^{-4}$

Table A-2. Experimental results for anisole HDO on CoMo/γ-Al_2O_3.

	$F_{anisole}$ [mol s^{-1}]	F_{phenol} [mol s^{-1}]	F_{cresol} [mol s^{-1}]	$F_{benzene}$ [mol s^{-1}]	$F_{toluene}$ [mol s-^{1}]
1	$8.63\ 10^{-7}$	$5.30\ 10^{-7}$	$4.76\ 10^{-7}$	$3.29\ 10^{-9}$	$3.30\ 10^{-9}$
2	$8.97\ 10^{-7}$	$5.03\ 10^{-7}$	$5.84\ 10^{-7}$	$3.29\ 10^{-9}$	$3.47\ 10^{-9}$
3	$2.59\ 10^{-7}$	$4.38\ 10^{-7}$	$2.86\ 10^{-7}$	$5.79\ 10^{-9}$	$3.90\ 10^{-9}$
4	$3.24\ 10^{-7}$	$4.23\ 10^{-7}$	$2.36\ 10^{-7}$	$5.24\ 10^{-9}$	$3.87\ 10^{-9}$
5	$1.34\ 10^{-6}$	$9.48\ 10^{-7}$	$5.98\ 10^{-7}$	$9.01\ 10^{-9}$	$7.00\ 10^{-9}$
6	$1.50\ 10^{-6}$	$8.66\ 10^{-7}$	$5.10\ 10^{-7}$	$1.28\ 10^{-8}$	$5.05\ 10^{-9}$
7	$1.53\ 10^{-7}$	$4.57\ 10^{-7}$	$3.63\ 10^{-7}$	$2.09\ 10^{-8}$	$8.29\ 10^{-9}$
8	$1.68\ 10^{-7}$	$4.56\ 10^{-7}$	$3.53\ 10^{-7}$	$1.75\ 10^{-8}$	$6.45\ 10^{-9}$
9	$4.96\ 10^{-7}$	$6.82\ 10^{-7}$	$4.53\ 10^{-7}$	$1.70\ 10^{-8}$	$6.10\ 10^{-9}$
10	$5.01\ 10^{-7}$	$6.86\ 10^{-7}$	$4.46\ 10^{-7}$	$1.60\ 10^{-8}$	$5.85\ 10^{-9}$
11	$1.29\ 10^{-6}$	$9.26\ 10^{-7}$	$6.53\ 10^{-7}$	$3.11\ 10^{-8}$	$6.43\ 10^{-9}$
12	$1.31\ 10^{-6}$	$9.32\ 10^{-7}$	$6.37\ 10^{-7}$	$2.21\ 10^{-8}$	$5.38\ 10^{-9}$
13	$7.12\ 10^{-8}$	$4.77\ 10^{-7}$	$4.00\ 10^{-7}$	$3.00\ 10^{-8}$	$1.00\ 10^{-8}$
14	$5.98\ 10^{-8}$	$4.50\ 10^{-7}$	$4.46\ 10^{-7}$	$3.30\ 10^{-8}$	$1.10\ 10^{-8}$
15	$1.52\ 10^{-7}$	$8.93\ 10^{-7}$	$7.52\ 10^{-7}$	$3.40\ 10^{-8}$	$1.29\ 10^{-8}$
16	$5.05\ 10^{-7}$	$7.84\ 10^{-7}$	$8.90\ 10^{-7}$	$6.67\ 10^{-8}$	$4.04\ 10^{-8}$
17	$1.42\ 10^{-7}$	$1.37\ 10^{-6}$	$1.27\ 10^{-6}$	$9.00\ 10^{-8}$	$6.01\ 10^{-8}$
18	$1.51\ 10^{-7}$	$1.38\ 10^{-6}$	$1.25\ 10^{-6}$	$8.69\ 10^{-8}$	$5.83\ 10^{-8}$

A.2. Reaction conditions for anisole HDO catalyzed by $NiCu/ZrO_2$

Table A-3. Experimental conditions for anisole HDO on $NiCu/ZrO_2$.

	T [K]	P [Pa]	W [g]	$F_{anisole}$ [mol s^{-1}]	F_{hexane} [mol s^{-1}]	F_{octane} [mol s^{-1}]	F_{N2} [mol s^{-1}]	F_{H2} [mol s^{-1}]
1	573	506625	0.50	$7.77\ 10^{-6}$	$4.20\ 10^{-5}$	$1.16\ 10^{-6}$	$1.86\ 10^{-3}$	$9.29\ 10^{-4}$
2	573	506625	0.50	$7.77\ 10^{-6}$	$4.20\ 10^{-5}$	$1.16\ 10^{-6}$	$1.86\ 10^{-3}$	$9.29\ 10^{-4}$
3	573	506625	0.50	$7.77\ 10^{-6}$	$4.20\ 10^{-5}$	$1.16\ 10^{-6}$	$1.86\ 10^{-3}$	$9.29\ 10^{-4}$
4	573	506625	0.50	$7.77\ 10^{-6}$	$4.20\ 10^{-5}$	$1.16\ 10^{-6}$	$1.86\ 10^{-3}$	$9.29\ 10^{-4}$
5	573	506625	0.50	$6.00\ 10^{-6}$	$3.57\ 10^{-5}$	$9.49\ 10^{-7}$	$1.55\ 10^{-3}$	$7.75\ 10^{-4}$
6	573	506625	0.50	$6.00\ 10^{-6}$	$3.57\ 10^{-5}$	$9.49\ 10^{-7}$	$1.55\ 10^{-3}$	$7.75\ 10^{-4}$
7	573	506625	0.50	$6.00\ 10^{-6}$	$3.57\ 10^{-5}$	$9.49\ 10^{-7}$	$1.55\ 10^{-3}$	$7.75\ 10^{-4}$
8	573	506625	0.50	$4.80\ 10^{-6}$	$2.85\ 10^{-5}$	$7.59\ 10^{-7}$	$1.24\ 10^{-3}$	$6.20\ 10^{-4}$
9	573	506625	0.50	$4.80\ 10^{-6}$	$2.85\ 10^{-5}$	$7.59\ 10^{-7}$	$1.24\ 10^{-3}$	$6.20\ 10^{-4}$
10	573	506625	0.50	$5.02\ 10^{-6}$	$2.82\ 10^{-5}$	$7.82\ 10^{-7}$	$1.24\ 10^{-3}$	$6.20\ 10^{-4}$
11	573	506625	0.50	$5.02\ 10^{-6}$	$2.82\ 10^{-5}$	$7.82\ 10^{-7}$	$1.24\ 10^{-3}$	$6.20\ 10^{-4}$
12	573	506625	0.50	$3.60\ 10^{-6}$	$2.14\ 10^{-5}$	$5.69\ 10^{-7}$	9.29 10-4	$4.65\ 10^{-4}$
13	573	506625	0.50	$5.18\ 10^{-6}$	$2.80\ 10^{-5}$	$7.74\ 10^{-7}$	$1.86\ 10^{-3}$	$6.20\ 10^{-4}$
14	573	506625	0.50	$5.18\ 10^{-6}$	$2.80\ 10^{-5}$	$7.74\ 10^{-7}$	$1.86\ 10^{-3}$	$6.20\ 10^{-4}$
15	573	506625	0.50	$5.18\ 10^{-6}$	$2.80\ 10^{-5}$	$7.74\ 10^{-7}$	$1.86\ 10^{-3}$	$6.20\ 10^{-4}$
16	573	506625	0.50	$5.02\ 10^{-6}$	$2.82\ 10^{-5}$	$7.82\ 10^{-7}$	$1.55\ 10^{-3}$	$6.20\ 10^{-4}$
17	573	506625	0.50	$5.02\ 10^{-6}$	$2.82\ 10^{-5}$	$7.82\ 10^{-7}$	$1.55\ 10^{-3}$	$6.20\ 10^{-4}$
18	573	506625	0.50	$5.02\ 10^{-6}$	$2.82\ 10^{-5}$	$7.82\ 10^{-7}$	$1.55\ 10^{-3}$	$6.20\ 10^{-4}$
19	573	506625	0.50	$5.02\ 10^{-6}$	$2.82\ 10^{-5}$	$1.16\ 10^{-6}$	$1.86\ 10^{-3}$	$9.29\ 10^{-4}$

Table A-4. Experimental conditions for anisole HDO on $NiCu/ZrO_2$ (continued).

	T [K]	P [Pa]	W [g]	$F_{anisole}$ [mol s^{-1}]	F_{hexane} [mol s^{-1}]	F_{octane} [mol s^{-1}]	F_{N2} [mol s^{-1}]	F_{H2} [mol s^{-1}]
20	573	506625	0.50	$5.02\ 10^{-6}$	$2.82\ 10^{-5}$	$7.82\ 10^{-7}$	$1.55\ 10^{-3}$	$6.20\ 10^{-4}$
21	573	506625	0.50	$5.02\ 10^{-6}$	$2.82\ 10^{-5}$	$7.82\ 10^{-7}$	$9.29\ 10^{-4}$	$6.20\ 10^{-4}$
22	573	506625	0.50	$5.02\ 10^{-6}$	$2.82\ 10^{-5}$	$7.82\ 10^{-7}$	$9.29\ 10^{-4}$	$6.20\ 10^{-4}$
23	573	506625	0.50	$5.02\ 10^{-6}$	$2.82\ 10^{-5}$	$7.82\ 10^{-7}$	$9.29\ 10^{-4}$	$6.20\ 10^{-4}$
24	573	506625	0.25	$2.33\ 10^{-6}$	$1.43\ 10^{-5}$	$3.85\ 10^{-7}$	$6.82\ 10^{-4}$	$2.11\ 10^{-4}$
25	573	506625	0.25	$2.33\ 10^{-6}$	$1.43\ 10^{-5}$	$3.85\ 10^{-7}$	$6.82\ 10^{-4}$	$2.11\ 10^{-4}$
26	573	506625	0.25	$2.33\ 10^{-6}$	$1.43\ 10^{-5}$	$3.85\ 10^{-7}$	$6.82\ 10^{-4}$	$2.11\ 10^{-4}$
27	573	506625	0.50	$5.01\ 10^{-6}$	$2.83\ 10^{-5}$	$7.08\ 10^{-7}$	$9.29\ 10^{-4}$	$9.29\ 10^{-4}$
28	573	506625	0.50	$5.01\ 10^{-6}$	$2.83\ 10^{-5}$	$7.08\ 10^{-7}$	$9.29\ 10^{-4}$	$9.29\ 10^{-4}$
29	573	506625	0.50	$5.02\ 10^{-6}$	$2.82\ 10^{-5}$	$7.82\ 10^{-7}$	$1.24\ 10^{-3}$	$6.20\ 10^{-4}$
30	573	506625	0.50	$5.02\ 10^{-6}$	$2.82\ 10^{-5}$	$7.82\ 10^{-7}$	$1.24\ 10^{-3}$	$6.20\ 10^{-4}$
31	573	506625	0.50	$5.02\ 10^{-6}$	$2.82\ 10^{-5}$	$7.82\ 10^{-7}$	$1.24\ 10^{-3}$	$6.20\ 10^{-4}$
32	573	506625	0.50	$5.02\ 10^{-6}$	$2.82\ 10^{-5}$	$7.82\ 10^{-7}$	$1.24\ 10^{-3}$	$6.20\ 10^{-4}$
33	573	506625	0.50	$5.02\ 10^{-6}$	$2.82\ 10^{-5}$	$7.82\ 10^{-7}$	$1.24\ 10^{-3}$	$6.20\ 10^{-4}$
34	573	506625	0.50	$5.02\ 10^{-6}$	$2.82\ 10^{-5}$	$7.82\ 10^{-7}$	$1.24\ 10^{-3}$	$6.20\ 10^{-4}$
35	573	506625	0.50	$5.02\ 10^{-6}$	$2.82\ 10^{-5}$	$7.82\ 10^{-7}$	$1.24\ 10^{-3}$	$6.20\ 10^{-4}$

Table A-5. Experimental results for anisole HDO on $NiCu/ZrO_2$.

	$F_{anisole}$ [mol s^{-1}]	F_{phenol} [mol s^{-1}]	F_{cresol} [mol s^{-1}]	$F_{benzene}$ [mol s^{-1}]	$F_{toluene}$ [mol s^{-1}]	$F_{cyclohexane}$ [mol s^{-1}]	F_{xylene} [mol s^{-1}]
1	$3.45\ 10^{-6}$	$2.60\ 10^{-7}$	$4.72\ 10^{-9}$	$3.10\ 10^{-6}$	$1.70\ 10^{-8}$	$5.32\ 10^{-7}$	$1.42\ 10^{-8}$
2	$3.87\ 10^{-6}$	$2.92\ 10^{-7}$	$5.81\ 10^{-9}$	$2.76\ 10^{-6}$	$1.62\ 10^{-8}$	$4.88\ 10^{-7}$	$1.32\ 10^{-8}$
3	$3.84\ 10^{-6}$	$2.40\ 10^{-7}$	$4.95\ 10^{-9}$	$2.92\ 10^{-6}$	$1.55\ 10^{-8}$	$4.97\ 10^{-7}$	$1.23\ 10^{-8}$
4	$3.63\ 10^{-6}$	$2.53\ 10^{-7}$	$5.12\ 10^{-9}$	$2.99\ 10^{-6}$	$1.54\ 10^{-8}$	$5.51\ 10^{-7}$	$1.37\ 10^{-8}$
5	$2.09\ 10^{-6}$	$1.58\ 10^{-7}$	$3.46\ 10^{-9}$	$2.87\ 10^{-6}$	$1.63\ 10^{-8}$	$5.48\ 10^{-7}$	$1.47\ 10^{-9}$
6	$2.29\ 10^{-6}$	$1.56\ 10^{-7}$	$3.58\ 10^{-9}$	$2.65\ 10^{-6}$	$1.61\ 10^{-8}$	$5.37\ 10^{-7}$	$1.42\ 10^{-9}$
7	$2.34\ 10^{-6}$	$1.69\ 10^{-7}$	$4.07\ 10^{-9}$	$1.53\ 10^{-6}$	$1.66\ 10^{-8}$	$3.73\ 10^{-7}$	$1.07\ 10^{-9}$
8	$1.32\ 10^{-6}$	$1.14\ 10^{-7}$	$3.01\ 10^{-9}$	$2.18\ 10^{-6}$	$1.95\ 10^{-8}$	$6.14\ 10^{-7}$	$1.02\ 10^{-9}$
9	$1.20\ 10^{-6}$	$1.16\ 10^{-7}$	$2.54\ 10^{-9}$	$2.40\ 10^{-6}$	$1.72\ 10^{-8}$	$6.10\ 10^{-7}$	$8.88\ 10^{-10}$
10	$1.38\ 10^{-6}$	$5.68\ 10^{-8}$	$1.80\ 10^{-9}$	$2.60\ 10^{-6}$	$1.59\ 10^{-8}$	$6.72\ 10^{-7}$	$6.74\ 10^{-9}$
11	$1.27\ 10^{-6}$	$6.46\ 10^{-8}$	$1.80\ 10^{-9}$	$2.60\ 10^{-6}$	$1.60\ 10^{-8}$	$6.73\ 10^{-7}$	$6.47\ 10^{-9}$
12	$7.51\ 10^{-7}$	$8.35\ 10^{-8}$	$2.12\ 10^{-9}$	$1.93\ 10^{-6}$	$1.40\ 10^{-8}$	$5.60\ 10^{-7}$	$7.76\ 10^{-10}$
13	$2.63\ 10^{-6}$	$2.65\ 10^{-7}$	$5.37\ 10^{-9}$	$1.85\ 10^{-6}$	$1.18\ 10^{-8}$	$2.18\ 10^{-7}$	$1.03\ 10^{-8}$
14	$2.66\ 10^{-6}$	$2.62\ 10^{-7}$	$4.59\ 10^{-9}$	$1.82\ 10^{-6}$	$1.21\ 10^{-8}$	$2.16\ 10^{-7}$	$8.96\ 10^{-9}$
15	$2.24\ 10^{-6}$	$2.95\ 10^{-7}$	$5.46\ 10^{-9}$	$2.09\ 10^{-6}$	$1.36\ 10^{-8}$	$2.47\ 10^{-7}$	$1.00\ 10^{-8}$
16	$2.10\ 10^{-6}$	$6.82\ 10^{-7}$	$2.54\ 10^{-8}$	$1.90\ 10^{-6}$	$1.27\ 10^{-8}$	$2.27\ 10^{-7}$	$6.78\ 10^{-9}$
17	$1.67\ 10^{-6}$	$1.07\ 10^{-7}$	$2.54\ 10^{-9}$	$2.43\ 10^{-6}$	$1.65\ 10^{-8}$	$4.68\ 10^{-7}$	$6.80\ 10^{-9}$
18	$1.65\ 10^{-6}$	$1.19\ 10^{-7}$	$2.76\ 10^{-9}$	$2.38\ 10^{-6}$	$1.54\ 10^{-8}$	$4.51\ 10^{-7}$	$8.31\ 10^{-9}$
19	$1.94\ 10^{-6}$	$1.09\ 10^{-7}$	$2.55\ 10^{-9}$	$2.26\ 10^{-6}$	$1.40\ 10^{-8}$	$4.10\ 10^{-7}$	$7.45\ 10^{-9}$

Table A-6. Experimental results for anisole HDO on $NiCu/ZrO_2$ (continued).

	$F_{anisole}$ [mol s^{-1}]	F_{phenol} [mol s^{-1}]	F_{cresol} [mol s^{-1}]	$F_{benzene}$ [mol s^{-1}]	$F_{toluene}$ [mol s-^{1}]	$F_{cyclohexane}$ [mol s^{-1}]	F_{xylene} [mol s^{-1}]
20	$1.58\ 10^{-6}$	$1.26\ 10^{-7}$	$2.98\ 10^{-9}$	$2.97\ 10^{-6}$	$1.62\ 10^{-8}$	$1.05\ 10^{-6}$	$3.91\ 10^{-10}$
21	$7.04\ 10^{-7}$	$3.26\ 10^{-8}$	$1.40\ 10^{-9}$	$2.72\ 10^{-6}$	$1.60\ 10^{-8}$	$1.10\ 10^{-6}$	$5.06\ 10^{-10}$
22	$8.29\ 10^{-7}$	$2.96\ 10^{-8}$	$1.32\ 10^{-9}$	$2.64\ 10^{-6}$	$1.64\ 10^{-8}$	$1.12\ 10^{-6}$	$5.35\ 10^{-10}$
23	$8.83\ 10^{-7}$	$2.73\ 10^{-8}$	$1.92\ 10^{-9}$	$1.09\ 10^{-6}$	$1.16\ 10^{-8}$	$1.63\ 10^{-7}$	$7.41\ 10^{-9}$
24	$6.47\ 10^{-7}$	$5.59\ 10^{-8}$	$1.54\ 10^{-9}$	$1.00\ 10^{-6}$	$1.07\ 10^{-8}$	$1.68\ 10^{-7}$	$7.54\ 10^{-9}$
25	$5.62\ 10^{-7}$	$5.94\ 10^{-8}$	$1.62\ 10^{-9}$	$1.19\ 10^{-6}$	$1.13\ 10^{-8}$	$1.61\ 10^{-7}$	$6.66\ 10^{-9}$
26	$6.33\ 10^{-7}$	$4.73\ 10^{-8}$	$1.00\ 10^{-9}$	$1.19\ 10^{-6}$	$1.13\ 10^{-8}$	$1.61\ 10^{-7}$	$6.66\ 10^{-9}$
27	$1.21\ 10^{-6}$	$2.88\ 10^{-8}$	$1.83\ 10^{-9}$	$2.21\ 10^{-6}$	$1.16\ 10^{-8}$	$1.40\ 10^{-6}$	$9.43\ 10^{-9}$
28	$8.13\ 10^{-7}$	$3.20\ 10^{-8}$	$1.58\ 10^{-9}$	$2.07\ 10^{-6}$	$1.02\ 10^{-8}$	$1.92\ 10^{-6}$	$7.94\ 10^{-9}$
29	$3.60\ 10^{-6}$	$2.93\ 10^{-7}$	$9.60\ 10^{-9}$	$8.23\ 10^{-7}$	$5.20\ 10^{-9}$	$2.41\ 10^{-7}$	$9.15\ 10^{-9}$
30	$3.62\ 10^{-6}$	$2.79\ 10^{-7}$	$9.58\ 10^{-9}$	$8.17\ 10^{-7}$	$5.37\ 10^{-9}$	$2.31\ 10^{-7}$	$7.44\ 10^{-9}$
31	$7.92\ 10^{-7}$	2.06 10-8	$1.78\ 10^{-9}$	$2.71\ 10^{-6}$	1.84 10-8	$8.11\ 10^{-7}$	$3.18\ 10^{-10}$
32	$1.38\ 10^{-6}$	5.68 10-8	$1.80\ 10^{-9}$	$2.60\ 10^{-6}$	1.59 10-8	$6.72\ 10^{-7}$	$6.74\ 10^{-9}$
33	$1.27\ 10^{-6}$	6.46 10-8	$1.80\ 10^{-9}$	$2.60\ 10^{-6}$	1.60 10-8	$6.73\ 10^{-7}$	$6.47\ 10^{-9}$
34	$1.43\ 10^{-6}$	8.24 10-8	$2.16\ 10^{-9}$	$2.50\ 10^{-6}$	1.53 10-8	$6.63\ 10^{-7}$	$6.26\ 10^{-9}$
35	$1.42\ 10^{-6}$	8.25 10-8	$2.44\ 10^{-9}$	$2.53\ 10^{-6}$	1.51 10-8	$6.49\ 10^{-7}$	$7.09\ 10^{-9}$

Table A-7. Experimental results for anisole HDO on $NiCu/ZrO_2$ (continued).

	$F_{methylcyclohexane}$ [mol s^{-1}]	F_{CH4} [mol s^{-1}]	F_{MeOH} [mol s^{-1}]
1	$2.38\ 10^{-9}$	$4.94\ 10^{-6}$	$3.48\ 10^{-7}$
2	$2.39\ 10^{-9}$	$4.21\ 10^{-6}$	$3.45\ 10^{-7}$
3	$2.32\ 10^{-9}$	$4.31\ 10^{-6}$	$2.62\ 10^{-7}$
4	$2.57\ 10^{-9}$	$4.35\ 10^{-6}$	$2.76\ 10^{-7}$
5	$2.27\ 10^{-9}$	$4.35\ 10^{-6}$	$3.58\ 10^{-7}$
6	$2.20\ 10^{-9}$	$4.30\ 10^{-6}$	$3.41\ 10^{-7}$
7	$2.76\ 10^{-9}$	$7.21\ 10^{-6}$	$5.06\ 10^{-7}$
8	$2.52\ 10^{-9}$	$5.58\ 10^{-6}$	$1.00\ 10^{-6}$
9	$2.43\ 10^{-9}$	$4.85\ 10^{-6}$	$6.17\ 10^{-7}$
10	$2.75\ 10^{-9}$	$4.49\ 10^{-6}$	$4.38\ 10^{-7}$
11	$2.71\ 10^{-9}$	$4.62\ 10^{-6}$	$4.53\ 10^{-7}$
12	$2.20\ 10^{-9}$	$3.79\ 10^{-6}$	$4.38\ 10^{-7}$
13	$1.19\ 10^{-9}$	$3.02\ 10^{-6}$	$3.23\ 10^{-7}$
14	$1.56\ 10^{-9}$	$2.98\ 10^{-6}$	$3.22\ 10^{-7}$
15	$1.46\ 10^{-9}$	$3.51\ 10^{-6}$	$3.73\ 10^{-7}$
16	$1.65\ 10^{-9}$	$3.44\ 10^{-6}$	$4.06\ 10^{-7}$
17	$1.97\ 10^{-9}$	$4.65\ 10^{-6}$	$6.14\ 10^{-7}$
18	$2.31\ 10^{-9}$	$4.40\ 10^{-6}$	$5.39\ 10^{-7}$
19	$1.79\ 10^{-9}$	$3.92\ 10^{-6}$	$4.28\ 10^{-7}$

Table A-8. Experimental results for anisole HDO on $NiCu/ZrO_2$ (continued).

	$F_{methylcyclohexane}$ [mol s^{-1}]	F_{CH4} [mol s^{-1}]	F_{MeOH} [mol s^{-1}]
20	$2.40\ 10^{-9}$	$4.50\ 10^{-6}$	$5.81\ 10^{-7}$
21	$3.48\ 10^{-9}$	$4.68\ 10^{-6}$	$3.31\ 10^{-7}$
22	$3.44\ 10^{-9}$	$4.89\ 10^{-6}$	$3.78\ 10^{-7}$
23	$3.48\ 10^{-9}$	$4.75\ 10^{-6}$	$3.91\ 10^{-7}$
24	$1.27\ 10^{-9}$	$3.68\ 10^{-6}$	$8.55\ 10^{-7}$
25	$1.24\ 10^{-9}$	$4.36\ 10^{-6}$	$1.16\ 10^{-6}$
26	$9.43\ 10^{-10}$	$3.22\ 10^{-6}$	$6.50\ 10^{-7}$
27	$4.42\ 10^{-9}$	$4.37\ 10^{-6}$	$2.56\ 10^{-7}$
28	$4.36\ 10^{-9}$	$4.55\ 10^{-6}$	$1.90\ 10^{-7}$
29	$1.57\ 10^{-9}$	$1.49\ 10^{-6}$	$1.42\ 10^{-7}$
30	$1.42\ 10^{-9}$	$1.47\ 10^{-6}$	$1.36\ 10^{-7}$
31	$2.85\ 10^{-9}$	$5.78\ 10^{-6}$	$7.95\ 10^{-7}$
32	$2.75\ 10^{-9}$	$4.49\ 10^{-6}$	$4.38\ 10^{-7}$
33	$2.71\ 10^{-9}$	$4.62\ 10^{-6}$	$4.53\ 10^{-7}$
34	$2.73\ 10^{-9}$	$4.38\ 10^{-6}$	$4.54\ 10^{-7}$
35	$2.66\ 10^{-9}$	$4.48\ 10^{-6}$	$4.36\ 10^{-7}$

Appendix B

Gas chromatograph method

B.1. Introduction

The analysis of the reactor effluent is performed with a designed method that provides a qualitative separation of the various compounds within an acceptable analysis time. The method is dependent on the type of the column, which in these experiments was a non-polar capillary column (DB-1, 60 m x 0.25 mm i.d. x 0.25 µm dimethylpolysiloxane).

B.2. Temperature profile for experiments with the CoMo/γ-Al_2O_3 catalyst

The designed temperature profile, with a total analysis time of 32 minutes, is shown in Figure B-1 and Table B-1.

Table B-1. Input data for the temperature profile for the experiments performed over a CoMo/γ-Al_2O_3 catalyst.

Rate [K min^{-1}]	Next temperature [K]	Hold time [min]
	343	10
3	409	0

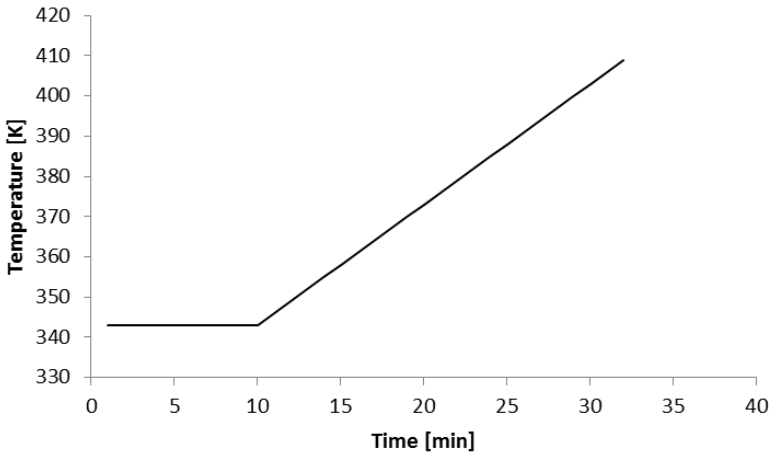

Figure B-1. Designed temperature profile for the experiments performed over a CoMo/γ-Al_2O_3 catalyst.

Other specifications for the analysis are listed in Table B-2.

Table B-2. Settings of the DB-1 column.

Parameter	Condition
Temperature	
Inlet	523 K
Detector	573 K
He inlet flow rate	0.82 ml min^{-1}
Split ratio	1:1
Detector	
H_2 flow rate	40 ml min-1
Air flow rate	450 ml min^{-1}
Make up gas (N_2) flow rate	0 ml min^{-1}

In Table B-3 the retention times, corresponding to the mentioned temperature program, are listed for various products. The identification of the peaks was done by identifying the composition by a GCxGC, and injecting these compounds into the GC.

Table B-3. Retention times for various compounds for the experiments performed over a CoMo/γ-Al_2O_3 catalyst.

Compound	Retention time [min]
Ethane	6.360
Hexane	7.665
Benzene	8.411
Toluene	10.947
Anisole	17.291
Phenol	20.592
Cresol	24.834

B.3. Temperature profile for experiments with the $NiCu/ZrO_2$ catalyst

A new temperature profile, with a total analysis time of 38 minutes, was developed for the experiments over the $NiCu/ZrO_2$ catalyst and is shown in Figure B-2 and Table B-4. This profile starts at a lower temperature, resulting in a better separation of the lighter compounds. Other specifications for the analysis are listed in Table B-2.

Table B-4. Input data for the temperature profile for the experiments performed over a $NiCu/ZrO_2$ catalyst.

Rate [K min^{-1}]	Next temperature [K]	Hold time [min]
	313	5
3	343	0
5	408	10

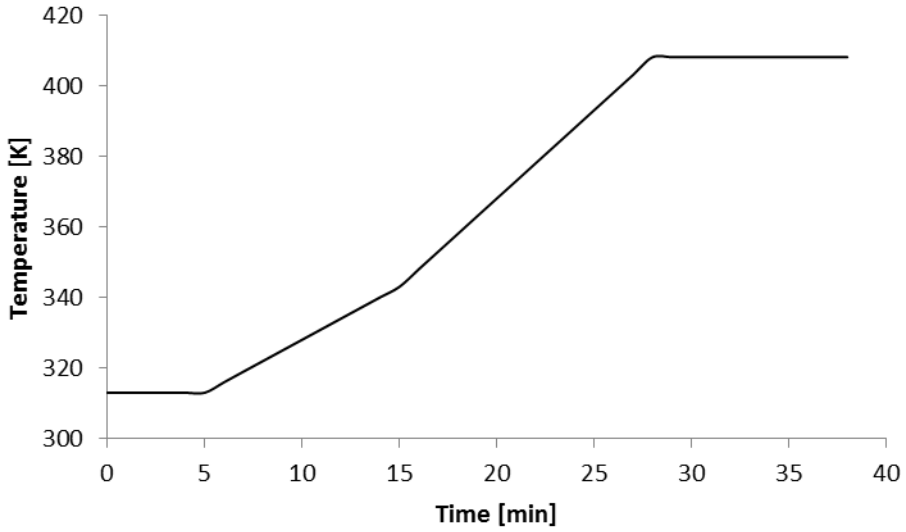

Figure B-2. Designed temperature profile for the experiments performed over a $NiCu/ZrO_2$ catalyst.

In Table B-5 the retention times, corresponding to the mentioned temperature program, are listed for various products. The identification of the peaks was also done by identifying the composition by a GCxGC, and injecting these compounds into the GC.

Table B-5. Retention times for various compounds for the experiments performed over a $NiCu/ZrO_2$ catalyst.

Compound	Retention time [min]
Methane	6.653
Methanol	6.740
Hexane	9.616
Methylcyclopentane	10.501
Benzene	11.160
Cyclohexane	11.664
Cyclohexene	12.152
Methylcyclohexane	14.406
Toluene	15.719
Octane	17.877
Xylene	21.001
Cyclohexanone	21.747
Cyclohexanol	21.927
Anisole	22.403
Methylcyclohexanone	24.211
Phenol	25.510
Cresol	27.792

Appendix C

Calibration factors

C.1 Introduction

The response of the FID in the gas chromatograph is proportional to the detected carbon ions of the analyzed compound. To calculate quantitatively the results from the GC analysis, a calibration factor is used. This factor is a correction as function of the response of a given compound to the FID.

The calibration factors encountered during the thesis for various compounds are listed below.

C.2 Calibration factors for the experiments with the CoMo/γ-Al_2O_3 catalyst

Table C-1. Calibration factors for the reactants and products observed during the HDO of anisole on CoMo/γ-Al_2O_3 catalyst.

Compound	Retention time [min]	Calibration factor [-]
Ethane	6.360	1.00
Hexane	7.665	1.00
Benzene	8.411	2.55
Toluene	10.947	2.55
Anisole	17.291	1.76
Phenol	20.592	1.31
Cresol	24.834	1.90

C.3 Calibration factors for the experiments with the $NiCu/ZrO_2$ catalyst

Table C-2. Calibration factors for the reactants and products observed during the HDO of anisole on $NiCu/ZrO_2$ catalyst.

Compound	Retention time [min]	Calibration factor [-]
Methane	6.653	0.99
Methanol	6.740	0.24
Hexane	9.616	0.98
Methylcyclopentane	10.501	1.04
Benzene	11.160	1.25
Cyclohexane	11.664	1.04
Cyclohexene	12.152	0.89
Methylcyclohexane	14.406	1.04
Toluene	15.719	1.25
Octane	17.877	1.00
Xylene	21.001	1.25
Cyclohexanone	21.747	0.79
Cyclohexanol	21.927	0.79
Anisole	22.403	1.04
Methylcyclohexanone	24.211	1.07
Phenol	25.510	1.07
Cresol	27.792	0.79

Appendix D
Reaction conditions to obtain intrinsic kinetics

D.1 Introduction

One of the objectives of this thesis, is the construction of a fundamental kinetic model for anisole and phenol HDO. In this kinetic model, the reactor is assumed to operate in an ideal isothermal plug flow regime, i.e. without mass or heat transfer limitations. Therefore, the experimental data obtained from the HTK-1, should only depend on the kinetics of the reactions, i.e. intrinsic kinetic data.

This chapter contains criteria that were used to verify intrinsic kinetics. A general criterion for intrinsic kinetics is given by D-1, meaning that the production rate difference due to a gradient, should be smaller than 5 %.

$$\left|\frac{R^{obs} - R^{intr}}{R^{intr}}\right| < 0.05 \qquad \text{D-1}$$

Where R^{obs} is the observed rate of production and R^{intr} is the intrinsic rate of production, both expressed in kg_{cat} s mol^{-1}. The production rate of a component *A* for stoichiometric multiple reactions is given by

$$R_A = \sum_{i=1}^{N} \nu_{iA} r_i \qquad \text{D-2}$$

With N: the number of reactions [-]

ν_{iA}: the stoichiometric coefficient [-]

r_i: the reaction rate for reaction i [kg_{cat} s mol^{-1}]

The reaction rate is given by

$$r = k\, f(C_A) = A exp\left(-\frac{E_a}{RT}\right) f(C_A) \qquad \text{D-3}$$

With k: the rate coefficient, for a first order reaction [s^{-1}]

A: the pre-exponential factor, for a first order reaction [s^{-1}]

E_a: the (apparent) activation energy of the reaction [J mol^{-1}]

R: the universal gas constant [J mol^{-1} K^{-1}]

T: the temperature [K]

$f(C_A)$: a function of the concentration of the reactant A [reaction dependent]

D.2 The plug flow reactor

D.2.1 Criteria for plug flow

The reactor model, as discussed in Chapter 3, assumed an ideal plug flow regime. This model assumes that the reactants flow continuously through a tube like a plug, and the following assumptions are made:

- there is only flow in axial direction, i.e. parallel to the reactor axis;
- the flow is uniform in the radial direction, i.e. perpendicular to the reactor axis;
- forced convection takes place.

The radial diffusion is described by an effective radial diffusion coefficient $D_{r,eff}$, using the Péclet number Pe'_{mr}.

$$Pe'_{mr} = \frac{u d_p}{D_{r,eff}} \qquad \text{D-4}$$

With u: the gas velocity [m s^{-1}]

d_p: diameter of the catalyst pellets [m]

$D_{r,eff}$: the effective radial diffusion coefficient [m_{fluid}^3 $m_{reactor}^{-1}$ s^{-1}]

Deviations from plug flow can be caused by a more loose packing of the catalyst pellets near the wall, resulting in a radial velocity profile. Froment[1] was able to take the wall effects into account with a correction factor on the Péclet number, where d_t is diameter of the reactor [m].

$$\frac{Pe'_{mr}}{1 + 19.4\left(\frac{d_p}{d_t}\right)^2} = \frac{u d_p}{D_{r,eff}} \qquad \text{D-5}$$

The wall effects can be neglected when the denominator is close to unity. As a rule of thumb, criterion D-6 is chosen.

$$\frac{d_t}{d_p} > 10 \qquad \text{D-6}$$

The concentration profile of a reactant A, C_A, in an plug flow reactor with effective axial diffusion $D_{a,eff}$ and a first order reaction is given the following equation.

$$C_A = C_{A,0} \exp(-k\tau_0) \exp\left(\frac{(k\tau_0)^2}{Pe_a}\right) \qquad \text{D-7}$$

With $C_{A,0}$: the initial concentration of reactant A [mol s^{-1}]

τ_0: the residence time of the plug [s], calculated as $\tau_0 = \frac{L_{bed}}{u}$

Pe_a: the Péclet number [-] based on the length of the catalyst bed L_{bed} [m], calculated as $Pe_a = \frac{uL_{bed}}{D_{a,eff}}$

Whereas, for an ideal plug flow reactor the concentration profile is given by D-8.

$$C_A = C_{A,0} \exp(-k_1\tau_0|_{PFR}) \qquad \text{D-8}$$

Thus, the second exponential in D-7 takes the deviation from ideality into account. The effect of axial diffusivity can be neglected when D-9 is fulfilled.

$$\frac{\tau_0|_{PFR}}{\tau_0} = 1 - \frac{k\tau_0}{Pe_a} > 0.95 \qquad \text{D-9}$$

The Péclet number Pe_a can be related to the catalyst pellet diameter via D-10.

$$Pe'_a = \frac{Pe_a d_p}{L_{bed}} \qquad \text{D-10}$$

Substituting D-10 into D-9 and rearranging yields criterion D-11.

$$\frac{L_{bed}}{d_p} > \frac{20k\tau_0}{Pe'_a} \qquad \text{D-11}$$

The conversion profile for a plug flow reactor is given by D-12, where X_A is the conversion of reactant A [-].

$$X_A = 1 - \exp(-k\tau_0) \qquad \text{D-12}$$

Combining D-11 with D-12 yields a criterion for the negligibility of axial diffusion effects, given by D-13. For n-th order reactions, the right-hand side of D-13 should be multiplied with n.

$$\frac{L_{bed}}{d_p} > \frac{20}{Pe'_a} \ln\left(\frac{1}{1 - X_A}\right) \qquad \text{D-13}$$

Introducing typical values, $Pe'_a = 1$ and $X_A = 0.9$, results in a often used rule of thumb[2]:

$$\frac{L_{bed}}{d_p} > 50 \qquad \text{D-14}$$

From the rules of thumb, D-6 and D-14, it can be concluded that the diameter of the catalyst pellets should be smaller than 600 µm. For the experiments the catalyst is pelletized in diameters between 400 µm and 600 µm to satisfy the criteria. Smaller diameters would satisfy the criteria, but the catalyst pellets could be blown out of the reactor as well as increase the pressure drop.

D.2.2 Criteria for isothermicity

A reactor is considered isothermal if the temperature deviation is sufficiently small to limit production rate deviations.

$$0.95 < \frac{R_A(T)}{R_A(T + \Delta T)} < 1.05 \qquad \text{D-15}$$

One can distinguish isothermicity in the axial and in the radial direction. An axial temperature profile may be present in the reactor, i.e. a higher temperature at the outlet of the reactor than at the inlet, due to the heat produced during the reaction. To improve the axial isothermicity, the catalyst bed can be diluted with inert material, e.g. α-alumina or porcelain. By diluting the catalyst bed, the heat production per unit volume will decrease and the effective conductivity will increase. Nevertheless, the dilution may affect the conversion. When the dilution is too large, the reactants have a smaller opportunity to interact with the catalyst. Therefore, Berger *et al.*[3] proposed a maximum dilution degree b [$m_{intert}^3\ m_{inert+cat}^{-3}$].

$$b < \frac{1}{1 + 10X_{dil}\left(d_p / L_{bed}\right)} \qquad \text{D-16}$$

With X_{dil}: the conversion obtained with a diluted catalyst bed [-]

From criterion D-16, it is clear that a longer catalyst bed and a lower pellet diameter allow a larger dilution. On the other hand, the ratio of the catalyst bed to the catalyst pellet diameter is already determined by criterion D-14. Using this criterion, a maximum dilution degree of 99 vol% [$m_{intert}^3\ m_{inert+cat}^{-3}$] is allowed. During the experiments a dilution of 50 vol% is used.

Due to the lower packing of the catalyst pellets near the wall, the temperature will decrease near the wall resulting in a radial temperature profile. Radial isothermicity is easier to achieve at small tube diameters, but criterion D-14 is then less satisfied. To avoid this, the pellet diameter should also be decreased, which will increase the pressure drop over the bed (see section D.2.3).

Mears[4] has derived criterion D-17 to validate the radial isothermicity inside a tubular reactor assuming a maximum deviation of 5 % to the intrinsic production rate. When the temperature at the wall is measured instead of the temperature at the centerline of the bed, criterion D-18 is applied. In the latter, the Biot number accounts for the heat transfer trough the reactor wall.

$$\Delta T_{rad} = \frac{R_{v,A}^{obs} |\Delta_r H| (1-\varepsilon_b)(1-b) d_t^2}{32 \lambda_{er}} < \frac{0.05 R T_w^2}{E_a} \qquad \text{D-17}$$

$$\Delta T_{rad} = \left(1 + \frac{8}{Bi_w}\right) \frac{R_{v,A}^{obs} |\Delta_r H| (1-\varepsilon_b)(1-b) d_t^2}{32 \lambda_{er}} < \frac{0.05 R T_w^2}{E_a} \qquad \text{D-18}$$

With ΔT_{rad}: the radial temperature difference [K]

$\Delta_r H$: the reaction enthalpy [J mol^{-1}]

$1-\varepsilon_b$: the fraction of the reactor volume occupied by the catalyst bed [m_{bed}^3 $m_{reactor}^{-3}$]

$1-b$: the fraction of the catalyst bed occupied by the catalyst [m_{cat}^3 m_{bed}^{-3}]

λ_{er}: the effective radial heat conductivity of the catalyst bed [W $m_{reactor}^{-1}$ K^{-1}]

T_w: the temperature near the wall [K]

Bi_w: the Biot number at the internal reactor wall [-], defined as $Bi_w = \frac{\alpha_w d_t}{\lambda_{er}}$

α_w: the heat transfer coefficient between the catalyst bed and the internal reactor wall [W $m_{reactor}^{-2}$ K^{-1}]

For those criteria two parameters, the effective radial heat conductivity of the catalyst bed λ_{er} and the heat transfer coefficient between the catalyst bed and the internal reactor wall α_w, should be known, for which correlations can be found in literature.

D.2.3 Pressure drop

Due to the presence of the catalyst and inert particles, a pressure drop takes place. Since the pressure drop influences the kinetics, it should be limited. When criterion D-19 is satisfied, the effect of pressure drop is negligible[3].

$$\Delta P < \frac{0.2 P_{tot}}{n} \qquad \text{D-19}$$

With ΔP: the pressure drop over the catalyst bed [Pa]

P_{tot}: the feed pressure [Pa]

n: the reaction order [-]

The pressure drop over the tubular reactor follows from the application of the laws of conservation of momentum.

$$\frac{\Delta P}{h_{bed}} = \frac{f_m \rho_g u_s^2}{d_{pe}} \qquad \text{D-20}$$

With f_m: the modified friction factor [-]

ρ_g: the gas density [kg m^{-3}]

u_s: the superficial gas velocity [m_f^3 $m_{reactor}^{-2}$ s^{-1}], defined as the ratio of the volumetric flow to the cross area of the reactor

d_{pe}: the equivalent pellet diameter [m], calculated as six times the ratio of the particle volume and the external surface area

Several empirical correlations exist for the estimation of the pressure drop of the reactor. A correlation for the friction factor follows from the widely applied Ergun equation[3]. This correlation is valid in the range of $0.1 < Re < 1000$.

$$f_m = \frac{(1-\varepsilon_b)}{\varepsilon_b^3}\left(1.75 + 150\frac{(1-\varepsilon_b)}{Re})\right) \qquad \text{D-21}$$

With f_m: modified friction factor [-]

ε_b: bed porosity [m_{void}^3 m_{bed}^{-3}]

Re: Reynolds number [-], the ratio of inertial forces to viscous forces

and

$$Re = \frac{d_{pe}\rho_g u_s}{\mu_g} \qquad \text{D-22}$$

With μ_g: gas viscosity [kg m^{-1} s^{-1}]

D.3 Transport limitations on pellet scale

To measure intrinsic kinetics, not only radial and axial gradients on reactor scale must be avoided but also those in and around catalyst pellets. Hence, the observed production rate $R(T_b, C_b)$ should be the consequence of reaction at (T_b, C_b). From Figure D-1 it is clear, that this is not that obvious due to the gradients in and around a catalyst pellet. One can

distinguish four cases: external temperature gradients, internal temperature gradients, external concentration gradients and internal concentration gradients.

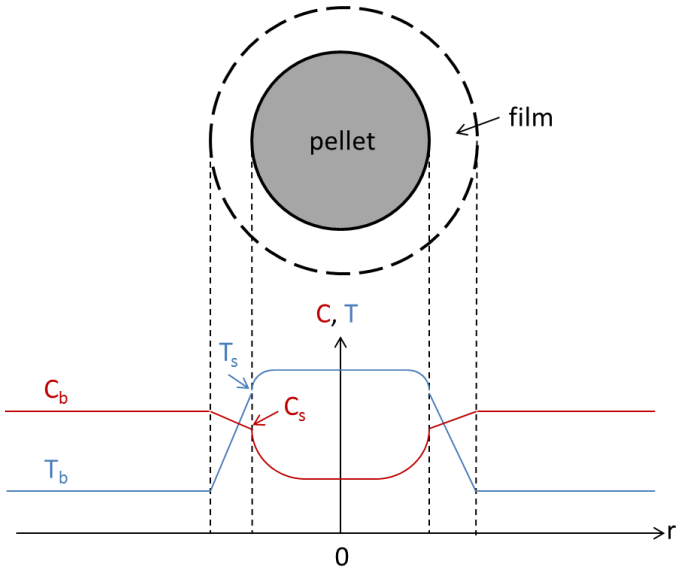

Figure D-1. Concentration (red) gradient and temperature (blue) profile for an exothermal reaction around and inside a catalyst pellet. The subscript b indicates bulk and s indicates surface.

On lab scale, internal temperature gradients are rather unimportant due to the small pellet diameter and good heat conductivity. Furthermore, the concentration gradients are more distinct around than in the catalyst pellet. The following order often holds for the presence of gradients[5]:

external temperature gradients	>	external concentration gradients	>	internal concentration gradients	>	internal temperature gradients

Criteria to allow the measurement of intrinsic kinetics, i.e. when the effect of the heat and mass transport limitations is negligible, will be discussed in the next subsection by considering that only one of the gradients cannot be neglected.

D.3.1 External heat transport limitations

Due to the exothermic reaction, the temperature in the bulk will be different from the temperature at the surface of the catalyst pellet. A linear temperature profile is assumed in the boundary layer around the pellet (Figure D-1). External heat transfer can be described based on the energy balance:

$$R_{v,A}^{obs}(-\Delta_r H)\left(\frac{\pi}{6}d_p^3\right) = \alpha_p(T_s - T_b)(\pi d_p^2) \qquad \text{D-23}$$

With α_p: the heat transfer coefficient between the catalyst pellet and the gas [W m_{cat}^{-2} K^{-1}]

T_s: the external surface temperature [K]

T_b: the bulk gas temperature [K]

The observed volumetric production rate is given by D-2, where the rate coefficient is temperature dependent by the Arrhenius law (D-3). Substitution of equation D-23 in criterion D-1 yields in a criterion with only observable or calculable quantities.

$$\Delta T_{film} = (T_s - T_b) = \frac{R_{v,A}^{obs} |\Delta_r H| d_p}{6\alpha_p} < \frac{0.05 R T_b^2}{E_a} \qquad \text{D-24}$$

With ΔT_{film}: the temperature difference over the film surrounding the catalyst particle [K]

In this criterion two parameters can be varied, being the catalyst pellet diameter d_p and the bulk gas temperature T_b. The diameter of the catalyst pellet is predetermined by the criteria D-6 and D-14 for plug flow.

The heat transfer coefficient between the catalyst pellet and the gas, α_p, can be calculated from the j_H–factor according to Chilton-Colburn[6].

$$j_H = \frac{\alpha_p}{c_p \phi_m} Pr^{\frac{2}{3}} = Nu_p Re_p^{-1} Pr^{\frac{-1}{3}} \qquad \text{D-25}$$

With c_p: the isobaric heat capacity of the catalyst pellet [J kg^{-1} K^{-1}]

ϕ_m: the mass flux [kg $m_{reactor}^{-2}$ s^{-1}]

Pr: the Prandlt number [-], the ratio of momentum diffusivity to thermal diffusivity

Nu: the Nusselt number [-], the ratio of convective to conductive heat transfer

and

$$Pr = \frac{\mu_g c_p}{\lambda} \qquad \text{D-26}$$

$$Nu_p = \frac{\alpha_p d_p}{\lambda} \qquad \text{D-27}$$

For packed bed reactors, the j_H–factor can be calculated from e.g. the correlation of de Acetis and Thodos[7].

$$j_H = \frac{1.10}{Re_p^{0.41} - 0.15} \text{ for } 13 < Re_p < 2136 \qquad \text{D-28}$$

D.3.2 External mass transport limitations

The reaction on the catalyst will also affect the concentration profile of the reactant, with a higher concentration of the reactant in the bulk than at the surface of the catalyst pellet. Due to the conversion of the reactant, a concentration gradient will be present in the film around the catalyst pellet. The concentration profile is assumed to be linear in the boundary layer (Figure D-1) and can be described with a mass balance over the boundary layer:

$$k_{f,A}\left(\pi d_p^2\right)\left(C_{A,b} - C_{A,s}\right) = R_{v,A}^{obs}\left(\frac{\pi}{6} d_p^3\right) \qquad \text{D-29}$$

With $k_{f,A}$: the mass transfer coefficient of reactant A [$m_{fluid}^3\ m_i^{-2}\ s^{-1}$]

$C_{A,b}$: the bulk concentration of reactant A [mol m_{gas}^{-3}]

$C_{A,s}$: the concentration of reactant A at the external pellet surface [mol m_{gas}^{-3}]

Based on this mass balance across the film around the catalyst pellet, criterion D-1 can be written as D-30 in which only observable or calculable quantities appear.

$$\mathrm{Ca} = \frac{C_{A,b} - C_{A,s}}{C_{A,b}} = \frac{R_{v,A}^{obs}}{k_{f,A} a_v C_{A,b}} < 0.05 \qquad \text{D-30}$$

With Ca: Carberry number [-]

a_v: the specific external surface area of a single catalyst particle [$m_i^2\ m_{cat}^{-3}$]

In this criterion, only the concentration of the reactant in the bulk $C_{A,b}$ can be varied.

The mass transfer coefficient of reactant A, $k_{f,A}$, can be calculated from the j_D–factor according to Chilton-Colburn[6].

$$j_D = \frac{k_{f,A}^0 y_{f,A} \rho_g}{\phi_m} Sc^{\frac{2}{3}} = ShRe_p^{-1} Sc^{-\frac{1}{3}} y_{f,A} \qquad \text{D-31}$$

With $k_{f,A}^0$: the mass transfer coefficient of reactant A [$m_{fluid}^3\ m_i^{-2}\ s^{-1}$]

$y_{f,A}$: the film factor [mol fraction]

Sc: the Schmidt number [-], the ratio of momentum diffusivity to mass diffusivity

Sh: the Sherwood number [-], the ratio of convective to diffusive transport

and

$$Sc = \frac{\mu_g}{\rho_g D_A} \qquad \text{D-32}$$

$$Sh = \frac{k_{f,A}^0 d_p}{D_A} \qquad \text{D-33}$$

With D_A: the molecular diffusion coefficient of component A [m_{fluid}^3 $m_{reactor}^{-1}$ s^{-1}]

The film factor corrects for non-equimolar counter diffusion the film around the catalyst pellet and is defined in D-34.

$$y_{f,A} = \frac{\left(1 + \delta_A y_{A,b}\right) - \left(1 + \delta_A y_{A,s}\right)}{\ln\left(\frac{1 + \delta_A y_{A,b}}{1 + \delta_A y_{A,s}}\right)} \qquad \text{D-34}$$

With

$$\delta_A = \frac{1}{|\nu_A|}\sum_{j=1}^{N} \nu_j \qquad \text{D-35}$$

For packed bed reactors, the j_D–factor can be calculated from e.g. the correlation of Gupta and Thodos[8].

$$j_D = 0.01 + \frac{0.863}{Re_p - 0.483} \text{ for } 1 < Re_p \qquad \text{D-36}$$

D.3.3 Internal mass transport limitations

Inside the catalyst pellet, a concentration profile may be present due to the presence of diffusion limitations. This concentration profile can be derived based on the mass balance of reactant A over an infinitesimally small spherical shell of the catalyst.

$$N_A S|_r + R_v dV - N_A S|_{r+dr} = 0 \qquad \text{D-37}$$

With $N_{A,r}$ the molar flux of reactant A in the radial direction r [mol m^{-2} s^{-1}]. The molar flux of a reactant can be expressed via the Fick's law (D-38).

$$N_{A,r} = -D_A \frac{dC_A}{dr} \qquad \text{D-38}$$

Integration is easily managed by introduction a dimensionless group φ, known as the Thiele modulus.

$$\varphi = \frac{1}{a_v}\sqrt{\frac{k_v}{D_A}} \qquad \text{D-39}$$

For first order reactions, the integration results in the following concentration profile.

$$\frac{C_A}{C_{A,s}} = \frac{d_p}{2r} \frac{\sinh\left(r\sqrt{\frac{k_v}{D_A}}\right)}{\sinh\left(\frac{d_p}{2}\sqrt{\frac{k_v}{D_A}}\right)} \qquad \text{D-40}$$

When the Thiele modulus is approaching zero, in other words, the diffusion coefficient is high compared to the reaction rate, the concentration across the catalyst is uniform and almost equal to the surface concentration. On the other hand, a high value of the Thiele modulus corresponds to a fast the reaction rate compared to the diffusion rate, resulting in a concentration profile.

The relationship between diffusion and reaction limitations is defined by the effectiveness factor η.

$$\eta = \frac{actual\ reaction\ rate}{reaction\ rate\ at\ the\ external\ surface} = \frac{\int_V R_V(C_A)dV}{R_V(C_{A,s})V} \qquad \text{D-41}$$

Substitution of D-40 into D-41 yields in D-42.

$$\eta = \frac{1}{\varphi}\left(\frac{1}{\tanh(3\varphi)} - \frac{1}{3\varphi}\right) \qquad \text{D-42}$$

Internal diffusion limitations are negligible when the Thiele modulus is approaching zero ($\varphi \ll 1$) and the effectiveness factor is sufficiently high ($\eta > 0.95$). For the calculation of the Thiele modulus, the intrinsic kinetics of the reactions have to be known. Therefore it is more convenient to use the Weisz modulus, since it is based on the measured production rate. The definition of the Weisz modulus Φ is given by D-43.

$$\Phi = \eta\varphi^2 \qquad \text{D-43}$$

The Weisz modulus for nth order kinetics is obtained by the introduction of a general expression for the Thiele modulus (the full derivation can be found in 'Chemical Reactors: Applications and Fundamentals'[2]).

$$\Phi = \left(\frac{n+1}{2}\right)\frac{R_{v,A}^{obs}}{a_v^2 D_{A,eff} C_{A,s}} \qquad \text{D-44}$$

With $D_{A,eff}$ the effective diffusion coefficient of component *A*, which is corrected for the porosity and tortuosity of the pellet [m^2 s^{-1}].

It follows that low values of the Thiele modulus correspond with low values of Weisz modulus and vice versa. So a criterion of the negligibility of internal mass transfer limitations is given by D-45.

$$\left(\frac{n+1}{2}\right)\frac{R_{v,A}^{obs}}{a_v^2 D_{A,eff} C_{A,s}} \ll 1 \qquad \text{D-45}$$

D.3.4 Internal heat transport limitations

Heat transport limitations can cause a temperature gradient inside the catalyst pellet. For exothermal reactions, the temperature in the center of the catalyst will be higher than at the external surface of the pellet (Figure D-1). An energy balance over the external surface of the catalyst pellet is given in D-46.

$$R_{w,A}^{obs}\rho_P(-\Delta_r H)\left(\frac{\pi}{6}d_p^3\right) = \lambda_p(\pi d_p^2)\left.\frac{dT}{dr}\right|_{r=\frac{d_p}{2}} \qquad \text{D-46}$$

With $R_{w,A}^{obs}$: the specific production rate of A [mol kg^{-1}_{cat} s^{-1}]

ρ_P: the density of the catalyst pellet [kg_{cat} m_{cat}^{-3}]

λ_p: the thermal conductivity of the catalyst particle [W m_{cat}^{-1} K^{-1}]

A criterion for the maximal internal temperature difference between the external surface and the average in the particle, ΔT_{int}, can be obtained by applying a Tayler expansion on the production rate around T_s.

$$\Delta T_{int} = \frac{R_{v,A}^{obs}|\Delta_r H| d_p^2}{60\lambda_p} < \frac{0.05RT_s^2}{E_a} \qquad \text{D-47}$$

D.4 References

1. Froment, G. F., FIXED BED CATALYTIC REACTORS—CURRENT DESIGN STATUS. *Industrial & Engineering Chemistry* **1967,** 59, (2), 18-27.
2. Marin, G. B. *Chemical Reactors: Fundamentals and applications*; Ghent University: 2014.
3. Berger, R. J.; Stitt, E. H.; Marin, G.; Kapteijn, F.; Moulijn, J., Eurokin. Chemical Reaction Kinetics in Practice. *CATTECH* **2001,** 5, (1), 36-60.
4. Mears, D. E., Diagnostic criteria for heat transport limitations in fixed bed reactors. *Journal of Catalysis* **1971,** 20, (2), 127-131.
5. Marin, G.; Yablonsky, G. S., *Kinetics of chemical reactions*. John Wiley & Sons: 2011.
6. Ancheyta, J., *Modeling and Simulation of Catalytic Reactors for Petroleum Refining*. Wiley: 2011.
7. Acetis, J. D.; Thodos, G., Mass and Heat Transfer in Flow of Gases Through Spherical Packings. *Industrial & Engineering Chemistry* **1960,** 52, (12), 1003-1006.
8. Gupta, A. S.; Thodos, G., Mass and heat transfer in the flow of fluids through fixed and fluidized beds of spherical particles. *AIChE Journal* **1962,** 8, (5), 608-610.

Appendix E

Labjournal